Asteroid Deflection and Active Debris Removal Methods with Spaceborne Lasers

PhD Thesis

Nicolas Thiry

Aerospace Center of Excellence
Mechanical and Aerospace Department
University of Strathclyde, Glasgow

May 28, 2020

This thesis is the result of the author's original research. It has been composed by the author and has not been previously submitted for examination which has led to the award of a degree.

Nicolas
Thiry

Digitally signed by Nicolas Thiry
DN: cn=Nicolas Thiry, o, ou,
email=nicolas.thiry@strath.ac.uk,
c=FR
Date: 2020.06.20 11:04:11 +02'00'

Preface/Acknowledgements

Due acknowledgement are extended to the following persons without whom the achievements in this thesis would simply not have been possible:

First, my most sincere thanks go to my research supervisor, Max Vasile, for his patient guidance, enthusiastic encouragement and useful critiques all along this research work. In particular, Max's dedication to the Stardust project was a key driver and source of motivation (and funding!) for all the ESRs and ERs. His high standards and continuous push to publish have hopefully ensured that this work won't go unnoticed.

Secondly, I'd like to thank my former collegues stardusters who really made this research experience unique: Georgios, Ioannis, Fabien, Marko, Helen, Chiara, Stefano, Natalia, Clemens, Davide, Kartik, Piyush, Massimo and Aaron. I am convinced that our different meetings across (and beyond!) Europe have permanently reshaped my personality and been a great source of enriching exchanges.

I am also grateful to my colleagues at the University of Strathclyde, in particular those from the ASCL and cFASTT research groups for the many useful discussions during the many coffee breaks and for providing some essential building blocks of this thesis work. Special thanks go to JuanMa, Marilena (who provided the updated MP-AIDEA optimizer), Romain, Nicollo (who coded the spherical shaping algorithm), Lorenzo (who provided the updated MACS optimizer), Jimmy-John, Carlos, Andreas, Chiara (who helped me to keep a tidy desk).

Then, I would like to acknowledge the students who worked with Massimiliano Vasile on the papers from which the results of Chapter 4 were taken: Christie Maddock, Federico Zuiani, Alison Gibbings, Camilla Colombo, and Joan-Pau Sanchez Cuartielles. They are the giants on whose shoulders I was able to stand.

I also feel indebted to the team of professor A. Sasoh at the University of Nagoya and in particular Dr. Wang Bin for organising and allowing us to run the pulsed laser experiment in their facility with such a short time frame. Similarly, I am grateful to professor Yamakawa and K. Yamagauchi for allowing the 2-weeks research exchange with the University of Kyoto. I also acknowledge prof. P. Lubin, prof. Gary Hughes and T. Brashears for allowing me to visit the laser laboratory at the University of California Santa Barbara in Summer 2014 and pleasant discussions during the 2014 and 2015 SPIE conferences.

Finally, I am grateful to my parents, grandparents, close and extended family, girlfriend and friends for their enduring support during these years.

Last but not least, I am grateful to the European Commission, who funded this project through its FP7 Marie Curie ITN scheme.

Publications

Part of the work presented in this thesis has been the object of the following publications:

Books

- Asteroid and Space Debris Manipulation: Advances from the Stardust Research Network, Progress in Astronautics and Aeronautics (2016), co-author of chapter 14(Methods and Techniques for Asteroid Deflection) and 18(Lasers for Asteroid and Debris Deflection)

Journal papers

- Thiry, N., & Vasile, M. (2017). Statistical multi-criteria evaluation of non-nuclear asteroid deflection methods. Acta Astronautica, 140, 293-307.

- Thiry, N., & Vasile, M. (2017). Theoretical peak performance and optical constraints for the deflection of an S-type asteroid with a continuous wave laser. Advances in Space Research, 59(5), 1353-1367.

- Vasile, M., & Thiry, N. (2016). Nuclear cycler: An incremental approach to the deflection of asteroids. Advances in Space Research, 57(8), 1805-1819.

Conference Proceedings

- Thiry, N., & Vasile, M. (2016). Statistical multicriteria evaluation of asteroid deflection methods. In Proceedings of the 2016 International Astronautical Congress
- Thiry, N., Vasile, M., & Monchieri, E. (2016, March). Mission and system design for the manipulation of PHOs with space-borne lasers. In Proceedings of the 2016 IEEE Aerospace Conference
- Vetrisano, M., Cano, J. L., Thiry, N., Tardioli, C., & Vasile, M. (2016, March). Optimal control of a space-borne laser system for a 100 m asteroid deflection under uncertainties. In Proceedings of the 2016 IEEE Aerospace Conference
- Vetrisano, M., Cano, J. L., Thiry, N., Tardioli, C., & Vasile, M. (2015, October). Asteroid's orbit and rotational control using laser ablation: Towards high fidelity modeling of a deflection mission. In Proceedings of the 25th International Symposium on Space Flight Dynamics
- Thiry, N., & Vasile, M. (2015, September). Deflection of uncooperative targets using laser ablation. In Nanophotonics and Macrophotonics for Space Environments IX (Vol. 9616, p. 96160X). International Society for Optics and Photonics.
- Vetrisano, M., Thiry, N., & Vasile, M. (2015, March). Detumbling large space debris via laser ablation. In Proceedings of the 2015 IEEE Aerospace Conference
- Thiry, N., & Vasile, M. (2014, September). Recent advances in laser ablation modelling for asteroid deflection methods. In Nanophotonics and Macrophotonics for Space Environments VIII (Vol. 9226, p. 922608). International Society for Optics and Photonics.

Poster Presentation

- Thiry, N., & Vasile, M. (2015, April). Impact of tumbling rate of the performance of a CW laser deflection system for asteroids. In 4th IAA Planetary Defense Conference, Frascati

- Vetrisano, M., Thiry, N., Tardioli, C., Gonzales, J. L. C., & Vasile, M. Asteroids orbit and rotational control using laser ablation: Advances in Physical and Simulation Modeling.

Abstract

Several deflection methods have been proposed over the years to mitigate the risk of impact between an asteroid and the Earth. Most of the strategies proposed fall into two categories: impulsive and slow-push. Impulsive strategies are usually modelled with an instantaneous change of momentum given by, for example, a nuclear explosion (nuclear interceptor) or the hypervelocity impact of a spacecraft (kinetic impactor) with the asteroid. Slow-push methods, on the other hand, allow for a more controllable deflection manoeuvre by exerting a small continuous and controllable force on the asteroid over an extended period of time. However, these methods generally rely on large propellant reserve required to rendezvous with the target and apply the deflection action. Laser ablation intends to resolve this difficulty by using the material the target is made of in order to generate the required thrust. When irradiating a target with sufficient laser intensity, an ablated mass can be ejected at high velocity,thus exerting a reaction force on the target that can be used to propel itself. By selecting the appropriate laser technology and tayloring the system parameters based on the target application, it is theoretically possible to build an efficient space-based laser system. According to our calculations, the levels of performance of such a system (in term of thrust delivered per watt invested in the process) would be on the same order of magnitude as existing Ion Engines. By taking into account the propellant consumption and considering end-to-end deflection scenarios in a statistically representative sample of asteroid deflection scenarios, we show that laser ablation outperform other popular slow-push deflection strategies as the gravity tractor and the Ion Beam Shepherd (IBS). Extrapolation of the laser ablation method is also proposed for the case where the target is a manmade piece of debris orbiting around the Earth instead of an asteroid. In this case, pulsed lasers rather than CW lasers are considered in order to maximize the achievable laser intensity (TW/m^2 can be achieved even with a few watts of average power and moderate optics) with the same available average power. The choice of a pulsed laser allows considering larger operation distances and ensures that each layer of material ablated during a laser pulse will be small enough that it will not become a new threatening piece of debris by itself. Comparison between predicted and experimental results are illustrated for several material typically encountered in space debris objects, such as metallic alloys and CFRP. The different results highlight the interest for the laser ablation method as a global strategy to manipulate both manmade and natural objects and indicate its potential complementarity with other strategies such as the kinetic impactor method currently envisaged for asteroid deflection.

Contents

Chapter 1

Introduction

Figure 1.1: Space Situational Awareness (image: ESA)

The recent years have seen a growing awareness in the general public about potential hazards linked with the space environment on infrastructures on the ground and in space. Generally speaking, such hazards stem from possible collisions between objects in orbit, harmful space weather and potential strikes by natural objects, such as asteroids, that cross Earths orbit. In order to monitor those threats, space agencies around the world started to run dedicated Space Situational Awareness (SSA) Programmes. Among others, ESA started running its SSA programme on 1 January 2009. In parallel to these programmes, an international research effort has allowed over the years to deepen our understanding of the different types of risks posed by the space environment. In particular, this thesis was funded by the European Commission through the FP7 Stardust Marie Curie ITN. Stardust was a pan-european training and research network led by the University of Strathclyde and devoted to develop and master techniques for asteroid and space debris monitoring, removal/deflection and exploitation. The scientific programme focused on a number of underpinning areas of research and development that are fundamental to any future and present initiative aiming at mitigating the threat posed by asteroids and space debris, and was divided into three major research areas: Modeling and Simulation, Orbit and Attitude Estimation and Prediction, and Active Removal/Deflection of Non-cooperative Targets.

In this context, this thesis document synthetizes some of the main findings regarding the potential of laser ablation to manipulate both asteroids and space debris from a theoretical and practical perspective. As part of this effort, a refined model was developped to simulate the thrust achievable with laser ablation in order to predict the ouctome of a laser-based asteroid deflection or debris removal mission. For space debris, the results of our model are compared with experimental results on several materials commonly encountered in the space industry. In the case of asteroid deflection, this model is used to benchmark the performance of the laser-based method against a set of other popular techniques.

The threats and opportunities posed by asteroids and space debris are reviewed in the next 2 sections, outlining potential commonalities between these natural and man-made objects. The third section formally introduces the objective of this thesis and the relevance of a laser-based strategy to tackle both issues.

1.1 Asteroids

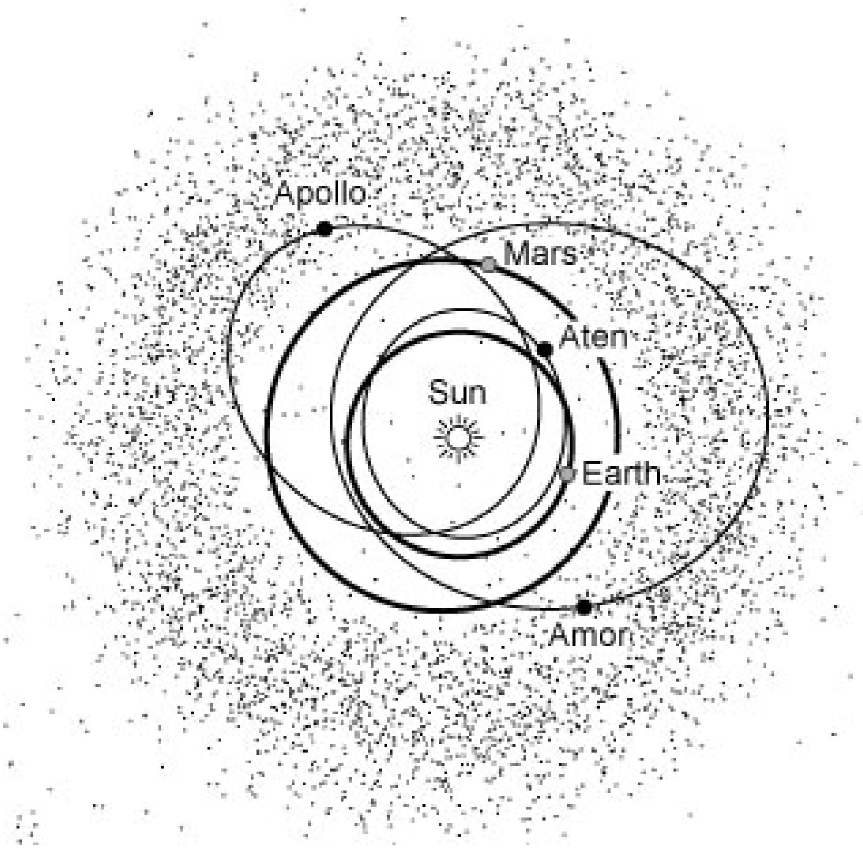

Figure 1.2: Near Earth Asteroids classification

Asteroids constitute remnants of the solar system formation situated in the inner solar system. Most asteroids are currently located within the main asteroid belt which is a circumstellar disc roughly located between the orbits of Mars and Jupiter. The orbit of asteroids in the asteroid belt is altered by the orbits of the other planets. In articular, their orbit can be strongly perturbed when their orbital period around the sun enters in a resonance with the orbital period of Jupiter around the Sun. When such resonances occur, asteroids from the main asteroid belts can be sent further inward the solar system and become Near Earth Asteroids (NEA). Near Earth Asteroids (NEA) are defined as asteroids with perihelia lower than 1.3 astronomical units (AU). The NEAs can be further classified according to their semi-major axis and eccentricity:

- Apollos (62%): Earth-crossing NEAs with semi-major axes larger than Earth's orbit: mathematically, they have a semi-major axis $a > 1.0$ AU and aperihelion distance $q < 0.983$ AU.
- Atens (6%): Earth-crossing NEAs with semi-major axes smaller than Earth's: mathematically, they have a semi-major axis $a < 1.0$ AU and apohelion distance $Q > 0.983$ AU.
- Amor (32%): Earth-approaching NEAs with orbits strictly exterior to Earth's orbit: an Amor asteroid's perihelion distance (q) is greater than Earth's aphelion distance (1.017 AU).
- Atiras (only a few known asteroids): Earth-approaching NEAs with orbits strictly inside Earth's orbit: an Atira asteroid's aphelion distance (Q) is smaller than Earth's perihelion distance (0.983 AU).

Potentially Hazardous Asteroids represent a subportion of NEAs which are deemed to represent a risk as they could come into a collision course with the Earth due to perturbations affecting their orbits (Chapman, 2004). They are defined based on parameters that assess their potential to make a threatening close encounter with the Earth. Specifically, PHAs are NEAs with a Minimum Orbit Intersection Distance (MOID[1]) with the Earth's orbit that is less than 0.05 AU and an absolute magnitude H[2] of 22 or less. In other words, asteroids that cannot get any closer to the Earth (i.e., MOID) than 0.05 AU or are smaller than about 120 m in diameter (i.e., for $H = 22.0$ and an assumed albedo of 20%) are not considered PHAs.

Popularized by science-fiction movies such as Deep Impact or Armageddon, the usual fear associated with asteroids is that of a large impactor (10km) causing global-scale devastation. However, despite evidences such as the Chicxulub crater pointing out that

---

[1] Which is formally defined as the distance between the closest points of the osculating orbits of two bodies

[2] Which for solar system bodies such as asteroids is defined as the apparent magnitude that the object would have if it were one astronomical unit (AU) from both the Sun and the observer, and in conditions of ideal solar opposition (an arrangement that is impossible in practice)

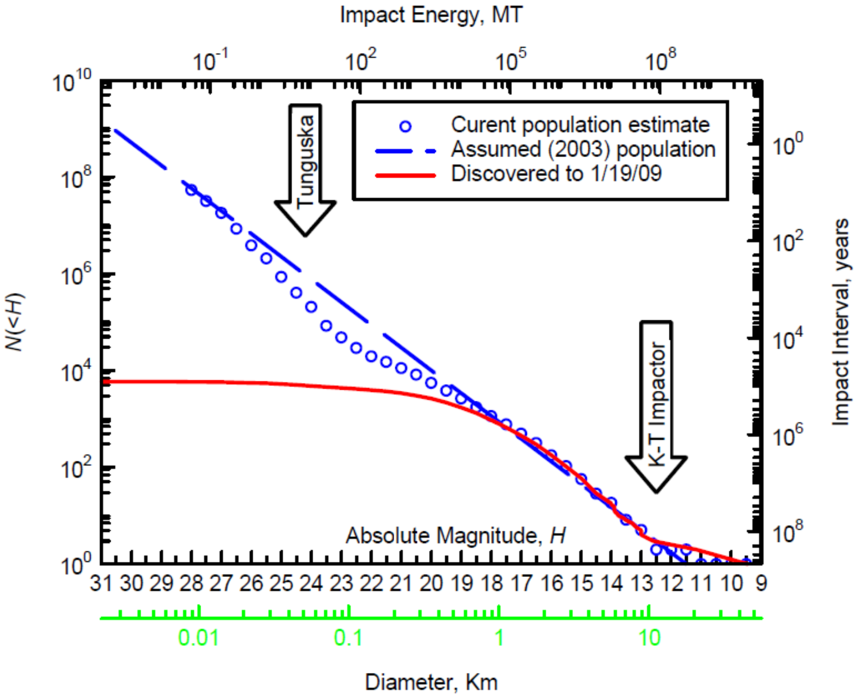

Figure 1.3: Impact frequency and percentage of NEA discovered as a function of their size (Harris and DAbramo, 2015)

such events indeed happened in the past and will happen again, the impact frequency of such events is very low. For instance, the impact frequency of a 10km bolide is about one every 100 millions of years (Bottke et al., 1994; Harris and DAbramo, 2015), as can be seen on Fig. 1.3.

On the other hand, smaller bodies, such as the asteroid responsible for the Chelyabinsk event in 2013 are much more frequent and thus more likely to represent an immediate threat to our terrestrial assets. For instance, the asteroid that struck Tunguska in 1908 was only about 60 meters across (Chyba et al., 1993), yet knocked down 80 million trees over an area of 2000 square kilometers. Considering the consequences of asteroid impact together with their likelyhood, some authors have in fact suggested that the relative threat caused by asteroid impacts is comparable if not more important than for other natural catastrophe such as tornados or floods (Chapman and Morrison, 1994). Similarly than what is done with other natural threats, it is therefore reasonable - if not economically sound (Matheny, 2007) - to develop methods allowing to mitigate the risks posed by such collisions.

1.2 Space Debris

Contrary to natural objects such as asteroids, space debris consist of man-made components which are the legacy of over 50 years of human activity in space and no longer serve a useful purpose. As of January 2017, it was estimated that there were about 166 millions pieces of debris smaller than 1 cm and about 750'000 between 1 to 10 cm [3]. As part of a global effort to contain the growth of the debris population, the Inter-Agency Space Debris Coordination Committee (IADC) has issued precise post-mission disposal (PMD) guidelines, especially orbital decay in less than 25 years. Western space agencies (NASA, ESA, CNES, JAXA) have translated these guidelines into internal codes of conduct. However, legally binding rules are still missing at the international level with France being the only country in the world to have translated the space debris mitigation guidelines into a national law (Loi des Operations Spatiales).

In any case, even if space debris mitigation measures will reduce the growth rate, statistical models indicate that long-term proliferation is still expected, even with full mitigation compliance, and even if all launch activities were halted (Liou and Johnson, 2006). This is an unfortunate indication that the population of large and massive objects has already reached a critical concentration in LEO, such that collisions between existing objects are sufficient to sustain future debris population growth. In parallel to the IADC mitigation measures, Active Debris Removal programmes (ADR) to reduce the number of large and massive objects will likely become necessary in order to stabilise the space debris population in the future.

---

[3] `https://www.esa.int/Our_Activities/Operations/Space_Debris/Space_debris_by_the_numbers`

1.3 A Contactless Solution with Laser Ablation

In spite of the clear differences in their origin and orbital environment, asteroids and space debris share a number of commonalities: both are uncontrolled objects whose orbit is deeply affected by a number of perturbations, both have an irregular shape and an uncertain attitude motion, both are made of inhomogeneous materials that can respond unexpectedly to a deflection action. For both, accurate orbit determination is required. More importantly, both need to be removed (or deflected) before they impact with something valuable for us.

Several deflection methods have been proposed over the years to mitigate the risk of an impact of a PHA with the Earth. Most of the strategies proposed fall into two categories: impulsive and slow-push. Impulsive strategies are usually modelled with an instantaneous change of momentum given by, for example, a nuclear explosion (nuclear interceptor) or the hypervelocity impact of a spacecraft (kinetic impactor) with the asteroid. Slow-push methods, on the other hand, allow for a more controllable deflection manoeuvre by exerting a small continuous and controllable force on the asteroid over an extended period of time. Clearly, impulsive methods are not suited for an active debris removal mission. Also, methods involving a physical contact with the target such as nets or harpoons, will require an initial detumbling of the target. On the other hand, slow-push methods such as the Ion Beam Sherpherd (or the Gravity Tractor) can operate at a safe distance from the target without physical contact or prior detumbling. However, in general, such methods eventualy rely on their propulsion subystem and propellant reserve to perform the removal (or deflection) maneuver[4].

Slow-push ablation-based methods (using solar concentrator or laser ablation) intend to solve this last difficulty by using the material of the target (asteroid or the space debris) in order to generate the required thrust (Maddock et al., 2007). During the ablation process, an ablated mass, ejected at high velocity, exerts a reaction force on the target

---

[4] This will be made more clear to the reader when these methods are presented into details in Chapter 4

that is used to propel itself. In previous works (Kahle et al., 2006; Vasile and Maddock, 2010), however, it was shown that the contamination of the solar collectors, severely limits the effectiveness of direct solar ablation with concentrators. On the other hand, if the deflection is achievable in a given limit time, laser ablation techniques require a lower mass into space than electric propulsion methods (Vasile et al., 2014). The use of lasers, compared to directly focusing the light of the Sun, implies higher conversion losses but has the distinctive advantage to provide high light intensity at lower average power and longer distance from the target. The main interest for this latter method was demonstrated by Sanchez et al. (2009), who included it in a comparative assesment of various asteroid deflection techniques. More recently, the laser ablation method has been investigated by Gibbings (2014) who examinated the composition of the plume ablated by a 90W CW laser during experiments carried in a vacuum chamber and derived an improved model of the laser ablation process and plume formation. In parallel to this, Vasile and Maddock (2012) have investigated the design of formation orbits enabling the use a multi-spacecraft system for the deflection of asteroids. The results from these different studies have been useful to better understand the different physical processes, isolate the relevant parameters acting during the ablation process and outline the overall technical feasibility of the method. On the other hand, these studies did not investigate in details the complex link between the different laser parameters considered (e.g. beam diameter, laser power, material properties), type of target materials and the impact of those on the expected performance of the laser ablation process. Also, due the relatively small number of asteroids considered by Sanchez et al. (2009) a possible bias introduced by the choice of these asteroid deflection scenarios could not be excluded form the preliminary findings. The aim of the present thesis is therefore to expand upon these findings and fill the knowledge gaps by adressing the following questions

- What laser technology to consider for a space mission?
- What are the key sizing parameters of a laser deflection system?
- How does laser ablation compare against other asteroid deflection strategies?

- What difference does it make if the target is a space debris or an asteroid?

These 4 questions form the central theme of this thesis and will be addressed sequentially from Chapter 2 to 7:

- In Chapter 2, the different laser technologies and some relevant high power applications are reviewed. Speculative concepts are also presented in the context of asteroid deflection and space debris removal.

- In Chapter 3, we rederive a model of the laser ablation process from conservation laws. and derive a link between key performance indicators of the methods with the key sizing parameters of the laser system as well as physical parameters of the material the target is made of. These results were published in the Advances in Space Research journal (Thiry and Vasile, 2017b).

- In Chapter 4, the concepts and computational techniques that will be used in this work in order to predict the outcome of a given deflection action. The mathematical concepts presented in this Chapter were summarized from the work of students who previously worked with Prof. Massimiliano Vasile on the topic of asteroid deflection. In particular, due acknowledgement for the results of this Chapter go to: Christie Maddock, Federico Zuiani, Alison Gibbings, Camilla Colombo, and Joan-Pau Sanchez Cuartielles. In Appendix B, a novel technique, named the nuclear cycler, and published by the authors(Vasile and Thiry, 2016) in the Advances for Space Research journal is also described.

- Chapter 5 the practical implementation of a laser-based deflection method for several mission scenarios is investigated. A preliminary sizing exercise is undertaken for a realistic case.

- In Chapter 6 the laser ablation method is benchmarked against other popular non-nuclear deflection using a statistical multi-criteria assessment. While a similar assessment had already been performed in the work of Sanchez et al. (2009), our work goes further by considering a much larger and more representative set of deflection scenarios and includes an end-to-end sizing exercise of each mission (using in each case global optimisation techniques together with computed transfer trajectories to the asteroid). These results have been presented at the 2016 IAC conference and published in the Acta Astronautica journal (Thiry and Vasile, 2017a).

- Chapter 7 illustrates how laser ablation could also be used to tackle the space debris issue. Within this chapter, the results of a mathematical model of the laser ablation process are discussed and compared with experimental thrust measurements performed in collaboration with Nagoya University on samples made of commonly encountered space materials such as CFRP, Al, and Ti alloys. Additional ideas are discussed for potential active debris removal missions to LEO and GEO objects.

Chapter 2

Laser technology and applications

When they were invented in the early 1960s, lasers were initially called "a solution looking for a problem". Nowadays, things have changed considerably and our standard way of life would not be what it is without them. From the QR code scanner at the airport gate to LASIK performing eye surgery in hospital or even the laser communication terminals onboard the Sentinel 2 satellites, lasers have found a purpose in pretty much every discipline. Fundamental properties of lasers and their working principle are examinated in the next section. Terrestrial and space-based applications are then presented while the last section discusses somes applications which have been proposed in the context of asteroid deflection and space debris removal.

2.1 Laser technology

The word laser is an acronym for *Light Amplification by Stimulated Emission of Radiation.* As illustrated on Fig. 2.1, a laser, in its most simple form, consists of (Balembois and Forget, 2007):

1. an amplifying medium(1): necessary to amplify the light that travels through it by exploiting the process of *stimulated emission.* It can be solid, liquid or gaseous.
2. a power source(2): necessary to provide ('pump') the energy to the amplifying medium in order to create right conditions for the light amplification. It can be optical (e. g.the Sun, flash lamps, diodes or even other lasers), electrical (gas

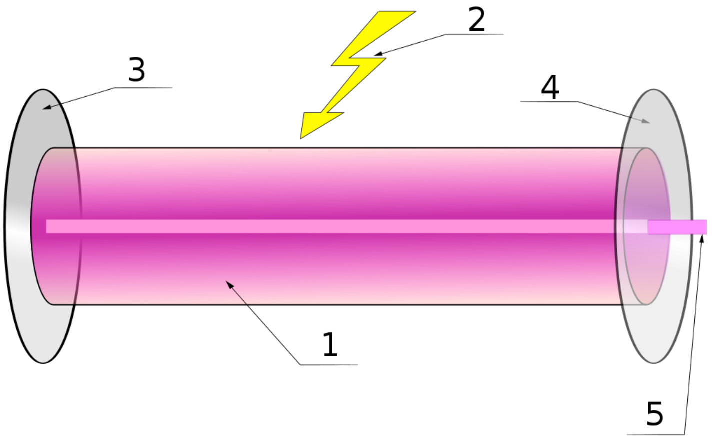

Figure 2.1: Components of a typical laser (source: Wikimedia Commons CC BY-SA 3.0)

discharge tubes, electric current in semi-conductors) or even chemical (chemical reactions).

3. an optical resonator(3)(4): required to amplify the light source making the process of stimulated emission predominant over the process of spontaneous emission within the amplifying medium. In its simplest form, it consists of two parallel mirrors between which the light can bounce back and forth augmenting the probability of stimulated emission to occur before it can leave the cavity through one of the mirrors that is not completely reflective.

2.1.1 General Principle

In order to comprehend better the operation of a laser, let us now consider the laser physics by analyzing the words composing the acronym laser (i. e. light and stimulated emission). In physics, the term *light* refers to an electromagnetic radiation of any wavelength, whether visible or not. In the context of lasers, it is convenient to define several spectral domains of interest. The visible spectrum goes from 400 nm to 700 nm and corresponds to the range of sensitivity of the human eye. The near infrared (NIR) spreads from 700 nm to 10 μm and anything beyond this is in the far infrared

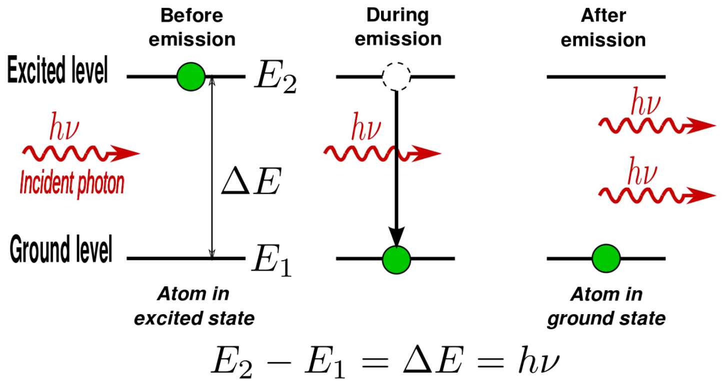

Figure 2.2: Stimulated emission by an atom (source: Wikimedia Commons CC BY-SA 3.0)

(FIR) region. On the other hand, the spectral domain between 200 nm and 400 nm is considered as the ultraviolet radiation while anything below 200 nm is in the deep ultraviolet region (DUV) (CVI Laser Optics and Melles Griot, 2013). Furthermore, light can be considered as a flux of discrete particles called photons which exhibit both wave-like and particle-like properties. These particles have a constant speed in vacuum (the speed of light), $c = 2.998 \times 10^8 \, {}^{m}\!/\!{}_{s}$, and their energy is given by

$$E = h\nu$$

where ν is the wave frequency and h is Planck's constant ($h = 6.62 \times 10^{-34} \mathrm{J} \cdot \mathrm{s}$).

Interactions between matter and light can be split into three mechanisms:

1. spontaneous absorption: an electron transit from a lower energy level to a higher one by absorbing a photon.

2. spontaneous emission: an electron spontaneously emits a photon to transit from a higher energy level to a lower one.

3. *stimulated emission*: the transition of an electron from its excited state to its ground state is achieved by interaction of the latter with a photon having the energy equal to the energy gap ΔE between the excited and the ground state. The electron stimulated to make the transition will emit a photon having the

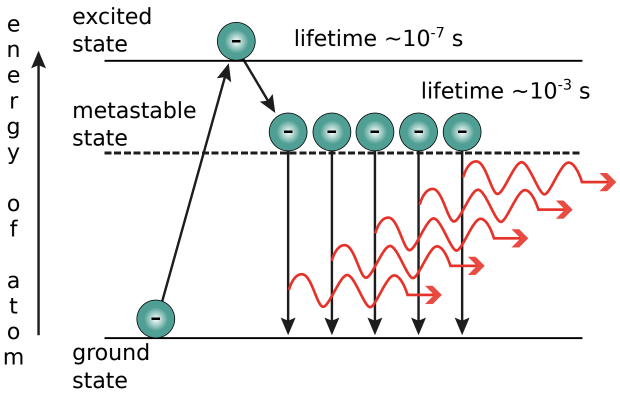

Figure 2.3: Schematic representation of population transitions

exact same energy, direction and phase as the incident photon.

To obtain a laser medium, obviously, the stimulated emission has to be dominant over the other two mechanisms. However, this is not an easy task given that in a material, for a radiative transition, the three mechanisms are always present at the same time. An incident photon has the same probability of being absorbed by a ground-state electron as of being amplified by an excited-state electron. Moreover, in a thermal equilibrium the Boltzmann's distribution indicates that a population of atoms with lower level of energy will always be larger than the one with the higher level of energy. Thus, in thermal equilibrium, any collection of atoms will constitute an absorber. To overcome this problem a condition of "population inversion" needs to be achieved in a medium so that the population N_2 of higher energy is always larger than the population N_1 with the lower energy. The most common approach for producing a population inversion in a laser medium is to add energy to the system in order to excite atoms or molecules into higher energy levels. An atom stays at the excited state only momentarily before falling into an intermediate state called metastable state. Atoms stay at the metastable state for a rather long time which causes the number of atoms at the metastable state being larger than that at the ground state. Population inversion is a key to producing laser, because it ensures that the number of atoms transiting form the metastable level to the ground state will always be bigger than those transiting the other way around, so that the number of photons in the medium will increase.

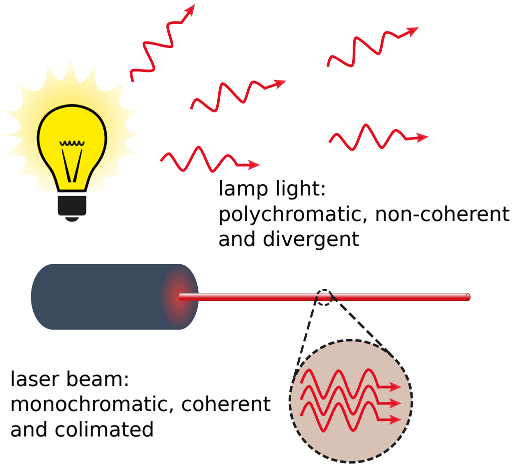

Figure 2.4: Laser properties

As illustrated on Fig. 2.4, the main properties of a laser light produced from stimulated emission are (Kwok-san and Shiu-sing, 2000; Paschotta):

1. narrow linewidth: light that comes out of a laser device has narrow spectral bandwidth which in case of a laser emitting in the visible spectrum means that the beam will be monochromatic (e. g. red, green or blue). On the other hand, generic sources of light, such as a light bulb or a candle, emit light over a wide range of wavelengths of the electromagnetic spectrum which is why we tend to perceive it as having a white color;

2. coherence: laser light is composed of photons having all the same phase which results in a good ability of a laser beam to produce interference patterns. An unwanted effect of this property, however, is a tendency of laser beam to form speckle patterns.

3. directivity: laser light is generally emitted in the form of a beam that has a well-defined direction and a very low divergence, meaning that the radius of a laser beam does not change significantly during a medium propagation distance. This is due to the angular selectivity of the oscillator cavity and collinear photons produced during the stimulated emission.

2.1.2 Laser types

Lasers can be classified according to the nature of the lasing medium. Common types are: semiconductor lasers, solid-state lasers, fiber lasers, dye lasers and gas lasers (Balembois and Forget, 2007; Paschotta). Other less common types of lasers worth mentioning are: chemical and nuclear pumped lasers, free electron lasers, and X-ray lasers (Paschotta).

Another distinction of the lasers can be made on their operation mode. Two possible operation modes of lasers are the continuous-wave (cw) mode and the pulsed mode. The usage of one over the other depends on whether the output power of the laser beam needs to be continuously emitted or not. Typical time scales used when talking about laser operation modes are the following (Lucas and Zhang, 2012):

- millisecond: 0.001 s which is the time between two wing flaps of a housefly;
- microsecond: 10^{-6} s which is the duration of a high-speed, strobe light flash;
- nanosecond: 10^{-9} s which is the duration of molecules fluorescence;
- picosecond: 10^{-12} s which is the switching time of the world's fastest transistor;
- femtosecond: 10^{-15} s which is the pulse width of the world's fastest laser;
- attosecond: 10^{-18} s which is the shortest time measurable by a device.

Continuous-wave (cw) operation mode generates, in time, a continuous emission of a laser beam. This also implies that the pumping source is constantly injecting energy into the lasing medium during the operation of the device. With this mode, very narrow linewidths of the output radiation can be achieved, typically of only a few kilohertz. The first cw laser was a helium-neon laser emitting a 1153 nm beam. Nowadays, different types of lasers can be operated in cw mode. The most common fall into the following categories: gas lasers, solid-state lasers and dye lasers (Paschotta).

Pulsed mode, on the contrary, emits radiation in the form of short pulses repeating at a given rate. With this method very high pulse energies and peak powers can be obtained, while the optical bandwidth of the pulses tends to be wider compared to the cw mode. The generation of pulsed beams can be achieved by using a cw laser and a fast shutter that opens and closes at fixed intervals. However, this method, although intuitive, suffers from efficiency issues and the duration of the pulses would then be limited by the velocity of the shutter (around 1 ms for the fastest mechanical shutter). Thus to obtain high energy pulses having very short duration, the following methods are commonly used (Paschotta; Balembois and Forget, 2007):

- gain switching: this method (usually employed for semiconductor lasers) uses the pump source to quickly change the gain of the lasing medium in order to obtain pulses that are from a few nanoseconds to a few picoseconds long and have energies around a few picojoules;

- Q-switching: this method uses the modulation of the intracavity losses (i. e. the quality factor of the laser cavity) to obtain very short pulses (in the nanosecond range) with repetition rates of up to a few kilohertz and energies of a few milijoules or more. The peak power that can be achieved with Q-switched lasers can be a few orders of magnitudes higher than the power obtainable with cw lasers (in the megawatt range or even higher);

- mode-locking: this method (or better a series of methods) uses an active element (an optical modulator) or a nonlinear passive element (a saturable absorber), placed within the optical cavity in order to obtain ultrashort pulses (in the range of a few pico or even femtoseconds) having repetition rates of up to a few gigahertz and pulse energies that range from a few picojoules to a few nanojoules. The average power that can be achieved with mode-locked laser oscillators is of the same order of magnitude as that obtainable with cw lasers. Femtosecond mode-locking laser amplifiers can reach the peak power in the terawatt range, with up to 100 mJ per 10 fs pulse.

2.1.3 High Power Laser Technology trade-off

Several technical challenges arise whenever high output power is requested from a laser device. The most common ones are (Paschotta):

- powerful energy source(s): to generate very powerful laser beam, obviously, a powerful energy source is needed. This latter can consist of either just one source or several of them. Moreover, another laser can be used as an energy source of a high-power laser. In fact, to date, the highest output powers in cw mode are only achievable with diode-pumped lasers;

- high wall-plug efficiency: this parameter is especially important if a laser is operated for extended periods of time in continuous-wave mode. Its high values are very difficult to reach due to variety of factors, thus a trade-off must be made;

- limited thermal effects: heat generation in a laser is inevitable. This is true, even if the laser medium is fairly efficient. Thus, to avoid degrading beam qualities, efficiency losses or even damage to the lasing medium, thermal energy of the laser must be limited. This can be achieved trough an efficient thermal management and cooling of the device during its operation;

- limited nonlinear effects: these effects are particularly relevant for fiber lasers and the ability to manage them is fairly important. They limit the level of power achievable by a laser, and have to be dealt with a proper choice of fiber structure and laser system architecture. Some of these effects are: stimulated Raman scattering, Brillouin scattering and four-wave mixing;

- high optical damage threshold: whenever high optical intensities are achieved, the risk of damaging the laser optics of the device increases. Thus, optics with very high optical damage threshold needs to be chosen whenever high power radiation is involved. Moreover, it is vital to keep the device sealed and free of dust particles which can cause the damage to the optics even if optical intensities are well below limiting threshold;

- limited misalignment and vibrations: lasers are very sensitive to misalignment and vibration of their optical components. This is particularly true in the case of high-power lasers where huge optical intensities are produced. Thus, careful opto-mechanical design is required to preserve the laser performances once integrated in a carrier (aircraft or any vehicle).

Furthermore, those add to specific requirements of the space sector which impose a system as compact and reliable as possible. To date, the most likely to fulfill these unique challenges are solid state lasers.

Solid-state lasers are, in general, lasers having a solid lasing media based on doped crystals or glasses or even on semiconductor materials[1]. The pumping mechanisms can be optical (flash lamps or laser diodes) or electrical (in case of semiconductor lasers). They are capable of very high output powers and variable beam qualities. Moreover, they can be operated either in continuous or pulsed mode (Paschotta).

Based on the type of lasing media and the type of pumping mechanisms, various solid-state lasers can be made. Describing all of them however goes beyond the scope of this chapter so we will concentrate our attention in particular on two types of solid-state lasers: laser diodes and diode pumped solid-state lasers (DPSSL).

Diode lasers are a particular type of semiconductor lasers where an electrical current flows through a gain medium, made of a p-n junction. They are generally built as edge-emitting lasers, meaning that the semiconductor wafer emits the laser light from its edge after the laser beam has propagated along the direction of the wafer itself. This property makes them suitable to be stacked together in order to create one-dimensional bars or even two-dimensional arrays, known as “stacking”. In this configuration several low-power sources can be arranged together to obtain a compact high-power device capable of emitting thousand of watts. The most common arrangement of these stacks is in vertical position as illustrated in Fig. 2.5. The maximum obtainable wall-plug efficiency with these devices is around 60 %[2] although the beam quality and brightness

---

[1] Note however that often semiconductor lasers are not included in the solid-state category. They are instead considered as a separate type of lasers (Paschotta)

[2] This is true for devices emitting in the 700-1000 nm range of wavelengths. For higher wavelengths the efficiency quickly drops below 30%.

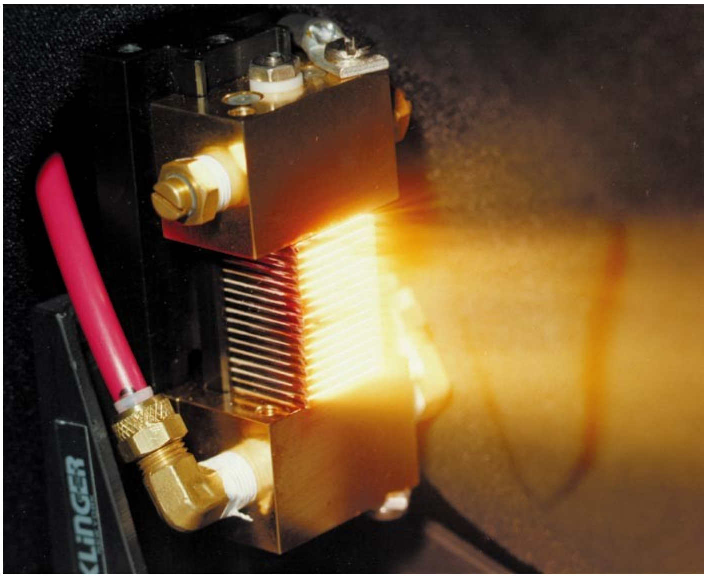

Figure 2.5: High power laser diode array (source: Wikimedia Commons)

are relatively low. Moreover, due to strongly asymmetric and high divergence of their beams, diode lasers require very complex beam forming optics. The beam itself cannot propagate very far, although it can be focused at a short distance. All this makes these devices perfect for being used as energy sources for other lasers. Alternatively, they can be used in all applications that do not require high beam quality such as material processing, welding, etc (Paschotta; Bourdon, 2013).

Diode pumped solid-state lasers (DPSSL) are optically pumped devices that exploit the properties of diode lasers to obtain miniature devices capable of achieving excellent efficiencies and high output powers while at the same time maintaining good beam qualities. This is possible by using diode lasers as a pumping source and some kind of crystal or piece of glass as the lasing medium. The advantages of this approach, when compared to the usage of flash lamps as energy sources, are (Paschotta):

- compactness of the laser device: limited size of the energy source, power supply and cooling mechanisms contribute to the overall compact size of DPSSL devices especially if compared to the output power that they are capable of emitting;
- decreased electrical consumption: electrical consumption of DPSSL devices is

drastically lower if compared to solid-state lasers using lamps as pumping mechanisms. This is due to the high efficiency of the power source which contributes to the overall very high wall-plug efficiency of theses devices (i.e. around 30 %);

- decreased cooling demands: these devices require a decreased thermal management due to their overall compact dimensions and high efficiency. Nevertheless, thermal effects in DPSSL remain one of the downsides of these systems, as it will be evidenced shortly;
- extended lifetime: diodes are very rugged energy source that can endure around 6000 hours, which makes them very durable energy source. The downside is that this durability is easily influenced by a variety of factors and their eventual exchange in a device is very expensive;
- wide variety of gain media: lasing medium can be chosen from a wide range of materials based on a wavelengths that we would like to achieve. With discharge lamps this wouldn't be possible due to their lower brightness.

However, despite all the laudable properties, these devices also exhibit some disadvantages that need to be taken into account if the application requires high power output. The main are: the high thermal effects and higher cost per watt of pump power when compared to lamp pumping (Paschotta; Bourdon, 2013).

To date, the highest output power achievable with a DPSSL was demonstrated by Northrop Grumman. The obtained power was 105 kW and it was possible by coherently combining 7 slab lasers (15 kW each). The demonstrated operation time was 300 s[3] (Bourdon, 2013).

The applications of these devices vary greatly and encompass all possible areas of laser applications (Paschotta).

Fiber lasers are essentially very long solid-state lasers (see Fig. 2.6) in which the input laser light is guided through the fiber by total internal reflection (see Fig. 2.7).

---

[3] Note that this operation time was repeatable so it is not to be intended as the lifetime limit of the laser device.

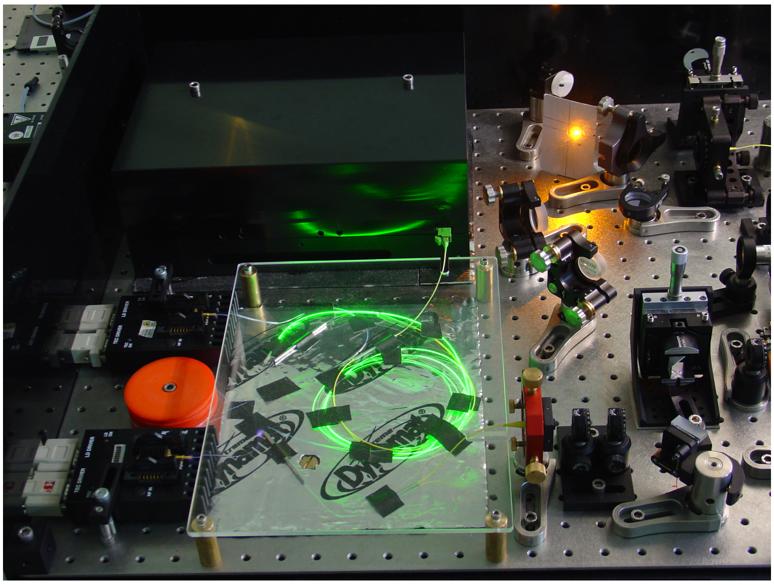

Figure 2.6: Close-up view of femtosecond fiber laser system (source: Chair of Alfred Leitenstorfer, University of Konstanz)

The laser medium is a doped fiber core (often ion-doped silica) while the internal clad (often undoped silica) acts as a pump guide. The laser dopants used in most cases are rare earth elements such as erbium (Er^{3+}), neodymium (Nd^{3+}), ytterbium (Yb^{3+}), thulium (Tm^{3+}) or praseodymium (Pr^{3+}). Typical length of a fiber is around 5 m (Paschotta; Bourdon, 2013). The pumping source in most cases is a laser diode. Thus this particular type of lasers can be seen as an evolution of previously described diode pumped solid-state lasers. This is the reason why they are considered separately in this chapter although they are effectively DPSSL devices.

Their advantages over the other solid-state lasers are essentially (Paschotta; Bourdon, 2013):

- high power capabilities: diode pumped fiber lasers can achieve powers of several kilowatts from a single fiber. Physical limitations indicate that the maximum achievable power can be in the range from 20 kW to 40 kW (for cw operation mode);
- improved thermal management: high surface-to-volume ratio of a fiber provides extended area for the thermal exchange which avoids excessive heating of one

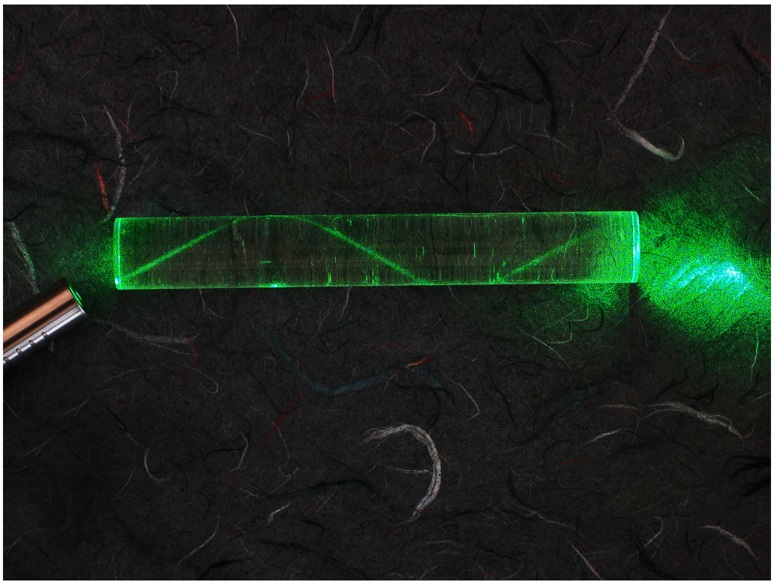

Figure 2.7: Demonstration of the working principle of a fiber laser (source: Wikimedia Commons CC BY-SA 3.0)

particular area and distributes the heat over the whole length of the fiber;

- excellent beam quality: beam quality of the fiber laser is intrinsically excellent due to the spatial filtering provided by the core of the fiber;
- fiber splicing: by using the principle of fusion splicing of fibers it is possible to obtain very long laser devices that have rugged fiber joints characterized by lower transition losses, weaker reflections and are not affected by misalignment problems.
- very high gain: wall-plug efficiency of up to 50 % can be expected while the optical to optical efficiency could be up to 85 %, obtained with Yb^{3+}core-dopant;
- compact and resistant design: fiber glass diode pumped lasers consist of two very compact and rugged devices which in turn makes the them very wear-resistant, sealed and at the same time very compact devices. The fiber itself can be coiled and the laser beam can propagate over long distances without interfering with the surrounding environment.

The limitations of this technology, on the other hand, are (Paschotta; Bourdon, 2013):

- damage threshold: the power intensities reached in recent years are very close to the damage threshold of the glass material itself indicating that in current state, fiber lasers have reached their maximum power limit;
- cooling limits: 100 W/m is the power of dissipation per unit length of a fiber reached with air-cooled devices. Thus, other methods of cooling (e. g. water-cooling) need to be considered in order to increase the output power. Otherwise lowering the concentration of laser dopants could ease the cooling process but it will at the same time increase the effects of nonlinearities;
- nonlinearities: nonlinear effects are present in fiber lasers and are one of the factors limiting their performance;
- non trivial design: in most cases, the design of a fiber laser is more difficult than other solid-state lasers due to a variety of factors.

However, despite those limitations, fiber lasers appear as a revolution of solid-state lasers and remain one of the candidates for any application that requires very high optical intensities, low consumption, high beam qualities and wide range of wavelength tunability (Paschotta; Bourdon, 2013).

Beam combining techniques are required to achieve high power output by combining multiple beams into a single beam. The two main techniques are coherent beam combining and spectral beam combining:

- Coherent beam combining requires to achieve mutual temporal coherence of the combined emitter beams operated at the same wavelength. As indicated in Fig. 2.8a, the coherence is usually achieved by means of individual phase modulator placed at the output of each emitter beam.
- On the other hand, as illustrated in Fig. 2.8b, the general principle of spectral beam combining is to have several beams with non-overlapping optical spectra and combine them at some kind of wavelength-sensitive beam combiner such as prisms, diffraction gratings, dichroic mirrors or volume Bragg gratings.

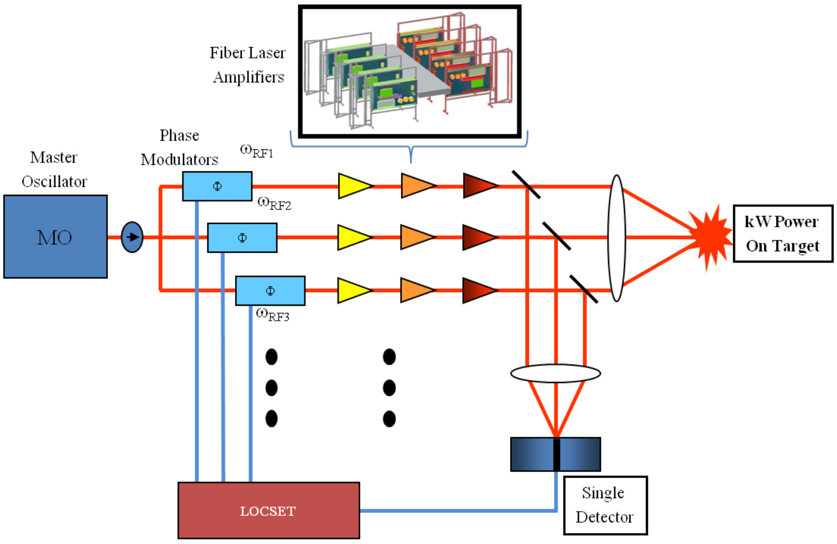

(a) Coherent Beam Combination (image: AFRL/RDL)

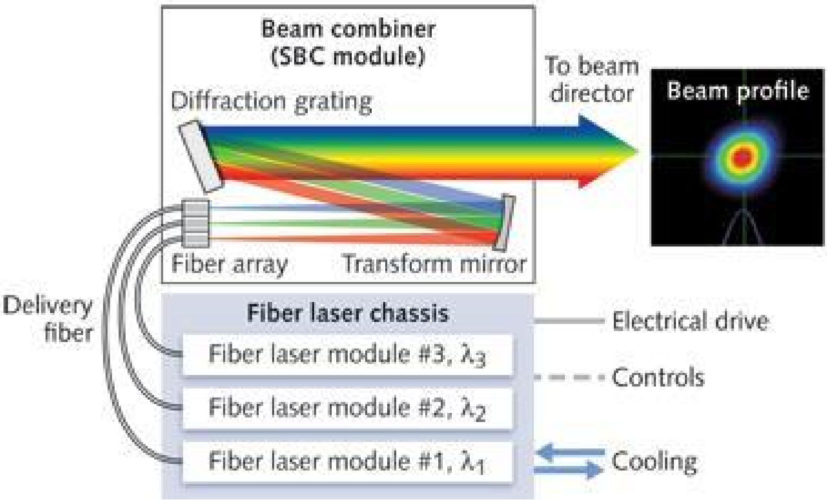

(b) Spectral Beam Combination (image: Lockheed Martin)

Figure 2.8: Beam combining methods

Both techniques have demonstrated high power outputs and high efficiencies. However, for applications that do not require a narrow bandwidth, the spectral beam combining offers the distinct advantage of not requiring precise wavelength, polarization, and phase control. This in particular reduces the difficulty of maintaining stable operations at high power levels over extended durations. In addition, such arrays also allows the separate beams to be overlapped in both the near and far fields without spatial interference.

2.2 Overview of some Relevant High-Power Laser Applications

2.2.1 Inertial Confinement Fusion

As represented in Fig. 2.9 inertial confinement fusion is a type of nuclear fusion that attempts to initiate nuclear fusion reactions by heating and compressing a fuel target (pellet of deuterium and tritium) with a laser. The main purpose is to scale down the processes happening in fusion bomb (where a fission bomb is used instead of lasers to initiate the fusion reaction), thus opening up peaceful applications such as nuclear fusion power but also allowing to reproduce the extreme conditions of a nuclear bomb in a laboratory. The 2 largests facilities in the world are the National Ignition Facility (NIF) located in the USA and Laser Megajoule facility located near Bordeaux in France. It is worthwhile mentionning that initial results on the ability of lasers to deliver an impulse on ablated target have been derived from the results of inertial confinement fusion experiments (Phipps et al., 1988).

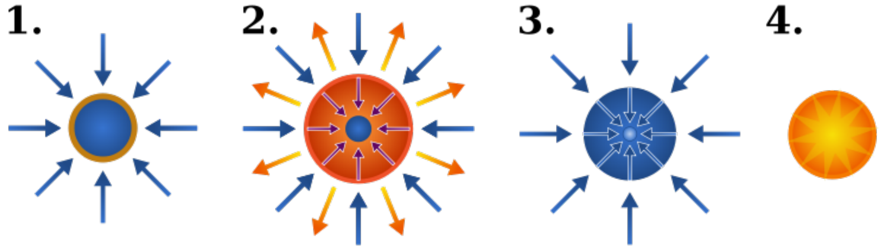

Figure 2.9: Schematic of the stages of inertial confinement fusion using lasers (source: Wikimedia Commons)

2.2.2 Military

The use of laser for military purposes started with the need from superpowers to defend themselves from a potential ballistic missile strike. In the US, the Star Wars program was developed with the displayed intention to prevent a nuclear attack through an ICBM. Different methods were considered at the time:

- Spaceborne laser weapons were intended but their actual implementation did not succeed due to launch failures, the outer space treaty and the end of the cold war.
- Ground based laser weapons
- Airborne laser weapons

Figure 2.10: The HEL MD that took out mortars and UAVs in flight using its vehicle-mounted 10 kW laser (image: Boeing)

Following the cancellation of the program, the projects focuses nowadays on the ground-based approach:

- Coherent beam combining: EXCALIBUR is the most recent among many DARPA projects to develop a 100 KW solid-state laser by combining coherently the beams from high power (kW class) fiber lasers. A first milestone aims to develop a 50kW version.

- Incoherent beam combining: the US Navy plans on developing a laser weapon system to equip its aircraft carriers. The platform would consist of a 6x8kW fiber lasers from IPG with the 6 beams overlapped on the same point of the target. A trial campaign held in 2009-2010 demonstrated the feasability of the technique with multiple drones destroyed by the system. The main effect visible on the videos was a gas tank drilling followed by fuel inflammation.

- Spectral beam combining: The High Energy Laser Mobile Demonstrator (HEL-MD, see Fig. 2.10) intends to build a 60kW model using the spectral beam combination technique. A recent demonstration showed a 'Qassam-type' rocket destroyed at 1.5 km with a 10 kW fiber model.

2.2.3 Optical Communications

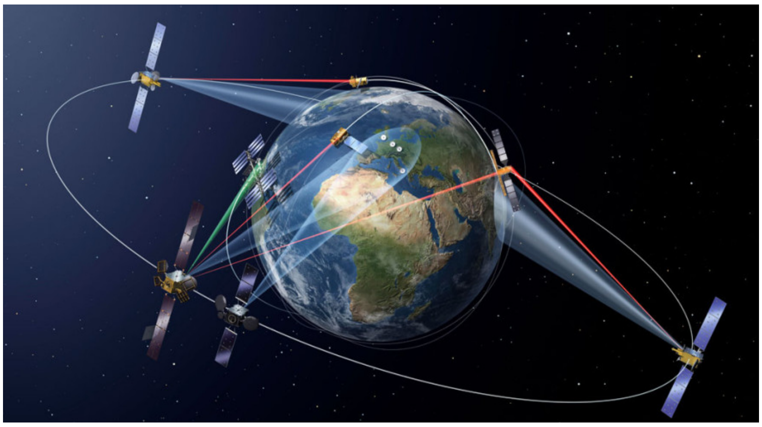

Figure 2.11: Laser optical communications (image: ESA)

Laser communication terminals onboard satellites (see Fig. 2.11) have demonstrated the capacity to establish high bandwidth free space optical communications over distances on the order of hundreds of thousands of kilometers have been demonstrated and are presently implemented on some LEO satellites (e.g. Sentinel 2) which use laser communication to relay their data to a fleet of GEO satellites (EDRS system) responsible for beaming it to the ground. The inter-satellite optical link allows a datarate up to 1.8 Gbit/s.

2.2.4 Remote Sensing

Pulsed Laser are used in either the Raman spectrometry and Laser Induced Breakdown Spectrometry techniques. Raman spectrometry allows to deduce the molecular composition through laser excitation of the sample while the LIBS technique, used on the curiosity rover (see Fig. 2.12a), allows to investigate the elementary composition of a sample by ionizing its molecule. Pulsed lasers are also used in LIDARS, which constitute 3D laser-scanning methods with applications covering various field such as geodesy, geomatics, archaeology, geography, geology, geomorphology, seismology, forestry, atmospheric physics, laser guidance, airborne laser swath mapping (ALSM), and laser altimetry. Lidars are notably used by autonomous cars and the Aeolus spacecraft (see Fig. 2.12b).

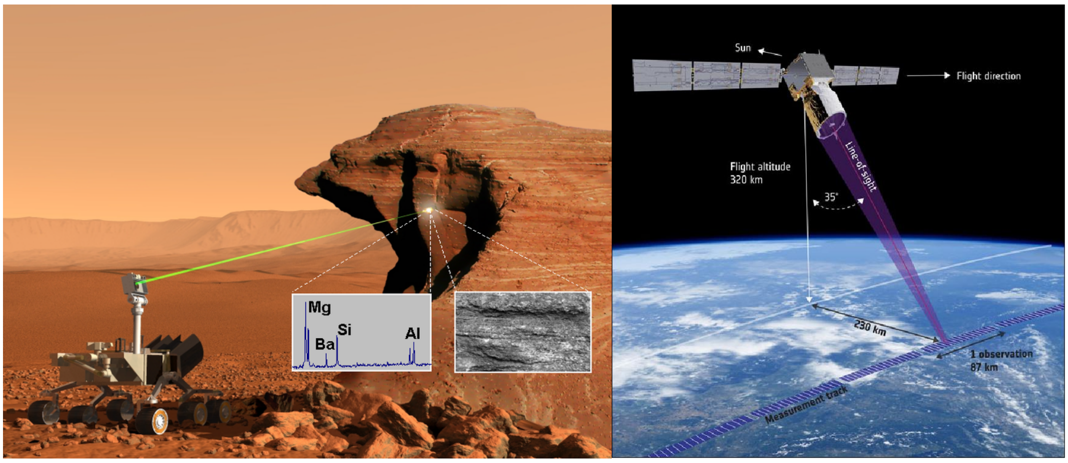

(a) LIBS used by the curiosity rover (image: NASA) (b) Lidar onboard the Aeolus satellite (image: ESA)

Figure 2.12: Remote sensing applications of lasers

2.2.5 Laser Propulsion

Following the same principle as a solar sail, the concept of photonic laser thruster uses the radiation pressure to propel an object:

$$F = \frac{2P_{laser}}{c} \tag{2.1}$$

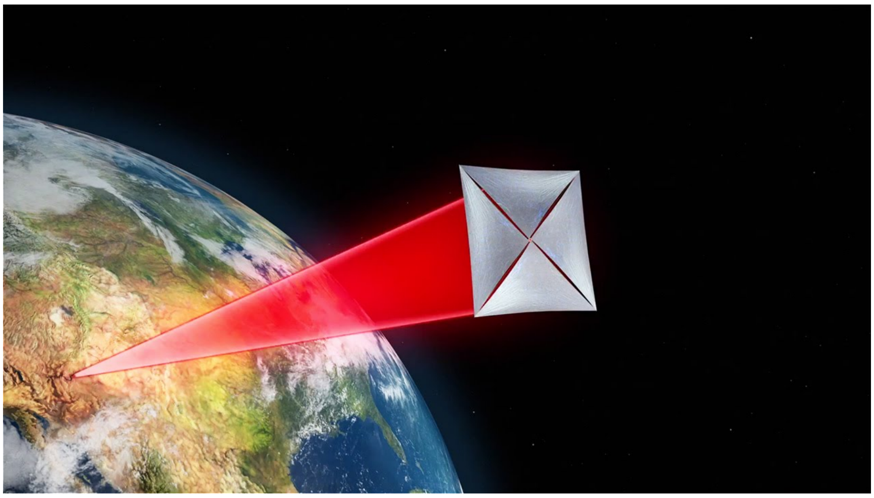

Figure 2.13: Starshot Concept (image: Breakthrough initiatives)

Recently, the Breakthrough initiative revealed the starshot concept (see Fig. 2.13) which aims to visit the alpha centauri system with nanosails (initially in LEO) propelled by a ground-based array of high power lasers.

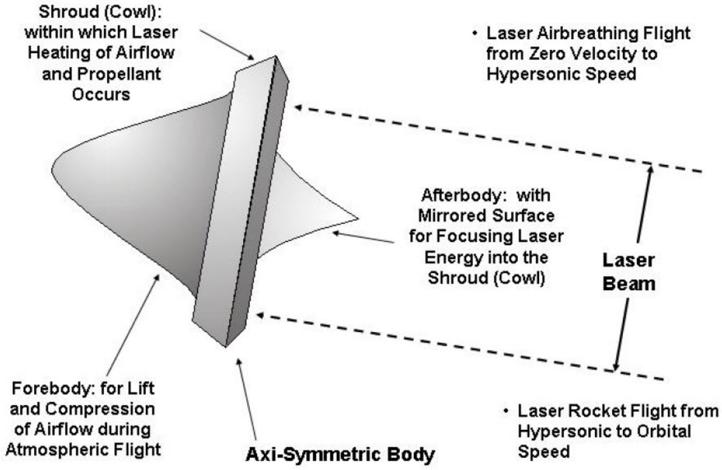

Figure 2.14: Lightcraft project (Davis and Mead Jr, 2008)

Another interesting concept depicted in Fig. 2.14 is the approach followed by pulsed plasma propulsion, which induces plasma breakdown of a gas near the object. The transfer of momentum to the object is achieved by an expanding shock wave. Note that this approach was demonstrated by real flight experiments during the Lightcraft project. Unfortunately, this method requires the craft to operate in a gaseous environment and can thus not work in space.

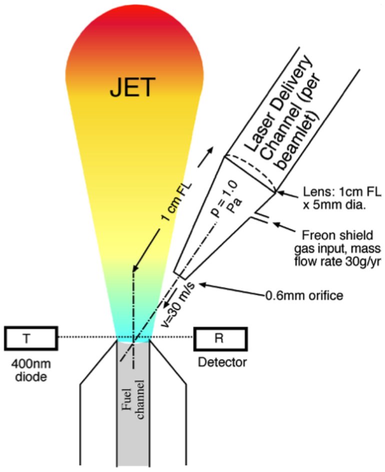

Figure 2.15: Laser ablation propulsion (image: Photonic Associates)

Another way of transferring momentum remotely to an object is to use the high power density of the laser beam to ablate the surface material of the object. This propulsion method is called ablative laser propulsion and is illustrated on figure 2.15. In the laser ablation process, ablated matter expands suddenly as it is removed from the object, thus resulting in high speed ejection of matter from the object. Not only this method can work in vacuum since the object material is used as its own propellant, but also laser ablation can in principle work with many different materials, even almost transparent ones. Both cw and pulsed lasers can be used, pulsed laser requiring less focusing capability of the optics to achieve a high beam power density at the same average power. Also, the thrust direction is not correlated with laser beam direction but only depends on the orientation of the surface of the material.

2.3 Proposed Applications for Asteroid Deflection and Space Debris Removal

Owing to their ability to push a target from a safe distance and without requiring propellant or prior detumbling, various concepts have emerged in the literature to tackle the space debris and asteroid issue with lasers. The different concepts envisaged either the use photonic propulsion or laser ablation propulsion. Compared to photonic propulsion, laser ablation permits to achieve thrust levels which are several orders of magnitude higher while still not requiring propellant for the maneuver as the ablated target material is in fact used to propel itself. Typical escape velocities of the ablated material are on the order of several km/s depending on the type of laser system employed (Phipps et al., 1988). The following subsections illustrate several concepts that have been proposed for active debris removal (ADR) and asteroid deflection. In the next chapter, we will investigate into more details the theoretical thrust delivered through laser ablation of materials commonly encountered in space debris and asteroids.

2.3.1 Active debris removal

ADR methods currently investigated by the European Space agency involve a flexible or rigid capture of the debris by the spacecraft using a robotic arm, a harpoon or even a net (Biesbroek et al., 2013). The deorbitation with these methods involve a somewhat complex sequence of rendezvous and docking operations which will generally involve at least a preliminary stabilization of the target at close range in order to damp its rotation rate. On the contrary, concepts to perform active debris removal with laser ablation involve remote operations which can either be ground-based or space-based with a chaser operating at a safe distance from its target. Since the thrust generated by laser ablation on the target is perpendicular to the ablated surface, the thrust direction is independent to the tumbling rate. Initial detumbling of the target is thus not required even though it can be theoretically be achieved through a smart laser steering strategy (Vetrisano et al., 2015). This implies that relatively small lasers (few hundreds of Watts) could be used in combination of an other ADR method requiring prior target stabilization. In the next paragraph, we illustrate proposed concepts where laser ablation is intended to be used as the main ADR system.

Laser systems proposed to clean-up orbital debris were initially ground-based, as illustrated by the Orion concept in Fig. 2.16. The main difficulty of these systems is to beam the laser light accross the atmosphere and deliver the impulse on a target located at several hundreds of kilometers of distance. The atmosphere has two major effects on the laser beam: scintillation, which causes incoherence and spreading of the beam, and nonlinear effects, which spread the beam in wavelength, spatially, or both. Due to difficulty to beam a sufficiently large energy at a long distance over the short period during which its target is in its field of view, the Orion study focused on removal of small debris between 1-10 cm, with a laser system requiring 20-100kW (Phipps et al., 1996).

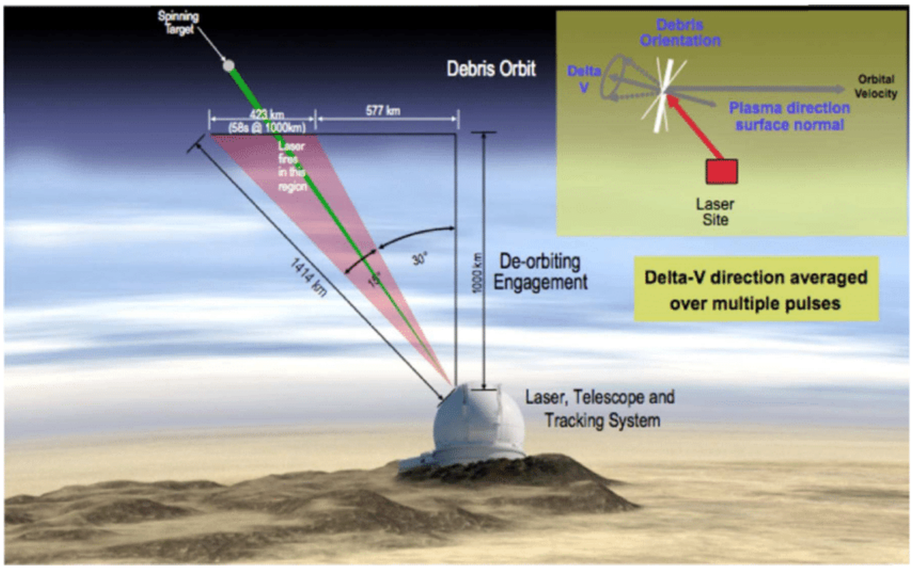

Figure 2.16: Orion concept for ground-based debris removal (Phipps et al., 1996)

More recently, Phipps introduced the idea of a spaceborne ultraviolet laser system for space debris clearing called LADROIT (Phipps, 2014). Compared to the ground-based system, LADROIT (see Fig. 2.17) would consist in a large satellite operating from a slightly eccentric polar orbit to cover the range of altitudes from 560 to 760km. This satellite does not rendezous with the debris (thus saving the energy cost of matching orbit) but rather engages any debris that appears in its field of view. Despite not matching the debris orbit, operating from space rather than from the ground allows to reduce the laser operations range and thus lower the size of the laser system. On the other hand, the proposed concept leads to a relatively complex mission with a 10-tons satellite accomodating a 15kW (average optical power) laser system and a somewhat optimistic pointing capability (0.5 μrad).

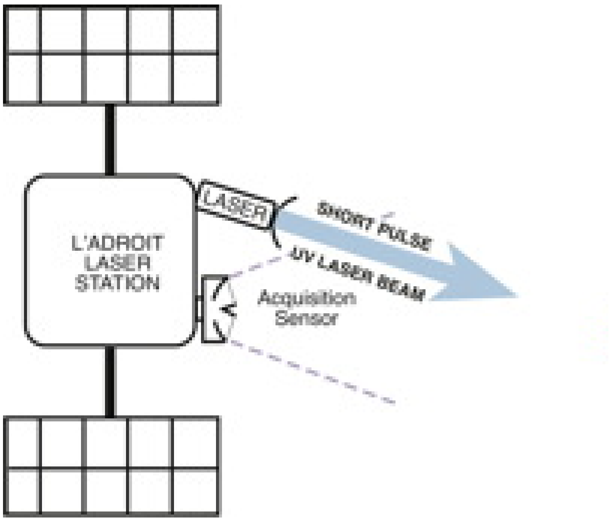

Figure 2.17: LADROIT concept (image: photonic associates)

Arguably, a smaller laser debris removal system could be achieved if the mission was allowed to rendezvous with its target prior to the removal operations, although this would limit eventually the number of debris that can be removed by a single system (due to the propellant cost of matching the debris orbit). Hence the LADROIT and ORION concepts might be economically suitable for small debris. On the other hand, a rendezvous strategy could be preferrable for larger targets (>1-ton) which could be clustered in specific orbital regions. This is why we will concentrate on this option in Chapter 7 of this thesis.

2.3.2 Asteroid deflection

Several mission concepts using in-space laser ablation have been investigated in the past using a single laser powered by nuclear reactors (Park and Mazanek, 2005; Yoo et al., 2009) or swarms of lasers powered by the Sun (Vasile and Maddock, 2012). A swarm of spacecraft flying in formation in the proximity of the target asteroid allows combining multiple beams to produce a high thrust level while keeping the power and thermal systems to a manageable size and complexity on each individual spacecraft. In addition, the swarm offers a more reliable system (Zuiani et al., 2012) in the case of failure of a single spacecraft and a more controllable thrust vector as ablating different parts of the asteroid surface will reduce the uncertainty on the direction of the resultant thrust vector.

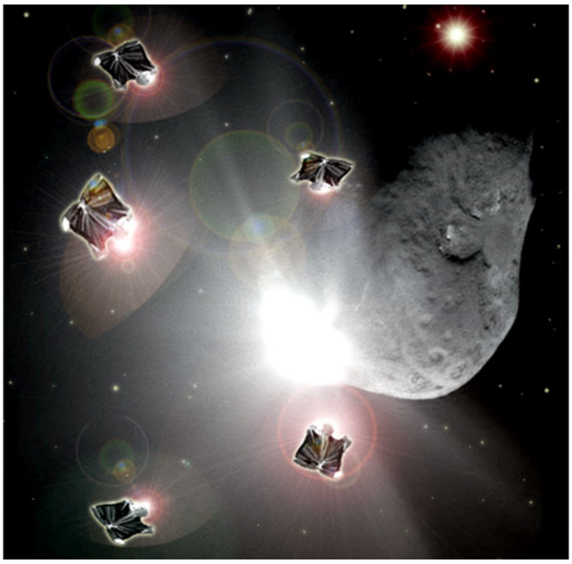

Figure 2.18: Laser bees concept (image: Christie Maddock, University of Strathclyde)

Recently a study supported by the European Space Agency, indicated the feasibility of laser ablation at changing the orbital velocity of a 130 tons S-type asteroid by 1 m/s in less than 1 year. The concept, called Light Touch[2] (Vasile et al., 2013), was considering the use of a commercial fibre laser, installed on a 453kg spacecraft, and requiring between 460W and 860W of input power.

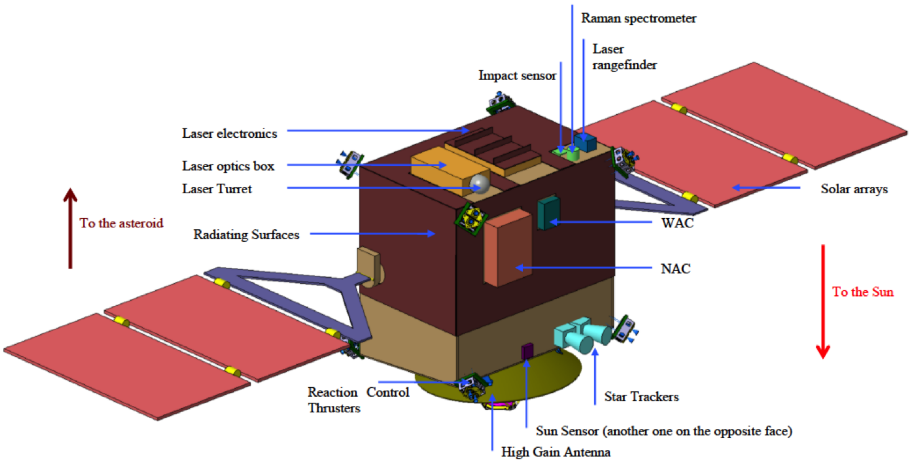

(a) Radial configuration

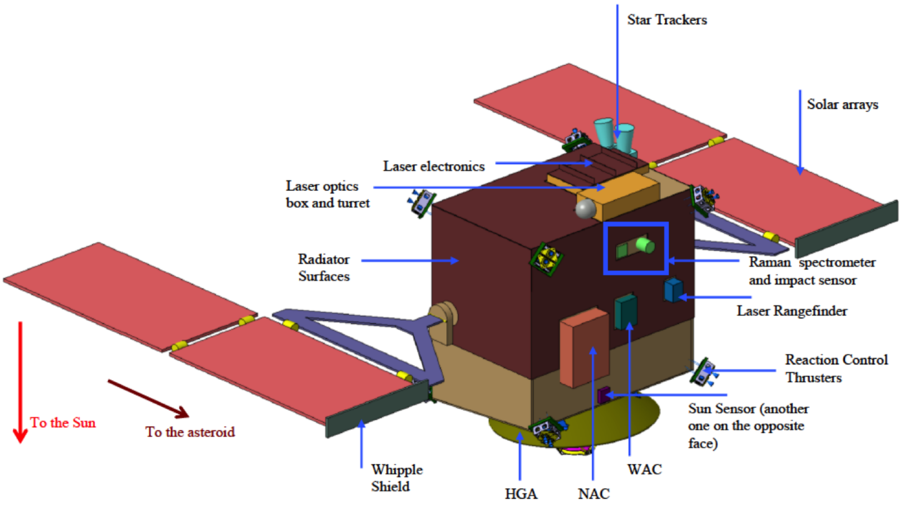

(b) Leading/trailing configuration

Figure 2.19: Light Touch2 concept

Chapter 3

Theoretical thrust performance of a laser ablation system

The performance of laser-based deflection methods depends on the ability of the laser system to turn its high optical power into a high kinetic power of the ablated ejecta. This chapter presents a theoretical model to evaluate the thrust generated when ablating a rotating target under a moderate light intensity($<$100GW/m^2). While the developments in the chapter explicitly consider a monochromatic light source in the near-infrared region (such as a Nd:YAG laser), the general results could be extended to the case where the light source is a solar concentrator device. The key metric to assess the performance of ablation-based methods is the thrust coupling coefficient which is given by the ratio between thrust and associated incident optical power required. The model introduced in this chapter improves over previous attempts (Vasile et al., 2014, 2013) as it more rigorously derives, from conservation laws, the thrust as a function of the laser sizing parameters as well as the material properties and rotation speed of the asteroid. The link between performance, laser parameters, and target properties is established and further analysed through refined numerical calculations.

3.1 Mechanical Coupling During the Ablation Process

Materials considered in this chapter are forsterite (Mg_2SiO_4, representative of S-type asteroids which are thought to dominate the inner belt population) as well as several materials that can be found in space debris such as aluminium, titanium alloys and carbon fibers. Assumed properties can be reviewed in table 3.1. Note that the values of thermal conductivity, density and absorptivity are effective values in the temperature range of interest[1]. In particular, the thermal conductivity of liquid aluminium alloys and metals can be less than half of the one at room temperature (Powell et al., 1966)Ẇhen available, high temperature electric resistivity measurements can be used to reconstruct the thermal conductivity using the Wiedemann-Franz law (Boivineau et al., 2006).

Table 3.1: Material properties considered for the computations

Quantity	Symbol	Mg_2SiO_4	Al2024 - T3	Ti 6Al-4V	Carbon Fiber	Unit
Density (sol - liq)	ρ	3280	2780 - 1800	4506 - 4110	1780	kg/m^3
Thermal Conductivity	k	2	100	16	20	$W{\cdot}m^{-1}\cdot K^{-1}$
Heat Capacity (liq)	c_l	1464	1177	984	-	$J{\cdot}kg^{-1}\cdot K^{-1}$
Heat Capacity (solid)	c_s	1264	1063	702	2000	$J{\cdot}kg^{-1}\cdot K^{-1}$
Vaporization Enthalpy	E_v	14.16	10.53	8.85	59.33	MJ/kg
Melting Enthalpy	E_m	0.508	0.397	0.295	-	MJ/kg
reference temperature	T_{ref}	3000	2790	3560	3915	K
reference pressure	p_{ref}	4448.9	1e+5	1e+5	1e+5	pa
Melting point	T_m	2171	925	1941	4600	K
Gas Constant	R^*	208	308	173	692	$J{\cdot}kg^{-1}\cdot K^{-1}$
Heat ratio (gas)	γ	1.26	1.67	1.67	1.67	-
Emissivity	ϵ	0.9	0.07	0.19	0.9	-
Absorptivity(1.06μm)	A	0.8	0.2	0.4	0.6	-
Rest temperature	T_∞	298	298	298	298	K

A 1D approach is selected which means that the thermal gradients in the lateral directions are assumed to be much smaller than the thermal gradients in the axial direction. This is typically valid for laser ablation processes in which the heated layer thickness is much smaller than the laser spot radius. With α the thermal diffusivity of the material, equal to the ratio between the thermal conductivity k and the product of the

---

[1] Absorptivity values taken from Freitag et al. (2014) for CFRP and from Rosen et al. (1982a) for Al2024 - T3 and Ti 6Al-4V

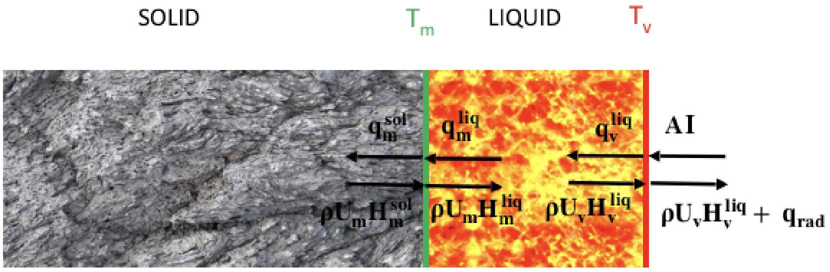

Figure 3.1: Energy transport during the ablation process. H is the enthalpy per unit mass and q the conduction heat flux.

density ρ and the heat capacity c_l so that $\alpha = \frac{k}{\rho c_l}$, the heated layer thickness grows approximately with $\sqrt{\alpha t}$ in the transient regime and becomes proportional to $\frac{\alpha}{U^2}$ when a standing evaporation wave with interface recession speed U develops in the steady-state regime (Anisimov and Khokhlov, 1995). With the notable exception of carbon, the surface temperature reached during the ablation process is substantially higher than the triple point of the substance considered. Therefore the ablated material undergoes successive phase transformations before reaching the vapour state and a very thin layer of molten material is formed under the ablation front. With reference to Fig. 3.1, a simple energy balance allows us to express the energy absorbed by thermal conduction through the different interfaces and to derive the continuity relation along the vaporization and melting fronts:

$$q_v^{\text{liq}} = AI - q_{rad} - \rho U_v E_v \tag{3.1}$$

$$q_m^{\text{liq}} = q_m^{\text{sol}} + \rho U_m E_m \tag{3.2}$$

In which I is the laser intensity, A is the absorption of the interface at the laser wavelength, E_v and E_m are vaporization and melting enthalpies, q_v^{liq} and q_m^{liq} are the conduction fluxes on the liquid side of the vapor/liquid and liquid/solid interfaces respectively, U_v and U_m are the recession speeds of these 2 interfaces and ρ without index denotes the density in the condensed state. The mass flow during the vaporization process is a consequence of the thermodynamical non-equilibrium at the interface. As they vaporize, the molecules acquire a net translational velocity component through colli-

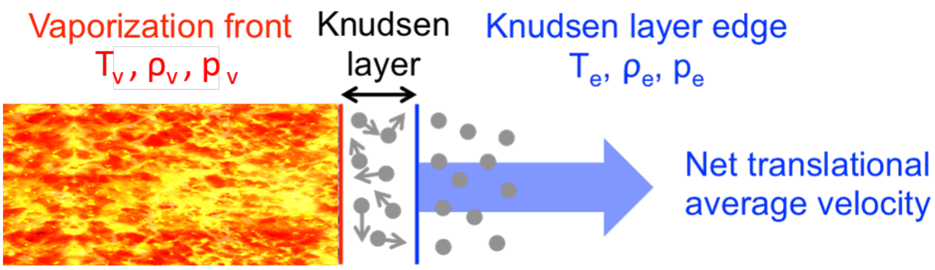

Figure 3.2: The Knudsen Layer

sions at the molecular level, resulting in their distribution function becoming a shifted Maxwellian distribution (Knight, 1979) . The finite layer through which the drift velocity can be acquired is called the Knudsen layer and is treated in the model as a gas-dynamic discontinuity (Knight, 1979). The jump conditions are given in equation 3.3 :

$$
\begin{aligned}
m &= \sqrt{\frac{\gamma}{2}}M_e = \frac{u_e}{\sqrt{2R^*T_e}} \\
\frac{T_e}{T_v} &= \left[\sqrt{1+\pi\left(\frac{\gamma-1}{\gamma+1}\frac{m}{2}\right)^2} - \sqrt{\pi}\frac{\gamma-1}{\gamma+1}\frac{m}{2}\right]^2 \\
\frac{\rho_e}{\rho_v} &= \sqrt{\frac{T_v}{T_e}}\left[(m^2+\frac{1}{2})e^{m^2}\operatorname{erfc}(m) - \frac{m}{\sqrt{\pi}}\right] \\
&\quad + \frac{1}{2}\frac{T_v}{T_e}\left[1-\sqrt{\pi}me^{m^2}\operatorname{erfc}(m)\right]
\end{aligned}
\tag{3.3}
$$

In this expression, the indices v and e refer the state of the vaporized matter directly after the interface and on the edge of the Knudsen layer, as indicated on Fig. 3.2; M$_e$ represents the local Mach number on the edge of the Knudsen layer which is dependent on the environment downstream and γ is the heat capacity ratio in the gas mixture (see table 3.1). For expansion in vacuum, the flow reaches the sonic limit at the edge of the Knudsen layer((Knight, 1979)). The flow then becomes supersonic through isentropic expansion in vacuum (Kahle et al., 2006), meaning that the environment downstream of the Knudsen layer cannot influence the evaporation process. Due to the mass conservation and using the perfect gas law, the mass flow per unit area ρU_v can be directly computed from equation 3.3 once the temperature T$_v$ of the interface is known:

$$\rho U_v = \rho_e u_e = \rho_e \sqrt{\gamma R^* T_e} = \alpha_v \frac{p_v}{\sqrt{2\pi R^* T_v}} \tag{3.4}$$

By rearranging the terms, one can show that the term on the right of this equation is equivalent to the Hertz-Knudsen-Langmuir formula in vacuum taking an evaporation fraction α_v of

$$\alpha_v = \frac{\rho_e}{\rho_v} \sqrt{\frac{2\pi\gamma T_v}{T_e}} \tag{3.5}$$

The liquid near the interface is on the other hand assumed to be near equilibrium (Knight, 1979). Therefore, a Clausius-Clapeyron relation is used to obtain the dependency between p_v and T_v in the gas:

$$\log\left(\frac{p_v}{p_{ref}}\right) = \frac{E_v}{R^*}\left(\frac{1}{T_{ref}} - \frac{1}{T_v}\right) \tag{3.6}$$

When sufficient time is allowed to heat the target, the ablation proceeds in a steady-state regime and $U_v = U_m = U$. Therefore, the internal energy of any control volume becomes invariant with respect to time. This means that the heat conducted under the ablation front q_v^{liq} is balanced by the heat required to heat and melt the flow of material from the rest temperature T_∞ to the surface temperature T_v:

$$q_v^{\text{liq (steady)}} = \rho U \left(E_m + c_l(T_v - T_m) + c_s(T_m - T_\infty)\right) \tag{3.7}$$

In this regime, an implicit relation can thus be found to link the interface temperature to the laser intensity I:

$$\begin{aligned} \overbrace{AI}^{\text{Laser}} = {} & \overbrace{\epsilon\sigma\left(T_v^4 - T_\infty^4\right)}^{\text{Radiation emission losses}} \\ & + \underbrace{\rho U \left(E_v + E_m + c_l(T_v - T_m) + c_s(T_m - T_\infty)\right)}_{\text{Power convected away by the vaporization process}} \end{aligned} \tag{3.8}$$

in which the Stefan-Boltzmann law was assumed for the radiation flux: $q_{rad} = \epsilon\sigma\left(T_v^4 - T_\infty^4\right)$.

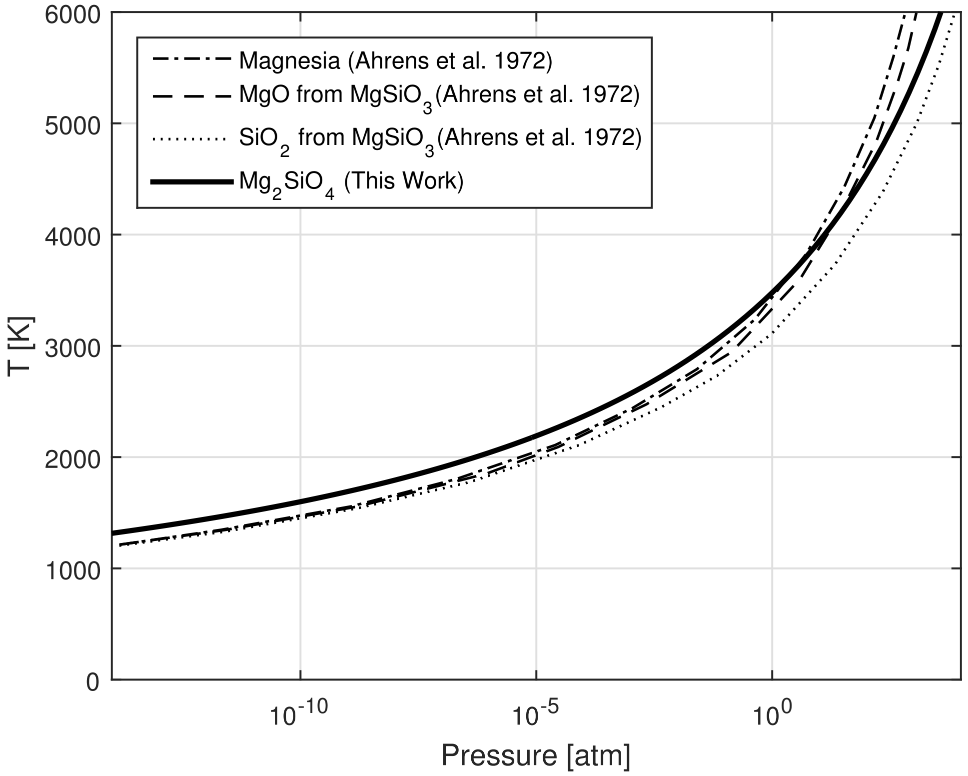

Figure 3.3: Equilibrium pressure p_v of Forsterite as a function of the surface temperature T_v

Determining the surface temperature from the flux, the net force per unit area p_{eff} under the spot can be computed by summing the rate of momentum change and the pressure at the edge of the Knudsen layer:

$$p_{\text{eff}} = p_e + \rho_e u_e^2 = (1 + \gamma M_e^2) p_e = (\gamma + 1) p_e \tag{3.9}$$

Note that using the saturation pressure p_v directly instead of p_{eff} would yield to an overestimation of the thrust by about a factor 2. This is due to the fact that in the neighbourhood of the ablation front, the distribution in the gas molecules is close to an half-range Maxwellian distribution, plus a contribution of the backscattered molecules (Rosen et al., 1982a). The thrust coupling coefficient C_m provides a figure of merit for the laser-based deflection methods. It is defined as the ratio of the force exerted by the power injected :

$$C_m = \frac{p_{\text{eff}}}{I} \tag{3.10}$$

Assuming the ablation proceeds in steady-state, Fig. 3.4 shows the thrust coupling coefficient computed for Forsterite and several materials that can be found on space debris. The values predicted seem to stall between 10 to 100 $\mu N/\text{W}$, which is consistent with the existing literature (Phipps et al., 2010). When transient effects are neglected, we see that the ablation threshold is essentially driven by the absorptivity-emissivity ratio of the material, with a high ratio (aluminium alloys) favouring the ablation onset. On the other hand, the plateau value reached by the coupling coefficient is essentially linked with the absorptivity-vaporization enthalpy ratio of the material. This explains why Forsterite, which has a much higher absorptivity than the other materials, has a better coupling coefficient than carbon, titanium and aluminium alloys. On the other hand, carbon has a higher absorptivity than aluminium but also requires a much higher Vaporization energy.

3.2 Impact of the 3D thermal conduction fluxes

One key assumption underneath the result in Fig. 3.4 is that the thermal gradient is perpendicular to the illuminated surface and dissipation in lateral directions is negligible (1D assumption). This assumption is equivalent to saying that the thickness of the heated layer is small compared to the diameter of the laser beam. It is, therefore, important to compute an estimation of this thickness to check when this 1D assumption holds for a given laser system. For the sake of simplicity, we consider here identical material properties in the molten and solid phases. As this assumption is not necessary for the analytical model of the previous section, it is only used here to derive a simple expression of the temperature profile while the actual heat capacities of the solid and molten phases actually vary by about 16% if one refers to table 3.1. The temperature distribution as a function of the depth z can be computed by solving the 1D advection-

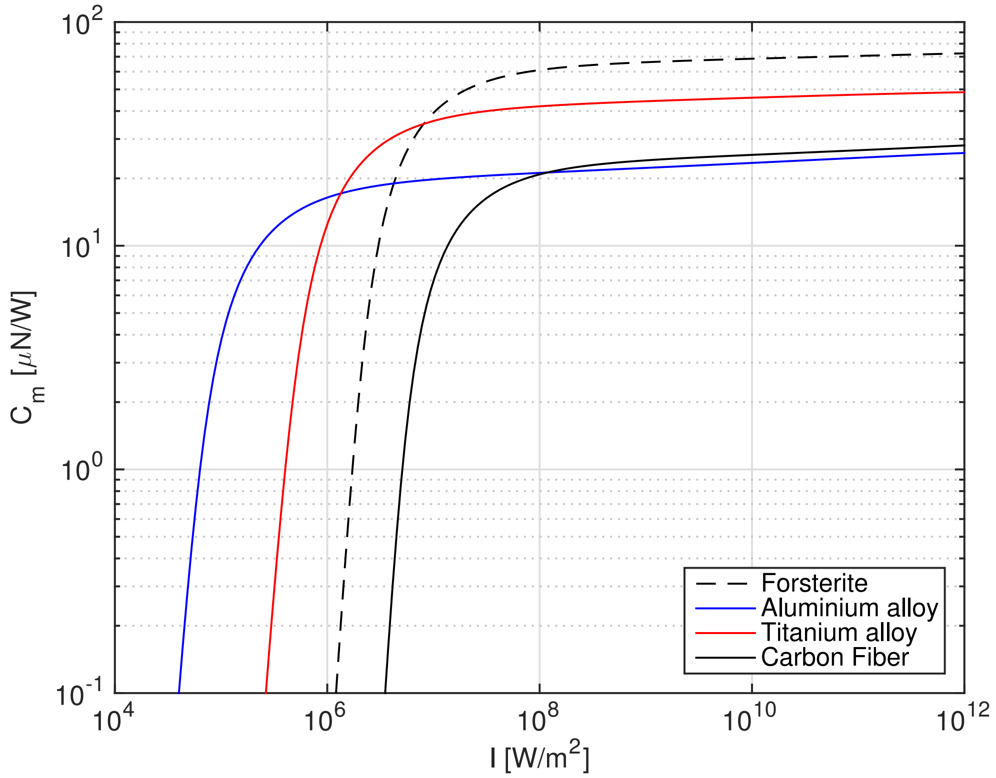

Figure 3.4: Thrust coupling as a function of the laser intensity for Forsterite and several materials found on space debris

diffusion problem:

$$u\frac{dT}{dz} + \alpha\frac{d^2T}{dz^2} = 0 \tag{3.11}$$

where $\alpha = \frac{k}{\rho c}$ is the thermal diffusivity. The generic solution is in the form $T(z) = A\exp\left(-\frac{u}{\alpha}z\right) + B$. The temperature profiles can be computed both in the molten and solid phases by setting the following boundary conditions:

$$T(z = 0) = T_v \tag{3.12}$$

$$T(z = z_m) = T_m \tag{3.13}$$

$$T(z \to \infty) = T_\infty \tag{3.14}$$

The resulting temperature distribution through the condensed phases is then given by:

$$T(z) = \begin{cases} \frac{T_v - T_m}{1-\exp\left(-\frac{u}{\alpha} z_m\right)} \exp\left(-\frac{u}{\alpha} z\right) + \frac{T_m - \exp\left(-\frac{u}{\alpha} z_m\right) T_v}{1-\exp\left(-\frac{u}{\alpha} z_m\right)} & \text{if } z < z_m \\ (T_m - T_\infty) \exp\left(-\frac{u}{\alpha}(z - z_m)\right) + T_\infty & \text{if } z_m < z \end{cases} \tag{3.15}$$

The location of the melting front is obtained by using the heat balance at the melting interface:

$$\frac{ku}{\alpha} \frac{T_v - T_m}{\exp\left(\frac{u}{\alpha} z_m\right) - 1} = \frac{ku}{\alpha}(T_m - T_\infty) + \rho u H_m \tag{3.16}$$

and by rearranging the terms of Eq. (3.16), we find:

$$z_m = \frac{\alpha}{u} \log\left(\frac{T_v - T_m}{T_m - T_\infty + \frac{H_m}{c}} + 1\right) \tag{3.17}$$

Figure 3.5 shows the resulting temperature distribution in the asteroid material according to Eq. (3.15) if the laser intensity is such that a temperature of 3000K is reached at the vaporization front. The value l_c is defined as $l_c = \alpha/u$ and would correspond to the intersection of the slope of the temperature profile at $z = 0$ with the horizontal axis $T = T_\infty$ if H_m was equal to 0.

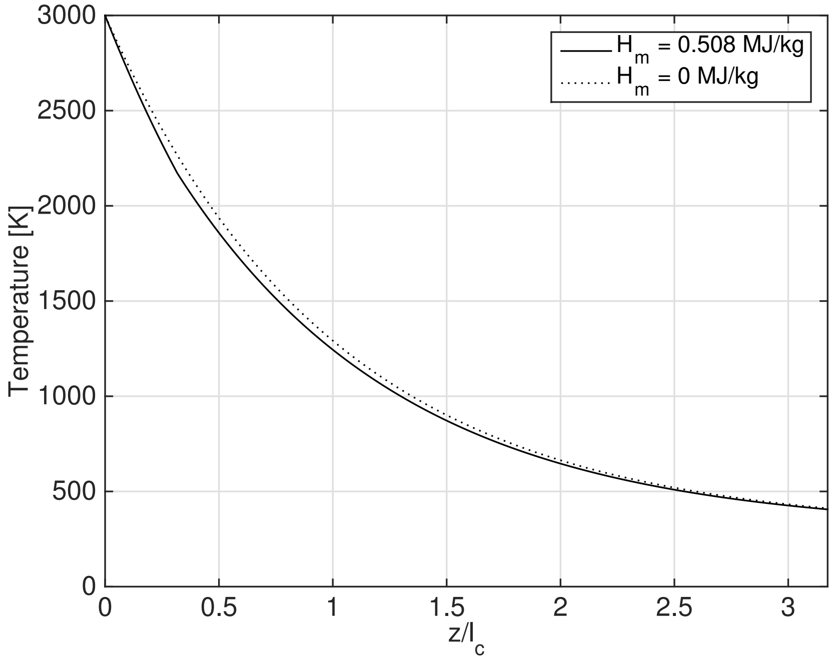

Figure 3.5: Temperature distribution under the laser spot as a function of the normalized depth for different values of the melting enthalpy H_m

The exponential temperature distribution in figure 3.5 shows that the layer of material that is heated from a temperature close to the rest temperature T_∞ to the surface temperature T_v is indeed proportional to l_c. The thermal gradient in the axial direction is therefore proportional to $\frac{T_v - T_\infty}{l_c}$ while the diameter of the laser beam D_b drives the importance of the thermal gradients in the lateral directions. As a consequence, one can expect that the 1D assumption is justified whenever the ratio $\frac{D_b}{l_c}$ is high enough.

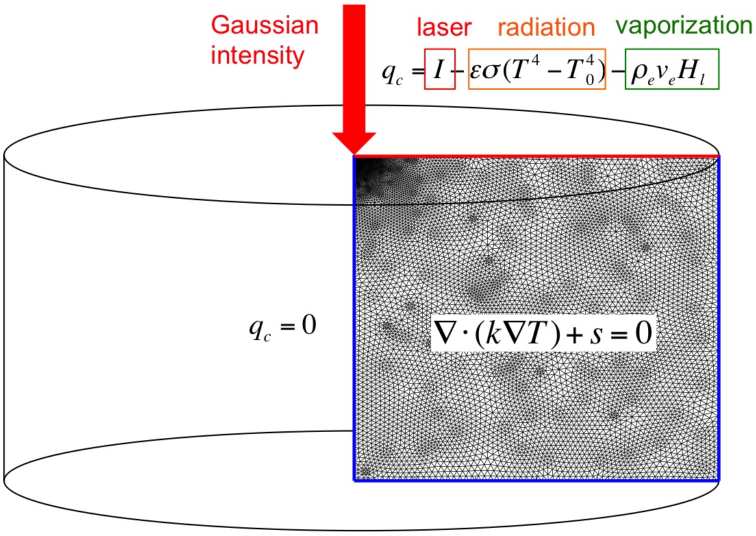

Figure 3.6: 3D Axis-Symmetrical Model showing mesh and BCs

The dimensional analysis above does not account for non-linear effects caused by the radiation losses in the direct neighbourhood of the laser spot. Moreover, due to the Gaussian intensity profile, deviations from the 1D approach can also occur because part of the energy reaches the target too far from the centercore of the beam and, therefore, can not contribute to the ablation process. To investigate these effects, we developped a 3D Finite Element Model (FEM), as represented in Fig. 3.6. This model was implemented in Matlab© taking advantage of the PDE toolbox to solve the heat Eq. (3.18) in cylindrical coordinates. In a frame attached to the target, this equation writes:

$$\nabla \cdot (k\nabla T) + s = 0 \tag{3.18}$$

In this equation, s represents a volumic source term which is equal to zero if we assume that the asteroid material is opaque and the power from the laser beam is absorbed at the surface of the ablation spot. However, in the case of a partially transparent material, this term could account for the absorption of the beam intensity through the depth of the material. A typical mesh can be seen on Fig. 3.6. The mesh criterion and geometry size is automatically adapted in function of the user-defined output power and diameter of the laser beam. These were initially adjusted by following a thorough sensitivity study to ensure they do not compromise the quality of the results. The boundary conditions are imposed as follow:

- Along the symmetry axis and far region:

$$q_c = 0 \tag{3.19}$$

- On the top surface:

$$q_c = AI - \epsilon\sigma\left(T_v^4 - T_\infty^4\right) - \rho u H_l \tag{3.20}$$

In Eq. (3.20), H_l represents an augmented enthalpy which accounts for the total energy required to heat the flow of material leaving the asteroid.

$$H_l = H_v + H_m + c_{sol}(T_m - T_\infty) + c_{liq}(T_v - T_m) \tag{3.21}$$

The main transverse mode of the laser beam (TEM00) is accounted in the model by inputting a Gaussian intensity distribution:

$$I = \frac{8P}{\pi D^2}\exp\left(\frac{-8r^2}{D_b^2}\right) \tag{3.22}$$

In this expression, D represented the diameter of the laser beam defined classically as four times the standard deviation of the TEM00 mode. Far from the center of the laser beam, this intensity vanishes together with the vaporization process so that Eq. (3.20)

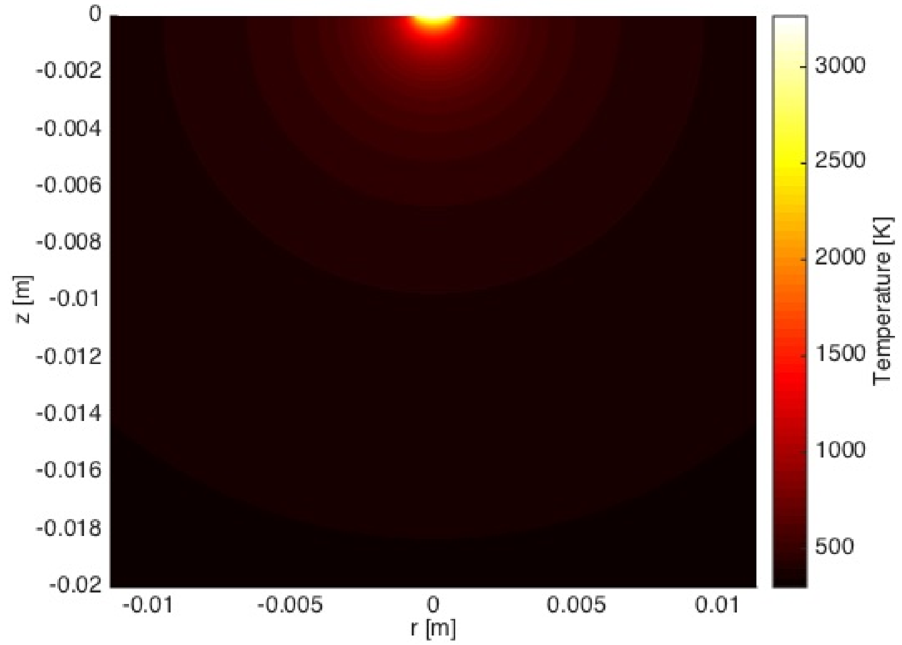

Figure 3.7: Example of calculated temperature distribution under the laser spot with P=100W and D=2mm

naturally tends to the simple radiative boundary conditions:

$$q_c = -\epsilon\sigma\left(T_v^4 - T_\infty^4\right) \tag{3.23}$$

By comparison to the analytical model, the radiations on the sides of the laser spot will now represent an additional energy drain. A non-linear solver is used to find the temperature distribution that is consistent with the heat-equation and the non-linear boundary conditions.

As illustrated on Fig. 3.7, the results of the FEM model provide the temperature profile on the surface and inside the computation domain. From this surface temperature, one can reconstruct the net thrust by calculating the following integral over the spot area:

$$\begin{aligned} F &= \int_{spot} p_e + \rho_e v_e^2 dS \\ &= \int_{spot} (1+\gamma) p_e dS \end{aligned} \tag{3.24}$$

The thrust coupling coefficient is now computed by dividing the total force F by the optical power of the laser P:

$$C_m = \frac{F}{P} \tag{3.25}$$

The thrust coupling coefficient was computed for three different power outputs, 0.1 kW, 1 kW and 10 kW, and a spot diameter ranging from 1 to 32mm. Figure 3.8 shows that, for a given amount of power, reducing the spot size increases the momentum transferred to the asteroid, as also predicted by the 1D model. Note that, for a given intensity, the C_m for the 10kW laser case is the closest to the one predicted by the 1D model. An explanation can be found in the result represented in figure 3.9. The figure shows the relative efficiency η of the 3D model as a function of the D/l_c ratio. The relative efficiency η_{3D} is defined as the ratio between the thrust coupling predicted by the 3D numerical model and the one predicted by the 1D analytical model. Figure 3.9 shows that when $D > 3l_c$, η_{3D} is higher than 70%. As the ratio D/l_c increases, η_{3D} tends to an asymptotic value of approximately 87%. The residual 13% difference between the 3D and 1D predictions is explained by the Gaussian intensity distribution of the laser beam. In fact, when a uniform distribution is used instead, η_{3D} tends to 100% as D/l_c goes to infinity. This can be observed on Figure 3.8 where the asterisk represents the FEM solution for 10kW of optical power and uniform beam distribution.

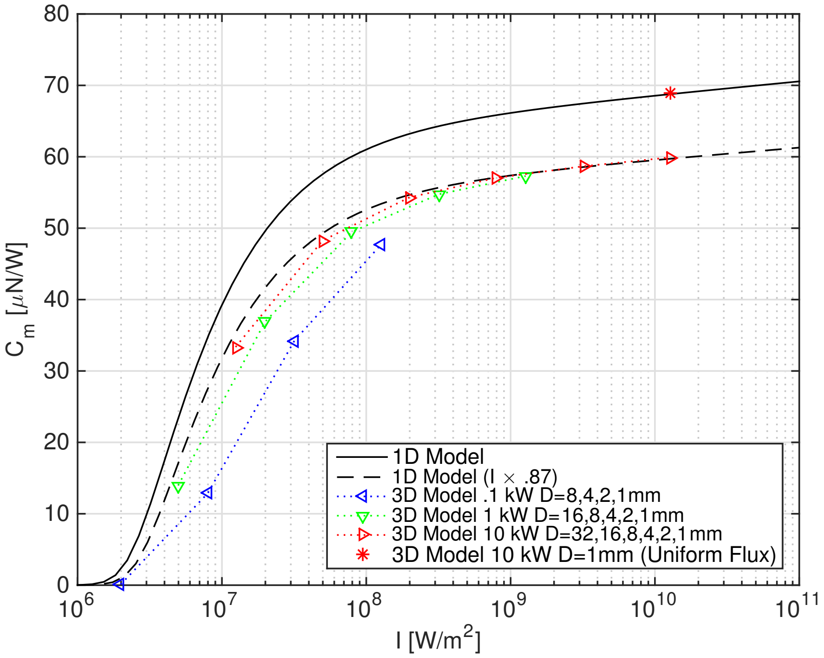

Figure 3.8: Thrust coupling coefficient as a function of the laser intensity

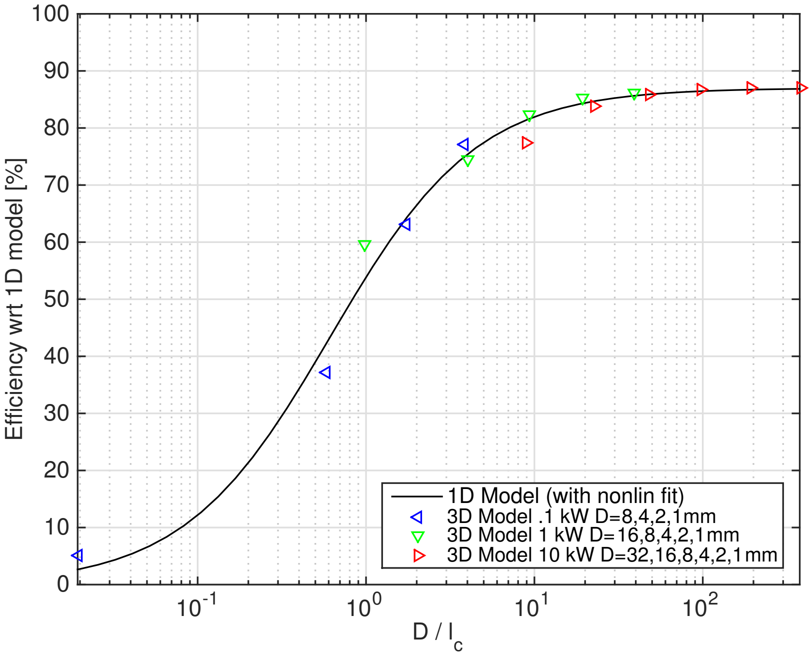

Figure 3.9: η_{3D} as a function of $\frac{D}{l_c}$: The black curve represents a sigmoid fit.

3.3 Model for a non-stationary target

Another assumption of the ideal model is that the time allowed to heat a given point at the surface is long enough so that transient effects can be neglected. In practice, the tumbling motion of the target induces a limitation on the time available to heat a given point at its surface, as illustrated on Fig. 3.10. Considering the relative velocity of the ablated surface respectively to the laser beam v$_{rel}$ and the diameter D of the laser beam, a mean heating time τ can be computed as

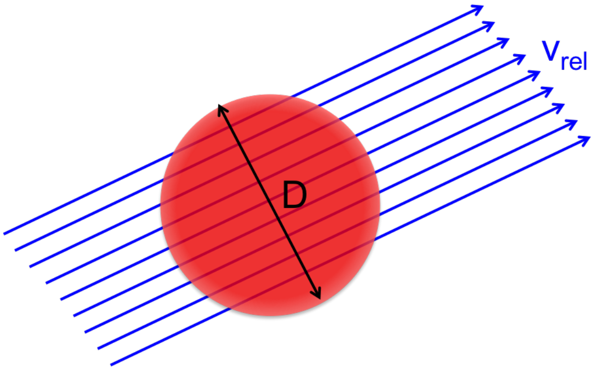

Figure 3.10: Motion of a surface point under the laser beam

$$\tau = \frac{\pi}{4}\frac{D}{v_{rel}} \tag{3.26}$$

In which the $\frac{\pi}{4}$ coefficient is due to the cylindrical shape of the laser beam (points crossing the beam on its sides will remain exposed less time than points passing through the centre). Therefore, in order to understand how the tumbling motion affects the ablation process, the transient heat equation needs to be solved. An enthalpy formulation with a frame attached to the moving ablation front is selected in Eq.(3.27), allowing to handle the different phase transitions in a more convenient way:

$$\frac{\partial(\rho H)}{\partial t} = -\frac{\partial q}{\partial z} + \frac{\partial(\rho U_v H)}{\partial z} \tag{3.27}$$

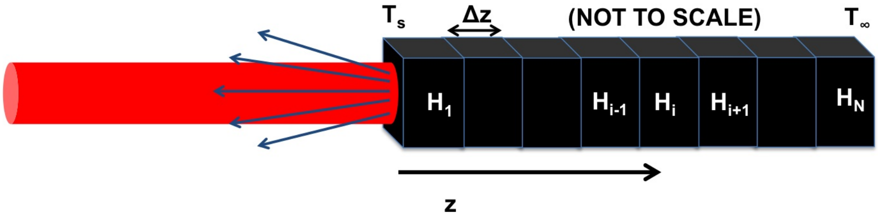

Figure 3.11: Discretization of the computation domain

In this equation, U_v is the recession speed of the ablation front and q, the heat flux, which is expressed through the common Fourier law $q = -k\frac{dT}{dz}$.

As illustrated in Figure 3.11, Eq.(3.27) can be solved numerically by discretizing the computation domain with N cells along the depth direction z and applying the conservation of the enthalpy to each of them as follows:

$$\frac{d(\rho H)_i}{dt} = -\frac{q_{i+1/2} - q_{i-1/2}}{\Delta z} + U_v(T_1)\frac{(\rho H)_{i+1} - (\rho H)_i}{\Delta z} \tag{3.28}$$

In which i is the index of the control cell and we wrote $U_v(T_1)$ to recall that the recession speed U_v is computed from the interface temperature T_1. The temperature T_i of the i^{th} control cell is recovered in real time from the enthalpy which is for convenience defined equal to 0 at the melting temperature:

$$T_i = T_m + \frac{H_i}{c_s} \qquad \text{if } H_i \leq 0 \tag{3.29}$$

$$T_m \qquad \text{if } 0 < H_i < E_m \tag{3.30}$$

$$T_m + \frac{H_i - E_m}{c_l} \qquad \text{if } H_i \geq E_m \tag{3.31}$$

The heat fluxes on the sides of the i^{th} control cell are then computed from the Fourier law using central differences:

$$q_{i+1/2} = -k\frac{T_{i+1} - T_i}{\Delta z} \tag{3.32}$$

$$q_{i-1/2} = -k\frac{T_i - T_{i-1}}{\Delta z} \tag{3.33}$$

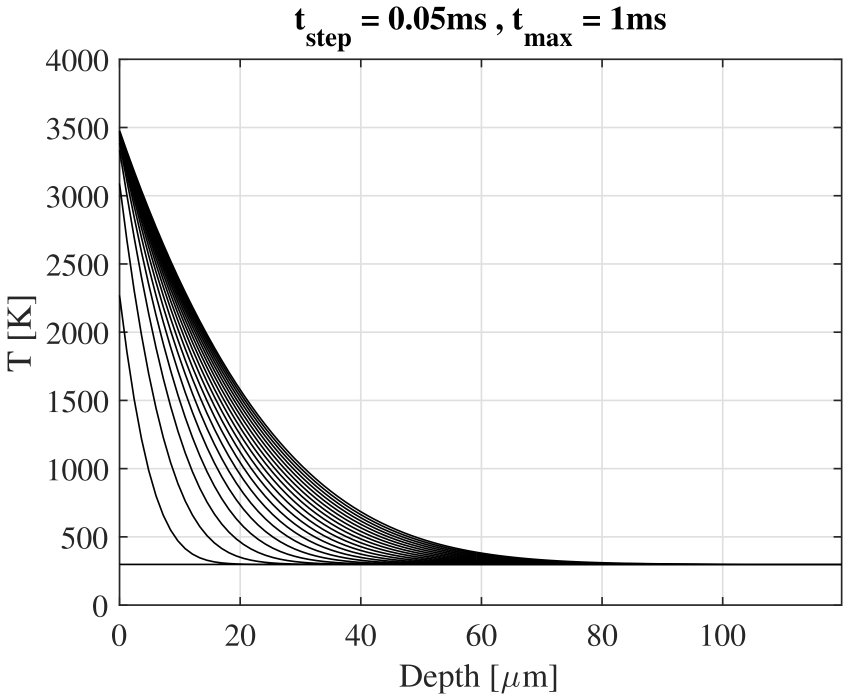

Figure 3.12: Temperature evolution through the depth of an asteroid material under a laser beam with I = 1GW/m^2

The boundary conditions are also introduced through the heat fluxes on the left of the first cell and on the right of the last cell respectively:

$$q_{1/2} = AI - q_{rad}(T_1) - \rho U_v(T_1)E_v \tag{3.34}$$

$$q_{N+1/2} = -k\frac{T_\infty - T_N}{\Delta z} \tag{3.35}$$

As already explained in Eq.(3.1), the boundary condition for $q_{1/2}$ simply states that the heat flux conducted through the gas/liquid interface equates the transmitted power density to which is subtracted the flux radiated away (approximated from the Stefan-Boltzmann law of emission of a black body) and the heat required to vaporize the flow crossing the interface. Eq.(3.28) is integrated in Matlab© using ode23t which is suitable for moderately stiff problems. Fig. 3.12 shows the temperature evolution under the surface of an asteroid exposed under a laser beam intensity I of 1GW/m^2. The time-dependent thrust coupling coefficient C_m^{tr} is recovered from the surface temperature at each time-step and an effective thrust coupling coefficient C_m is simply obtained by

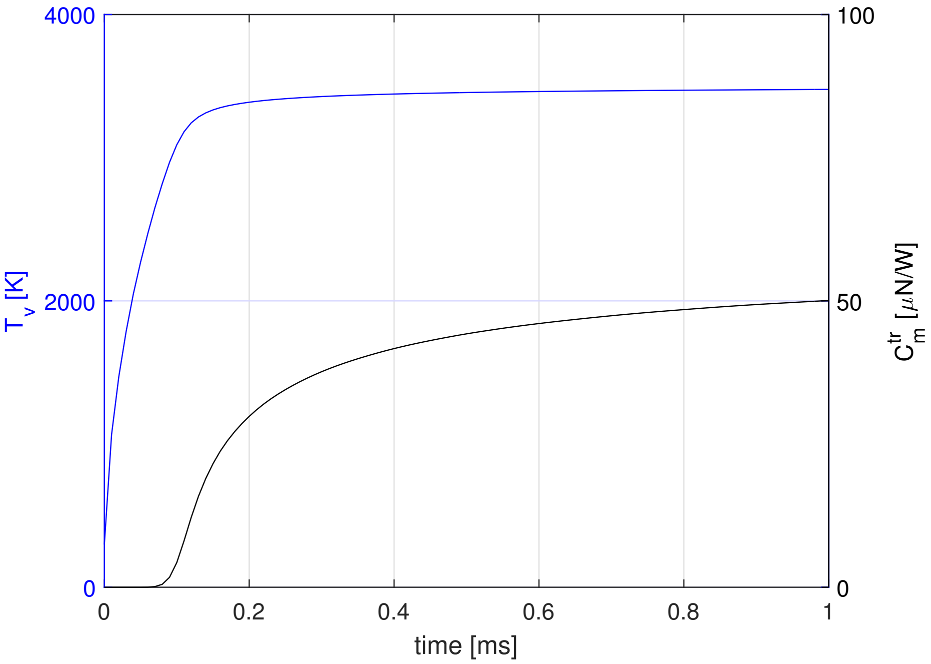

Figure 3.13: Evolution of the surface temperature T_v and the thrust coupling coefficient C_m^{tr} for forsterite and $I = 1GW/m^2$

averaging its value over the exposition period:

$$C_m = \frac{0.87}{\tau} \int_0^{\tau} C_m^{tr} dt \tag{3.36}$$

In which the 0.87 factor accounts for the losses due to the non-uniform power density of the laser beam, as demonstrated in the previous paragraph. Using the same example as in Fig. 3.12, Fig. 3.13 now illustrates the time-evolution of the surface temperature T_v of the ablation front and the thrust coupling coefficient.

We repeated these computations for a wide range of laser intensities and exposition time τ. The results can be seen for forsterite on Fig. 3.14 and a 1mm thin panel of aluminium alloy on Fig. 3.15. For this second simulation, the reduction of the debris thickness was also considered by integrating the variation of the thickness h through time together with the previous set of equations:

$$\frac{dh}{dt} = -U_v \text{ with } h_0 = 1\text{mm} \tag{3.37}$$

The second boundary condition was also modified to the boundary condition of a free surface:

$$q_{N+1/2} = q_{rad}(T_N) \tag{3.38}$$

It appears that the ablation threshold is shifted towards higher intensities following a trend line in logarithmic scales such that $(I\sqrt{\tau})_{\text{Threshold}}$ is a constant. If one neglects the melting and vaporization processes, it can be shown (Anisimov and Khokhlov, 1995)

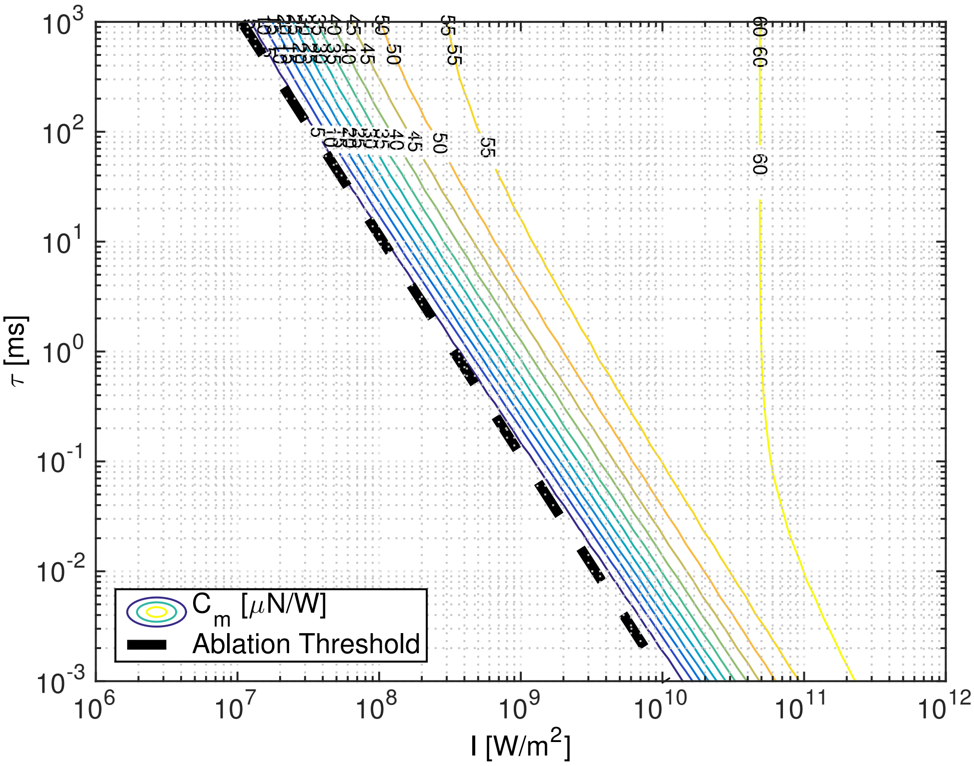

Figure 3.14: Thrust coupling coefficient as a function of the mean heating time τ and the laser intensity for Forsterite

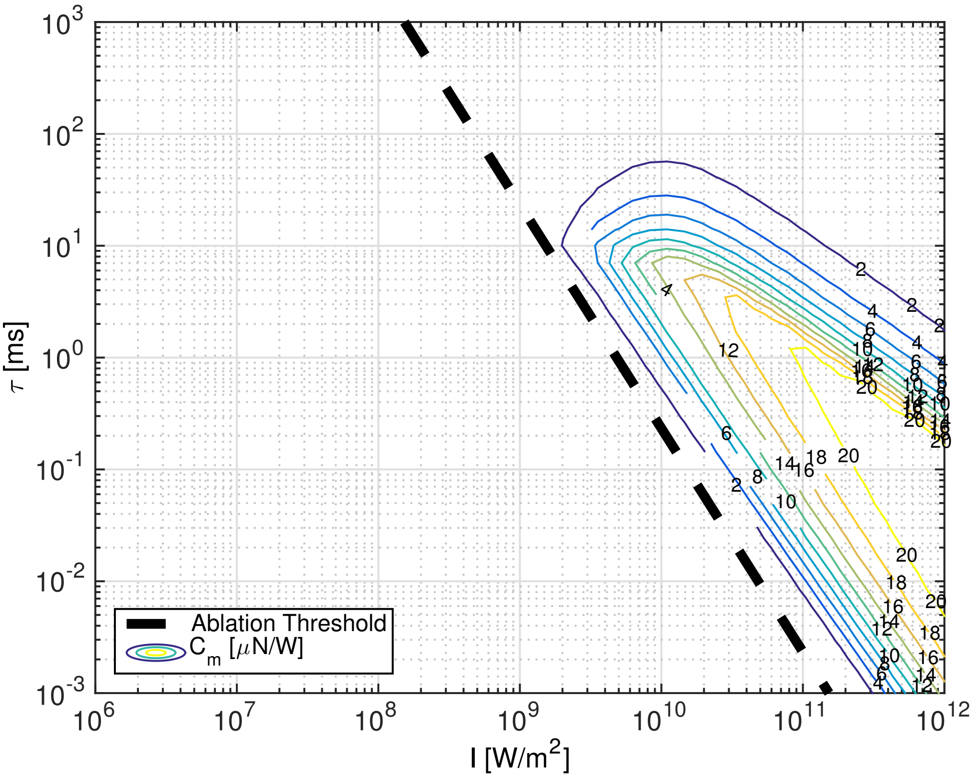

Figure 3.15: Thrust coupling coefficient as a function of the mean heating time τ and the laser intensity for a 1mm panel of Al 2024-T3

Table 3.2: Calculated Ablation Onsest for the Different Materials Considered in This Study

Material	Forsterite	Al2024 - T3	Ti 6Al-4V	Carbon Fiber	Unit
$(I\sqrt{\tau})_{\text{Threshold}}$	0.106E+8	1.607E+8	0.58E+8	0.45E+8	W $\text{m}^{-2}s^{1/2}$

that the temperature inside the material increases with respect to time according to :

$$T(z,t) - T_\infty = \frac{2AI}{k}\sqrt{\alpha t}\,\text{ierfc}\left(\frac{z}{2\sqrt{\alpha t}}\right) \tag{3.39}$$

Using the the reference temperature as a first approximation and inverting this relation in z=0 allows to estimate the ablation threshold $(I\sqrt{\tau})_{\text{Threshold}}$:

$$(I\sqrt{\tau})_{\text{Threshold}} \approx \sqrt{\frac{\pi}{4}\frac{\Gamma \Delta T_{\text{ref}}}{A}} \tag{3.40}$$

In which Γ is the thermal inertial of the material $\Gamma = \sqrt{\rho c_l k}$.

The ablation threshold was computed for the different materials in table 3.2 and is represented by the dashed black line on figures 3.14 and 3.15 and appears to be consistent with the result of the numerical model. The thickness reduction with the recession of the ablation front was also integrated together with Eq.(3.28) during the computations in the case of the thin aluminium panel and therefore a higher limit on the exposition time as a function of the intensity is also visible in figure 3.15. It corresponds to the time required to dig through the 1mm panel. From this figure, one can also see that the region of high efficiency only exists for a combination of very short exposition time and high intensities. This is a direct consequence of the finite thickness of the material and supports the use of a pulsed laser system in the case of orbital debris rather than a CW laser system.

3.4 Plasma Ignition Threshold

The last assumption in our model is that operations are carried at a sufficiently low intensity level so that ionization losses can be neglected. When plasma dominates the laser produced plume, increasing intensity yields to a reduced efficiency in the coupling coefficient. In this regime, the dependence between the laser intensity and the thrust coupling coefficient follows a power law on the form $C_m \propto \left(I\lambda\sqrt{\tau}\right)^{-1/4}$ (Phipps et al., 1996). In the last expression, τ is the pulse duration and λ the laser wavelength. The processes leading to plasma formation under CW laser irradiation have been investigated (Poueyo-Verwaerde et al., 1993). Initially, an energy flux on the order of 100GW/m^2 is required to accelerate the free electrons in the vapor by inverse Bremsstrahlung until their kinetic energy becomes sufficient to ionize the atoms of the vapor by an avalanche process. Indeed, a necessary condition for the development of this electron avalanche is that the growth rate of electron energy by IB is higher than the losses due to elastic collisions with neutral atoms in the plume (Poueyo-Verwaerde et al., 1993). This condition translates in a CW intensity threshold approximately equal to

$$I_{plasma}^{CW}(TW/m^2) \approx \frac{6E_i(eV)}{\lambda^2(\mu m)A} \tag{3.41}$$

In which E_i is the ionization potential and A the atomic mass number. According to this expression, for laser frequencies in the infrared and typical values of ionization potentials and atomic masses, the plasma ignition threshold is at intensities ranging between 10GW/m^2 and 1TW/m^2.

For pulsed laser, an empirical value of the plasma ignition threshold was found (Phipps et al., 1988) as

$$I_{plasma}^{pulsed}\sqrt{\tau} = 4.8\text{E+}08 W m^{-2} s^{1/2} \tag{3.42}$$

The time-dependency of Eq. 3.42 might give the impression that in the CW case ionization can occur at relatively low intensities. However, the model from which this expression was derived assumes that absorption of the laser intensity by the plume is done in a time short enough that its 3-dimensional expansion can be neglected. In the case of interest both the expansion and absorption happen simultaneously. Typically, the length of the zone where laser heating dominates over the expansion has a characteristic dimension on the order of the beam spot diameter. To understand which value to give to τ in Eq. 3.42 in the case of a CW laser, one must thus estimate the time it takes for the plume to cross such a distance. With a typical ejection speed of 1km/s and beam diameters ranging from 1 to 30mm, one obtains with the above formula threshold intensities ranging from 88GW/m^2 to 480GW/m^2, which is in agreement with Eq. 3.41.

Last but not least, we also implemented a dynamical model of the vapor-plasma transition taking into account the IB absorption by a cloud of vapor with an initial density and internal energy predicted by our equilibrium model. Once vaporized, this cloud, which we assume to be optically thin initially, will absorb part of the laser light through IB. The evolution of its internal energy is driven by

$$\frac{dE}{dt} = \alpha_{IB} I \tag{3.43}$$

In which α_{IB} is the inverse Bremsstrahlung coefficient given by

$$\alpha_{IB}(m^{-1}) = 1.97\text{E}{-29}\frac{Z^3 n_e^2 \lambda^2}{T^{3/2}} \approx 1.97\text{E}{-29}\frac{\eta^2 n_{TOT}^2 \lambda^2}{T^{3/2}} \tag{3.44}$$

Where n$_{TOT}$ is the number density of atoms in the vapor cloud and η is the ion fraction which can be computed considering the Saha-Edberg equation with the customary simplifications:

$$\frac{\eta^2}{1-\eta} = \frac{1}{n_{TOT}}\left(\frac{2\pi k_B T m_e}{h^2}\right)^{3/2} \exp\left(-\frac{E_i}{k_B T}\right) \tag{3.45}$$

The internal energy of an ideal plasma is given by

$$E = n_{TOT}\left[\frac{3}{2}(1+\eta)k_B T + \eta E_i\right] \tag{3.46}$$

Eq. 3.43, 3.44, 3.45, and 3.46 form a closed system which can be dynamically integrated to find the ion fraction as a function of time. A typical result for aluminium is given on Figure 3.16. Our results agree qualitatively with previous works (Phipps et al., 1988) for short pulses up to a duration of approximatively 1 millisecond, beyond which significant

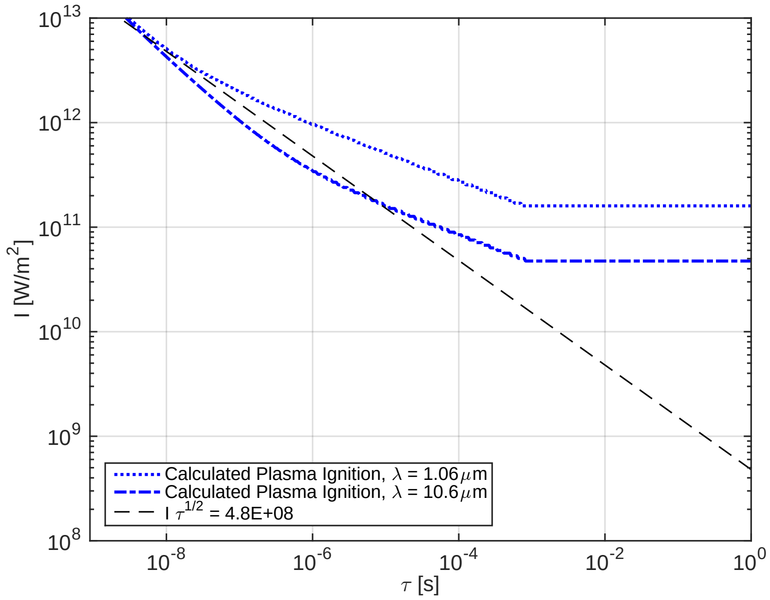

Figure 3.16: Plasma ignition threshold as a function of the intensity I and duration τ for Aluminum

deviation occurs as 3D expansion becomes the limiting factor for plasma ignition and the ignition threshold is only dependent on laser wavelength and intensity as predicted by the CW model (Poueyo-Verwaerde et al., 1993). The intensity threshold for plasma ignition found by our model is around 100GW/m^2, which is again in agreement with the previous values (Poueyo-Verwaerde et al., 1993; Phipps et al., 1988). In the rest of this thesis, the intensity levels for CW lasers are assumed to be low enough so that plasma effects can be neglected. In Chapter 7, this assumption will be reconsidered in the case of pulsed laser systems and space debris materials.

3.5 Contamination issues

According to previous studies (Gibbings et al., 2013), the impingement with the plume of gas and debris, generated by the ablation process, could build up enough material on the surface of the solar arrays to reduce the output power below the ablation threshold. A contamination model was adapted from the work of Kahle (Kahle et al., 2006). From the surface temperature T$_v$, the density ρ_e and the velocity u_e are computed on the edge of the Knudsen layer where, for expansion in vacuum, the flow reaches the speed of sound. The model assumes two different flow regimes in the near field and in the far field: in the near field. According to Kahle, the density at an arbitrary distance r from the reservoir and angle β measured from the local surface normal is approximately given in the continuum flow regime as :

$$\rho(r,\beta) = \rho_e A_p \frac{D^2}{(2r+D)^2}\left[\cos\left(\frac{\pi\beta}{2\beta_{max}}\right)\right]^{\frac{2}{\gamma-1}} \tag{3.47}$$

The jet constant A$_p$ and the limiting expansion angle β_{max} are assumed as equal to 0.345 and 130.45 degrees respectively. The stagnation pressure p_0 and density ρ_0 can easily be computed using the isentropic relations:

$$\frac{\rho_e}{\rho_0} = \left(1+\frac{\gamma-1}{2}\right)^{\frac{-1}{\gamma-1}} \tag{3.48}$$

$$\frac{p_e}{p_0} = \left(1+\frac{\gamma-1}{2}\right)^{\frac{-\gamma}{\gamma-1}} \tag{3.49}$$

The Mach number M , pressure p and the velocity in the continuum regime can be computed considering an isentropic expansion of the plume:

$$M^2 = \frac{2}{\gamma - 1}\left[\frac{\rho}{\rho_0}^{1-\gamma} - 1\right] \tag{3.50}$$

$$\frac{p}{p_0} = \left(1 + \frac{\gamma - 1}{2}M^2\right)^{\frac{-\gamma}{\gamma-1}} \tag{3.51}$$

$$u = \sqrt{\frac{\gamma M^2 p}{\rho}} \tag{3.52}$$

The transition from the continuum regime to the free molecular regime happens when the distances between the molecules becomes too large for them to interact. In his simplified model, Kahle proposes to use a sudden transition when the mean free path of the molecules $\mathrm{l}_{\mathrm{mfp}}$ become larger than the beam diameter:

$$l_{\mathrm{mfp}} = \frac{kT}{p\sqrt{24}\pi r_{\mathrm{mole}}^2} > D \tag{3.53}$$

with the molecular radius $\mathrm{r}_{\mathrm{mole}}$ estimated around $2 \cdot 10^{-10}$m. Once in the free molecular regime, the assumption is that the velocity becomes constant while the density still decreases with respect to the inverse of the quadratic distance to the spot. The contamination model then assumes that only a fraction x_s of the particle impinging on the solar array will stick to it so that the growth of the contamination layer over time can be predicted as

$$\frac{dm_A}{dt} = x_s \cdot F(\psi) \cdot u(r, \beta) \cdot \rho(r, \beta) \tag{3.54}$$

In the last expression, ψ represents the angle between the normal to the solar panels and the impingement direction of the plume. The view function F is defined as following:

$$\begin{aligned} F &= \cos(\psi) && \text{if } -\frac{\pi}{2} < \psi < \frac{\pi}{2} \\ &= 0 && \text{otherwise} \end{aligned} \tag{3.55}$$

Assuming the arrays are pointed towards the sun and the thrust manoeuvre is acted in the tangential direction with respect to the trajectory of the asteroid with the spacecraft remaining in the same orbital plane during the operations, we have:

$$\cos(\psi - \beta) = -\frac{he}{a(1-e^2)V}\sin(\theta) \tag{3.56}$$

In which h is the angular momentum, e the eccentricity of the orbit, V the velocity of the spacecraft and θ the true anomaly. Finally, a degradation factor χ can be computed using the Beer-Lambert-Bougier law:

$$\chi(t) = \exp\left(-\alpha m_A(t)\right) \tag{3.57}$$

where α is the mass attenuation coefficient which is about 10^4 cm^2/g for Forsterite (Kahle et al., 2006). From experimental investigations, it was found that this contamination model predicts correctly the contamination level with a sticking coefficient x_s of 0.5 (Gibbings et al., 2013) . Over the course of the deflection action a contamination layer will grow on the solar arrays with the degradation factor decreasing slowly from an initial value of 1. This will reduce over time the available input power to the laser system.

It is assumed in this model that the contamination process will not affect the optics of the laser system, despite the fact that this one will have a much higher view factor than the solar arrays. At the typical operation distances considered in this work (>100m), the molecules impinging on the mirror surfaces are indeed in a frozen free molecular flow state(with a flow rate on the order of $1\mu g s^{-1} m^{-2}$). With proper coating, the main deposition process is multilayer physisorption and the bonding energy of the Van der waals force is estimated to be less than 80kJ/mol. Desorption will also take place and the average residence time a molecule remains attached depends on the temperature of the mirror:

$$t_{res} \approx t_0 \exp\left(\frac{\Delta H_{des}}{RT}\right) \tag{3.58}$$

in which t_0 corresponds to the period of vibration of the bond between the adsorbed molecule and the substrate and is frequently taken to be about 100 femtoseconds.

Eq.(3.58) shows that the time during which the plume molecules will stick to the mirror surfaces can be anywhere between very long to very short depending on the temperature of the mirror. Maintaining a temperature of 50°C or periodically heating the mirror to this temperature should suffice to eliminate the thin contamination layer that would otherwise grow on these surface (residence time is less than 1 second at 50°C). Note that, in fact, as such a layer will grow, the absorption of laser light by the mirror A_{mirror} and thus the equilibrium temperature of this mirror would increase, hinting at the possibility of a passive decontamination process. This self-cleaning action of the optics by the laser beam was confirmed experimentally (Gibbings et al., 2013). As an example, consider the case of a 24cm diameter mirror illuminated by a 2.4kW laser. This corresponds to a power density around 53kW/m^2 on the mirror surface and is safely below its damage threshold. If the mirror is thermally insulated from the rest of the spacecraft structure, its equilibrium temperature can be computed by equating the absorbed laser power with the power radiated. Considering the black-body radiation law, the relationship must satisfy:

$$A_{\text{mirror}} I_{\text{mirror}} = 2\sigma T_{\text{mirror}}^4 \tag{3.59}$$

Fig.3.17 shows the equilibrium temperature and mean residence time of the asteroid particles as a function of the absorption of the primary mirror of the laser optics.

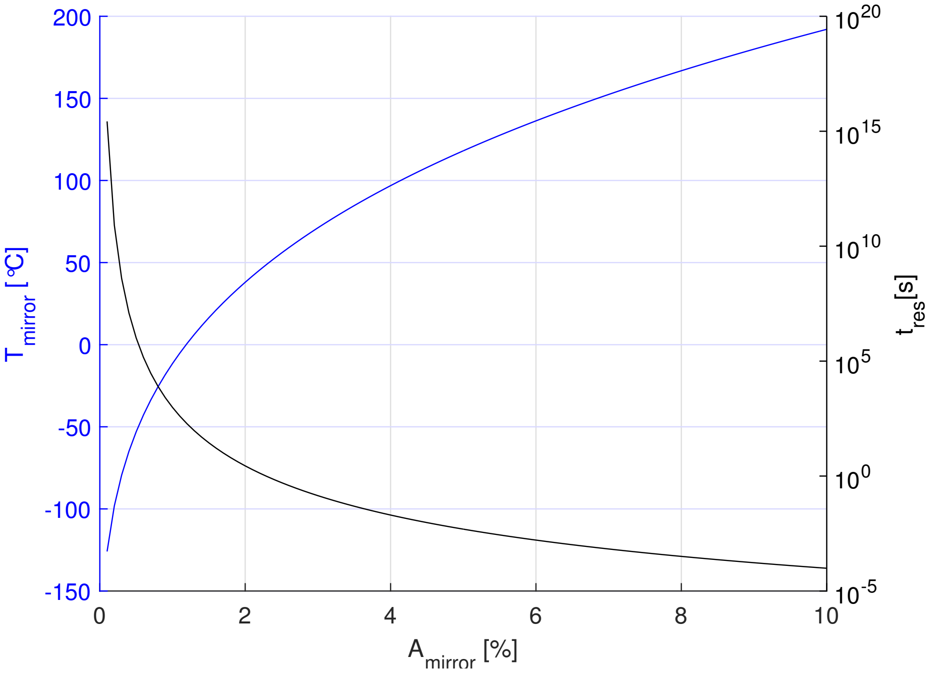

Figure 3.17: Equilibrium temperature and mean residence time of dirt particles as a function of the optical absorption of the mirror

Chapter 4

Fundamental of asteroid deflection : theory, methods and challenges

This chapter covers the basic principles and formulas to assess the outcome when using a generic impulsive or slow-push deflection method on an asteroid. Example of these methods are then presented together with simple analytical models that can be used to evaluate their performance and to design a potential deflection mission. The chapter is divided in two parts. The first part explains how a given acceleration or a given Δv can be used to divert the trajectory of an asteroid and avoid a collision with the Earth. Analytical formula are provided for the case of an impulsive and low thrust deflection action in the case in which the variation of the orbit of the asteroid remains small and the altered trajectory remains proximal to the original one. The second part tackles the technological aspect of the different deflection methods. Physical models are derived and formula are presented to compute the Δv or the acceleration resulting from a given deflection strategy. Some performance indicators are also introduced, providing an objective framework to compare these alternative deflection strategies with the laser ablation method.

4.1 Basic Deflection Principles and Computational Tools

The orbit of an asteroid can be modified in different ways depending on the direction in which the deflection action is applied. With reference to Figure 4.1a one can define a local reference frame centred in the centre of mass of the asteroid, with the y-axis aligned with the velocity vector $\mathbf{v}$, the z-axis aligned with the angular momentum $\mathbf{h}$ and the x-axis aligned with the local normal $\mathbf{n}$ contained in the orbit plane. The deflection action can be projected on these axes to give the three deflection components a_t, a_n and a_h. By aligning the deflection action with one of these three coordinate directions one can produce the following modifications of the orbit:

- Change the energy of the orbit by aligning the deflection action along the velocity direction
- Rotate the orbit in its plane by aligning the deflection action in the normal direction
- Modify the inclination of the orbit or rotate the line of the nodes by aligning the deflection action along the z-axis

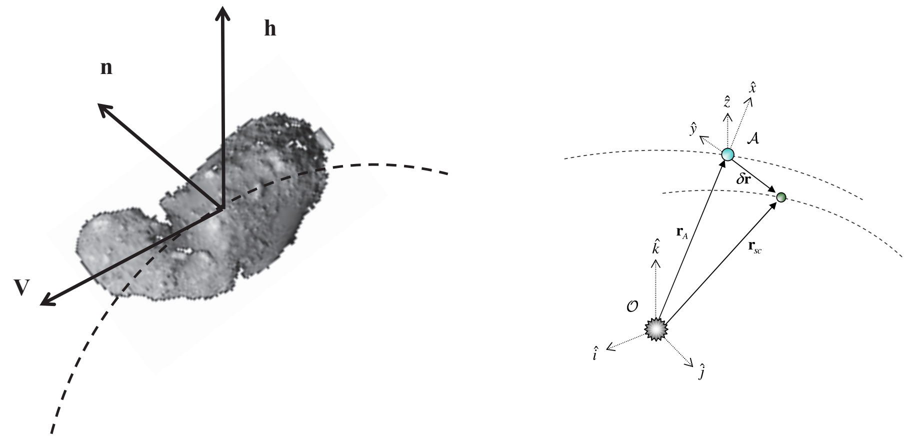

(a) (b)

Figure 4.1: a) Tangential v, normal n, and bi-normal h reference frame, b) Definition of the r-t-h Hill's reference frame $\mathcal{A}$ centered on the undeflected asteroid.

The result of a deflection action can be deduced by looking at Gauss' planetary equations:

$$
\begin{aligned}
\frac{da}{dt} &= \frac{2a^2v}{\mu}\alpha_t \\
\frac{de}{dt} &= \frac{1}{v}\left[2(e+cos\theta)\alpha_t - \frac{r}{a}\sin\theta\alpha_n\right] \\
\frac{di}{dt} &= \frac{r\cos\theta^*}{h\sin i}\alpha_h \\
\frac{d\Omega}{dt} &= \frac{r\sin\theta^*}{h\sin i}\alpha_h \\
\frac{d\omega}{dt} &= \frac{1}{ve}\left[2\sin\theta\alpha_t + \left(2e+\frac{r}{a}\cos\theta\right)\alpha_n\right] - \frac{r\sin\theta^*\cos i}{h\sin i}\alpha_h \\
\frac{dM}{dt} &= -\frac{\sqrt{1-e^2}}{ve}\left[2\left(1+\frac{e^2r}{p}\right)\sin\theta\alpha_t + \frac{r}{a}\cos\theta\alpha_n\right] + n
\end{aligned}
\tag{4.1}
$$

where a is the semi-major axis, e the eccentricity, i the inclination, Ω the right ascension of the ascending node, ω the argument of the pericentre, θ the true anomaly and M the mean anomaly of the orbit of the asteroid. α_t, α_n, and α_h represent the perturbating acceleration in the tangential, normal and bi-normal directions respectively. The quantity θ^* is the sum of the true anomaly and the argument of the pericentre, μ is the gravity parameter of the Sun, r is the distance of the asteroid from the Sun, $v = \|\mathbf{v}\|$ the modulus of the velocity of the asteroid on its orbit, h the modulus of the orbit angular momentum, p the semi-latus rectum and $n = \sqrt{\mu/a^3}$.

A deflection action along the y-axis would produce a variation of a and M and a variation of e and ω if not applied at $\theta = k\pi$ with $k = 0, 1, ...$ A deflection action along the z-axis would produce a variation of Ω and i and a variation of ω if not applied at $\theta^* = k\pi$ with $k = 0, 1, ...$ Finally, a deflection action along the x-axis would produce a variation of ω and a variation of e and M if not applied at $\theta = k\pi$ or $\theta = \pi/2 + k\pi$ with $k = 0, 1, ...$ respectively.

Looking at the last equation in Eqs. (4.1), one can see that a deflection action can have two effects on M: one does not modify n and is what can be called a *geometric variation* of M, the other is a variation of n induced by a variation of a. This latter effect produces a change in the time of arrival of the asteroid at the point of Minimum Orbit Intersection Distance (MOID), or point where the geometric distance between the orbit of the Earth and the un-deviated orbit of the asteroid is at its minimum. A deflection action a_t along the velocity of the asteroid would yield both a change in n and a geometric variation of M.

By inspecting Gauss planetary equations one can derive a qualitative indication of how to act on an asteroid to modify its orbit. The next step is to quantitatively compute the deflection produced by a given deflection action. Here and in the following the word deflection will refer to the variation of the position of the asteroid with respect to its nominal (un-deflected) orbit at a given time.

4.1.1 First Order Impulsive Deflection Analytical Formulas

In the case of an impulsive variation of the velocity of the asteroid, the deflection action generates an instantaneous modification of the orbital parameters. Gauss' planetary equations (4.1) can be re-written as follows (Sanchez et al., 2009):

$$\begin{aligned}
\delta a &= \frac{2a^2 v}{\mu}\delta v_t \\
\delta e &= \frac{1}{v}\left[2(e+cos\theta)\delta v_t - \frac{r}{a}\sin\theta\delta v_n\right] \\
\delta i &= \frac{r\cos\theta^*}{h\sin i}\delta v_h \\
\delta\Omega &= \frac{r\sin\theta^*}{h\sin i}\delta v_h \\
\delta\omega &= \frac{1}{ve}\left[2\sin\theta\delta v_t + \left(2e+\frac{r}{a}\cos\theta\right)\delta v_n\right] - \frac{r\sin\theta^*\cos i}{h\sin i}\delta v_h \\
\delta M &= -\frac{\sqrt{1-e^2}}{ve}\left[2\left(1+\frac{e^2 r}{p}\right)\sin\theta\delta v_t + \frac{r}{a}\cos\theta\delta v_n\right] + \delta n(t_f - t_d)
\end{aligned} \tag{4.2}$$

where:

$$\delta n = \sqrt{\frac{\mu}{(a+\delta a)^3}} - \sqrt{\frac{\mu}{a^3}}$$

t_d is the time of application of the impulsive deflection action, t_f is the time at which the variation of the orbital elements is measured and $\delta v_t = \alpha_t\delta t$, $\delta v_n = \alpha_n\delta t$, $\delta v_h = \alpha_h\delta t$. The evolution of the deviated orbit can be described in the Hill's reference frame centered in the undeviated asteroid (see Figure 4.1b) where now the x-axis is aligned with the radial direction. In this reference frame the position vector of the deviated asteroid is $\delta\mathbf{r} = [x \;\; y \;\; z]^T$. If δr is small compared to r, the components of $\delta\mathbf{r}$, at a given θ along the undeviated orbit, can be related to the variation of the orbital parameters (4.2), through the following set of linearised proximity equations (Schaub and Junkins, 2003):

$$\begin{aligned}
x &\approx \frac{r}{a}\delta a + \frac{ae\sin\theta}{\nu}\delta M - a\cos\theta\delta e \\
y &\approx \frac{r}{\nu^3}\left(1+e\cos\theta\right)^2\delta M + r\delta\omega + \frac{r\sin\theta}{\nu^2}\left(2+e\cos\theta\right)\delta e + r\cos i\delta\Omega \\
z &\approx r\left(\sin\theta^*\delta i - \cos\theta^*\sin i\delta\Omega\right)
\end{aligned} \tag{4.3}$$

with $\nu = \sqrt{1+e^2}$. When $t_f = t_{\text{MOID}}$ and the true anomaly in Eqs. (4.3) is the one of the MOID then $\delta\mathbf{r}$ is the deviated position of the asteroid at the point of the MOID.

By combining Eqs. (4.2) with Eqs. (4.3), one can compute the deflection at the time of the MOID as a function of the deflection impulse at time t_d in the following matrix form (Vasile and Colombo, 2008):

$$\delta\mathbf{r}(t_{\text{MOID}}) = \mathbf{A}_{\text{MOID}}\mathbf{G}_d\delta\mathbf{v} = \mathbf{T}\delta\mathbf{v} \tag{4.4}$$

where the matrix $\mathbf{A}_{\text{MOID}}$ and $\mathbf{G}_d$ are:

$$\mathbf{A}_{\text{MOID}} = \begin{bmatrix}
\frac{r_{\text{MOID}}}{a} - \frac{3}{2}\frac{e\sin\theta_{\text{MOID}}}{\nu}\frac{\sqrt{\mu}}{a^{3/2}}\Delta t & -\frac{3}{2}\frac{r_{\text{MOID}}}{\nu^3}(1+e\cos\theta_{\text{MOID}})^2\frac{\sqrt{\mu}}{a^{3/2}}\Delta t & 0 \\
-a\cos\theta_{\text{MOID}} & \frac{r_{\text{MOID}}\sin\theta_{\text{MOID}}}{\nu^2}(2+e\cos\theta_{\text{MOID}}) & 0 \\
0 & 0 & r_{\text{MOID}}\sin\theta^*_{\text{MOID}} \\
0 & r_{\text{MOID}}\cos i & -r_{\text{MOID}}\cos\theta^*_{\text{MOID}}\sin i \\
0 & r_{\text{MOID}} & 0 \\
\frac{ae\sin\theta_{\text{MOID}}}{\nu} & \frac{r_{\text{MOID}}}{\nu^3}(1+e\cos\theta_{\text{MOID}})^2 & 0
\end{bmatrix} \tag{4.5}$$

$$\mathbf{G}_d = \begin{bmatrix} \frac{2a^2 v_d}{\mu} & 0 & 0 \\ \frac{2(e+\cos\theta_d)}{v_d} & -\frac{r_d}{a v_d}\sin\theta_d & 0 \\ 0 & 0 & \frac{r_d \cos\theta_d^*}{h} \\ 0 & 0 & \frac{r_d \sin\theta_d^*}{h \sin i} \\ \frac{2\sin\theta_d}{e v_d} & \frac{2e+(r_d/a)\cos\theta_d}{e v_d} & -\frac{r_d \sin\theta_d^* \cos i}{h \sin i} \\ -\frac{\sqrt{1-e^2}}{e v_d} 2\left(1+\frac{e^2 r_d}{p}\right)\sin\theta_d & -\frac{\sqrt{1-e^2}}{e v_d}\frac{r_d}{a}\cos\theta_d & 0 \end{bmatrix} \tag{4.6}$$

and

$$\delta n(t_f - t_d) = \delta n \Delta t \cong -\frac{3}{2}\frac{\sqrt{\mu}}{a^{5/2}}\Delta t \; \delta a \tag{4.7}$$

The subscript d indicates that quantities are taken when the deflection is applied. The norm of the deflection at the time of the MOID is:

$$\|\mathbf{r}(\mathbf{t}_{\text{MOID}})\| = \delta\mathbf{r}^T \delta\mathbf{r} = \delta\mathbf{v}^T \mathbf{T}^T \mathbf{T} \delta\mathbf{v} \tag{4.8}$$

which is a quadratic form in $\delta\mathbf{v} = \delta v \hat{\mathbf{v}}$. As such, if $\mathbf{V}$ is the matrix of the eigenvectors of the matrix $\mathbf{T}^T\mathbf{T}$ one can write:

$$\|\mathbf{r}\| = \delta v^2 \hat{\mathbf{v}}^T \mathbf{V} \mathbf{T}^T \mathbf{T} \mathbf{V}^T \hat{\mathbf{v}} = \delta v^2 \sum_{i=1}^{N} \lambda_i (\mathbf{q}_i^T \hat{\mathbf{v}})^2 \le \delta v^2 \lambda_{max} \sum_{i=1}^{N} (\mathbf{q}_i^T \hat{\mathbf{v}})^2 \tag{4.9}$$

and by taking the unit vector $\hat{\mathbf{v}}$ aligned with the eigenvector $\mathbf{q}_{max}$ corresponding to the maximum eigenvalue λ_{max} one gets:

$$\|\delta\mathbf{r}_{\mathbf{t}_{\text{MOID}}}\|_{max} = \delta v^2 \lambda_{max} \tag{4.10}$$

It is possible to show that for a Δt smaller than a specific $\Delta t_{\text{PHA}} < T_{\text{PHA}}$, different for every asteroid, the component perpendicular to the motion dominates the other two while for larger Δt, the tangential component becomes dominant. These conclusions are consistent with the results in Conway (2001).

We can now consider a deflection applied with a relatively large Δt and only in the tangential direction (i.e., $\delta v_n = \delta v_h = 0$). In this case the components of the deflection in the Hill's reference frame simplify and reduce to:

$$
\begin{aligned}
x &\simeq r\frac{2av}{\mu}\delta v_t + \frac{ae\sin\theta}{\nu}\left(-\frac{3\Delta t v}{\sqrt{a\mu}}\right)\delta v_t \\
y &\simeq \frac{r}{\nu^3}(1+e\cos\theta)^2\left(-\frac{3\Delta t v}{\sqrt{a\mu}}\right)\delta v_t
\end{aligned}
\tag{4.11}
$$

where for small deflections and large warning times Δt, the variation of eccentricity δe can be considered negligible compared to the variation in semimajor axis and in mean anomaly. From Eqs. (4.11) one can see that both the radial and the transversal components of the deflection have a secular term due to the variation of M. The term in the radial direction, however, is multiplied times $\sin\theta$ and therefore is null for a MOID at $\theta = k\pi$ with $k = [0, 1, ...]$. On the contrary the transversal component can be written as:

$$
y \simeq -\frac{a^{3/2}}{r}\frac{\sqrt{1-e^2}}{\sqrt{\mu}}(3\Delta t v)\,\delta v_t
\tag{4.12}
$$

For almost circular orbits the radial components is almost aligned with the normal component and the transversal almost coincide with the tangential direction. Eqs. (4.11) then become:

$$
\begin{aligned}
x &\simeq \frac{2a^{3/2}}{\sqrt{\mu}}\,\delta v_t \\
y &\simeq -3\Delta t\,\delta v_t
\end{aligned}
\tag{4.13}
$$

From which one can derive that for a warning time $\Delta t > \frac{T_{\mathrm{PHA}}}{3\pi}$ the secular component exceeds the geometric component.

Representation on the Impact Plane

The deflection $\delta\mathbf{r}$ does not fully describe what happens at the point of the MOID. A better understanding can be gathered from the projection of the deflection on the impact plane or the plane perpendicular to the incoming relative velocity of the small body at the Earth at the time of the expected impact (Vasile and Colombo, 2008)(see Figure 4.2).

We can define a local reference system centered in the Earth with the axis perpendicular

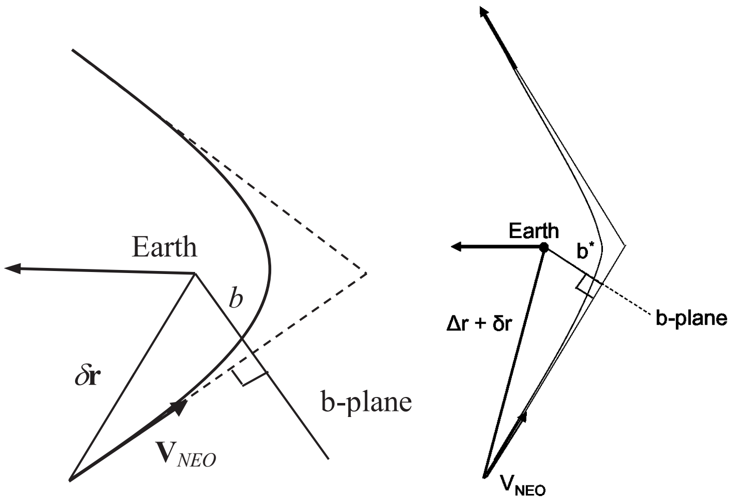

(a) (b)

Figure 4.2: The impact plane and b parameter

to the b-plane and aligned along the unperturbed velocity of the asteroid relative to the Earth, the axis ξ along the direction opposite to the projection of the heliocentric velocity of the Earth $\mathbf{v}_\mathrm{E}$ onto the b-plane, and the axis η that completes the reference system (see Fig. 4.2a). The general transformation from the radial, transversal, out-of-plane Hill's reference frame to the b-plane reference frame is:

$$\mathbf{x}_b = [\hat{\xi} \;\; \hat{\eta} \;\; \hat{\zeta}]\delta\mathbf{r} \tag{4.14}$$

where:

$$\hat{\eta} = \frac{\mathbf{V}_\mathrm{PHA}}{\|\mathbf{V}_\mathrm{PHA}\|} \quad \hat{\xi} = \frac{\mathbf{v}_E \times \hat{\eta}}{\|\mathbf{v}_E \times \hat{\eta}\|} \quad \hat{\zeta} = \hat{\xi} \times \hat{\eta}$$

The assumption is that the velocity along the deviated trajectory at the time of the MOID remains parallel to $\mathbf{V}_\mathrm{PHA}$. The proper representation would be on the instantaneous b-plane, perpendicular to the deviated relative velocity of the asteroid, however the maximum relative error between the plane perpendicular to the nominal relative velocity and the perturbed one is around 0.01, thus in the following we are using the former one which avoids the additional calculation of the velocity of the deflected asteroid. Moreover, for this analysis, we set to zero the distance at the MOID in order to have the Earth at the origin of the reference system on the b-plane. On the b-plane one can represent the distance b (called impact parameter) from the Earth to the intercept of the asymptote of the hyperbola of the deviated orbit of the asteroid:

$$b = \sqrt{\xi^2 + \zeta^2} \tag{4.15}$$

Because the hyperbolic trajectory is expected to be close to a straight line, b is typically a good estimation of the radius of the pericenter of the hyperbolic trajectory and hence the minimum distance from the Earth.

4.1.2 First Order Slow-push Deflection Formulas

For a slow-push action the variation of the orbital elements can be obtained by integrating Gauss' planetary equations in (4.1) over the time span $[t_i, \quad t_e]$ for which the deflection action is applied. If the deflection action stops at time $t_e < t_{\text{MOID}}$, the total variation of the orbital elements a, e, i, ω, Ω, at the MOID, is given by the integration of Gauss' equations up to time t_e. The total variation of M at the MOID is given by:

$$\delta M = \delta M_0 + (n_e - n)t_{\text{MOID}} + n_i t_i - n_e t_e \tag{4.16}$$

where δM_0 is the variation of M over the interval $[t_i, \quad t_e]$ and n_e is given by:

$$n_e = \sqrt{\frac{\mu}{(a + \delta a)^3}} \tag{4.17}$$

Once the variation of the elements at the MOID is available, proximity equations (4.3) can be used to compute the deflection at the time of the MOID and Eqs. (4.14) can be used to project the deflection on the impact plane and compute the b-parameter.

4.2 Deflection Technologies

Typical spacecraft operations can be done through impulsive (in the sense of near-instantaneous) or low-thrust orbital manoeuvres depending on the type of thrusters the spacecraft is equipped with (e.g. impulsive for high thrust chemical engine and low-thrust for Ion engines). Similarly, all the different asteroid deflection strategies that exist in the literature can be classified in two main categories depending on whether the deflection action is modelled with an impulsive change of velocity or with an extended thrust arc:

- Impulsive methods (e.g., kinetic impactor, nuclear blast)
- Slow push deflection methods (e.g., gravity tug, solar collector, low thrust tug, etc.)

However, in the case of an asteroid, this classification is not representative of the physical interaction between the deflecting spacecraft and the deflected object but, rather, a distinction of an operational nature to help in the definition of a particular mission and in the mathematical analysis of the outcome of the deflection.

In the previous section, we have seen how a general deflection action perturbs the trajectory of an asteroid. This section illustrates how this action can be physically achieved with the different technologies. The intention is not to be exhaustive but to discuss some representative methods and their technological implications. The strategies reviewed here are: the kinetic impactor, the nuclear interceptor, the Ion Beam Shepherd , the gravity tug, and the laser ablation methods. While the first two fall under the the impulsive category, all the others will require a longer action time and can thus be characterized as slow-push methods. In Chapter 6, a comparison of the non-nuclear deflection methods will be performed.

4.2.1 Kinetic Impactor

Perhaps one of the simplest way to transfer energy between a spacecraft and a target asteroid is to use the kinetic energy contained in the relative motion between the two bodies. Owing to this apparent simplicity, the kinetic impactor is, at the time this chapter is written, the most mature method for asteroid deflection and the only one that, to date, has been partially validated (Hampton et al., 2005). The impulsive change of velocity of the asteroid $\delta\mathbf{v}$ is commonly modelled with the conservation of the linear momentum after an inelastic collision:

$$\delta\mathbf{v} = \beta \frac{m_{s/c}}{m_{\mathrm{PHA}} + m_{s/c}} \Delta\mathbf{v}_{s/c} \tag{4.18}$$

where β represents a momentum enhancement factor that takes into account the fraction of mass ejected during the impact and $\Delta\mathbf{v}_{s/c}$ is the velocity of the spacecraft relative to the asteroid, $m_{s/c}$ is the mass of the spacecraft and m_{PHA} the one of the asteroid. Despite the apparent simplicity of this equation, getting an accurate value for the momentum enhancement factor is critical in order to assess the efficiency of the kinetic impactor method and defining an accurate value for this parameter is still a matter of active research. High fidelity hydrodynamics codes are used to assess the importance of the contribution from the ejecta as a function of the asteroid composition and impact angle (Housen and Holsapple, 2015).

Since $\delta\mathbf{v}_{\mathrm{A}}$ in Eq. (4.18) depends on the relative velocity between impactor and asteroid, the effectiveness of the kinetic impactor depends on the trajectory of the impactor and thus on the launch date and on the transfer strategy. One can show this dependency by finding an estimation of the energy required to achieve a given $\Delta v_{s/c}$. Let us restrict to the case in which the orbits of the Earth, asteroid and impactor are all in the same plane and the asteroid is impacting the Earth at an apsidal point. In this case the impact between the spacecraft and the asteroid should preferably occur at the perihelion as demonstrated in Section 4.1.1. Assuming an impact at the perihelion r_p of the orbit of a PHA with semimajor axis a_{PHA}, we have:

$$\begin{aligned} \Delta v_{s/c} &= \sqrt{\tfrac{2\mu}{r_p} - \tfrac{\mu}{a_{\mathrm{PHA}}}} - \sqrt{\tfrac{2\mu}{r_p} - \tfrac{\mu}{a_{\mathrm{PHA}}+\delta a}} \quad for \;\; \delta a > 0 \\ \Delta v_{s/c} &= \sqrt{\tfrac{2\mu}{r_p} - \tfrac{\mu}{a_{\mathrm{PHA}}+\delta a}} - \sqrt{\tfrac{2\mu}{r_p} - \tfrac{\mu}{a_{\mathrm{PHA}}}} \quad for \;\; \delta a < 0 \end{aligned} \tag{4.19}$$

where the semimajor axis of the orbit of the impactor is $a_{\mathrm{PHA}} + \delta a$. The Δv required to transfer from the Earth to an orbit with semimajor axis $a_{\mathrm{PHA}} + \delta a$ is:

$$\Delta v_T = \sqrt{\frac{2\mu}{r_{\mathrm{E}}} - \frac{\mu}{r_{\mathrm{E}} + \delta a + \delta a_{\mathbb{N}}}} - \sqrt{\frac{\mu}{r_{\mathrm{E}}}} \tag{4.20}$$

where $a_{\mathrm{PHA}} = r_{\mathrm{E}} + \delta a_{\mathbb{N}}$. By combining Eq.(4.19) and Eq.(4.20) one can get the dependency of the departure Δv as a function of the desired impact Δv:

$$\Delta v_{s/c} = \Delta v_{\mathsf{T}} - \sqrt{\frac{2\mu}{r_{\mathrm{E}}} - \frac{\mu}{r_{\mathrm{E}} + \delta a_{\mathbb{N}}}} + \sqrt{\frac{\mu}{r_{\mathrm{E}}}} \tag{4.21}$$

From Eq.(4.21) one can see that for high $\delta a_{\mathbb{N}}$ the kinetic impactor requires no Δv_{T} to achieve good $\Delta v_{s/c}$ but as $\delta a_{\mathbb{N}}$ tends to 0 the variation of velocity required to achieve the desired deflection increases significantly. This very simple calculation leads to two key considerations:

- while the kinetic impactor seems to be the strategy of choice for deep crossers (PHAs with high semimajor axis and high eccentricity), it might not be ideal for shallow crossers (PHAs with semimajor axis close to 1 AU and low eccentricity)
- the energy required to increase the $\Delta v_{s/c}$ needs to be provided by a propulsion system. A high I_{sp} propulsion system becomes necessary in the case of shallow crossers. The Δv that needs to be delivered by the propulsion system is proportional to the desired impact Δv.

These considerations do not take into account the phasing between the asteroid and the Earth. if the phasing was included, then the launch date would play an important role as the achievable $\Delta v_{s/c}$ and the energy required for the transfer would depend on the launch date as well (Vasile and Colombo, 2008). Once the launch date and transfer energy are defined, the primary challenge in the practical implementation of this deflection strategy is certainly the targeting of the asteroid at high velocity. Eq. (4.18) would suggest that the challenge is simply not to miss the target. This alone would make hitting the asteroid with solar or electric sails more difficult than with conventional propulsion methods due to the limited control authority and long reaction

Table 4.1: Different types of asteroids

	NEAs(%)	PHAs (%)	Impactors
Q < 1.05 AU	1%	1%	11%
Q > 0.95 AU	8%	22%	38%
Deep Crossers	61%	77%	53%
Low Inc. (i <5)	6%	25%	38%

time. Increasing $\Delta v_{s/c}$ further exacerbates the problem. However, the enhancement factor does depend on the relative motion between impactor and surface, therefore the angle of impact as well as the rotation motion of the asteroid play an additional role. Therefore, the challenge becomes to hit the target in the right spot with the right angle, avoiding shallow elevation angles especially in the case the surface material is brittle or easily removed. The hypothesis of inelastic impact in this case would need to be reassessed.

Another concern with the kinetic impactor is the level of energy involved during the collision. As explained by P et al. (2009), in some cases, the minimum level of energy required to deviate an asteroid by a distance that ensures a successful deflection may rise above the theoretical catastrophic fragmentation limit, which is defined as the specific energy required to completely fracture an asteroid. As a consequence, an asteroid that underwent an impulsive deflection attempt may fragment in a number of pieces having different mass and velocity. If f_r is the fragmentation ratio, defined as:

$$f_r = \frac{m_{max}}{m_{\mathrm{PHA}}} \tag{4.22}$$

where m_{max} is the mass of the largest fragment and m_A the initial mass of the asteroid, then a catastrophic fragmentation is defined as a fragmentation where $f_r < 0.5$. Previous work (P et al., 2009)) have shown that, in the case of a fragmentation, the probability that a large fragment (large enough to cause damage) impacts the Earth never goes to zero even if the deflection is applied far in advance of the predicted impact.

4.2.2 Nuclear Interceptor

Nuclear devices are able to carry the highest energy density among all of the deviation methods currently available, which make them a very attractive option among the possible mitigation strategies. The energy released during the explosion is carried by the debris of the exploded spacecraft and by the radiation. Table 4.2 shows the fraction f_i (with $i \in \{1,2,3,4,5\}$) of energy associated to each of the products of the explosion for the case of a fusion and fission devices (Glasstone and Dolan, 2007; Hammerling and Remo, 1995). The energy delivered during the explosion, Y_0, is computed from the yield-to-mass ratio and is conservatively assumed to have a value YTW=0.75 ktons/kg for fusion devices and YTW = 0.075 ktons/kg for fission devices[1]:

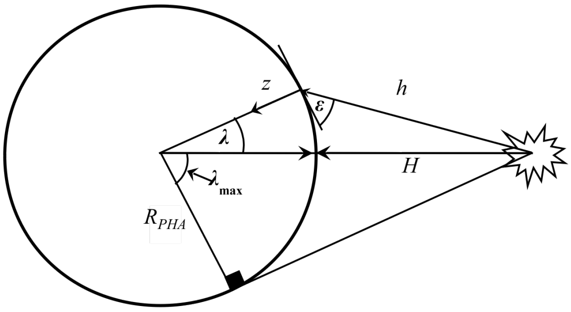

Figure 4.3: Standoff configuration for the nuclear interceptor method

Table 4.2: Energy fraction f_i over all the products of a nuclear explosion

Source	1–X-ray	2–Neutrons	3–Gamma rays	4–Debris	5–Others
Fission	0.7	0.01	0.02	0.2	0.07
Fusion	0.55	0.2	0.01	0.2	0.04

$$Y_0 = YTW m_{wh} \tag{4.23}$$

where m_{wh} is the mass of the bomb. In this paper, no buried or surface detonation are considered due to the added difficulty of landing and digging on an asteroid and only stand-off explosions are modelled.

---

[1] From data available online at http://nuclearweaponarchive.org/

With reference to Fig. 4.3, the explosion is assumed to happen at a distance H from the surface of the asteroid, therefore, only a portion m_{debris} of the total mass of debris $m_{s/c}$ will hit the surface:

$$m_{debris} = S m_{s/c} \tag{4.24}$$

If one assumes that the exploding device sees a spherical cap with radius R_{PHA}, then the fraction S can be expressed as:

$$S = \frac{1}{2} - \frac{\sqrt{H}}{2} \frac{\sqrt{H + 2R_{\mathrm{PHA}}}}{R_{\mathrm{PHA}} + H} \tag{4.25}$$

The ejection velocity of the debris v_{debris} is then computed from the fraction $f_4 = 0.2$ (see Table 4.2) of the total energy Y_0 released during the blast:

$$v_{debris} = \sqrt{\frac{2 f_4 Y_0}{m_{s/c}}} \tag{4.26}$$

The variation of velocity δv_{debris} due to the debris cloud only is then given by:

$$\delta v_{debris} = \beta S_{sc} \frac{m_{debris} v_{debris}}{m_{\mathrm{A}}} \tag{4.27}$$

where S_{sc} is a scattering factor and β the momentum enhancement factor (Tedeschi et al., 1995) which is conservatively assumed to be equal to 2.

The contribution from the radiations is derived from the Beer-Lambert law of absorption. Given a radiation with frequency ν and knowing the incident radiation energy per unit area $I_0^{\nu}(\lambda)$ and the depth z, the energy per unit area $I^{\nu}(\lambda, z)$ transmitted beyond a given depth is computed as follows:

$$I^{\nu}(\lambda, z) = \sin\epsilon(\lambda) I_0^{\nu}(\lambda) \exp\left(-\rho_{\mathrm{PHA}} \kappa_{\nu} \frac{z}{\sin\epsilon(\lambda)}\right) \tag{4.28}$$

The incident radiation density $I_0^{\nu}(\lambda)$ is given by:

$$I_0^{\nu}(\lambda) = \frac{f_i}{4\pi h^2(\lambda)} Y_0 \tag{4.29}$$

where the h distance is computed as:

$$h = \sqrt{(H + (1 - \cos\lambda)R_{\text{PHA}})^2 + R_{\text{PHA}}^2 \sin^2\lambda} \tag{4.30}$$

and ϵ is given by:

$$\sin\epsilon = \frac{(R_{\text{PHA}} + H)\cos\lambda - R_{\text{PHA}}}{h} \tag{4.31}$$

The linear mass-absorption coefficient κ_ν for each type of radiation is given in Table 4.3 (Hammerling and Remo, 1995). Note that quantities in Table 4.3 are to be considered as mean values over the range of frequencies of X-rays and Gamma-rays.

Table 4.3: Opacity κ_ν, or linear mass-absorption coefficient, for an asteroid made of forsterite

Radiation type	X-Ray	Neutron	Gamma ray
Value	1.5 m^2/kg	0.0044 m^2/kg	0.005 m^2/kg

The amount of energy absorbed per unit mass at a given depth is then obtained by considering the cumulative absorption of each radiation type:

$$E(\lambda, z) = -\sum_\nu \frac{dI^\nu}{dz} = \sum_\nu \kappa_\nu I_0^\nu \exp\left(-\rho_{\text{PHA}}\kappa_\nu \frac{z}{\sin\epsilon(\lambda)}\right) \tag{4.32}$$

Part of this energy goes into the vaporization process of the asteroid, while the excess energy is converted into thermal excitation. The local average velocity of the gas molecules can then be estimated by writing a simple energy balance with E_v the total vaporization enthalpy per unit mass:

$$\bar{v}(\lambda, z) = \sqrt{2(E(\lambda, z) - E_v)} \tag{4.33}$$

where the assumption is that the vaporisation is so fast that losses by conduction and radiation can be neglected. Eq. (4.32) allows one to define a limit depth z_{MAX} below which the vaporization process cannot continue as the energy absorbed is lower than the vaporization enthalpy. Given a certain distance H and yield Y_0, the value of z_{max} is numerically computed by finding the value of z that satisfies the relationship $E(\lambda, z) = E_v$ for each λ considered. The change in linear momentum generated by the expelled material is then expressed, for an infinitesimal volume, as:

$$dP = \frac{\cos\lambda}{2}\rho_{\mathrm{A}}\bar{v}(\lambda, z)dV \tag{4.34}$$

where the cosine function comes from the fact that we only retain the tangential component and the $\frac{1}{2}$ factor is coming from the assumption of an equiprobable scattering of the gas molecules from the ablated surface over a hemisphere. The area of a spherical cap is given by:

$$S = 2\pi R_{\mathrm{PHA}}^2(1-\cos\lambda) \tag{4.35}$$

The infinitesimal volume dV is thus given by:

$$dV = 2\pi R_{\mathrm{PHA}}^2 \sin\lambda dz d\lambda \tag{4.36}$$

Integrating relation (4.34) and dividing by the mass of the asteroid eventually allows one to express the change of velocity $\delta v_{radiation}$ due to the radiations:

$$\delta v_{radiation} = \frac{\pi R_{\mathrm{PHA}}^2}{m_{\mathrm{A}}}\int_0^{\lambda_{max}}\int_0^{z_{max}(\lambda)} \rho_{\mathrm{PHA}}\bar{v}(\lambda, z)dz \sin\lambda\cos\lambda d\lambda \tag{4.37}$$

Fig. 4.4a shows the total $\delta v = \delta v_{radiation} + \delta v_{debris}$ imparted to an asteroid, with mass and density reported in Table B.1, assuming a fusion device of 600kgs at different altitudes of detonation and for different values of the enthalpy of vaporization, while Figure 4.4b shows the δv imparted to the same asteroid by a fission device of equal mass at different altitudes of detonation and for different values of the enthalpy of vaporization. Such a δv can be sufficient to provide a large deflection distance to an asteroid, even for relatively short warning times. A NASA analysis of deflection alternatives, conducted in 2007, stated (NASA, 2007):

"Nuclear standoff explosions are assessed to be 10 to 100 times more effective than the non-nuclear alternatives analyzed in this study. Other techniques involving the surface or subsurface use of nuclear explosives may be more efficient, but they run an increased risk of fracturing the target NEO. They also carry higher development and operations risks."

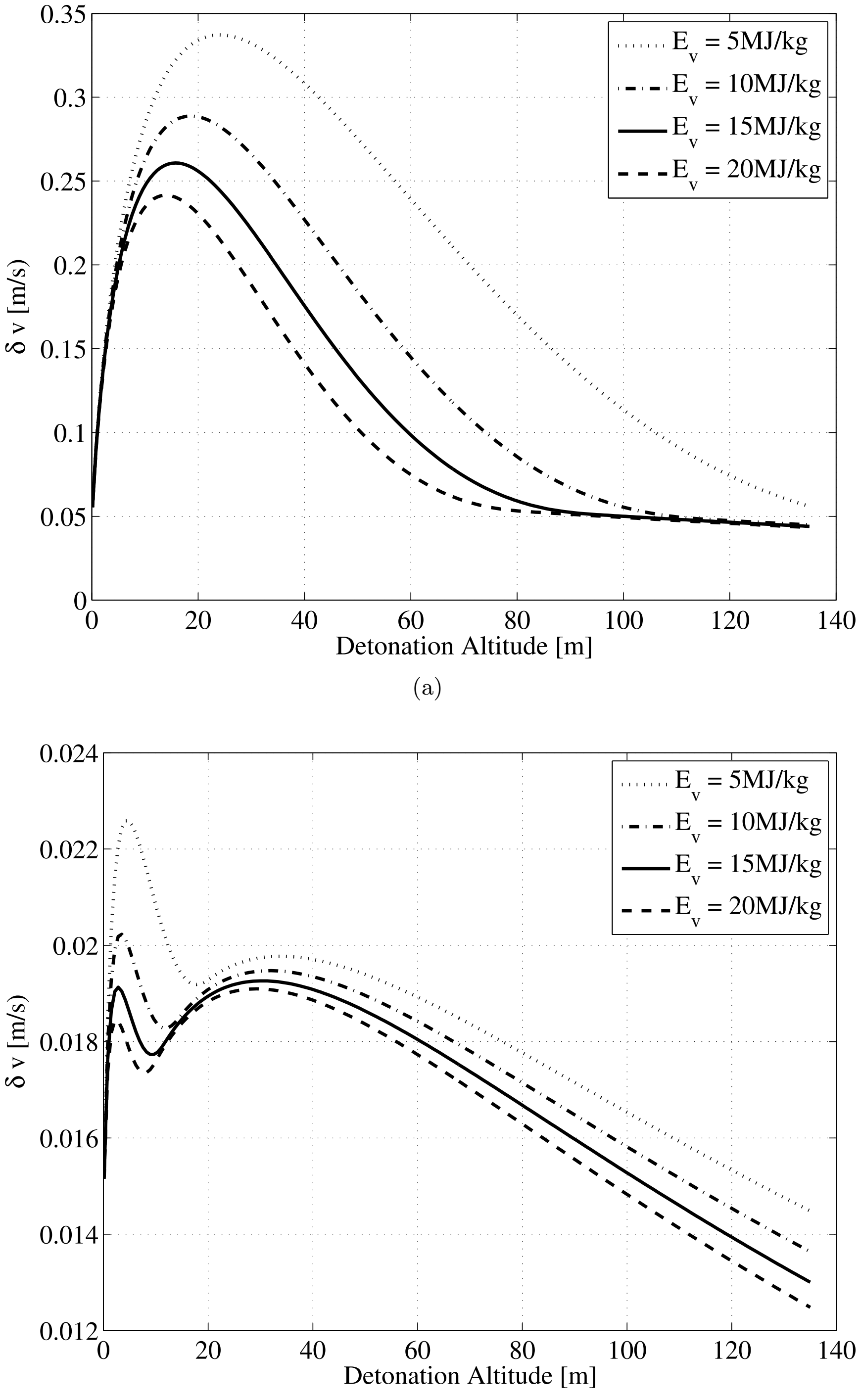

(a)

(b)

Figure 4.4: Impulsive change of velocity as a function of the detonation altitude for different values of the enthalpy of vaporization: a) 600kg fusion device, b) 600kg fission device

On the other hand, due to the politically sensitive nature of this method, a demonstration mission in the near future appears unlikely. Thus, this method will remain at a low maturity level compared to the kinetic impactor method. Another issue with the single nuclear interceptor method is the apparent sensitivity to the detonation altitude and fact that, in case something goes wrong, it will be more difficult to correct the asteroid trajectory compared to slow-push strategies. To remediate to this last difficulty, an incremental strategy, called the nuclear cycler method (Vasile and Thiry, 2016), is presented in Appendix B of this thesis.

Elongated Asteroid

In this section, we consider the case of an elongated asteroid with an elongation factor e_l - that is an ellipsoidal shape with semi-major axis $a_{\mathrm{I}} = e_l^{2/3} R_{\mathrm{A}}$ and semi-minor axes $b_{\mathrm{I}} = c_{\mathrm{I}} = \frac{R_{\mathrm{A}}}{e^{1/3}}$. The mean radius is still identical to the one used in the spherical case previously derived, so that the elongated and the spherical asteroids considered have an identical volume. Considering as a worst case scenario the configuration where the bomb is detonated along the longer side, the distance $h(\lambda)$ is now given as

$$h = \sqrt{(H + (1 - \cos\lambda) e_l^{2/3} R_{\mathrm{PHA}})^2 + \left(\frac{R_{\mathrm{PHA}}}{e_l^{1/3}}\right)^2 \sin^2\lambda} \tag{4.38}$$

We need now to distinguish between λ, the angle in elliptical coordinates corresponding to the concentric circle or radius a_{I} and $\tilde{\lambda}$, the angle between the normal to the ellipsoidal surface and the horizontal direction. They can be related through the following formula:

$$\cos\tilde{\lambda} = \frac{\cos\lambda}{\sqrt{1 + (e_l^2 - 1)\sin^2\lambda}} \tag{4.39}$$

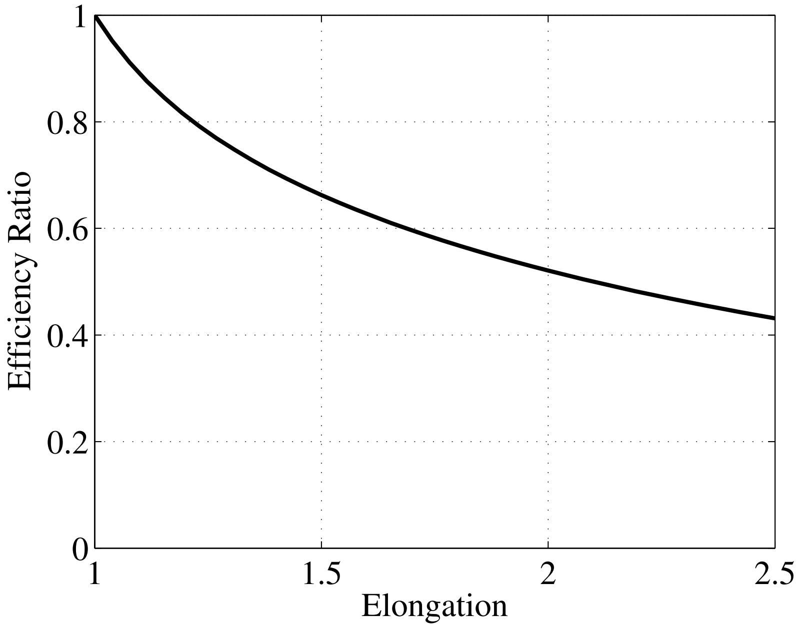

Figure 4.5: Performance comparison between the spherical case and a cigar-shaped asteroid as a function of the elongation

The value of $\sin\epsilon$ is obtained by computing the scalar product between the direction normal to the ellipsoidal surface $\mathbf{n}$ and the direction $-\mathbf{h}$, which gives

$$\sin\epsilon = \frac{\frac{e_l^{2/3}R_{\mathrm{PHA}}+H}{e_l^{2/3}R_{\mathrm{A}}}\cos\lambda - 1}{\frac{e_l^{1/3}h}{R_{\mathrm{PHA}}}\sqrt{\frac{\cos^2\lambda}{e_l^2}+\sin^2\lambda}} \tag{4.40}$$

Last but not least, the infinitesimal volume is now expressed as

$$dV = 2\pi e_l^{1/3} R_{\mathrm{PHA}}^2 \frac{\sin^2\lambda}{\sin\tilde{\lambda}} dz d\lambda \tag{4.41}$$

Keeping a constant detonation altitude of 17 m, Fig. 4.5 shows how the δv produced compares to the spherical case, considering again a 600 kg fusion device.

4.2.3 Gravity Tug

The Gravity Tractor (GT) exploits the mutual attraction between the spacecraft and the asteroid to progressively change the velocity of the asteroid. In the more traditional configuration, the spacecraft is placed at a distance d from the asteroid and two thrusters mounted in a slanted configuration, to avoid thrust impingement, would balance the gravity attraction. By doing so the net result is a constant acceleration on a compound spacecraft-asteroid, see Figure 4.6.

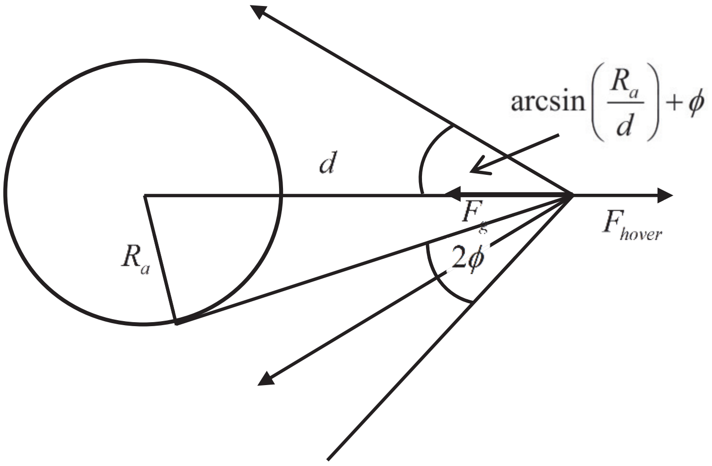

Figure 4.6: Sketch of the gravity tug approach with slanted engines

For the position of the spacecraft to be fixed, the gravity force must equate the net thrust F_{hover}:

$$F_{hover} = 2T_S \cos\left(\arcsin\left(\frac{R_{\mathrm{PHA}}}{d}\right) + \phi\right) \tag{4.42}$$

$$F_g = \frac{G m_{\mathrm{PHA}} m_S(t)}{d^2} \tag{4.43}$$

$$F_{hover} = F_g \tag{4.44}$$

where T_S is the thrust of a single engine in the slanted configuration, ϕ the half-divergence angle of the engine, R_a is the radius of the asteroid, m_{PHA} its mass, G

the gravity constant and $m_S(t)$ is the mass of the spacecraft at time t. The tugging acceleration is simply:

$$u_{gtug}(t) = \frac{Gm_S(t)}{d^2} \tag{4.45}$$

If the engines are assumed to be always on and the initial mass of the spacecraft is m_i, the mass of the spacecraft at time t can be expressed as:

$$m_S(t) = m_{S0} \exp\left(-\frac{Gm_{\mathrm{PHA}}(t-t_0)}{d^2 \cos\left(\arcsin\left(\frac{R_{\mathrm{PHA}}}{d}\right)+\phi\right) I_{sp} g_0}\right) \tag{4.46}$$

where I_{sp} is the specific impulse of the engine and g_0 the gravity acceleration on the surface of the Earth and t_0 is the beginning of the deflection action.

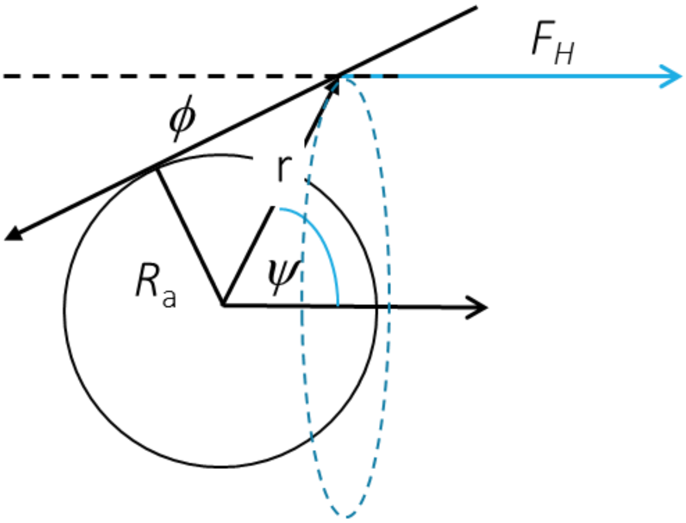

Figure 4.7: Sketch of the gravity tug approach with halo configuration

In the work of McInnes (2007) and Yamaguchi and Yamakawa a variant of the original gravity tractor concept was proposed to remove the need for a slanted configuration and to use the thrust more efficiently. The idea is to place the tractor on a displaced halo orbit that is artificially maintained by a constant thrust. If the plume of gas of the engine generating the thrust is not impinging the asteroid, the net result is traction on the asteroid in the direction of the thrust vector (see Figure 4.7). Compared to the slanted configuration, the halo configuration requires only one engine but the thrust delivered by the engine has to be lower or the distance from the asteroid has to be shorter.

With reference to Figure 4.7, the achievable tugging effect as a function of the divergence angle ϕ is:

$$u_H = \frac{Gm_H(t)}{R_{\text{PHA}}^2} \cos\psi \sin(\psi - \phi)^2 = \frac{Gm_H(t)}{R_{\text{PHA}}^2} \tau \tag{4.47}$$

The τ factor in (4.47) is represented in Figure 4.8 for different values of ϕ. The figures shows that τ cannot be 1 for any value of ψ. The theoretical maximum is about 0.385 and is realised when $\phi = 0$. In comparison the slanted configuration could theoretically approach a value $\tau = 1$ but this would require the spacecraft to hover just above the asteroid surface with its engines slanted at almost 180 degrees of each other. In fact, at the limit $\tau = 1$, the thrust required by the engines in the slanted configuration would be infinite.

For 2 given configurations, it is easy to show that the Halo configuration requires less propellant to achieve the same momentum transfer than the slanted configuration. For 2 spacecraft operating at a fixed distance, the ratio of propellant use is simply given by the cosine of the slant angle:

$$\frac{\Delta m_H}{\Delta m_S} = \cos\left(\arcsin\left(\frac{R_{\text{PHA}}}{d}\right) + \phi\right) \tag{4.48}$$

In summary, while the slanted configuration can achieve higher tractions and thus transfer more momentum to the asteroid in a shorter amount of time, the halo configuration will use less propellant mass to achieve the same momentum transfer.

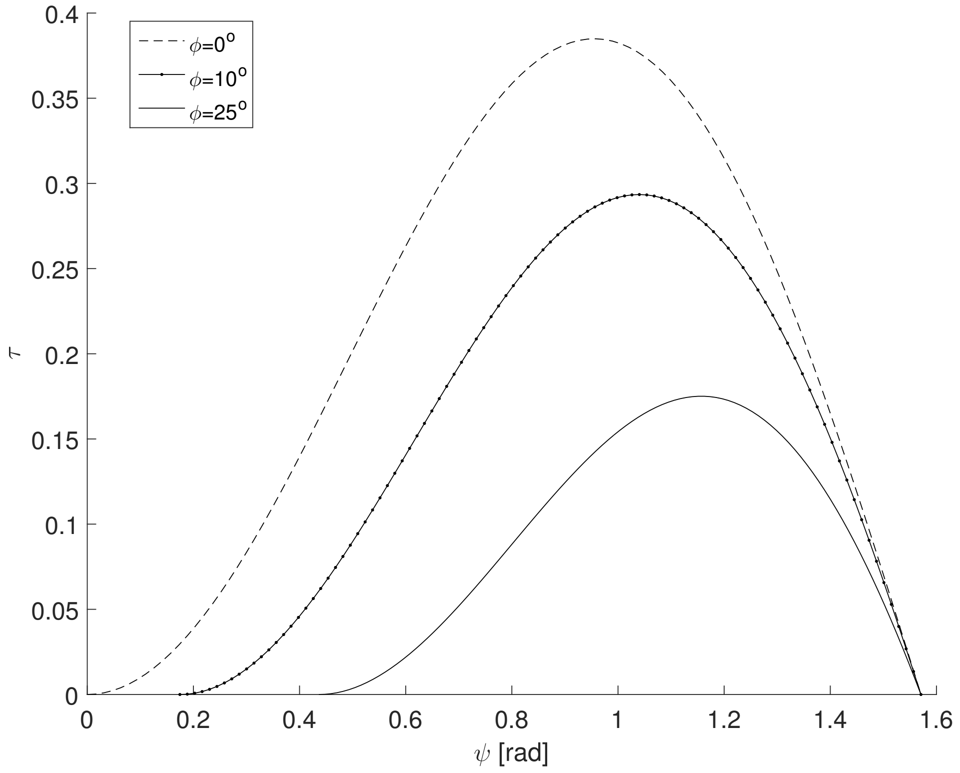

Figure 4.8: τ factor as a function of ψ

4.2.4 Ion Beam Shepherd

Ion beaming was initially proposed as a technique to remove space debris with the name Ion Beam Shepherd (IBS). Also applicable to the deflection of an asteroid (Bombardelli et al., 2013), the idea is to use an ion engine to transfer momentum to the space object by beaming a flow of ions. In order to maintain the relative position between the deflecting spacecraft and the asteroid, a second engine needs to be positioned on the opposite side of the spacecraft to balance the thrust coming from the engine beaming the ions on the asteroid.

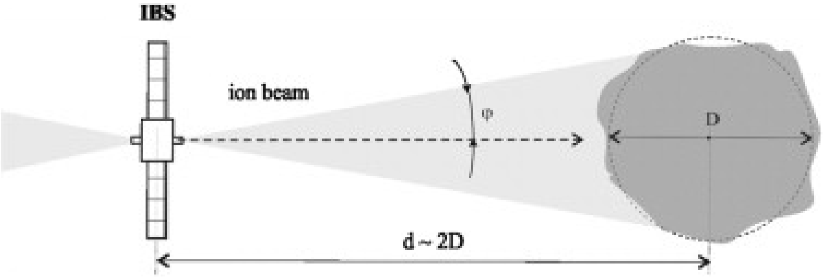

Figure 4.9: The IBS concept for asteroid deflection (Bombardelli et al., 2013)

In comparison to the gravity tractor method, the IBS method theoretically allows to deliver a larger thrust since it is not limited anymore by the gravity force between the spacecraft and the asteroid. The operations can also be carried out at a safer distance from the asteroid. The drawback is a a larger propellant consumption due to the need to operate a second engine on the opposite side the spacecraft for station-keeping. Moreover, the IBS still needs to operate at a sufficiently close distance from the asteroid to maximize the fraction of ions actually impinging on the asteroid. Indeed, any errors in beam pointing will reduce the fraction of ions that can intercept the asteroid, thus reducing the total transfer of momentum. In order to operate at a safe distance, a low divergence, high specific impulse beam will thus be required by the engine. Assuming the entire flow of Ions reaches the asteroid, the thrust of the IBS mission on the asteroid is equal to

$$F_{IBS} = C_{HET}\frac{P_{in}}{2} \tag{4.49}$$

where C_{HET} is equal to the thrust to power ratio of the engines, P_{in} the input power.

4.2.5 Laser ablation

Unlike the other slowpush methods introduced in this chapter, with laser ablation, the ability of the spacecraft to impart a thrust on a given asteroid will not rely on its propulsion subsystem but just on the parameters of its laser payload. Practically, the laser ablation thrust F_{LA} depends on the laser input power P_{in}, the electrical to optical (E/O) conversion efficiency of the laser system η_{LA}, and C_m, the thrust coupling coefficient

$$F_{LA} = \eta_{LA} C_m P_{in} \tag{4.50}$$

It was explained in chapter 3 that the two meaningful parameters impacting the ability of a laser system to convert optical power into thrust through the ablation process are 1) the laser intensity achieved at the ablation spot, and 2) the duration τ over which a given point at the surface of the target remains exposed under the laser beam. In fact, according to Fig. 3.14, the thrust coupling coefficient C_m in the vapor regime increases with $I\sqrt{(\tau)}$ to reach a plateau value around 55-60μN per Watt of optical power. Several observations can be made from this:

- Even at a moderate power, a CW laser system may be able to sustain an ablation process as long as a sufficient intensity is applied on the target
- Pulsed laser systems can deliver peak power levels that are several order of magnitude higher than their average power. For these lasers, the ability to focus the laser light on a tiny spot may not be so critical as for CW lasers, meaning that such lasers will be able to operate at a large distance from their target without requiring a large focusing optics. While these lasers may be practical for the needs of an active debris removal mission, their comparatively lower conversion efficiency make them less attractive for the problem of asteroid deflection.

Thus, for an asteroid deflection mission, a dedicated focusing optics would be necessary to achieve the required intensity at a given shooting distance. Considering a typical

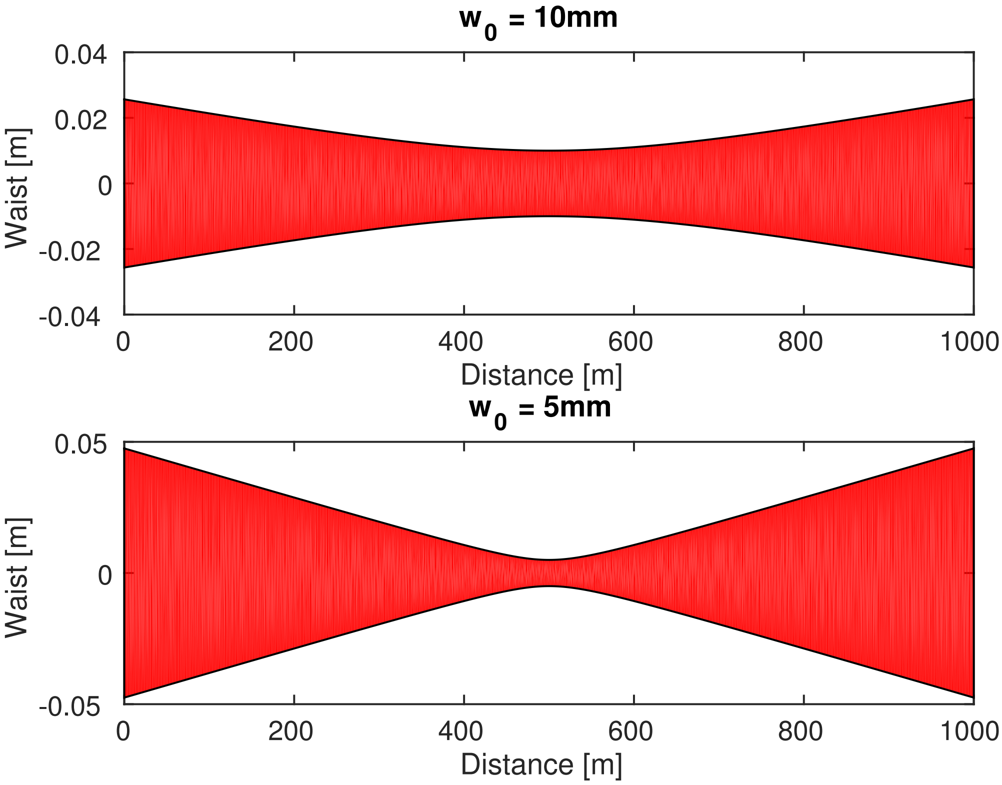

Figure 4.10: Example of laser beam propagation with λ=1064nm, $M^2 = 1.4$, f = 500m

Gaussian beam propagation, the beam radius will vary along the propagation direction according to

$$w = w_0\sqrt{1 + \frac{(z-f)^2}{z_r^2}} \tag{4.51}$$

In this equation, f is the focal length of the focusing optics, z_0 the beam waist at the focal distance and z_r the Rayleigh range given by

$$z_r = \frac{\pi w_0^2}{\mathcal{M}^2\lambda} \tag{4.52}$$

Where the $\mathcal{M}^2$ parameter represents the beam quality factor or beam propagation factor and represents the quality of the laser beam with respect to an ideal Gaussian beam. The Rayleigh range corresponds to the distance from the focal point at which the beam intensity is divided by a factor 2.

In particular, setting z=0 in equation 4.51 allows us to compute the radius of the focusing lens or mirror used by the spaceborne laser system. If $w_{primary}$ is the radius of the main mirror of the focusing optics, f the focal length (considered long with respect to the Rayleigh range), the diffraction limit imposes that the minimum mirror radius is:

$$w_{primary} \approx \mathcal{M}^2 \frac{\lambda f}{\pi w_0} \tag{4.53}$$

This last equation shows that the size of the optics will scale with the inverse of the required spot size. As an illustration, Fig. 4.10 show examples of beam propagation in vacuum from an initial focusing optics, assuming a 500m focal length and a required laser beam radius of 10mm and 5 mm respectively at the focal distance. For these 2 cases, the Rayleigh ranges are 212m and 53m respectively.

In practice, a beam expansion and focusing telescope would be required to focus the laser spot at the required size. On top of this, power scaling by combining multiple laser beams into a single beam may be necessary so as to obtain a single beam not only with correspondingly higher power but also with more or less preserved beam quality and thus with increased brightness. The two main beam combining techniques are coherent beam combining and spectral beam combining. We retain in this work the later approach which has been successfully deployed on several high power applications with very high efficiencies (Drachenberg et al., 2011).

A possible configuration for the laser system architecture is outlined in Fig. 4.11.
It essentially comprises 3 elements:

1. The fiber laser chassis which is connected to the electric bus and rejects heat towards the radiators.

2. The spectral beam combination (SBC) module which comprises the fiber array, a transform mirror and the diffraction grating which reflects the different beams with a different angle due to the slightly different wavelength so that the output is a single beam combining the uncoupled incident beams. Lockheed Martin is using this design in its 60 kW laser for the HEL-MD.

3. An off-axis beam expansion and focusing telescope

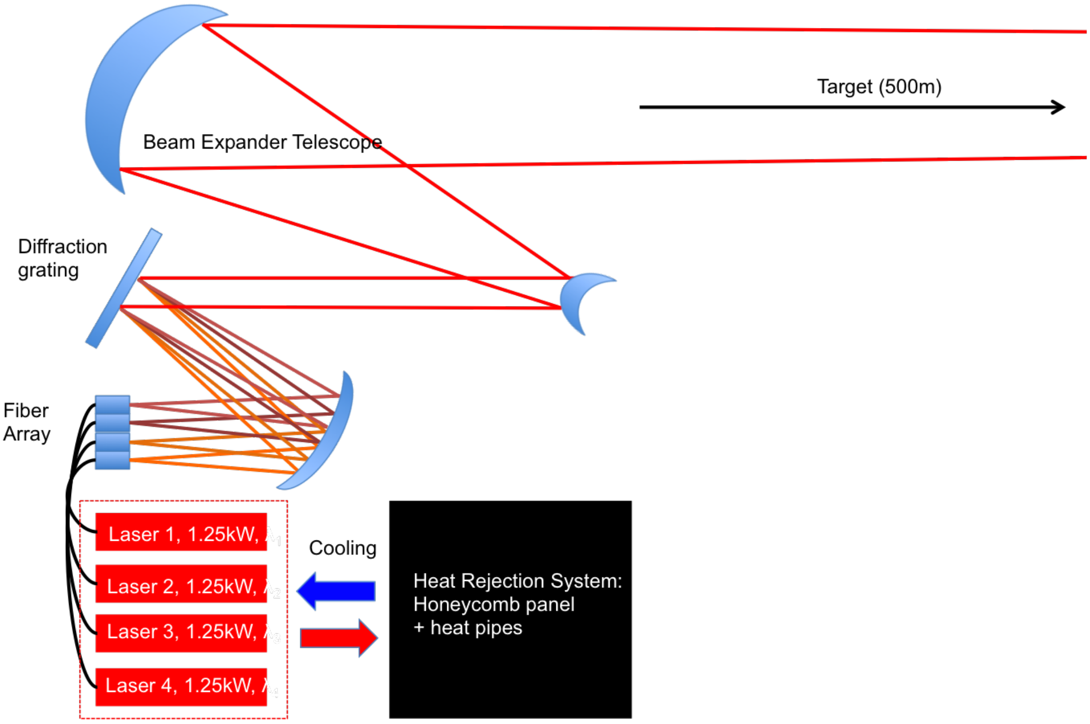

Figure 4.11: Example of passive, redundant and up-scalable laser-system design using a spectral beam combining technique and an off-axis beam expansion and focusing telescope

Note that the use of high reflective surfaces both in the SBC module and for the beam expansion telescope will limit the heat production by absorption of the incident light. On the other hand, the use of spectral beam combination technique provides a passive method to upscale the design to higher power, while allowing an increased redundancy in the laser system.

4.3 Qualitative comparison between impulsive and slow-push methods

In this section we provide a theoretical analysis of the energy required to increase the transfer of momentum during impact. In other words we consider the case in which the orbit of the impactor is modified so that the relative velocity between spacecraft and asteroid at impact is increased.

Consider a simple planar case in which the expected impact of the asteroid with the Earth is at an apsidal point. The impactor spacecraft is ramming into the asteroid at the same apsidal point with $\beta = 1$. The variation of velocity of the asteroid post impact with the spacecraft is:

$$\delta v = \frac{m_{s/c}}{m_{\mathrm{PHA}}}(\|q\| - \Delta v_T) \tag{4.54}$$

where q is the difference in velocity due to the difference between the orbit of the asteroid and the one of the Earth:

$$q = \sqrt{\frac{2\mu}{r_E} - \frac{\mu}{a_{\mathrm{PHA}}}} - \sqrt{\frac{\mu}{r_E}} \tag{4.55}$$

and Δv_T is the increment due to the transfer of the spacecraft on a suitable orbit:

$$\Delta v_T = \sqrt{\frac{2\mu}{r_E} - \frac{\mu}{r_E + \delta a_N}} - \sqrt{\frac{\mu}{r_E}} \tag{4.56}$$

.

The mass of the spacecraft at impact $m_{s/c}$ can be related to the mass at launch $m_{s/c,0}$ through:

$$\frac{m_{s/c}}{m_{s/c,0}} = e^{-\frac{\Delta v_T}{I_{sp} g_0}} \tag{4.57}$$

from which:

$$\delta v = \frac{m_{s/c,0} e^{-\frac{\Delta v_T}{I_{sp} g_0}}}{m_{\mathrm{PHA}}}(\|q\| - \Delta v_T) \tag{4.58}$$

Figures 4.12a and 4.12b show the δv for different asteroid semi-major axes, a_{PHA}, and different Δv_T, in the case of an $I_{sp} = 300s$ and an $I_{sp} = 3000s$ respectively. The figures show that for a low I_{sp} the optimal strategy is not to perform any transfer as the increase in momentum is proportional to Δv_T but the loss in mass is proportion to $e^{-\Delta v_T}$. This is a problem for asteroids with semi-major axis close to 1AU, low eccentricity and low inclination as a transfer produces a low gain in δv and a further increase in Δv_T might in fact lead to a decrease in the deflection.

The situation appears to be different for a high I_{sp}. In this case the gain provided by the transfer for high a_{PHA} is limited but the one provided for low a_{PHA} becomes interesting. Note that this analysis does not consider gravity losses and the time required to deliver the required Δv_T. Figure 4.13 shows the difference between the Δv required to rendezvous with the asteroid and Δv_T. A positive value indicates that a rendezvous is more expensive. Negative areas, instead, suggest that a rendezvous is a potential option. In this case, the value of the Δv difference could then be available to achieve a deflection with, for example, a slow push method. The figure gives an indication of when a kinetic impactor might be preferable to a slow-push technique. Another qualitative indication can be obtained by computing the required propellant mass to generate the same change in linear momentum given by a kinetic impactor. Assuming a constant low-thrust push on an asteroid, the mass of propellant required to deliver the variation of linear momentum in Eq. (4.57) is given by:

$$\Delta m I_{sp} g_0 = m_{s/c,0} e^{-\frac{\Delta v_T}{I_{sp} g_0}} (\|q\| - \Delta v_T) \tag{4.59}$$

to this, one has to add the mass required to inject the spacecraft into the orbit of the asteroid:

$$\Delta m_{LT} = m_{s/c,0} \frac{e^{-\frac{\Delta v_T}{I_{sp} g_0}} (\|q\| - \Delta v_T)}{I_{sp} g_0} + m_{s/c,0}(1 - e^{-\frac{q}{I_{sp} g_0}}) \tag{4.60}$$

The mass of the propellent on the kinetic impactor is instead given by Eq. (4.57) which then gives the relative mass fraction:

$$\frac{\Delta m_{LT}}{\Delta m_{KI}} = \frac{\frac{e^{-\frac{\Delta v_T}{I_{sp} g_0}} (\|q\| - \Delta v_T)}{I_{sp} g_0} + (1 - e^{-\frac{q}{I_{sp} g_0}})}{(1 - e^{-\frac{\Delta v_T}{I_{sp} g_0}})} \tag{4.61}$$

The relative mass fraction for an I_{sp}=3000s can be seen in Figure 4.14. The figure shows that, in this particular case, when the orbit of the asteroid approaches the one of the Earth the slow-push solution is up to 20% more efficient, which translates into 20% more deflection action, than increasing the energy of the kinetic impactor, albeit with a low-thrust propulsion system. It has to be noted that although this analysis is limited to a special case, some considerations are generally applicable. In particular, a highly inclined orbit favours a kinetic impactor in the same way an orbit with a high a_{PHA} does. On the contrary, for a shallow crosser with a low inclination, the mass loss coming from the rendezvous with the asteroid is limited compared to the increase in orbital energy of the kinetic impactor. Finally, if the slow-push action did not require any propellent at all the first term on the right hand side of Eq. (4.60) would translate in an additional % of deflection.

The analysis in this section is only qualitative but suggests that the low-thrust impactor proposed by some authors in the past (Conway, 1997) can be a valid alternative for some classes of asteroids, while for others, a simple direct injection with a single impulse is potentially optimal. The use of a low-thrust transfer for the kinetic impact become progressively more interesting as the propellant cost decreases (or the I_{sp} increases). For this reason, solutions using solar sails or electromagnetic sails have been considered in the past. These solutions, however, require careful considerations on the design of the navigation and control system to guarantee a successful impact at hyper-velocity due to the limited control authority. At the same time one can argue that if a slow push method requires low or zero propellant to deliver the required deflection action, then that method might be optimal in the case of low semimajor axis, low eccentricity and low inclination asteroids. Furthermore, if one combines a low-cost transfer with a zero-propellent slow push method then slow push become optimal for a wide range of targets.

In the following we will limit our comparison only to the simpler version of the kinetic impactor leaving the comparison with the low-thrust counterpart to a future work.

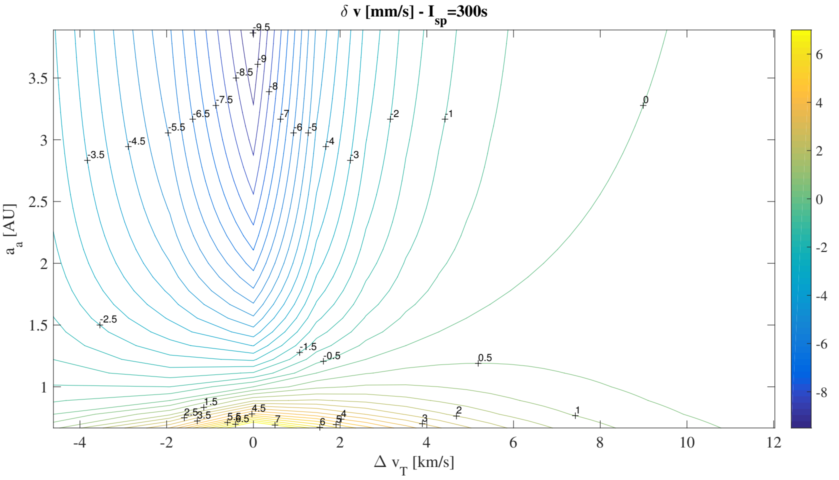

(a) $I_{sp} = 300s$

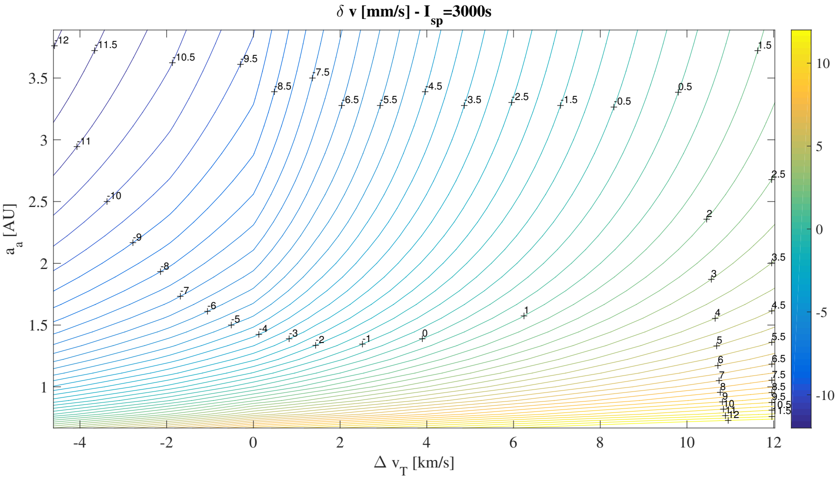

(b) $I_{sp} = 3000s$

Figure 4.12: Deflection δv for different semi-major axes and different Δv_T: a) contour lines of achievable δv imparted onto the asteroid given a departure Δv_T and asteroid semi-major axis a_{PHA} for an engine $I_{sp} = 300$s, b)contour lines of achievable δv imparted onto the asteroid given a departure Δv_T and asteroid semi-major axis a_{PHA} for an engine $I_{sp} = 3000$s

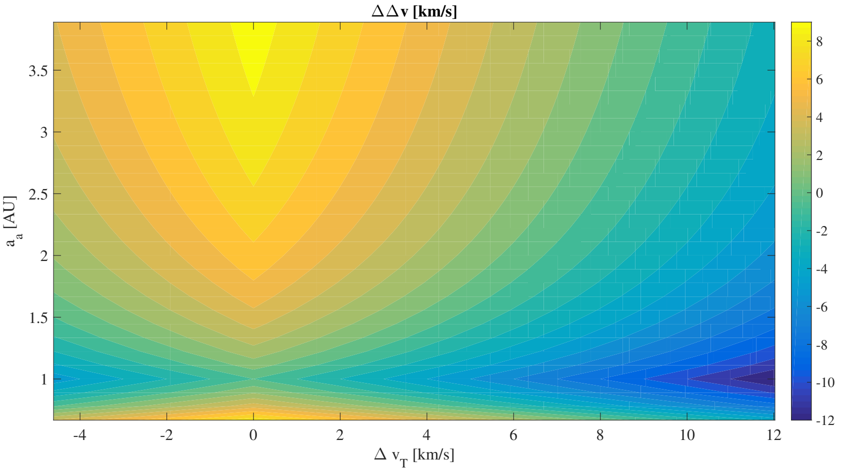

Figure 4.13: Δv difference for different semi-major axes and different Δv_T: negative values indicate that a low-thrust tug is preferable to a kinetic impactor.

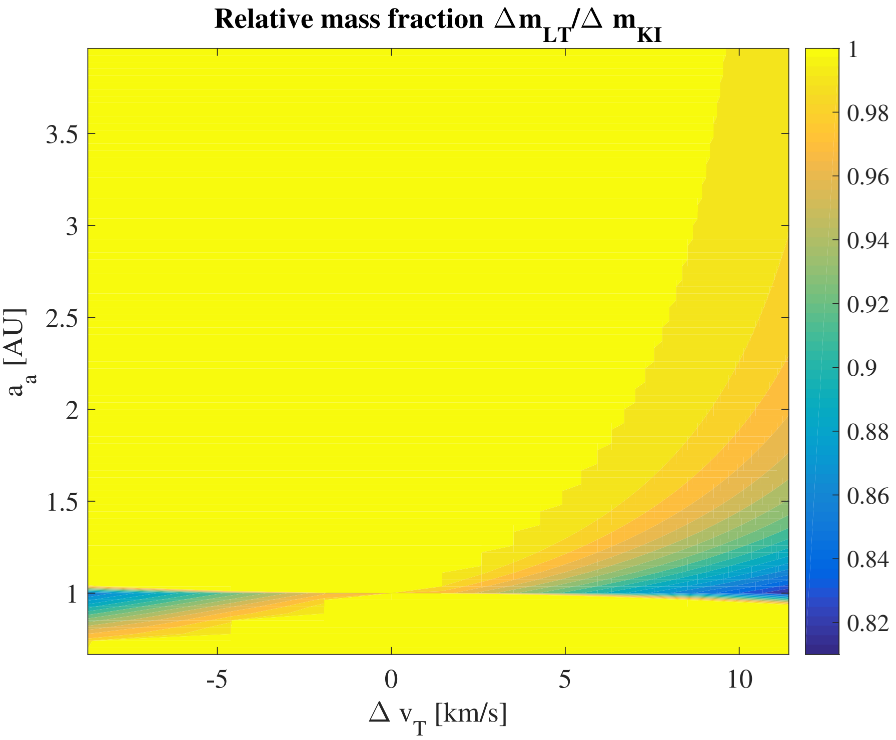

Figure 4.14: Relative mass fraction between low-thrust tug and kinetic impactor: fraction between the mass of propellant required to deflect an asteroid with a low-thrust tug and the mass of propellant required to deflect by the same amount the same asteroid but with a kinetic impactor.

Chapter 5

Mission design for the deflection of an asteroid with a laser

We estimate in this chapter the ability of a realistic asteroid deflection mission carrying a CW laser system and operating in the vicinity of a small (56m) and larger(100m) asteroid on a virtual collision course with the Earth. To this end, the thrust model developped in chapter 3 is integrated within an orbit propagator, following the methodology proposed in chapter 4. A bottom-up sizing exercise is also undertaken to estimate the spacecraft mass required for this mission. The results indicate that a medium class mission carrying a 5kW laser could ensure the deflection of a 56m asteroid while a formation of such spacecraft could also achieve the deflection of a larger (100m) threat. The last section of this chapter also outlays the description of a possible future demonstration mission to a binary asteroid system. Similarly to the concept proposed by the international AIDA mission, this mission would consider the deflection of the secondary asteroid while the measurement of the variation in the rotation period of the binary system would allow to assess the effectiveness of the deflection method. Compared to the AIDA mission which requires an impactor and an observer spacecraft, this mission would only require a single spacecraft, operating form the triangular (L4 or L5) Lagrangian point of the binary system to simultaneously exert the deflection and measure its effectivenes.

5.1 Asteroid Redirect Mission

Asteroid (2010 KJ37) is comparable in size with the asteroid that caused the Tugunska event in 1908 and is thus representative of near-future threats requiring potential mitigation actions to be taken. Two scenarios are investigated in this part: one with the original dimensions of the asteroid and another one with a 100m diameter and 1.37E+9 kg. In both cases, a 500m hovering distance is assumed and the deflection operations in proximity of the asteroid start 5 years prior to the virtual impact with the Earth. In order to form a virtual impact with the Earth in 2036, the orbital elements extracted from the JPL Horizons risk list were modified to a planar case, as can be seen in table 5.1:

Table 5.1: Orbital Elements for asteroid 2010 KJ37

Orbital Elements	Symbol	Value (Unmodified)	Value (VI)
Semi-major axis	a	1.102 AU	1.102 AU
eccentricity	e	0.058	0.088
inclination	i	11.28 deg.	0 deg.
ascending node	Ω	236.43 deg.	236.43 deg.
argument of perigee	ω	99.278 deg.	99.278 deg.
True anomaly (t_0)	θ	270.978 deg.	270.978 deg.

The orbit of 2010KJ37 is represented in figure 5.1. The transfer to the asteroid was computed considering the actual inclination of 2010 KJ37. Using chemical propellant, the best transfer option would require a Δv of 6.5km/s as indicated in figure C.1.

Lacking better information, the spinning rate of this asteroid is assumed from the formula

$$\omega_{\max} = \sqrt{\frac{4}{3}\pi\rho G} \tag{5.1}$$

which gives the spin limit for asteroids larger than 100m and thus represents an approximation in the smaller case. In a real deflection scenario, an initial observation phase would allow to reduce the uncertainty on the different properties of the target.

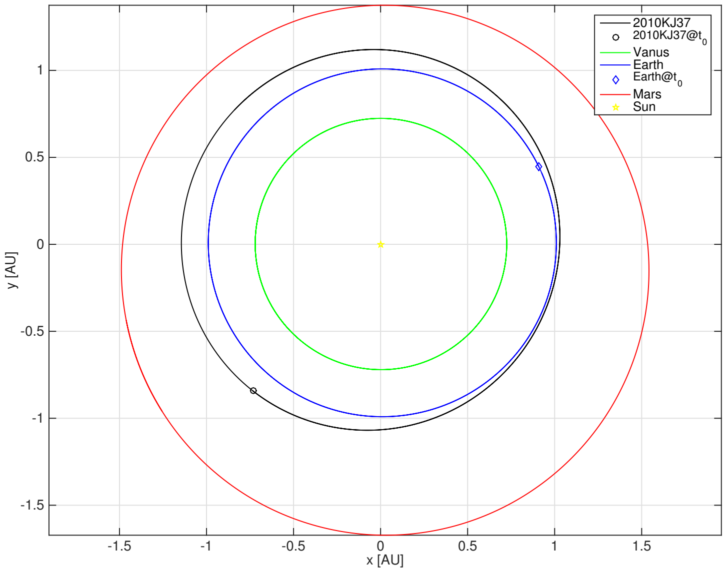

Figure 5.1: Orbit of asteroid 2010 KJ37

An estimate of the local surface velocity is then obtained by computing the product between the rotation speed and the asteroid radius, which gives a velocity of the ablated surface relative to the laser beam v_{rel} that varies between 23.9 mm/s for the 56m case and 42.9 mm/s for the 100m case.

5.1.1 Deflection Model

The modified trajectory is computed by integrating Gauss' planetary Eq. (4.1) using the initial values for the Keplerian elements in table 5.1. Note that, in the planar case, those equations can be simplified as following:

$$\frac{da}{dt} = \frac{2a^2V}{\mu}\alpha_t \tag{5.2}$$

$$\frac{de}{dt} = \frac{2(e+\cos(\theta))}{V}\alpha_t \tag{5.3}$$

$$\frac{d\omega}{dt} = \frac{2}{eV}\sin(\theta)\alpha_t \tag{5.4}$$

$$\frac{d\theta}{dt} = \frac{h}{r^2} - \frac{2\sin(\theta)}{eV}\alpha_t \tag{5.5}$$

In these equations, acceleration α_t is considered to be imparted in the tangential direction and can be computed at each time step by dividing the ablation thrust by the asteroid mass. The ablation thrust is computed using the model of sec. 3.3. The output power of the laser system considered is assumed to vary with respect to the square distance to the sun and will decrease over the lifetime due to contamination issues:

$$P_{\text{out}}(r/r_{\text{AU}}, t) = \chi(t)\frac{P_{\text{out}}(1, t_0)}{(r/r_{\text{AU}})^2} \tag{5.6}$$

Where r_{AU} is an astronomical unit. For a given amount of nominal output power at 1 AU $P_{\text{out}}(1, t_0)$ and a given optics able to focus the laser beam on a certain beam diameter D, the laser-matter interaction model returns the thrust generated and the mass flow rate impinging on the solar arrays, from which the growth of the contamination layer can be computed (see sec. 3.5). Note that for large asteroids and a small hovering distance, the model could also include the tugging effect of the spacecraft on the asteroid but this effect was not considered in the present case as the tugging force is about 3 orders of magnitude lower than the one due to laser ablation.

As explained in sec. 4.1.1, because the perturbed orbit of the asteroid is close to the original one, the achieved deviation $\delta\mathbf{r}$ can finally be computed from the integral variation of the orbital parameters $\delta\mathbf{k} = [\delta a,\, \delta e,\, \delta\omega,\, \delta M]$ at the expected minimum orbit intersection distance (MOID).

$$\delta r_r \approx \frac{r}{a}\delta a + \frac{ae\sin(\theta)}{\nu}\delta M - a\cos(\theta)\,\delta e \tag{5.7}$$

$$\begin{aligned} \delta r_\theta \approx\ & \frac{r}{\nu^3}\left(1 + e\cos(\theta)\right)^2 \delta M + r\delta\omega \\ & + \frac{r\sin(\theta)}{\nu^2}\left(2 + e\cos(\theta)\right)\delta e + r\cos(i)\delta\Omega \end{aligned} \tag{5.8}$$

in which $\nu = \sqrt{1-e^2}$, $\theta^* = \theta + \omega$ and M is the mean anomaly. From the deflection $\delta\mathbf{r}$ the impact parameter b at the time of the MOID can be computed using the projection method described in section 4.1.1.

5.1.2 Deflection Results

Eq. 5.2 were numerically integrated to predict the deflection achieved for a mission starting the deflection action 5 years prior to the virtual impact. The inputs of our model are the unperturbed Keplerian elements of the virtual impactor[1], the nominal output power of the laser system (theoretical output power at 1AU at the start of operations), the beam diameter achieved at the focal length of the focusing optics, the distance between the spacecraft and the target and the duration of the deflection action. The returned value is the miss-distance approximated by the projection of the deflection distance on the target plane (b parameter). Note that the actual value of output power is modulated during the integration to account for the growth of a contamination layer on the solar panels and variation of available power with the square distance to the sun. Figure 5.2 and figure 5.3 show the resulting deflection as a function of the nominal output power and focusing ability of the laser system in the case of a 56m, 2.4E+08 kg asteroid and a 100m, 1.37E+09kg asteroid respectively assuming a spacecraft flying at a 500m distance. The results show that even a moderate laser system with 2.4kW of output power could achieve the deflection within 5 years and with an optics able to focus the laser light on a 3mm spot at 500m distance. As one would reasonably expects, the results on figure 5.3 indicate that the power requirement scale approximately with the cube of the asteroid size. For this second case, a single spacecraft with 9.6kW of output power could achieve a deflection of about 2 Earth radii within the time imparted and an optics able to focus the laser on a 7mm spot. Alternatively, the deflection of the larger asteroid could be achieved by a formation of 4 smaller spacecraft generating 2.4kW of output power each. This option offers a greater redundancy in the case of failure of a single spacecraft and would also allow to fit the individual spacecraft in a medium-class launcher. If the swarm is not able to combine the beams in the far field, the beam diameter required to reach the same efficiency as in the single spacecraft option is reduced to 3mm. Indeed, keeping the beam diameter constant would imply a lower intensity on the target.

---

[1] Which was made co-planar with the Earth orbit for the sake of the virtual collision scenario. Virtual impactor scenarios in the next chapter will also consider virtual impacts scenarios in the more general, non-planar case.

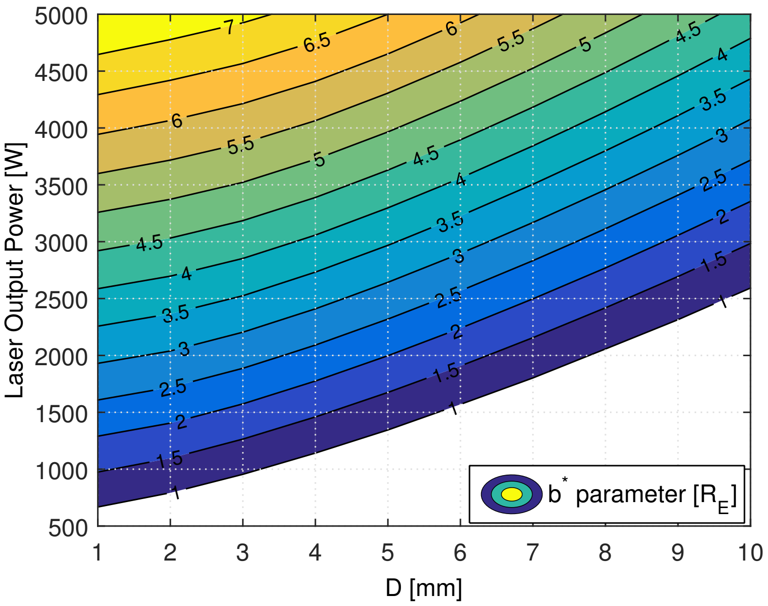

Figure 5.2: Miss-distance (normalized with respect to the Earth radius) achieved as a function of the available nominal output power at 1AU and focusing optics for the 56m case and 5 years of operation

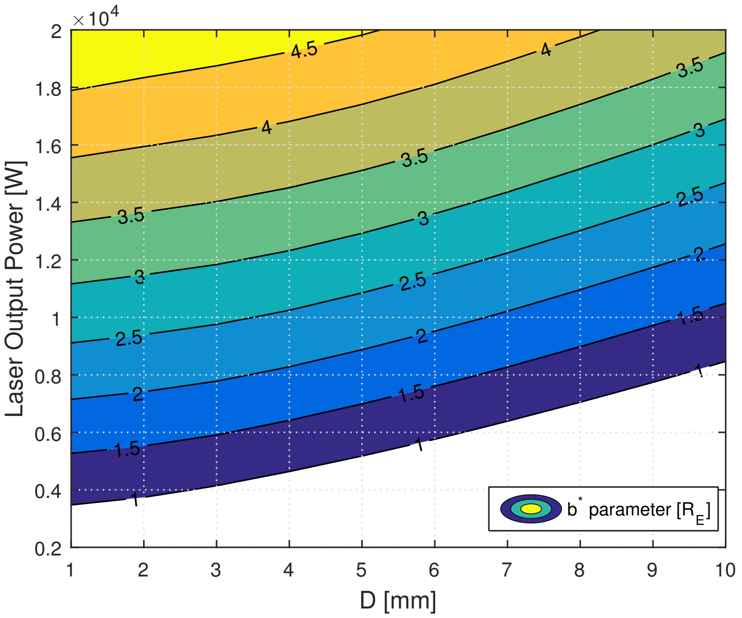

Figure 5.3: Miss-distance (normalized with respect to the Earth radius) achieved as a function of the available nominal output power at 1AU and focusing optics for the 100m case and 5 years of operation

5.1.3 Preliminary Spacecraft Sizing

According to the results in the last subsection, it appears that a single spacecraft or a swarm of 4 spacecraft carrying each a laser system producing 2.4kW of output power and with an optics able to focus the beam on a 3mm spot on the target would be sufficient to achieve the deflection maneuvre in less than 5 years of operation. In this subsection, we attempt to describe the laser system envisaged to realize this requirement in a power efficient, redundant and scalable way and converts the requirement on the laser system into general requirements on the spacecraft bus. Additionally, we provide in the first point some preliminary guidelines for the conception of the pulsed-laser system required in the debris case.

The mass of the laser system can be estimated by extrapolating previous results obtained during the sysnova study which considered the deflection of a small asteroid using a 860W laser (Vasile et al., 2013). From this study, a mass of 12 kg per kW of input power was found for the solid-state laser. The state-of-the-art efficiency of diodes is 70% and is expected to increase to 80% in the near future (Cramp et al., 2005). In this study, we considered an efficiency of 55%. The optics considered in the sysnova study consisted in a beam expansion and focusing telescope with a primary mirror of 100mm, which had an estimated mass of 9.9kg. The diameter of the primary mirror required to achieve a diffraction limited beam of 3mm at the focal distance f of 500m for a laser with a wavelength λ of 808nm and a M-squared value $\mathcal{M}^2$ of 1.4 is

$$D_{\text{primary}} = \mathcal{M}^2 \frac{4\lambda f}{\pi D_{\text{laser}}} = 24\text{cm} \tag{5.9}$$

As already explainedm the $\mathcal{M}^2$ parameter is the laser beam quality factor which characterizes the divergence of the beam with respect to a purely Gaussian laser beam. A higher value increases the requirements. Assuming the mass of the optics scales with the square of the diameter of the primary mirror, we obtain a mass of 57kg.

Assuming a combination efficiency of 91% (Drachenberg et al., 2011), a global laser system efficiency of 50% is considered. With additional margins of 20% both for the optics and the laser system, a total mass of 140kg is obtained for the laser payload as can be seen in table 5.2, in which CBE and DMM designate the current best estimate and deisgn maturity margins respectively.

Table 5.2: P/L mass budget

Component	number	CBE(kg)	DMM(kg)	CBE + DMM(kg)
Laser (1.25kW)	4	15	3	18
Optics	-	57	11	68
Total	-	117	23	140

The spacecraft subsystems must ensure the transfer from the Earth to the asteroid and provide the necessary power to the laser system in order to carry on the deflection mission successfully. The spacecraft also needs to maintain a 500m hovering distance and reasonable pointing accuracy during the 5 years duration of the proximity operations. After iterations on the design, a total wet mass of 1406kg was found for the spacecraft and the mass breakdown between the different subsystems can be reviewed in table 5.3. A C_3 escape energy of $2.25\text{km}^2/\text{s}^2$ was assumed with the remaining of the transfer completed with a low-thrust trajectory using Snecma's PPS-5000 hall effect thruster which has an Isp of 2300s and requires 5kW of input power (which are available during the transfer phase). A combination with 2 thrusters (with only 1 working at a time) and 2 PPU/TSU units is considered for redundancy against the failure of a single engine or the high voltage power converter. Lacking better information, a remaining transfer Δv of 6km/s was considered in the computations, with an additional safety margin of 30% (making it a total transfer Δv of 7.8km/s using the low-thrust engine and 1.5km/s from the launcher). One clear advantage of the low-thrust option is that it makes use the large available power during the transfer phase, which would otherwise remain unused since the laser only starts operating after rendez-vous with the asteroid. Triple junction GaAs solar cells from Azurspace are considered for the solar arrays which are made of two wings of 10.3m^2 each. Considering a packing efficiency of 85% and an electric conversion efficiency of 26.6%[2] (accounting for the damage from the radiations in the

---

[2] which is later multiplied by the contamination factor χ during the computations

Table 5.3: Spacecraft mass budget

Subsystem	CBE(kg)	DMM(kg)	Total(kg)
Payload	117	23	140
Avionics	50	-	50
AOCS	63	7	70
Power	78	16	94
Thermal	38	4	42
Propulsion	70	11	82
Harness	51	-	78
Structure	204	-	312
Dry Mass	643	186	**829**
System Mass Margin		20%	166
Dry Total			**995**
Propellant			411
Wet Mass			**1406**

interplanetary medium and the transmission of a coverglass with thickness of 100μm), this should provide about 6.43kW at 1AU. The AOCS consists of 4 RSI 45-745/60 reaction wheels placed in a redundant tetrahedral configuration. In addition to these a combination of 1N hydrazine thrusters are needed to facilitate orbit insertion and proximity manoeuvres required to compensate for the perturbations coming from the solar radiation pressure on the solar wings. The other perturbations, coming from the gravity of the asteroid and the laser recoil force are assumed to be compensated by the electric propulsion system and require only a negligible amount of Xenon propellant. The AOCS also includes 2 star trackers, a LIDAR and wide angle camera for navigation.

According to figure 5.4, a medium class launcher such as Soyuz or Falcon 9 could put the spacecraft on its interplanetary course (SpaceX, 2009) (Arianespace, 2006). Launch capabilities (in kg) for interplanetary missions depend on the characteristic energy C_3 which is a measure of the excess specific energy over that required to just barely escape from the Earth.

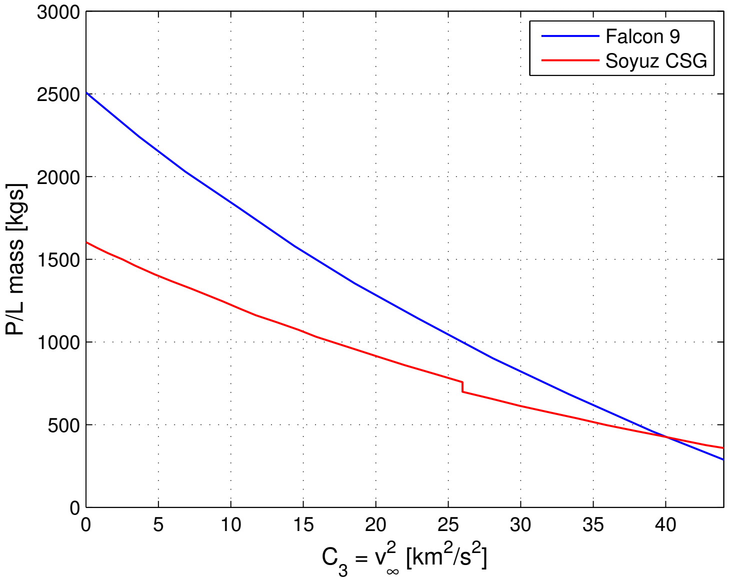

Figure 5.4: Interplanetary launch capabilities as a function of the C_3 energy for Falcon 9 and Soyuz CSG

For comparison, Nasa's Dawn spacecraft, which recently visited the dwarf planet Ceres using 3 NSTAR gridded ion thrusters and achieved a record cumulated Δv of 14km/s, had a wet mass of 1240 kg with 425 kg of Xenon propellant, a dry spacecraft mass of 815 kg and a solar array of 36.4m^2 able to deliver 10kW at 1AU. For more details on the spacecraft bus architecture, the reader can refer to Appendix C.

5.2 Demonstration mission to a binary asteroid system

In recent years, a demonstration mission called AIDA was proposed to demonstrate the Kinetic Impactor concept. IAs illustrated on Fig. 5.5, AIDA aims at hitting the secondary asteroid of the Didymos system, called Didymoon, and measuring the resulting change in orbital period. The expected variation of the orbital period that can be measured from Earth is 0.6% of the nominal period.

In this section we propose an alternative small size demo mission to prove the effective-

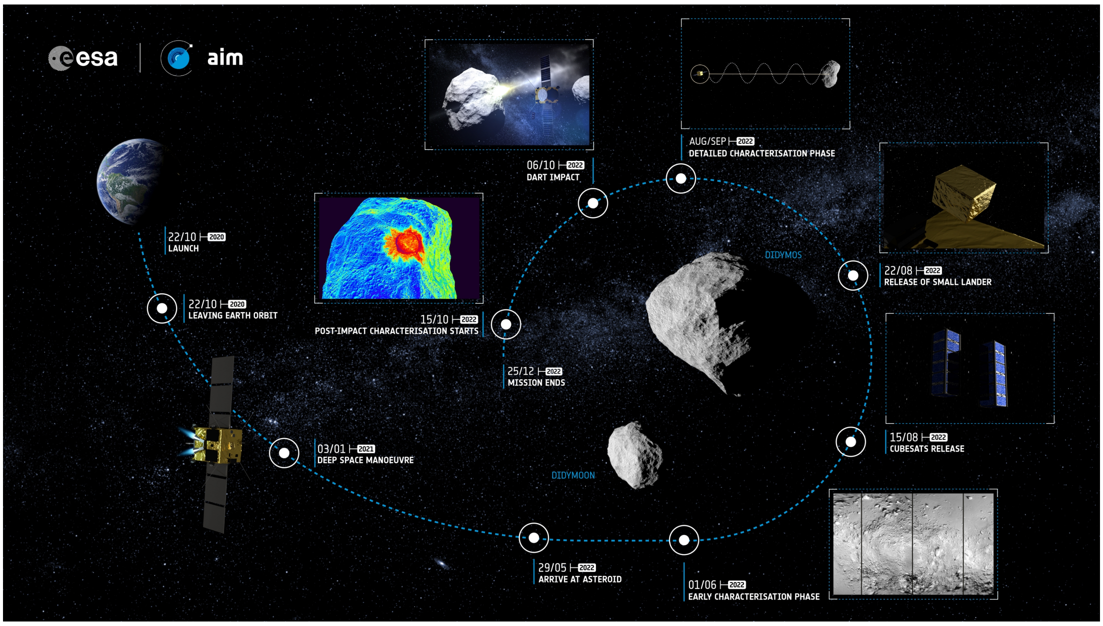

Figure 5.5: original AIDA mission concept (image: ESA)

ness of laser ablation at deflecting medium to small size asteroids. As for AIDA, the goal is to change the orbital period of the secondary asteroid of the Didymos system. Unlike AIDA, the change in momentum is achieved with laser ablation instead of an impactor. The spacecraft design could ne based on the Light Touch^2 mission concept developed under ESA contract by Vasile et al. (2013). The spacecraft is positioned at one of the two Lagrangian points (either L4 or L5) of the Didymos system.

5.2.1 Spacecraft Dynamics and Control

The equations of Motion in a co-rotating frame write:

$$\begin{aligned}
\ddot{x} - 2\dot{y} - x &= -\frac{(1-\mu)(x-\mu)}{r_1^3} - \frac{\mu(1-\mu+x)}{r_2^3} \\
\ddot{y} + 2\dot{x} - y &= -\frac{(1-\mu)y}{r_1^3} - \frac{\mu y}{r_2^3} \\
\ddot{z} &= -\frac{(1-\mu)z}{r_1^3} - \frac{\mu z}{r_2^3}
\end{aligned}$$

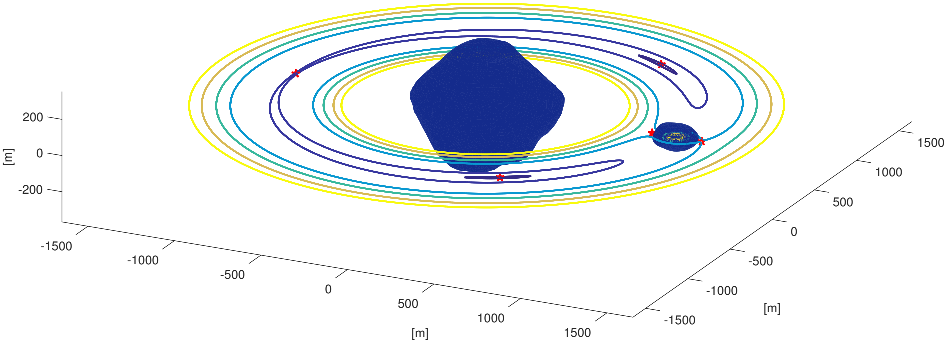

Figure 5.6: Zero velocity curves and libration points for the Didymos system

With μ the mass parameter equal to 0.0066. The Jacobi integral C is given by

$$C = \frac{1}{2}v^2 - \frac{1}{2}(x^2 + y^2) - \frac{1-\mu}{r_1} - \frac{\mu}{r_2}$$

Setting v=0 in the previous allows to compute so-called zero-velocity curves which are bounding the region of allowed motion. In absence of perturbation, there are 5 equilibrium points: 3 co-linear are unstable (L1, L2 and L3); 2 equilateral points (L4 and L5) are stable, represented by the red crosses on Fig. 5.6 Approximation of families of stable orbits can be found by linearizing the equations around the triangular points:

$$\begin{bmatrix} \delta\dot{x} \\ \delta\dot{y} \\ \delta\dot{z} \\ \delta\dot{u} \\ \delta\dot{v} \\ \delta\dot{w} \end{bmatrix} = \begin{bmatrix} 0 & 0 & 0 & 1 & 0 & 0 \\ 0 & 0 & 0 & 0 & 1 & 0 \\ 0 & 0 & 0 & 0 & 0 & 1 \\ \frac{3}{4} & \frac{\sqrt{27}(0.5-\mu)}{2} & 0 & 0 & 2 & 0 \\ \frac{\sqrt{27}(0.5-\mu)}{2} & \frac{9}{4} & 0 & -2 & 0 & 0 \\ 0 & 0 & -1 & 0 & 0 & 0 \end{bmatrix} \begin{bmatrix} \delta x \\ \delta y \\ \delta z \\ \delta u \\ \delta v \\ \delta w \end{bmatrix} + \text{H.O.T.}$$

When $\mu < 0.0397$, the system possesses 3 complex conjugate eigenvalues with negative real parts, meaning that the system possesses 3 stable real modes. To the 3 stable modes, correspond 3 families of orbit (2 in-plane H1/H2 and 1 vertical V1, see Fig. 5.7) around L4/L5. Any small displacement from the equilibrium yields to a bounded oscillation in the 3 modal directions. Closed orbits for larger displacements can be found using numerical methods and the linear solution as an initial guess.

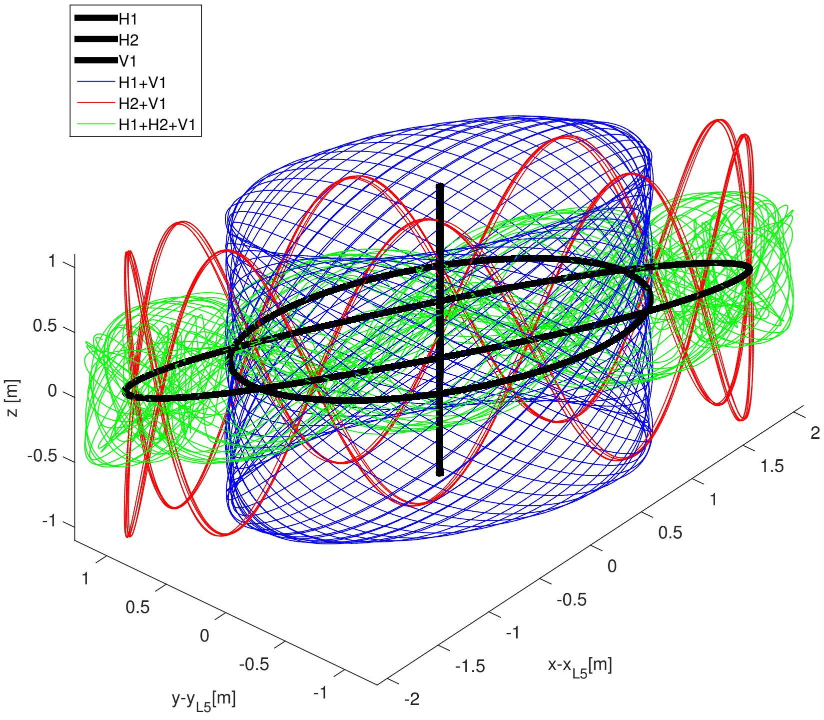

Figure 5.7: Families of orbit around L4/L5

5.2.2 Increase or Decrease of the Asteroid spin-rate

Assuming a perturbing force T is acting in the azimuth direction on the secondary, the variation of the orbit can be computed from the following equations:

$$\ddot{\theta} = \frac{T}{m_2 r} - \frac{2\dot{r}\dot{\theta}}{r}$$
$$\ddot{r} = -\frac{\mu}{r^2} + r\dot{\theta}^2$$

The perturbing force is generated by the ablation process induced by the laser hitting the secondary. The optics focusing the laser beam is assumed to be optimised to deliver a thrust coupling of $50\mu N/W_{opt}$, accounting also for possible loss due to the shape irregularity of the asteroid and the fact that the laser ablation thrust can only be oriented in the desired direction tangential with respect to the asteroid trajectory on average. Disturbing effects from the Sun on the motion of the secondary are assumed to be negligible and the gravity of the primary is assumed to be spherical as a first approximation. This means that no coupling between rotation and orbit motion of the secondary are considered.

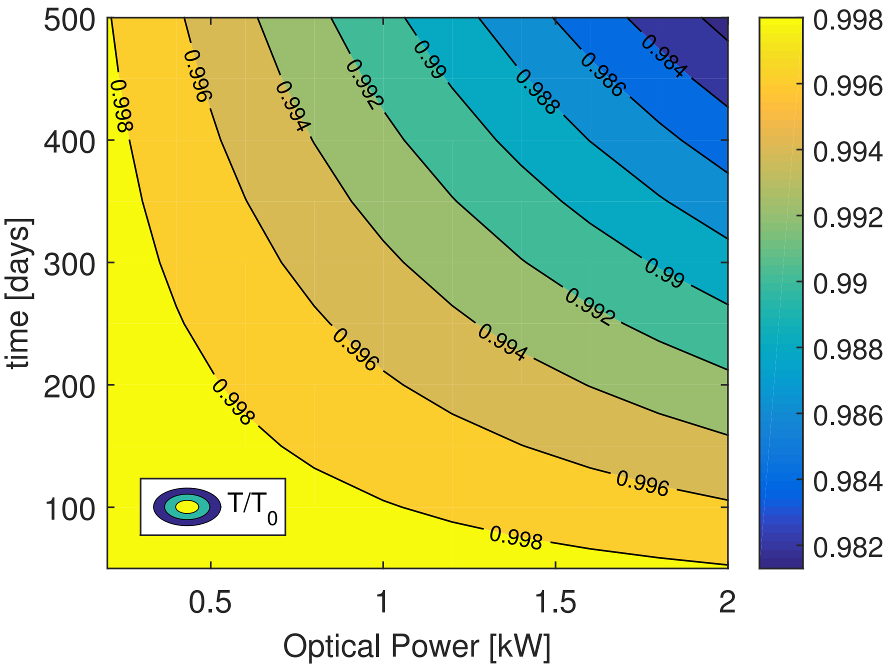

Figure 5.8: Variation of the orbital period as a function of the installed optical power

The AIDA mission expected a period reduction of 0.6% post-kinetic impact. Fig. 5.8 shows the variation of the orbit period induced by a laser with a given optical power ablating for a given period of time. The figure shows that a 1kW laser spacecraft could achieve the same orbit period variation expected by AIDA in less than 1 year. A 1kW optical power can be achieved with less than 3kW of installed power (Vasile et al., 2013). This figure is acceptable for a low-thrust mission and is reasonable even for a chemical mission in deep space. Furthermore, it is important to note that the required variation of the orbit period in AIDA was motivated by the observability of this change from ground. However, it was demonstrated that in situ observations can provide a continue monitoring of the change in orbit velocity with higher accuracy (Vetrisano et al., 2016). This result would allow the installation of a smaller laser operated for shorter period of time.

5.2.3 In-situ observation of the Asteroid composition

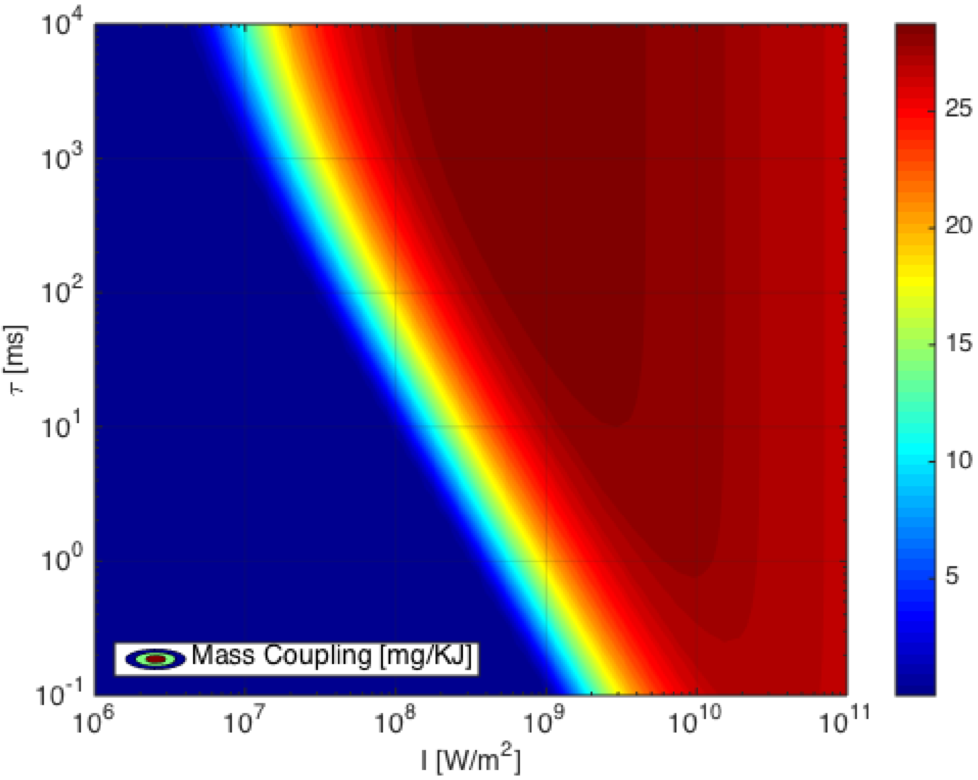

Figure 5.9: Mass flow as a function of the installed optical power

The mass removal during the ablation process will allow one to analyse the different compounds at different locations of the asteroid surface, using, for example, a Raman spectrometer. This analysis process can provide unique information on surface and subsurface composition of the secondary. Fig. 5.9 shows the mass flow as a function laser intensity and exposure time. The figure shows that with 1kW of optical power, a mass ejection rate > 25mg per second is to be expected.

Chapter 6

Statistical multi-criteria comparison between laser ablation and other non-nuclear deflection methods

The effectiveness of the laser ablation method is compared against the kinetic impactor, Ion beaming, and the gravity tractor methods in a wide range of virtual collision scenarios. A simple but realistic model of each deflection method was integrated within a systematic top-down approach to size the spacecraft and predict the achievable deflection for a given mission profile and a given maximum mass at launch. A sample of 100 synthetic asteroids was then created from the current distribution of NEAs and global optimisation methods were used to identify the optimal solution in each case according to two criteria: the minimum duration between the departure date and the time of virtual impact required to deflect the NEA by more than two Earth radii and the maximum miss-distance achieved within a total duration of 10 years. Our results provide an interesting insight into the range of applicability of individual deflection methods and argue the need to develop multiple methods in parallel for a global mitigation of all possible threats.

6.1 Asteroid Sampling Strategy

This section explains how we selected the asteroids forming the test set to compare the performance of different deflection methods. In previous works (Sanchez et al., 2009), the authors proposed a comparative analysis of several deflection methods considering a limited number of representative PHAs. A larger set of representative PHAs is considered in this new evaluation. To ensure that the choice of asteroid does not introduce a possible bias towards a given method, this sample of 100 synthetic PHAs is created from the current distribution of known NEAs. In all cases, the argument of perigee of the orbit of the PHA is modified so that the virtual asteroid crosses the ecliptic plane at a distance of 1AU from the Sun. A fixed asteroid mass of 4×10^9 kg is considered throughout this chapter (unless otherwise stated), which corresponds to an estimated diameter of 156m identical the size of asteroid 2011AG5 which was previously considered by NEOSHIELD and is also comparable to the size of Didymoon which will be the target of the AIDA demonstrator mission. Note that, in the original publication by the author (Thiry and Vasile, 2016), a larger impactor size of of 212m (10^{10}kg), was also considered. However, as the asteroid size did not impact the overal comparison results, only the 156m case will be presented in this chapter.

6.1.1 PHA Distribution

As in the work of Bach, the undeflected motion of the PHAs considered in this work is approximated by Keplerian orbits in a heliocentric frame and the Earth orbit is approximated with an exact circle of radius 1AU. Intuitively, this simplification induces two necessary but not sufficient conditions on the semi-major axis a and eccentricity e for impacting PHAs:

$$a(1-e) < 1 \text{ AU and } a(1+e) > 1 \text{ AU} \tag{6.1}$$

Using the criterion in Eq. (6.1), we extracted 8273 Earth-crossing NEAs from the NEODyS database presently maintained at the University of Pisa[1]. The distribution

---

[1] `http://newton.dm.unipi.it/neodys`

of these NEAs can be seen on Fig. 6.1 where the green lines represent the necessary crossing condition of Eq. (6.1).

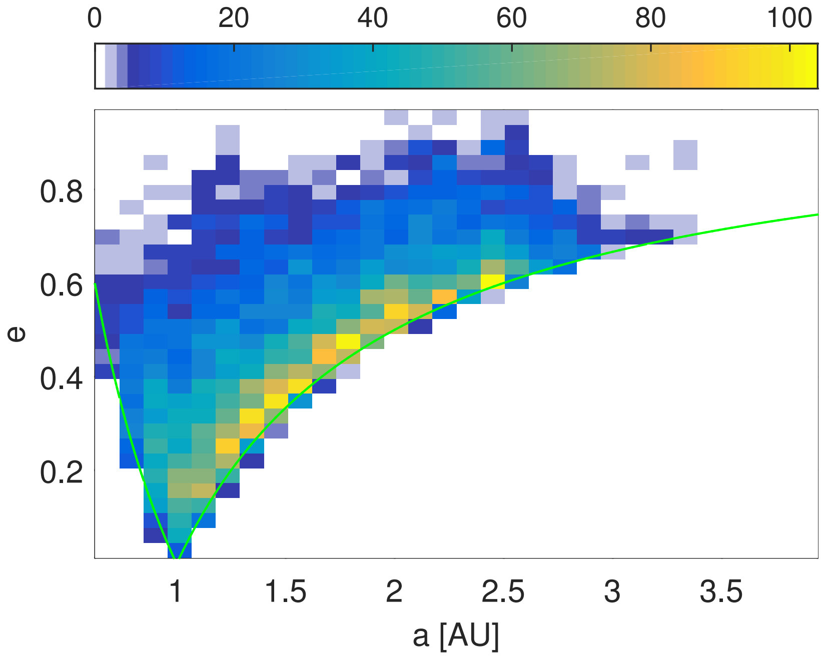

Figure 6.1: Distribution in semi-major axis and eccentricity of all known NEAs with an orbit crossing the heliocentric sphere of radius 1 AU

6.1.2 Virtual Impactor Model

Fixing the semi-major axis, eccentricity and inclination with their actual value from the extracted database, one independent element remaining to fix is the longitude of the ascending node node Ω of the PHA's orbital plane with respect to the ecliptic. However, since we neglect the small minute Earth orbit eccentricity, the impact epoch is arbitrary and we can choose to fix $\Omega = 0$ so that the PHA's orbital planes crosses the ecliptic along the vernal equinox direction. The last parameters to fix are the argument of perihelion ω and the true anomaly θ of the PHA at the impact epoch t_{MOID}. From the above simplifications, the argument of perihelion and the true anomaly may only adopt two distinct values to respect the impact condition:

$$1\text{AU} = \frac{a(1-e^2)}{1+e\cos\omega} \text{ and } \theta = 2\pi - \omega \tag{6.2}$$

The two solutions of Eq. (6.2) correspond to an impact with the ascending or the descending branch of the PHA respectively.

6.1.3 Sampling Strategy

We formed a sample of virtual impactors by randomly selecting 100 PHAs in the NEODyS database, using the method described in Sec. 6.1.2 and considering an equal probability of impact with the ascending or the descending branch of the PHAs. The distributions in semi-major axis, eccentricity and inclination of this test sample are plotted for further reference in Fig. 6.2.

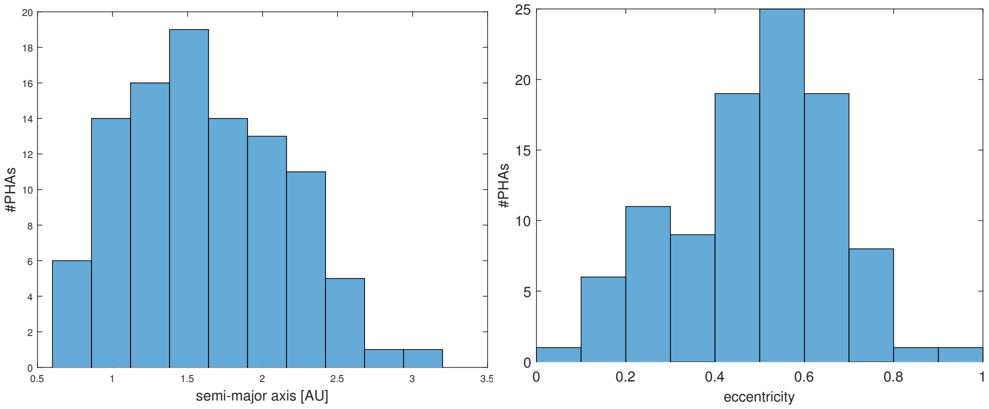

(a) semi-major axis (a)

(b) eccentricity (e)

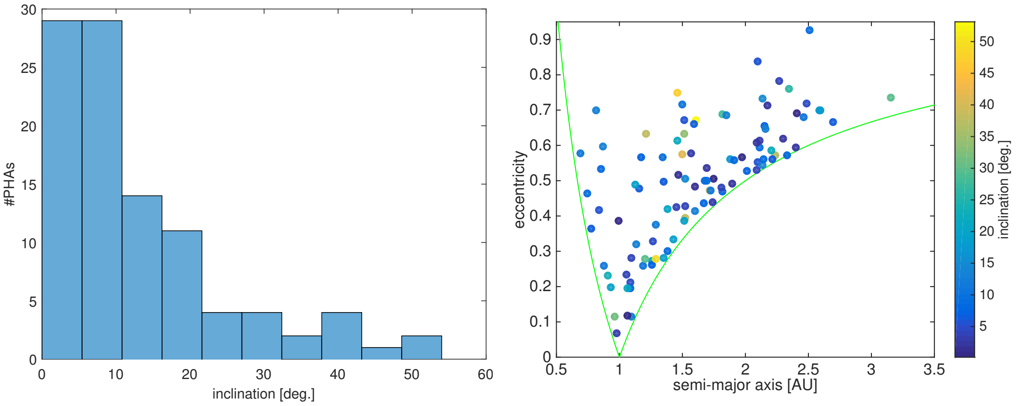

(c) inclination (i)

(d) a-e-i sample distribution

Figure 6.2: Distribution of the 100 PHAs randomly sampled from the NEODyS database

6.2 Deflection Methods

The deflection methods selected for the comparison in this chapter are: the kinetic impactor, the laser ablation, the ion beaming technique and the gravity tractor. For the kinetic impactor we will put to the test the simplest variant with highest technology readiness and direct injection in transfer orbit with the launcher. As for the gravity tractor, the halo orbit configuration is considered.

In addition to include additional methods such as the Ion Beam Shepherd and Laser ablation, the methodology in this chapter also differs from Sanchez et al. (2009) in that the deflection models are integrated with a revised system sizing (which includes the transfer to the asteroid) approach to quantify the mass breakdown of the spacecraft for the assumed launcher performance and predict the achievable deflection for a given epoch. The launcher considered is Delta 4 Heavy RS-68A upgrade version with a maximum interplanetary launch capability of 10 mt (for a $c_3 = 0$ km^2/s^2). The available system mass after the transfer to the target asteroid is used to assess the size of the deflection subsystem and thus evaluate the achievable deflection in the time remaining before the virtual impact with the Earth. For the case of the kinetic impactor, a direct injection ($c_3 > 0$) using a multiple-revolution Lambert arc is considered. For the case of slow-push methods, a low-thrust transfer with solar-electric propulsion is retained in order to take advantage of the large electrical power available which would otherwise remain unused during this transfer phase.

The following subsections provide a review of the assumptions to model each deflection methods considered as part of this assessment.

6.2.1 Kinetic Impactor

The idea of the kinetic impactor is to impart a slight alteration in the velocity of an asteroid by colliding a spacecraft into it at high speed. The simplest version of this deflection concept assumes a direct injection (single impulse) into an interception trajectory (with a given c_3) from the Earth to the asteroid. This interception trajectory is calculated as the solution of a multi-revolution Lambert arc. Therefore, the mass $m_{s/c}$ of the spacecraft and its relative velocity $\delta v_{s/c}$ at the deflection date t_d are a function of both the time of flight ToF and departure date t_D from the Earth as well as the interplanetary injection capability of the launcher. Figure 6.3 shows the launch capability of the Delta 4 Heavy RS-68A upgrade version, considered throughout this chapter, as a function of the c_3 escape energy (in km^2/s^2).

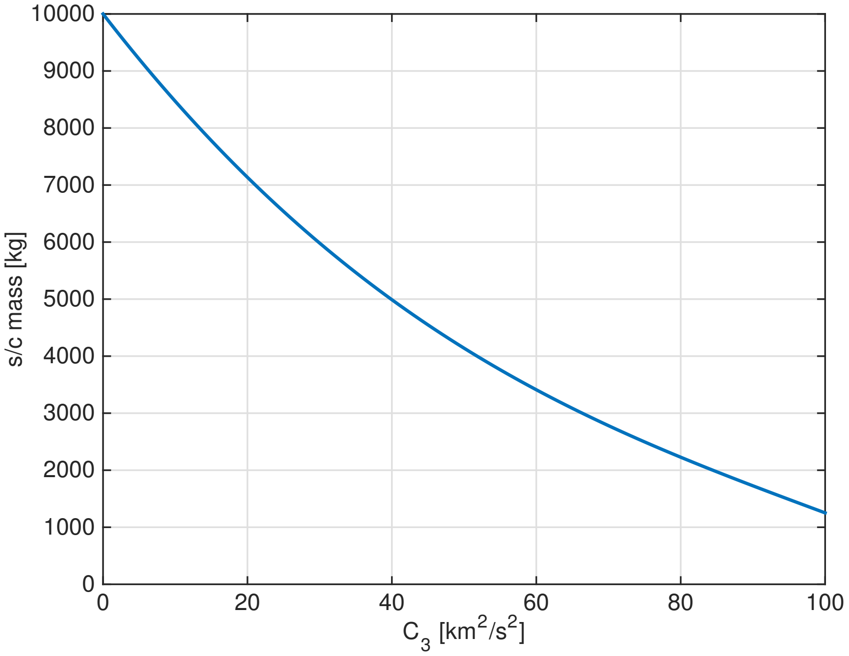

Figure 6.3: Spacecraft mass $m_{s/c}$ as a function of the c_3 escape energy from the regression laws of Wise et al. (2010) for the Delta IV Heavy - RS-68A upgrade version

The variation of velocity imparted by the spacecraft to the asteroid is then computed with a simple conservation of momentum equation, assuming a momentum enhancement factor $\beta = 1$:

$$\delta v = \beta \frac{m_{s/c}}{m_a} \delta v_{s/c} \tag{6.3}$$

Once the variation of the velocity is available, formulae (4.2) to (4.15) can be used to derive the modified asteroid orbit and to compute the impact parameter. As an illustrative example, Figure 6.4 shows the achieved impact parameter b as a function of departure date and time of flight considering a kinetic impactor injected into a transfer orbit by a Delta 4 Heavy rocket to a virtual version of 2011AG5[2].

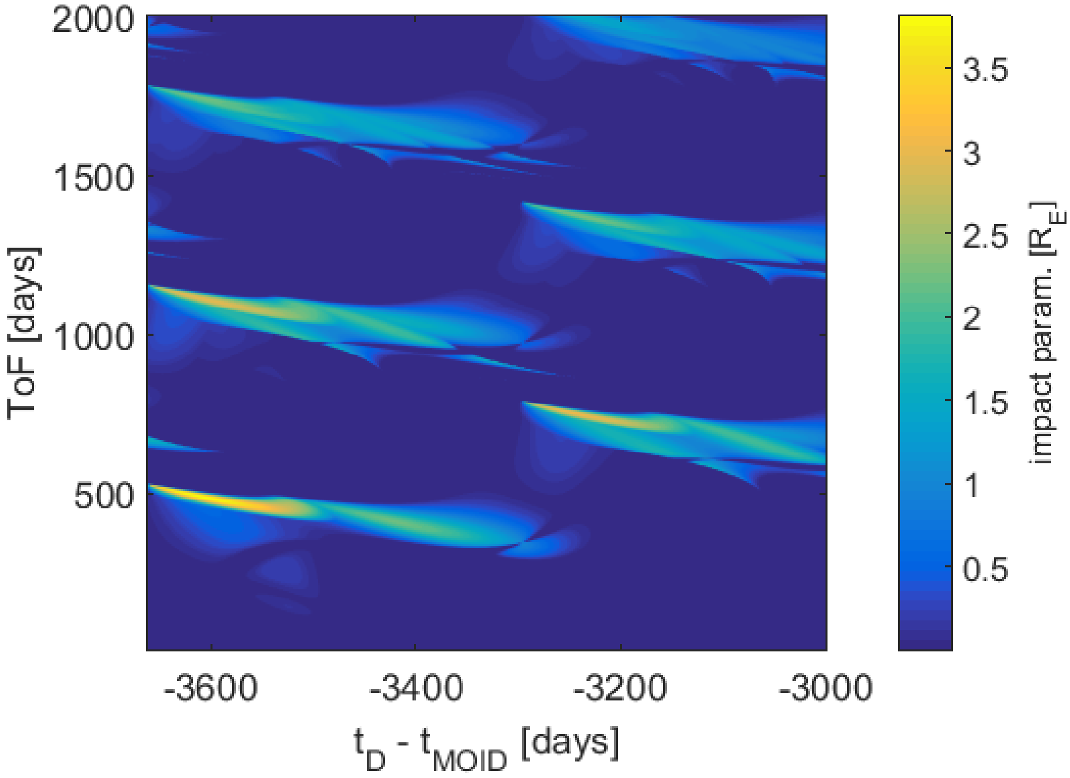

Figure 6.4: Impact parameter as a function of the departure date t_D and time of flight ToF for 2011AG5

6.2.2 Slow-push methods

Unlike the Kinetic Impactor method, for which a direct injection on an intercept course was considered, slow-push methods considered in this work require to rendez-vous with the asteroid. A low-thrust transfer trajectory from the Earth (considering an initial $c_3 = 0$) is considered in the case of these method, which allows using the electric propulsion system also during the transfer phase. The spherical shaping method introduced in the work of Novak and Vasile (2011) is used to compute low-cost, low-thrust trajectories

---

[2] See section 6.1 for more details on the virtual asteroid models

as a function of the ToF and departure epoch for the the mission. An example of calculated trajectory to asteroid 2011AG5, requiring a Δv of 7.8 km/s is shown in Fig. 6.5.

Considering an I_{sp} of 3000 s and given a departure mass, our algorithm returns the mass at arrival but also the maximum thrust and power required to realise this transfer. From this information, the mass required for the electric propulsion subsystem (EPS), power systems and radiators can be computed, assuming Solar Electric Propulsion as a primary power source (SEP). In the case of the gravity tug and IBS methods, an oversising coefficient is also considered, which can vary between 1 and 10. This oversising coefficient is defined as the ratio between the thrust available for deflection phase and the maximum thrust required to realize the transfer trajectory computed. It allows one to increase the thrust that can be generated during the later deflection phase but also penalises the amount of propellant mass that will be available during the deflection phase since more mass needs to be allocated to the different subsystems.

In line with the predicted performance of Orbital ATK's UltraFlex and Megaflex arrays, we consider a specific array mass of 10 kg/kW throughout this study, scaling with the power required at 1 AU. An additional 5 kg/kW, scaling with the peak power at perihelion, models the other components of the power subsystem, including PCDU.

Similarly, the Electric Propulsion Subsystem (EPS) is modelled with three core elements, whose mass vary as a function of the maximum thrust and input power:

1. Thruster assembly which includes in this case the thrusters and the gimbals on which they can be mounted to control the thrust orientation. A specific mass of 2 kg/kW together with a thrust to power ratio of 46 mN/kW are considered in the calculations and the thrusters are sized with respect to the peak thrust delivered during mission.

2. Power Processing Unit (PPU) which supplies the high voltage current required for the ion engines to work efficiently. The Thruster Selection Unit (TSU) itself allows to select the thruster fed by the PPU. The PPU/TSU is assumed to scale with the peak power during the mission with a specific mass amounting to 6 kg/kW.

3. Xenon Feed System (XFS) or Flow Control Unit (FCU) which usually includes a high pressure tank, a Xenon Control Assembly (XCA) which regulates the pressure and Xenon flow rate to the thrusters and the plenum tanks. The mass of the XFS is assumed to scale with the peak thrust with a specific mass of 1 kg/kW, which excludes the Xenon tank which itself is assumed to scale linearly with the propellant mass. The Dawn Xenon tank had a volume of 269L, could store up to 425 kg of Xenon and had a mass of 21.6 kg, giving a tankage fraction of 5%.

Parametric mass models are again considered for the other subsystems, including harness (5% of the wet mass), structure (20% of the launch mass), AOCS (5% of the wet mass), as well as a non-scalable mass of 50 kg to telecommunications and data handling. Radiators are also scaled with respect to the maximum available power, considering a heat sink of 50% of the available power, ability of the radiator to re-radiate 400W per square meter and an areal density of 5 kg/m^2.

Eventually, any remaining mass is allocated to the additional propellant (Gravity Tug and IBS methods) or the Laser system (Laser ablation method) that will be used during the deflection phase . If no mass is left prior to that step, the mission is considered infeasible with that particular combination of departure date, time of flight and oversizing coefficient.

For all methods, the deflection phase starts as soon as the spacecraft has rendezvoused with the PHA. The acceleration on the asteroid is assumed to be mparted in the tangential direction in average and is computed by

$$u_t = \frac{F_{method}}{m_{\mathrm{A}}} \tag{6.4}$$

In this equation, m_A is the mass of the asteroid and F_{method} the thrust delivered by the deflection system, which depends on the strategy considered. The thrust models already introduced in chapter 6.1 are recalled in table 6.1.

The parameters considered in these models are explained hereafter:

- For the IBS method, it is assumed that the engines work at the maximum of

Method	Ion Beam Shepherd (IBS)	Gravity Tractor (GT)	Laser ablation (LA)
F_{method}	$F_{IBS} = C_{HET}\frac{P_{in}}{2}$	$F_{GT} = \tau\frac{Gm_{GT}}{R_a^2}$	$F_{LA} = \eta_{LA}C_m P_{in}$

Table 6.1: Thrust models for each slow-push deflection method

their capability given the available power generated by the solar arrays P_{in}at the current distance from the sun. A thrust to power ratio (C_{HET}) of 46 mN/kW is considered. Only half of the thrust can be used for the deflection as the other half is needed for station-keeping of the IBS.

- For the GT method, the halo configuration introduced in 4.2.3 is considered, with an assumed divergence angle of 10° for our comparison. In the work of Sanchez et al. (2009), an optimised slanted configuration was considered instead. Practically speaking, the model for the GT method is very similar to IBS model except that it also considers a time-dependent maximum tugging thrust during the integration of the deflected orbit. This tugging thrust is computed considering the evolution of the mass of the spacecraft over the course of the deflection maneuver and a τ factor of 0.3. Compared to the IBS method, the sizing model also considers that engines are only required on one side of the GT (for station keeping) contrary to the IBS which requires engines on both sides of the spacecraft. Therefore, the GT method is more efficient in term of propellant consumption than the IBS method but has a maximum thrust limited by the mass of the spacecraft whereas in the case of the IBS method, this deflection thrust only depended on the engine onboard.

- For the LA method, conversion from input power to ablative thrust F_{LA} depends on the input power P_{in}, the electrical to optical (E/O) conversion efficiency of the laser system η_{LA}, and C_m, the thrust coupling coefficient, which is known to vary between 10 to 100 μN/W$_{optical}$ for most materials (Phipps, 2011). E/O efficiencies >39% have already been demonstrated by multi-kW spectrally beam combined fiber-coupled diode lasers (Honea et al., 2013). Focused development under the DARPA SHEDs program has also lead to extremely high power conversion efficiency in the 9xx-nm wavelength band, leading to diode bars with efficiency in excess of 74% and a clear route to efficiencies superior to 85% at room temperature (Crump et al., 2007). With demonstrated slope efficiency of optical fibers on the order of 80% (Jeong et al., 2004) and a demonstrated efficiency of spectral beam combining techniques of 91% (Drachenberg et al., 2011), we consider here a global E/O efficiency of 50%, as already assumed in the previous chapter. With reference to Fig. 3.14, one can see that for typical mean heating times on the order of 10–100 ms and typical CW laser beam intensities on the order of 1 GW/m^2 envisioned in our laser system, the thrust coupling has an expected value around 55–60μ N/W. This value will only be weakly affected by the temporal changes in operating conditions due to the variation of input power with respect to the square distance to the sun. To generate the intensity levels required, the optics should be designed using the diffraction limit focusing capability at the shooting distance. The optical components should also be designed so that they are exposed to intensity levels well under their damage threshold. As an example, an optics with a primary mirror of 60cm diameter would be enough to generate a 3 mm laser spot at a 1km shooting distance. For a 10 kW laser, this would correspond to an intensity of 1.4 GW/m^2 at the focal spot, but only 35 kW/m^2 on the primary mirror. With these considerations in mind, an effective value of 40 μN/W for the thrust coupling coefficient is used in the calculations. This is a conservative value taking also into account possible losses due to the shape irregularity of the asteroid and the fact that the laser ablation thrust can only be oriented in the desired direction tangential with respect to the PHA trajectory in average. In fact, as explained by Vetrisano et al. (2015, 2016) a smart laser steering strategy would allow to improve further the thrust directional efficiency. With comparatively larger distances than considered in the previous chapters, contamination is not expected to play a dominant role in the results. Furthermore, as shown in the ESA LightTouch2 study Vasile et al. (2013), by properly positioning the spacecraft with respect to the asteroid, aligning the arrays with the plume and adding Whipple shields the effect of contamination could be mitigated to the point that it can be considered negligible over the lifetime considered in this paper.

Knowing the acceleration on the asteroid, the modified orbit can be integrated and the miss-distance can be computed following the procedure detailed in section 4.1.2. The time of the end of the application of the deflection action is set to the time of the virtual impact t_{MOID} although if, at some point during the deflection, the propellant allocated to the deflection action goes to zero, the deflection action terminates and a null acceleration is considered for the remaining part of the integration.

Considering a wet mass of 1000 kg, the transfer of Fig. 6.5, as well as an oversizing factor of 1, Fig. 6.6 illustrates the resulting mass budget. The IBS spacecraft for this particular scenario would be able to generate a nominal thrust (in deflection mode) of 110 mN and nominal input power level of 4.78 kW at a distance of 1 AU from the Sun. Considering the same scenario as for the IBS, a summary of the mass budget considering a wet mass of 1000 kg is given in Figure 6.7 for the laser ablation method. For this specific case, the laser system would deliver an estimated nominal ablative thrust of 148 mN and nominal input power level of 7.4kW at a distance of 1AU from the Sun. For comparison, NASA's Dawn spacecraft, which recently visited the dwarf planet Ceres using 3 NSTAR gridded ion-thrusters and achieved a record cumulated Δv of 14 km/s, had a wet mass of 1240 kg with 425 kg of Xenon propellant, a dry spacecraft mass of 815 kg and a solar array of 36.4 m^2 able to deliver 10.3 kW at 1 AU.

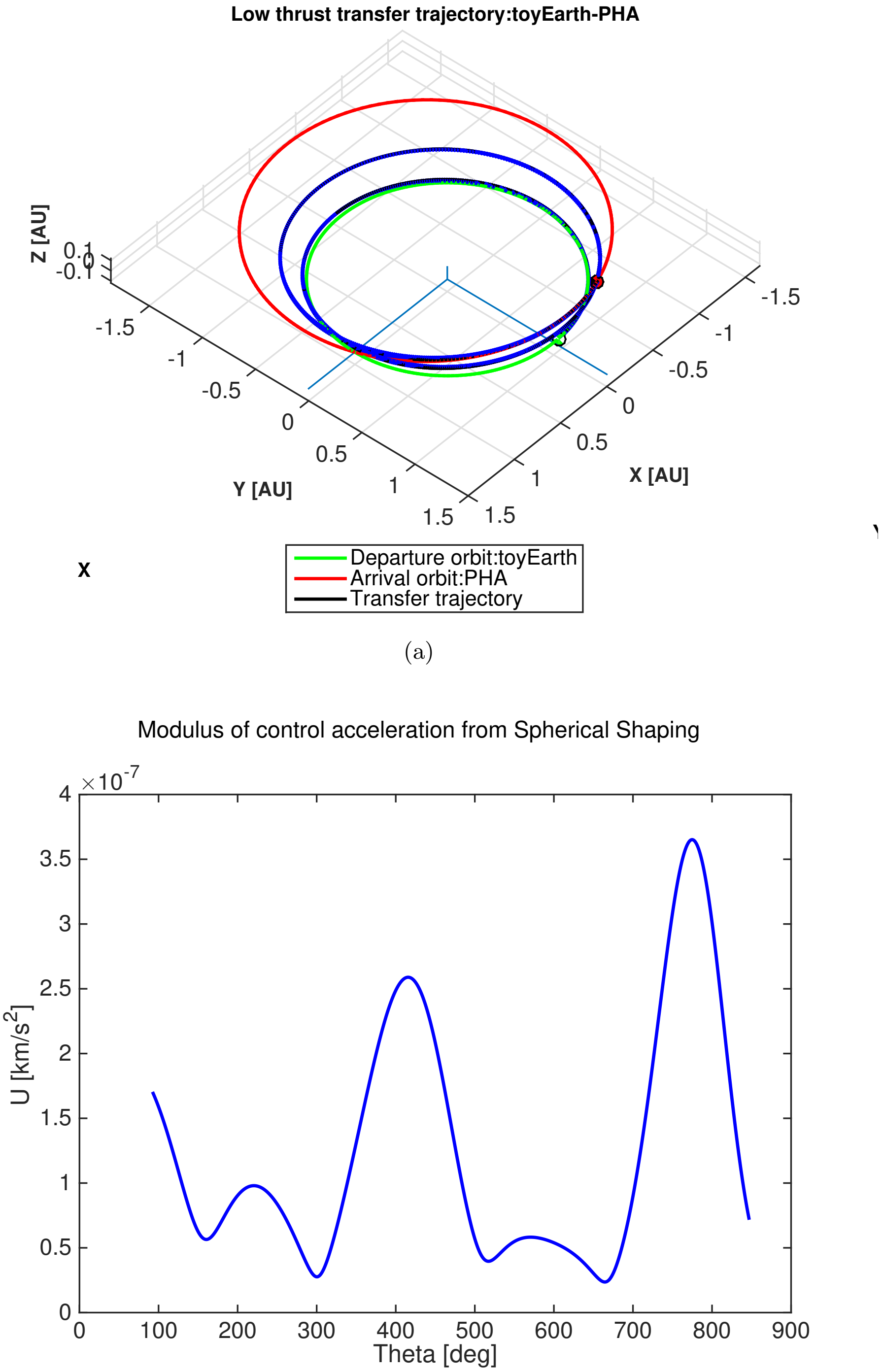

(a)

(b)

Figure 6.5: Example of calculated low thrust transfer trajectory and modulus of the control acceleration with the spherical shaping method for $ToF = 847$ days and $t_D = -3615$ days before virtual impact with 2011AG5

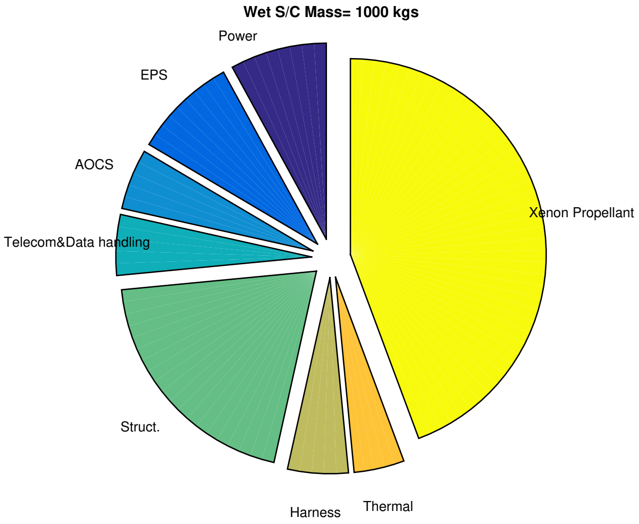

Figure 6.6: IBS mass budget for $ToF = 847$ days and $t_D = -3615$ days before virtual impact with 2011AG5 and an oversizing factor of 1

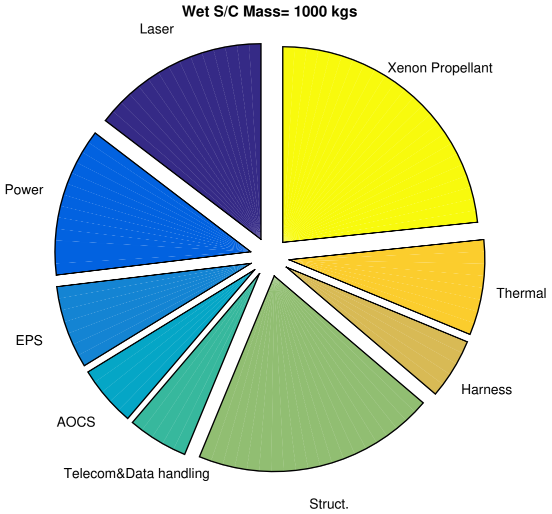

Figure 6.7: LS mass budget for $ToF = 847$days and $t_D = -3615$ days before virtual impact with 2011AG5

6.3 Global Optimisation Strategies

The optimisation of the deflection strategies requires the global exploration of the parameter space. Furthermore, it is desirable to investigate the trade-off between warning time and achievable miss distance. For this reason we used two global optimisation procedures one for single objective and the other for multi-objective optimisation of multi-modal functions: MP-AIDEA currently maintained by Di Carlo et al. (2015) and MACS2 currently maintained by Ricciardi and Vasile (2015). In the following we briefly present how each optimisation approach works and how it was used in the context of this thesis. The general approach is summarized on Fig. 6.8.

6.3.1 Optimisation with MP-AIDEA

For all methods, the impact parameter can be computed as a strongly non-linear function of the departure date t_D and the time of flight ToF, but also the oversizing coefficient in the case of the IBS method. For each mission scenario we globally explore the space of possible departure dates, transfer times and oversizing coefficients (in the case of the IBS) with a memetic algorithm called multi-population adaptive inflationary differential evolution algorithm (MP-AIDEA).

MP-AIDEA is a multi-population adaptive version of Inflationary Differential Evolution. Inflationary Differential Evolution is based on a simple but theoretically rigorous restart rule that allows an effective evolutionary heuristic, like Differential Evolution (DE), to avoid stagnation. In MP-AIDEA a number of populations, each one composed by a number of virtual agents, evolve in parallel in search of the global optimum. At each step of evolution, each agent uses DE heuristics to move from one site to another of the solution space and evaluates a new potential solution (a new possible combination of decision variables). The basic idea is to restart the evolutionary process when the populations contract within a given area in the solution space. At every restart of the evolutionary process a local search is run from the best individual in each population.

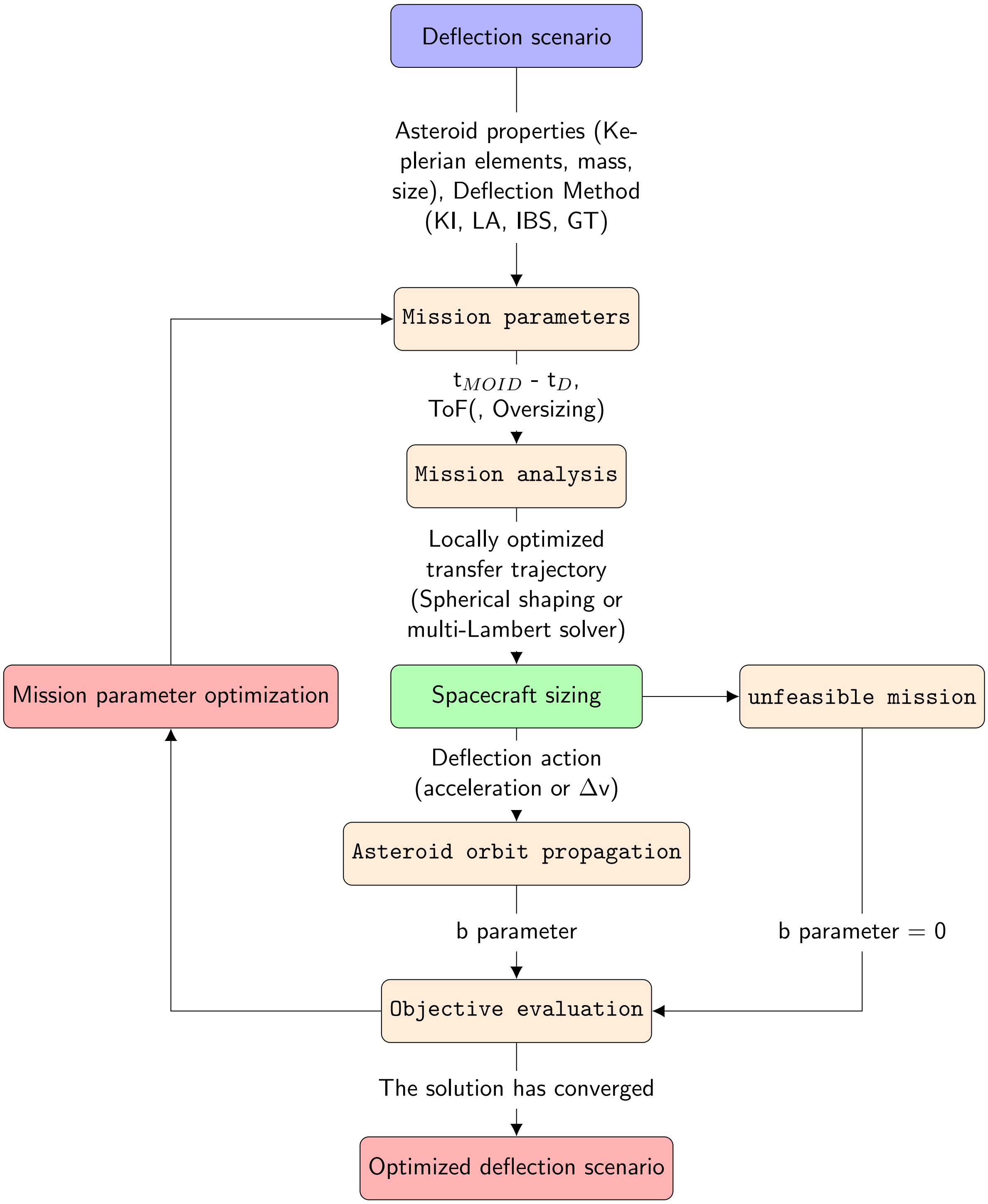

Figure 6.8: Deflection mission optimization process

All the discovered local minima are then stored in an archive. The restart process is such that the populations are initialised outside a trust region enclosing clusters of the already discovered minima in the archive. MP-AIDEA extends this concept by automatically adapting some key parameters governing the convergence of the algorithm. MP-AIDEA has been extensively tested on a range of difficult problems including real-world applications Di Carlo et al. (2019).

The decision variables handled by MP-AIDEA are the time of flight, ToF, and mission duration, $t_{mission} = t_{\mathrm{MOID}} - t_D$, and are limited by box constrains. The time of flight represents the time between mission departure from the Earth and arrival at the satellite while the mission time is the total time between Earth departure and the time of virtual impact between the asteroid and the Earth. Table 6.2 reports for each optimisation associated to each deflection method (KI=Kinetic Impactor, IBS=Ion Beam Shepherd, LA=Laser Ablation), the box constraints on the decision variables ToF and $t_{mission}$, the number of agents per population used by MP-AIDEA to search for the global optimum (#agents), the number populations (#pop) and total number of calls to the objective function (#fevals). These parameters were determined heuristically and offer a good compromise between accuracy and time of computation.

Method	ToF (days)	$t_{mission}$ (days)	#agents	#pop	#fevals
KI	[0, 1000]	[1000, 3662.42]	10	4	10000
IBS or GT	[300, 2000]	[2000, 3662.42]	15	4	1200
LA	[300, 2000]	[2000, 3662.42]	10	4	1000

Table 6.2: Parameters and box constrains used during the optimisation with MP-AIDEA

During each function evaluation, we also run an internal loop to evaluate the solution within the feasible range of number of revolutions for the trajectory computed by the Lambert solver and the spherical shaping algorithm. When more than one transfer are feasible for the combination of ToF and t_D, our fitness function only returns the solution with the number of revolution that provides the best miss-distance.

6.3.2 Optimisation with MACS2

Multi-Agent Collaborative Search (MACS2) is a memetic multi-objective optimisation framework that aims at identifying the set of Pareto optimal solutions. A solution x is said to be (weakly) Pareto optimal if there is no other solution y whose associated objectives are all better than the ones associated to x. The set of Pareto optimal solutions is called Pareto set and the set of values of the objective functions associated to Pareto optimal solutions forms the Pareto set. In MACS2 a population of virtual agents implements a number of local search heuristics intermingled by global communication heuristics that help the population to reconstruct an approximation of the Pareto set. Each agent explores a neighbourhood of the parameter (or solution) space, stores Pareto optimal solutions in an archive and shares information with the other agents in the population Ricciardi and Vasile (2015).

MACS2 was used to optimise both the mission duration and the impact parameter. Therefore, one objective function was defined as:

$$obj_1 = \begin{cases} (b - 2R_E)^2 \text{ if } b < 2R_E \\ 0 \text{ otherwise} \end{cases}$$

This definition forces the optimiser to find minimum time solutions that achieve at least a 2 Earth radii (R_E) deflection. The other objective function was defined as:

$$obj_2 = \text{ToF} + t_{defl} \tag{6.5}$$

where $t_{defl} = t_{\text{MOID}} - t_d$. Table 6.3 reports, for each optimisation associated to each deflection method (KI=Kinetic Impactor, IBS=Ion Beam Shepherd, LA=Laser Ablation), the box constraints on the decision variables ToF and t_{deflt}, the number of agents used by MACS2 to search for the Pareto set (#agents), and total number of calls to the two objective functions (#fevals) where one function call evaluates both objectives at the same time. These parameters were determined heuristically and offer a good compromise between accuracy and time of computation.

Method	ToF (days)	t_{defl} (days)	#agents	#fevals
KI	[0,1000]	[0,3662.42]	150	14000
IBS or GT	[300,2000]	[0,3662.42]	150	3000
LA	[300,2000]	[0,3662.42]	150	3000

Table 6.3: Parameters and box constrains used during the optimisation with MACS2

As an example of multi-objective optimization, we show here the Pareto fronts we obtained by considering the maximum miss-distance in minimizing the total duration from mission departure to the MOID epoch. The two asteroids considered in this case are a down-scaled version of (99942) Apophis and the actual asteroid 2011AG5 previously considered by NEOSHIELD. In both cases, the construction of the virtual impactor scenarios followed the approached detailed in section 6.1.2, considering the asteroid parameters of 6.4:

Asteroid	semi-major axis (a)	eccentricity (e)	inclination (i)	Mass
(99942) Apophis	0.92 AU	0.19	3.3 deg.	10^{10} kg
2011AG5	1.43 AU	0.39	3.7 deg.	4 $\times 10^9$ kg

Table 6.4: Parameters considered for the down-sized virtual (99942) Apophis and 2011AG5 asteroid example scenarios

The results are represented on Fig. 6.9. Interestingly, note that the Pareto optimum identified in Fig. 6.9b for a duration of 10 years is remarkably consistent with the maximum value found by evaluating the miss-distance over the entire parameter space in Fig. 6.4.

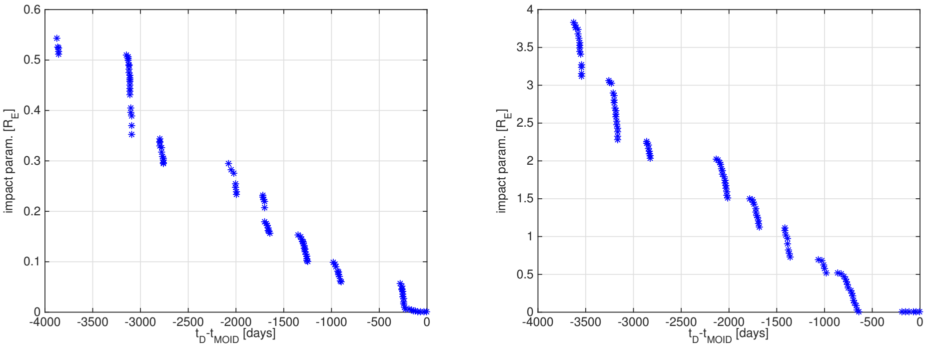

(a) Kinetic Impactor (Apophis)

(b) Kinetic Impactor (2011AG5)

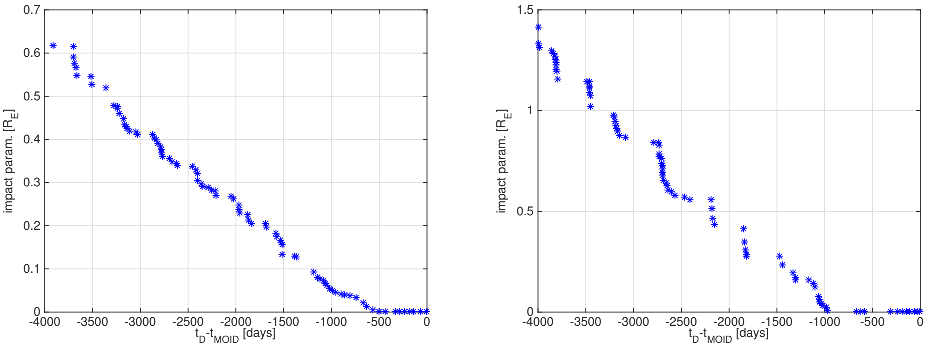

(c) Ion Beam Shepherd (Apophis)

(d) Ion Beam Shepherd (2011AG5)

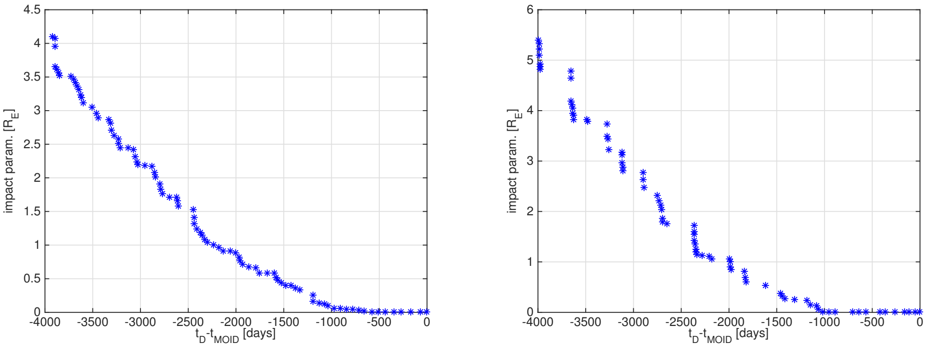

(e) Laser Ablation (Apophis)

(f) Laser Ablation (2011AG5)

Figure 6.9: Maximum miss-distance and maximum departure date for the deflection of a 10^{10} kg, 212 m diameter Apophis-like asteroid (left) and a 4 $\times 10^9$ kg, 156 m diameter 2011AG5-like asteroid (right) with a S/C launched by Delta 4 heavy

6.4 Results and Discussion

Using the methodology described in the previous section, we computed the maximum miss-distance within 10 years ($t_{\text{MOID}} - t_D < 10$ years) with MP-AIDEA and the minimum mission time ($t_{\text{MOID}} - t_D$) to achieve a miss-distance superior to 2 Earth radii with MACS2.

The results of the maximum miss-distance obtained with MP-AIDEA can be seen in Fig. 6.10 for the case of a 156 m asteroid. The Kinetic impactor outperforms the other methods in 82% of the scenarios. The laser ablation method had the edge in the remaining 18% of the cases, which corresponded to asteroids with easily accessible orbits from the Earth (low eccentricity, inclination and orbital period close to 1 year). Note that the dots on this plot have a different inclination (coming from the sample distribution in a, e, and i) so that dots with similar semi-major axis and eccentricity may not necessarily produce a similar result on this 2D plot.

The results of the minimum time to achieve a 2 Earth radii (2R_E) deflection can be seen in Fig. 6.11 for the case of a 156 m asteroid. In this plot, red points indicate non-feasible deflection solutions within a range of 10 years between departure date and MOID epoch. A total of 84 PHAs can be deflected by the Kinetic Impactor method, against 30 by the Laser Ablation strategy. Note that due to their low performance, the IBS and GT methods were not included in this second analysis. Interestingly, remark again that the KI method performs badly for a subset of virtual Impactor scenario having an orbital period close to 1 year and low eccentricity for which Laser Ablation possesses a superior deflection ability. This complementarity is highlighted if either the Kinetic Impactor or the Laser ablation can be considered. In that case, Fig. 6.11c shows that 92% of the PHAs can be deflected. The few asteroids that cannot be deflected in the prescribed time limit have an unfavourable phasing or are nearly tangent to the orbit of the Earth. Indeed, in these case we found that either the Kinetic Impactor or

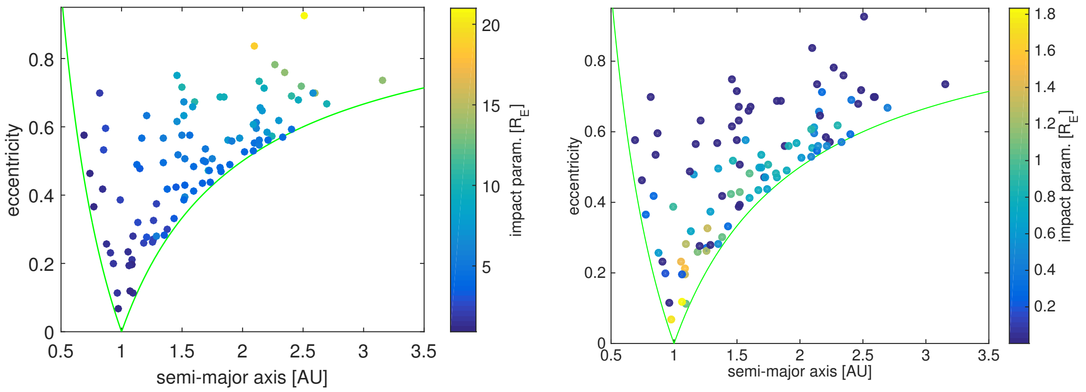

(a) Kinetic Impactor

(b) Ion Beam Shepherd

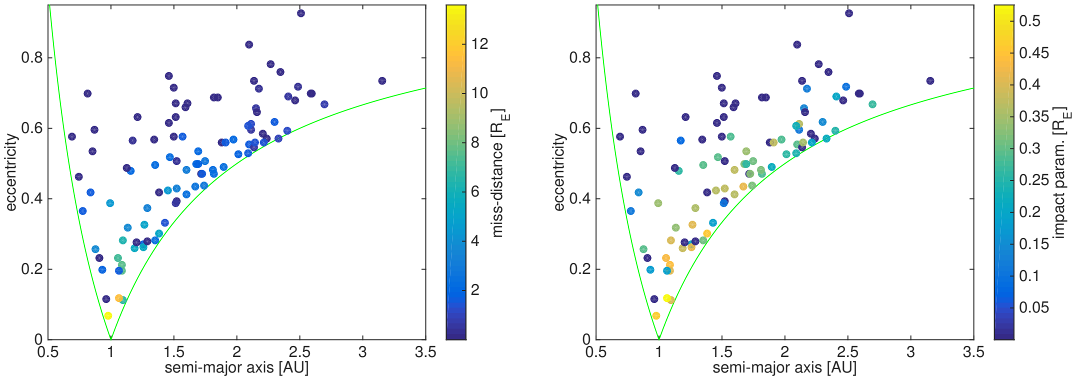

(c) Laser Ablation System

(d) Gravity Tractor

Figure 6.10: Optimal deflection of a 4×10^9 kg, 156 m diameter asteroid within 10 years of mission time

the Laser Ablation were falling short of 2 Earth radii limit although in some cases only by a few km.

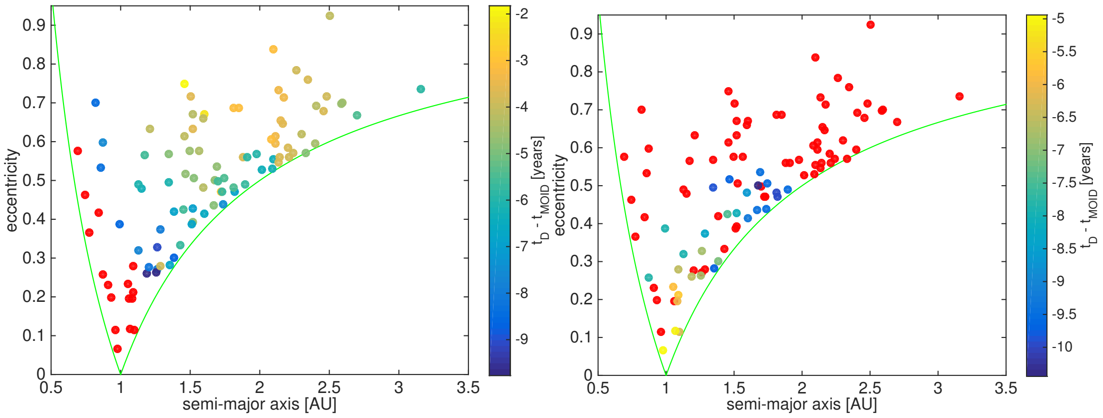

(a) Kinetic Impactor (b) Laser Ablation

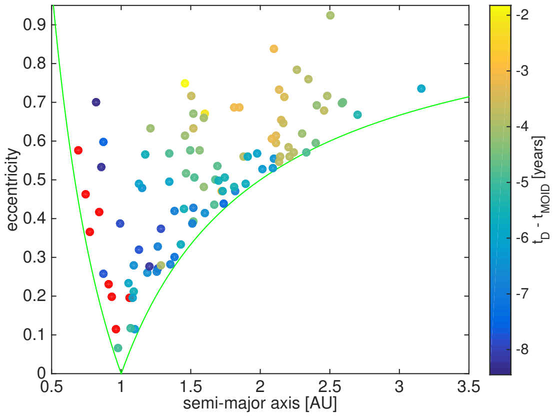

(c) Kinetic Impactor and Laser Ablation

Figure 6.11: latest departure time for the deflection of a 4×10^9 kg asteroid by 2 earth radii with a S/C launched by Delta 4 heavy. Red points indicate unsuccessful missions within 10 years

Chapter 7

Space debris removal with pulsed lasers

Despite their theoretical higher efficiency, CW lasers become unsuitable when it comes to the space debris issue. Indeed, debris components are usually made of thin layers of materials (with thicknesses typically on the order of 1mm or less). Moreover, the formation of molten bubbles in the evaporated cloud, typical of CW lasers (spallation phenomenon), must be avoided. A pulsed laser system is thus investigated in this chapter. In the first two sections, an updated laser model is introduced and discussed. This model works for very short impulse durations and debris made of a variety of materials encountered in the space industry. The impulse characteristics predicted by this model are then compared with experimental results for ablator targets made of aluminum alloys (Al 2024-T3), titanium alloys (Ti 6Al-4V) and Carbon Fiber Reinforced Polymers (CFRP). The experiments were conducted at Nagoya University (Japan) in a vacuum chamber using a pulsed solid-state laser with kHz repetition rate and a torsion pendulum. Possible applications to space debris are then presented in the remaining sections together with strategies to remove multiple objects in the high ranking hotspot regions considering a single chaser equipped with a 1-kW class pulsed laser system.

7.1 Revisited Laser Model

It was shown in chapter 3 that CW lasers become impractical to ablate thin debris components. Moreover, the formation of molten bubbles in the evaporated cloud (spallation) shall also be avoided to comply with the space debris mitigations guidelines. Fortunately, with a pulsed laser system, both these issues can be avoided as the duration of the pulses can be chosen to be much lower than the time required to dig through the object and the amount of matter ejected during each pulse. In addition, for short enough pulses, the laser system will be insensitive to the relative motion of the debris with respect to the laser beam.

The model developed in chapter 3 can be directly applied to the case of a pulsed laser by simply substituting the pulse duration in the τ parameter. Using the ablation threshold of Eq.(3.40), a non-dimensional intensity variable î can also be formed from the parameters of the problem :

$$\hat{I} = AI\tau^{1/2}\left(\frac{\pi}{4}\right)^{-1/2}\Gamma^{-1}\Delta T_{\mathrm{ref}}^{-1} \tag{7.1}$$

The results of the model for the different materials are plotted as a function of the non-dimensional intensity in figure 7.1 and compare well with experimental data. Both data sets were obtained by Rosen who studied the coupling on Al 2024-T3 Rosen et al. (1982b) and Ti 6Al-4V alloys Rosen et al. (1982a) using a XeF pulsed laser with 500ns pulses.

The previous model assumes that the ablated plume does not ionize. However, for short laser pulses, intensity levels >10TW/m^2 will occur on the targets. At these levels, ionization will occur and plasma are expected to dominate the ablated plume. Thus, a specific model to account for the plasma effects is therefore needed. The model considered in the following is based on the work of PhippsPhipps et al. (1988). In this model, the thrust coupling coefficient due to the plasma plume C$_{mp}$ is expressed as a

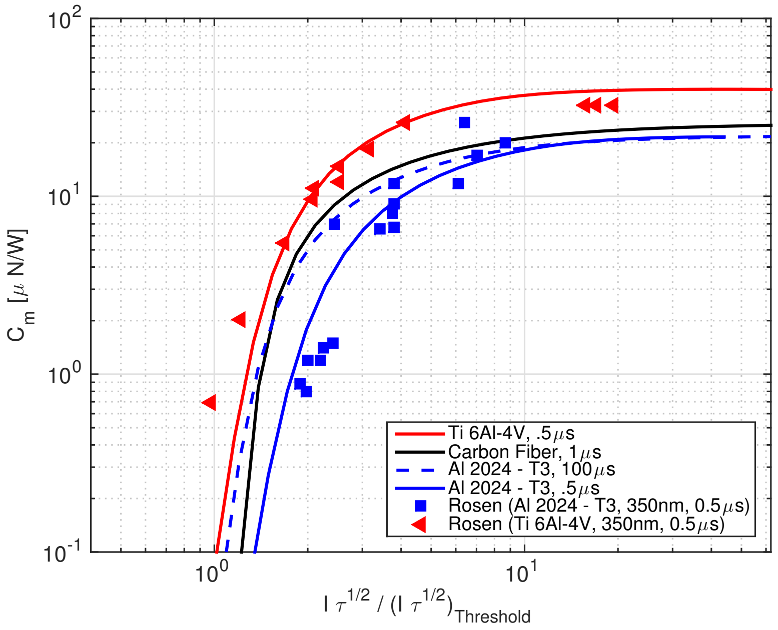

Figure 7.1: Thrust coupling as a function of $\hat{I}$ for several materials found on space debris

power law on the form:

$$C_{mp} = 1.84E-04 \frac{\Psi^{9/16}}{A^{1/8}\left(I\lambda\sqrt{\tau}\right)^{1/4}} \tag{7.2}$$

in which Ψ depends on the average atomic number A and the average ionization state Z:

$$\Psi = \frac{A}{2\left(Z^2(Z+1)\right)^{1/3}} \tag{7.3}$$

An empirical electron temperature in eV is also given by

$$T_e = 2.56 \frac{A^{1/8} Z^{3/4}}{(Z+1)^{5/8}} \left(I\lambda\sqrt{\tau}\right)^{1/2} \tag{7.4}$$

With these empirical relations, the Saha equation allows to determine the average ionization state in the plume

$$S_j = \frac{n_j}{n_{j-1}} = \frac{8.64E26}{n_e \theta^{3/2}} \frac{2u_j}{u_{j-1}} \exp\left(-\frac{\Delta E_j}{kT_e}\right) \tag{7.5}$$

Where ΔE_j is the jth ionization energy and u_j are the temperature-dependent quantum partition functions of level j. They can be computed from the Boltzmann law and knowing the degeneracies g_k of energy levels with respect to the ground ionization state

$$u_j = \sum_{k=1}^{\infty} g_k \exp\left(\frac{-\chi_{jk}}{kT_e}\right) \tag{7.6}$$

The relative ion fractions per state can then be computed from this:

$$P_j = \frac{n_j}{n_0} = \prod_{k=1}^{j} S_k \tag{7.7}$$

This allows computing the constants

$$R_1 = \frac{n_i}{n_0} = \sum_{j=1}^{j_{max}} P_j \tag{7.8}$$

$$R_2 = \frac{n_e}{n_0} = \sum_{j=1}^{j_{max}} jP_j \tag{7.9}$$

from which we can finally compute the average ionization state of the plume Z

$$Z = \frac{R_2}{R_1} \tag{7.10}$$

and the ionization fraction η_i

$$\eta_i = \left(1 + \frac{1}{R_1}\right)^{-1} \tag{7.11}$$

Finally the number density n_e is obtained as

$$n_e = \frac{pR_2}{kT_e(1 + R_1 + R_2)} \tag{7.12}$$

These equations form a closed system whose solution can be found by an iterative numerical scheme.

A model combining the features of the vapor model and the plasma model can be formed by expressing a composite impulse coupling coefficient C$_m$ from the plasma coefficient C_{mp} and the vapor coefficient C_{mv} as follows:

$$C_m = xC_{mv} + (1-x)C_{mp} \tag{7.13}$$

An empirical formulation for the weighting factor is chosen as follows

$$x = \left(\frac{C_{mp}}{C_{mv} + C_{mp}}\right)^2 \tag{7.14}$$

This empirical formulation allows to retrieve the limit cases for the prediction of C_m in the vapor and plasma regimes:

- C_m=C_{mv}=C_{mp} when the 2 coefficients are equal
- Regime where vapor dominates the ablation plume: C_m=C_{mv} when $C_{mp} \gg C_{mv}$
- Regime where plasma effects dominate the ablation plume: C_m=C_{mp} when $C_{mv} \gg C_{mp}$

7.2 Model Validation with Experimental Measurements

To check the validity of the laser model, the influence of the target material on the impulse generation was experimentally investigated. The experiments were conducted at Nagoya University (Japan) in a vacuum chamber with 0.7 m in diameter and 2.2 m in length as shown schematically in Fig.7.2. To simulate the space environment, the ambient pressure was kept at 10^{-2} Pa during all tests by applying a rotary pump backed up with a turbo molecular pump. A torsion pendulum with sub-μNs level impulse resolution placed in the chamber was used to measure the impulse bits. A 7ns FWHM pulse width, repetitive pulsed solid-state laser with kHz repetition rate was used as the laser source to ablate the targets. The laser was working in burst irradiation mode, which means that a burst including 200 identical pulses was irradiated in each test to generate each measured impulse. The temporal deflection signal of the pendulum after impulse was imparted to the target could be fitted to a damped oscillation expression: $B = A\sin(\omega t)\exp(-ct)$. The value of A in each test was derived from this fitting, and

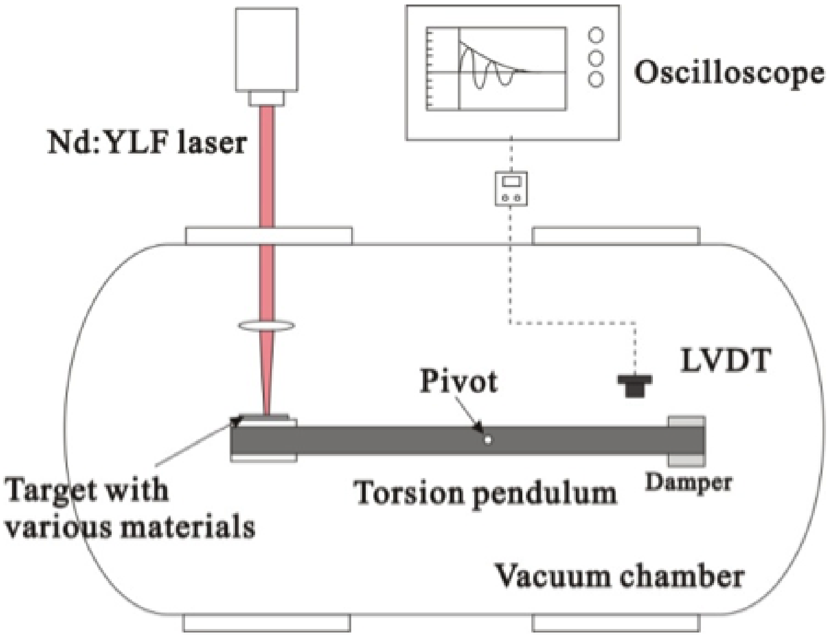

Figure 7.2: Experimental setup for laser ablation measurement

its relation with the imparted impulse was pre-calibrated by an impact hammer method.

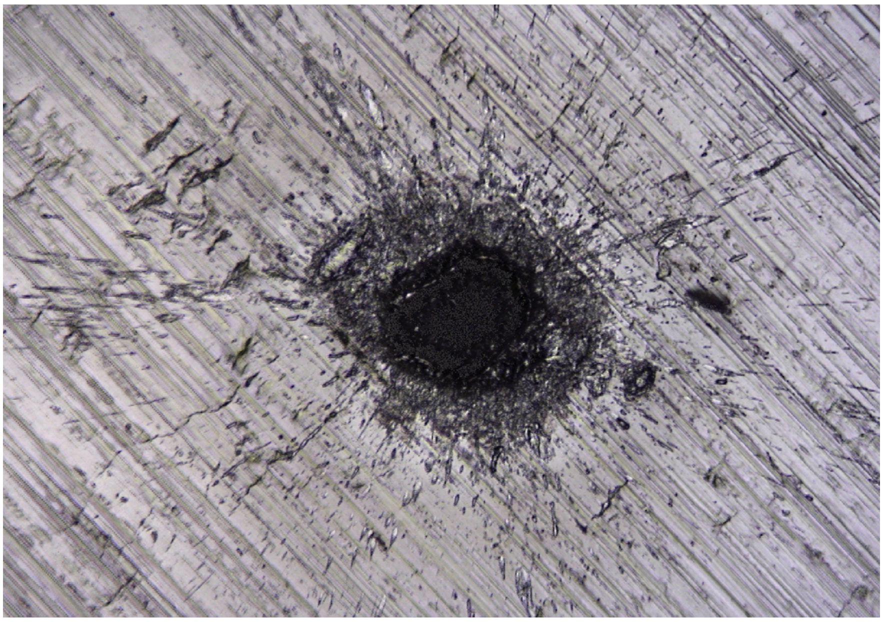

Figure 7.3: Example of hole formed in Al sample after 200 laser shots

As part of the results, Table 7.1 shows the impulse measurements obtained for the

Fluence Φ_P	$C_m^{Al2024-T3}$	$C_m^{Ti-6Al-4V}$	C_m^{CFRP}
6 J/cm^2	12.25±2.14 μN/W	18.85±0.96 μN/W	38.25±5.34 μN/W
8.4 J/cm^2	16.48±0.8 μN/W	19.52±0.92 μN/W	34.10±7.44 μN/W
11.8 J/cm^2	10.48±0.76 μN/W	19.23±1.42 μN/W	28.19±6.16 μN/W
13.6 J/cm^2	8.49±1.08 μN/W	16.01±1.10 μN/W	39.98±4.10 μN/W

Table 7.1: Measured impulse coupling and fluence levels

different materials at various fluence levels. Highest momentum coupling coefficient (C_m) were obtained when using CFRP at all studied fluence. Maximum impulse for CFRP was seen to vary in the range 30-40μN/W. For ablators made of Al alloy the C_m is in a similar range as obtained when ablating pure aluminum.

The comparison between the experiment and model is shown on Fig.7.4, 7.5, and 7.6. The results of the vapor model and pulsed model are also plotted independently for reference. The results show good agreement between the model and experiment, except in the case of Aluminum where the experimental results are closer to the vapor model predictions. This could be linked with the fact that Aluminum has a higher thermal conductivity than Titanium alloys and CFRP. Indeed, thermal transport theory predicts a higher ablation threshold (possibly resulting in a higher plasma ignition threshold) in that case.

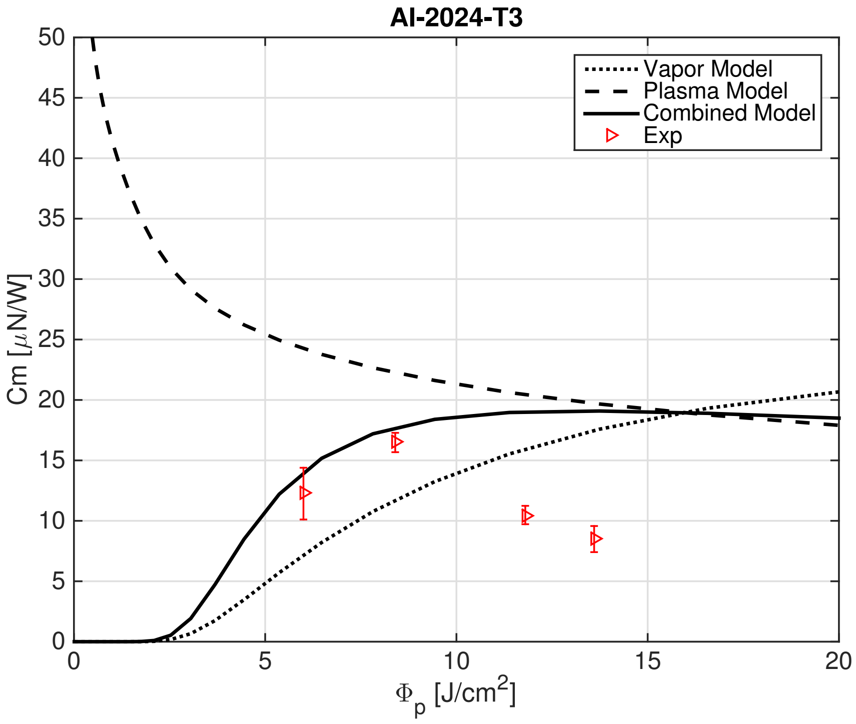

Figure 7.4: Impulse coupling of Al 2024-T3: comparison between models and experiment

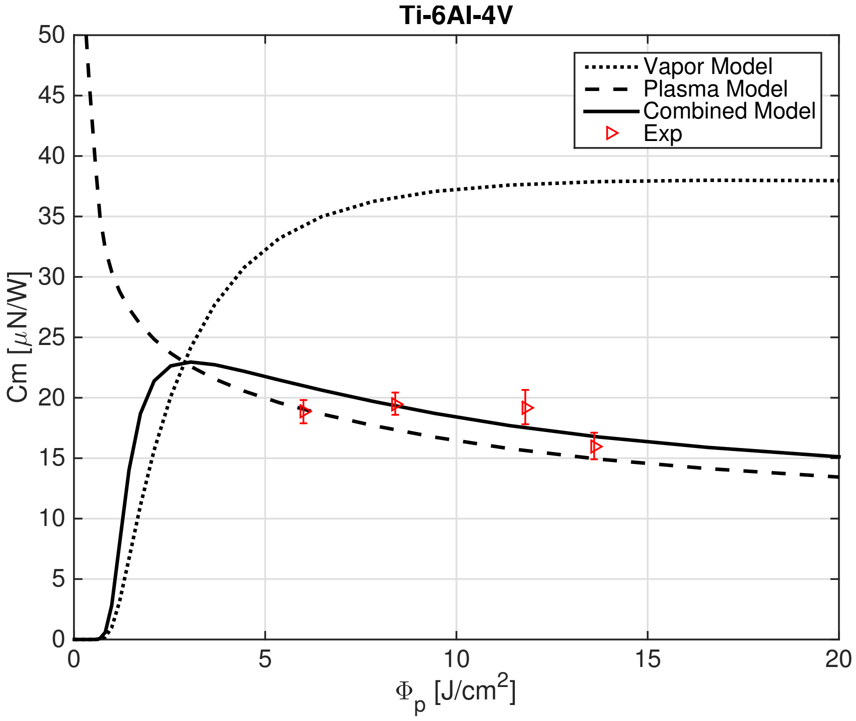

Figure 7.5: Impulse coupling of Ti 6Al-4V: comparison between models and experiment

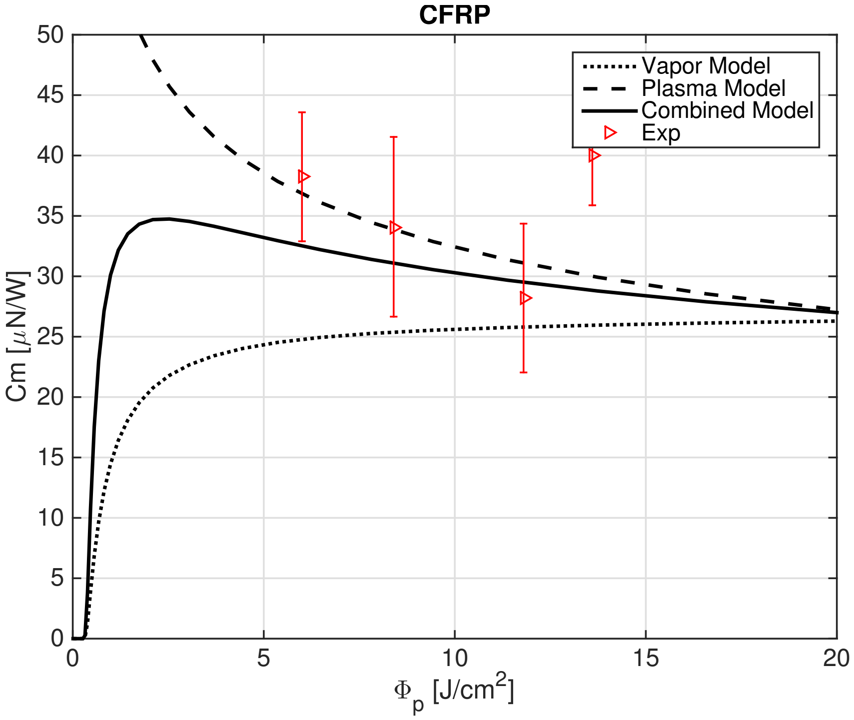

Figure 7.6: Impulse coupling of CFRP: comparison between models and experiment

7.3 Applications to LEO and GEO Objects

We now examinates applications of the laser ablation concept to an active debris removal mission with a chaser spacecraft equipped with a 1kW-class laser system.

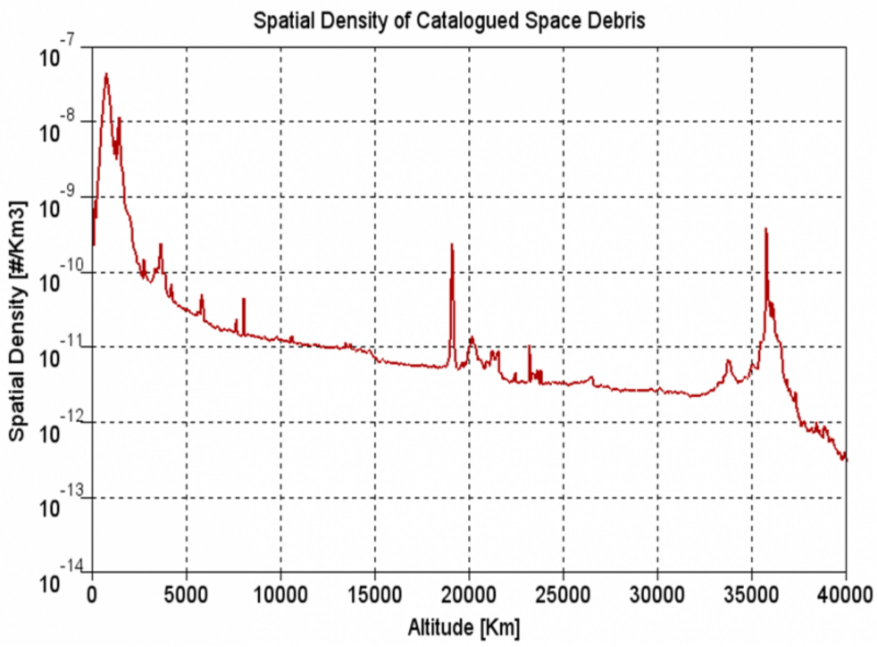

Figure 7.7: Distribution of space objects as a function of their altitude (image: CNES)

Fig. 7.7 shows the distribution of space objects as a function of their mean altitude. Peaks in this chart match with the main areas of interest for space applications or missions:

- The first peak correspond to objects in LEO in an altitude range comprised between 750km and 900km. Typical objects in this group are satellites with a near polar orbit such as the Iridium constellation or Earth observation satellites in a sun-synchronous-orbit such as Envisat
- The second peak correspond to objects in the MEO region such as the GPS, Galileo, and Glonass constellations.

- The third peak correspond to a group of objects occupying a region contiguous with the geostationnary ring (35786 km).

As mentionned in Chapter 2, ground-based or spaceborne laser systems were proposed in the past as active debris removal measures. The concepts envisaged, such as Orion or LADROIT, required average laser powers in excess of 15kW, leading to relatively ambitious architectures. For instance LADROIT, which would operate from a LEO parking orbit, has an estimated mass of about 10-tons. The authors argue that, despite its high cost (estimated around 560M$), such a concept would be benefitial due to its ability to engage thousands of objects per year without the need to transfer to their orbitPhipps (2014).

Arguably, a solution consisting in a chaser spacecraft operating at a smaller distance following orbital rendezvous would allow for a comparatively smaller laser system, and focusing optics, thus resulting in a lower spacecraft mass. The ability to operate from a shorter range would also allow to relax the pointing requirements, allow for a continuous monitoring of the disposal operations, but would come at at the cost of a shorter mission ifetime (limited by the available propellant to rendezvous with each target) and an overal lower number of targets that can be removed during the mission. While the Orion and LADROIT concepts seem better suited for the removal of small debris, a chaser solution could be better suited for larger debris, whose removal operations might require continuous operations and monitoring and could, in any case, serve as a proof of concept that could be implemented in the nearer term due to the simpler mission architecture. Moreover, models of the debris population growth have suggested that a yearly removal of at least 5 large pieces of debris would be sufficient to stabilise the debris population. Finally, compared to Orion and LADROIT, a chaser solution would only be able to engage a limited number debris objects that are within its orbital reach (considering the available propellant reserve). Such a system would thus be less likely to be used as a weapon but could be suitable for use in constellations. We focus in the next subsections on laser-based ADR chasers that can operate in in the LEO and GEO orbits currently included within the protected regions defined in the IADC guidelines.

7.3.1 Large Debris in LEO

As a first application, let us consider the case of an 8-ton man-made debris in sun-synchronous orbit around the Earth. A typical study case is ESA's envisat satellite which was lost in 2012 and is now flying uncontrolled at an altitude of 765km. The initial orbital elements used for our simulation can be reviewed in table 7.2: While the eclipses duration are initially identical due to the sun-synchronous nature of the original orbit, this will not remain true as the altitude of the satellite decreases. Eclipses are accounted in our calculations using a cylindrical shadow approximation which is reasonable for satellites in LEO (the Earth shadow cone being about 106 times longer than its diameter). The assumption is that the laser system only works when the solar panels can receive light from the sun. This configuration is judged to require less mass than an alternative configuration with larger batteries and a smaller laser system producing the same average power. The eclipses can be calculated by considering the ellipse resulting from the intersection between the shadow cylinder and the orbital plane of the spacecraft first and then calculating the intersections between this ellipse and the spacecraft trajectory.

Table 7.2: Orbital Elements of Envisat

Orbital Elements	Symbol	Value
Semi-major axis	a	7136 km
eccentricity	e	0.0000964
inclination	i	98.32 deg.
ascending node	Ω	346.77 deg.
argument of perigee	ω	72.18 deg.
True anomaly (t_0)	θ	0 deg.

With reference to figure 7.8, for a quasi-circular orbit, the semi-angular distance between the shadow entrance and the shadow exit of the spacecraft ψ can be computed as a function of the orbit radius and the angle between the orbit plane and the sun-earth

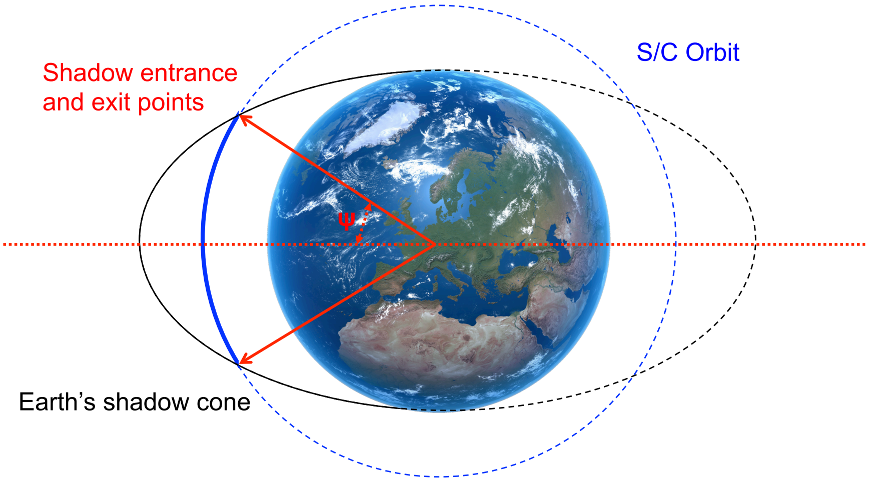

Figure 7.8: Shadow arc during the spacecraft trajectory (solid)

unit direction vector **s**:

$$\psi = \arcsin\left(\frac{\sqrt{R_E^2 - r^2\sin^2(\delta)}}{r\cos(\delta)}\right) \tag{7.15}$$

In this equation, R_E is the Earth radius (6371km). For a general orbit, a shadow function can be formed as a function of the spacecraft keplerian elements and the sun-earth direction vector expressed in the perifocal reference frameVallado and McClain (2001). The shadow function is computed as

$$\begin{aligned} g(\theta) = {} & R_E^2(1 + e\cos(\theta))^2 \\ & + a^2(1-e^2)^2\left(-s_x\cos(\theta) - s_y\sin(\theta)\right) - a^2(1-e^2)^2 \end{aligned} \tag{7.16}$$

An eclipse occur when both the function $g(\theta) > 0$ and the scalar product $\mathbf{s}\cdot\mathbf{r} > 0$. When the spacecraft is under the sunlight, a conservative thrust coupling coefficient of $15\mu N/W$ is assumed, which accounts for the fact that the thrust imparted is only tangential in average. The tangential acceleration on the satellite is thus:

$$\alpha_t = 0.000015 \times P_{out} \times \text{eclipse} \tag{7.17}$$

Where the eclipse factor is equal to 1 in sunlight and 0 in shadow. Considering this acceleration, Gauss Eq. (7.18) are integrated to compute the altitude evolution over time. These equations are slightly modify compared to 4.1 to include the secular effects of the Earth oblateness (J_2 term) on the ascending node Ω and argument of perigee ω.

$$\begin{aligned}
\frac{da}{dt} &= \frac{2a^2v}{\mu}\alpha_t \\
\frac{de}{dt} &= \frac{2}{v}(e + cos\theta)\alpha_t \\
\frac{di}{dt} &= 0 \\
\frac{d\Omega}{dt} &= -\frac{3}{2}nJ_2\frac{R_E^2}{a^2(1-e^2)^2}\cos i \\
\frac{d\omega}{dt} &= \frac{2}{ve}\alpha_t \sin\theta + \left(2e + \frac{r}{a}\cos\theta\right) + \frac{3}{2}nJ_2\frac{R_E^2}{a^2(1-e^2)^2}\left(\frac{5}{2}\sin^2 i - 2\right) \\
\frac{dM}{dt} &= -\frac{2\sqrt{1-e^2}}{ve}\alpha_t\left(1 + \frac{e^2r}{p}\right)\sin\theta + n
\end{aligned} \tag{7.18}$$

The results on Fig. 7.9 show the decrease of altitude as a function of the output power of the laser and the duration of the mission. Hence, a laser producing 3kW of output power would in theory allow to decrease Envisat's altitude down to 500km in a year. On the other hand, a spacecraft equipped with a **1 kW laser** could:

- Decrease the altitude of envisat down to 700km in less than a year.
- Decrease the altitude of a generic 1-ton debris down to 500km in 4 months.

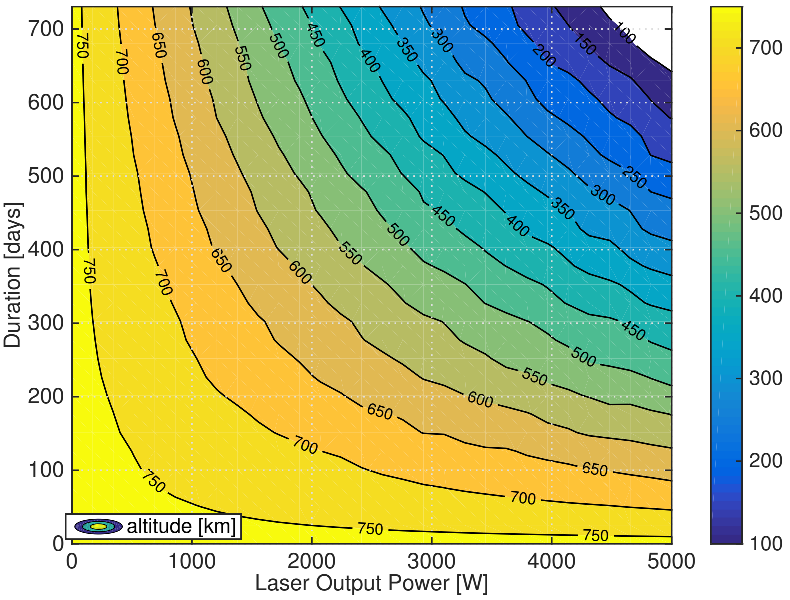

(a) 8-ton debris

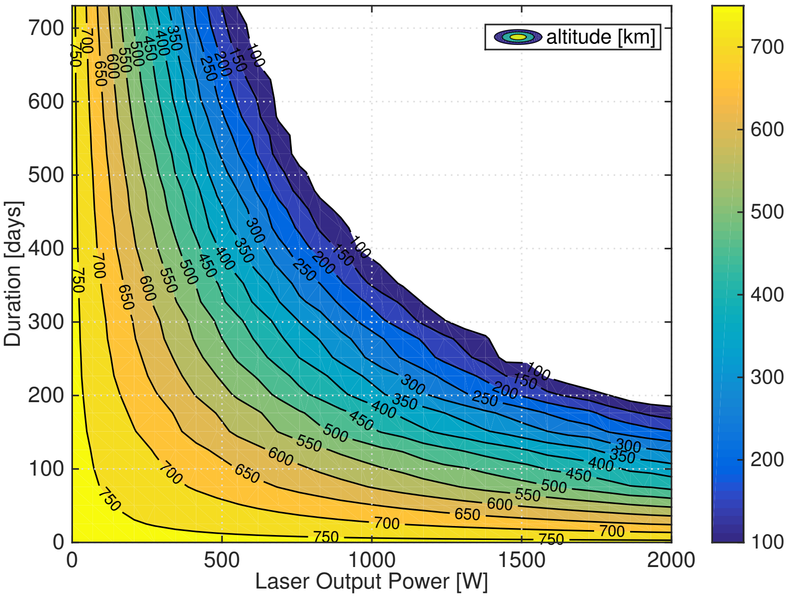

(b) 1-ton debris

Figure 7.9: Altitude decrease as a function of the duration of the deflection mission and laser output power

7.3.2 Debris Removal in GEO

Another particularly crowded orbital region is the geostationary ring (GEO), with communications satellites clustering over specific targets and sharing the same orbital path. When a satellite becomes a space debris, orbital perturbations in GEO cause longitude drift in the ascending node and precession of its orbital plane. Despite the low relative velocities between GEO objects (impact velocity peaks at about 1.5 km/s) a satellite would likely become inoperable after a collision. Large objects, such as solar-powered satellites, are especially vulnerable to collisions. With close approaches (within 50 meters) estimated at one per year, debris in GEO are thought to pose less short-term risk than debris in LEO. However, the presence of debris in GEO orbit limits the number of orbital slots, resulting in a loss of profit for the Telecommunication industry. As a mitigation measure, the ITU now requires proof that a satellite can be moved out of its orbital slot at the end of its lifespan. However, studies suggest that this measure alsone may be insufficient. Because the GEO orbit is too distant to accurately measure objects under 1 m, the nature of the problem is not well known. Satellites or boosters in other orbits, especially stranded in geostationary transfer orbit, are an additional concern due to their typically high crossing velocity.

An ADR vehicle carrying a laser ablation system could be used to move defunct satellites to empty spots in GEO, requiring less maneuvering and making it easier to predict future motion. Fig. 7.10 illustrates how a laser-carrying spacecraft operating in GEO could be used to rendez-vous and send successive defunct satellite into a graveyard orbit. A possible strategy could consist in the following sequence of operations:

1. Orbit raising using contactless strategy (laser or IBS)
2. Use drift of 15min/day between graveyard and GEO to be correctly phased with next target
3. transfer to the next target

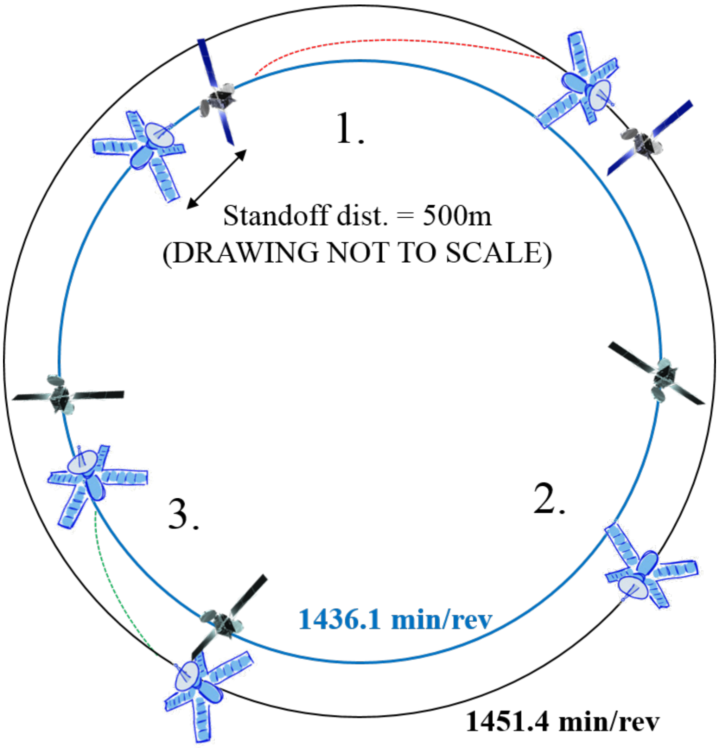

Figure 7.10: Possible laser debris removal strategy in GEO

Currently, the IADC guidelines only requires a $\Delta v \approx 11$ m/s to raise the orbit at the end of life by about 300km. This is about one order of magnitude lower than the $\Delta v \approx$ required for the disposal manoeuvre in LEO orbit. Considering an effective impulse coupling of $15\mu N/W_{optical}$, a chaser equipped with 1kW-class laser would be able to put an 8-Ton defunct satellite into a compliant graveyard orbit in less than 2 months.

In order to identify market opportunities for a laser-based ADR mission, we looked at possible debris candidates from the Celestrack and Satcat databases. Successive filterings (based on objetcs category, orbit eccentricity and period) were applied to the 12486 unclassified objects in order to retain 26 debris candidates located in the vicinity of the GEO ring. Reference to the identified GEO debris objects can be found in Table 7.3.

Renumbered ID	NORAD ID	Name
1	29014	EKRAN 2 DEB
2	12996	EKRAN 2 DEB
3	11581	EKRAN 2 DEB
4	20801	GOES 3 AKM
5	13753	1976-023 DEB
6	20837	METEOSAT-2 AKM (MAGE 1)
7	22266	HIMAWARI-3 AKM
8	40924	COSMOS 1700 DEB
9	20800	METEOSAT-4 AKM
10	26460	FENGYUN 2B AKM
11	25353	METEOSAT-7 AKM
12	23118	METEOSAT-6 AKM
13	38700	TITAN 3C TRANSTAGE DEB
14	38693	TITAN 3C TRANSTAGE DEB
15	30000	TITAN 3C TRANSTAGE DEB
16	25000	TITAN 3C TRANSTAGE DEB
17	25001	TITAN 3C TRANSTAGE DEB
18	28491	FENGYUN 2C AKM
19	29676	MSG-2 DEB [BAFFLE COVER]
20	29106	MSG-2 DEB [COOLER COVER]'
21	29642	FENGYUN 2D AKM
22	40987	FENGYUN 2E DEB
23	38072	FENGYUN 2F AKM
24	40990	MSG 4 DEB [BAFFLE COVER]
25	40989	MSG 4 DEB [COOLER COVER]
26	40369	FENGYUN 2G AKM

Table 7.3: List of candidate GEO debris from the Celestrack and Satcat databases

From the available orbital information, we estimated the ideal transfer cost between each of these 26 objects. Fig. 7.11 illustrates typical transfer windows between 2 such objects, using a high thrust transfer. The best transfer is simply retrieved as the one with the lowest cost over the period considered. Using the phasing strategy described earlier, one can in fact see that such a low cost transfer windows typically opens every 3 months. Note also that, as the chaser is assumed to follow the target during the disposal maneuver, the transfer from a given object to the next object is assumed to happen from an orbit that is 300 km higher than the initial target orbit.

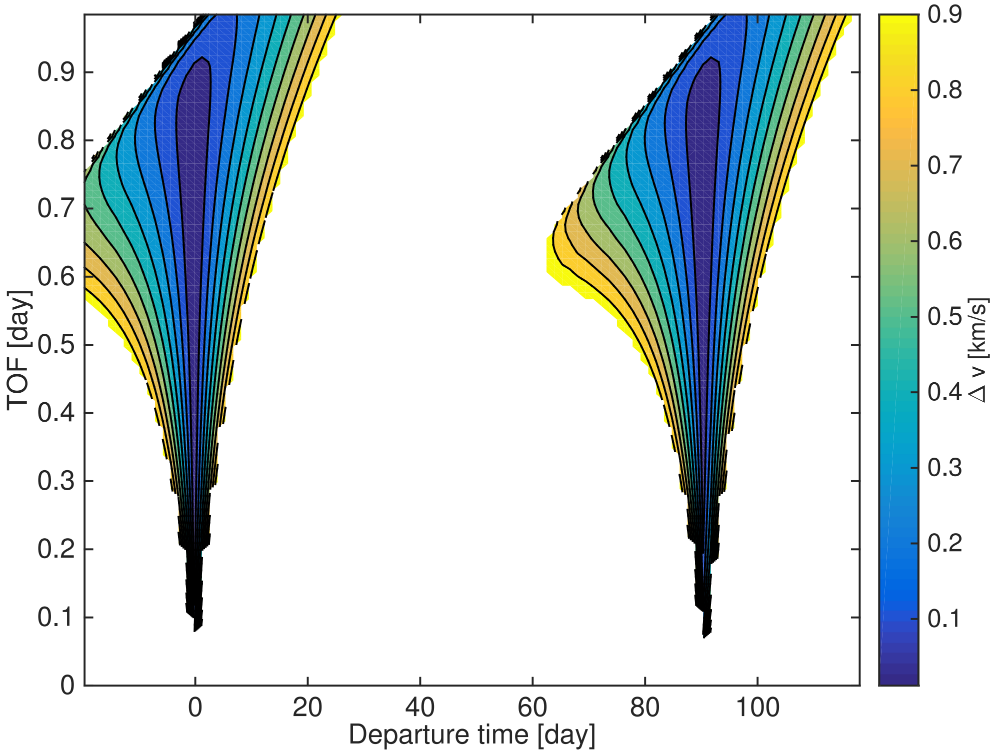

Figure 7.11: Example of transfer windows between 2 particular objects with a low transfer Δv

Objects with Δv transfer cost <200m/s are shown on Fig. Fig. 7.12. In this figure, IDs of these objects have been renumbered so that low-cost interobject transfers cluster close to the diagonal of the matrix allowed us to identify subgroups among these objects with a low transfer cost. In particular, objects 13-17 seem to have a common origin of one refers to Table 7.3. Finally, note that diagonal values (=11 m/s) in this matrix are irrelevant since they represent a transfer from the disposal orbit of an object to its original orbit.

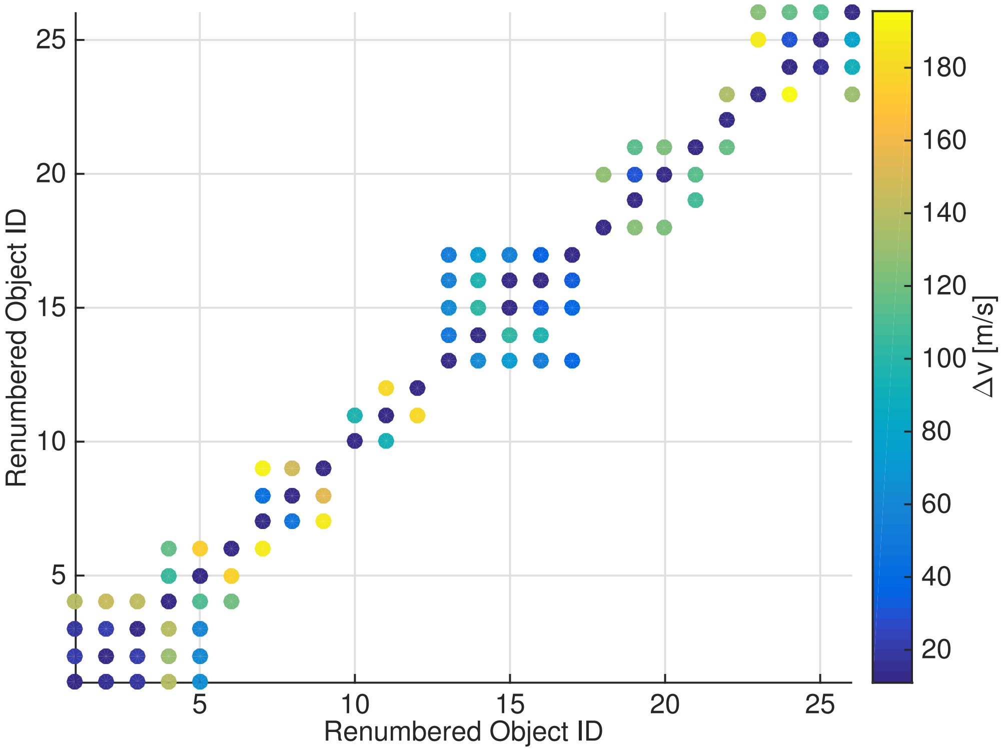

Figure 7.12: inter-object impulsive Δv transfer cost

Chapter 8

Conclusion

We examined throughout this thesis the potential of laser ablation to manipulate non-cooperative objects such as asteroids and space debris.

Laser technologies and relevant applications were presented in chapter 2. Then, in chapter 3, a new performance model was derived and its results analysed to identify the main sizing constrains on the optics and power of the laser system.

In chapter 4, the fundamentals of asteroid deflection were summarised. The operational concepts of some impulsive and slow-push deflection methods were also introduced. For the laser method, a redundant, scalable design was introduced, using (passive) spectral beam combining techniques and an off-axis beam expansion and focusing telescope. Already demonstrated on terrestrial applications this modular concept allows to combine separate beams with independent frequency and modulation both in the near and far fields without spatial interference. A sizing exercise was then conducted on an asteroid deflection mission in chapter 5. This sizing exercice was based on the results of chapter 3 and 4 for the laser ablation method. The idea of an alternative demonstration mission to the binary asteroid Didymos was also discussed. Benefiting from a small transfer Δv, this binary asteroid system is presently considered by the international AIDA consortium to demonstrate the capability of the Kinetic Impactor strategy. Operating from one of the triangular Lagrangian point to accelerate/decelerate the secondary asteroid, a laser-based strategy could perform in-situ observation and impart the deflection action with a single spacecraft carrying a 1-kW class laser.

In the case of asteroids, we benchmarked in chapter 6 the effectiveness of laser ablation against other popular non-nuclear deflection methods in a statistically representative set of virtual collision scenarios. For each of the scenarios, a fixed asteroid mass of $4{\times}10^{9}$kg[1] was considered together with the launch capacity of a Delta 4 Heavy RS-68A upgrade version rocket[2]. Our results indicate a superior deflection ability over slow-push methods, thanks to the fact that the laser deflection method is only bounded by the available power and duration of operations, but not the amount of propellant or the gravitational interaction between the asteroid and the spacecraft. When compared to an impulsive technique such as the Kinetic Impactor, laser ablation demonstrated a superior capability for a subset of virtual impactor scenario consisting in shallow crossers with a low transfer Δv . On the other hand, for deep crossers, the Kinetic Impactor method proved superior. Indeed, these asteroids require a large Δv for transfer but a low departure energy in the case a rendez-vous is not required. For the Kinetic Impactor, this means that a high collision impact can be formed at low departure cost. Despite representing a relatively smaller fraction of potentially hazardous asteroids, shallow crossers represent an opportunity for future exploration and demonstration (or even exploitation) missions. For future works, it would be interesting to check if similar conclusions would still be valid when compared to a Kinetic Impactor mission with a low thrust engine (instead of the direct injection assumed in this thesis for the Kinetic Impactor method). Similarly, it could be interesting to investigate whether a composite transfer strategy with non-null escape velocity and subsequent low-thrust transfer may improve the results for slow-push methods in the case of a short warning time. Moreover, as laser technology and solar power generation capacities keep improving over time, it will be important to maintain this comparative assesment up to date.

---

[1] Note that, in the original publication by the author (Thiry and Vasile, 2016), a larger impactor size of of 212m (10^{10}kg), was also considered leading to the same comparison results

[2] Likewise, a larger launch capacity could also be considered in case of a larger target

The applicability of the laser ablation method for active debris removal was also investigated in in chapter 7. The laser model of chapter 3 was adapted to the case where the target is a thin layered debris hit by repetitive impulses delivered by a pulsed laser system. The results of this model showed good agreement with experimental measurements on materials commonly encountered in the space industry. These experimental results were obtained during a collaboration with Nagoya University in Japan. In the remaining sections, we also illustrated possible applications to debris objects in LEO and GEO. Compared to previous works where authors considered a relatively large laser system operating at a long range from a parking orbit, the system we propose would need to transfer to the target orbit, hence increasing the propellant consumption and thus decreasing the amount of targets that can be removed during the mission lifetime. Despite this, transferring to the target object would allow to simply the laser system design by reducing its operational range from hundreds of kilometers to few hundreds of meters. This would allow for a relatively simpler and smaller mission. For future works, it would be interesting to further assess the feasibility of such a mission from the technical and economical point of view. A market analysis would also allow to better appreciate the real opportunities for such a mission compared to the larger concepts from the literature. Another interesting concept, in between the large systems proposed in the literature and the one proposed in this thesis, could consist in a laser-based collision avoidance system placed in a dawn-dusk parking orbit (allowing to maximize its power generation and facilitate waste heat management) and targeting small debris (1-10cm). A moderate size laser system could be envisaged in this case, considering also the fact that Δv required for collision avoidance are typically several orders of magnitudes lower lower than the ones needed for a complete disposal. This system would periodically engage small debris in polar orbits crossing the dawn-dusk orbital plane above the poles, leaving the rest of the orbit to recharge the spacecraft batteries. For this case, the main challenging point will be to develop the capability to lock and engage non-cooperative targets over long distances.

In conclusion, laser ablation is a promising method to manipulate uncooperative objects in space, especially when compared with other slow-push strategies. The levels of performance predicted are around $55\mu\mathrm{N/W}_{optical}$ for typical asteroid material and between $15\text{-}40\mu\mathrm{N/W}_{optical}$ for materials typically encountered in space debris. These levels are comparable to those of an Ion Engine without the propellant cost to move an object. In other words, whereas other slow-push methods are eventually limited by the available propellant reserve, the laser method is only limited by the available power resources. For a fixed mass, available power resources keep increasing over the years giving this method an even more positive outlook in the long term. The ability to operate at a safe distance from the object and without using propellant could greatly simplify the design of a future ADR mission or an asteroid deflection mission relying on a slow-push strategy. For future works, it would be interesting to further validate the performance models for this method and quantify the uncertainties linked with the target material. From a technical point of view, the main parameters that will impact the mission size and cost are the required installed power and the amount of dissipated power that the heat rejection system needs to cope with. Those mission parameters will essentially depend on the thrust coupling coefficient (quantifying the amount of thrust generated on the targer depending on the optical ouput power) and the electrical to optical conversion efficiency of the laser system. Experimental measurements of the thrust coupling coefficient with a CW laser on various sample materials would also allow to refine the laser model developped during this thesis. In parallel, an assesment of realistic laser conversion efficiencies in the context of a space mission shall be done. This assesment could result with the creation of a technological roadmap illustrating the different milestones that shall be met in order to qualify this technology for a future demonstration mission.

Bibliography

Sergei I Anisimov and Viktor A Khokhlov. *Instabilities in laser-matter interaction.* CRC press, 1995.

Arianespace. *Soyuz from the Guiana Space Centre User's Manual*, 2006.

Fabian Bach. A parametric assessment of the full pha phase space, and deflection feasibility using kinetic impactors. Technical report.

François Balembois and Sébastien Forget. Laser: Fundamentals, 2007. URL `http://www.optique-ingenieur.org/en/courses/OPI_ang_M01_C01/co/OPI_ang_M01_C01_web.html`.

Robin Biesbroek, Tiago Soares, Jacob Husing, and Luisa Innocenti. The e. deorbit cdf study: A design study for the safe removal of a large space debris. In *64th International Astronautical Congress (IAC), Beijing*, 2013.

M Boivineau, C Cagran, D Doytier, V Eyraud, M-H Nadal, B Wilthan, and G Pottlacher. Thermophysical properties of solid and liquid ti-6al-4v (ta6v) alloy. *International journal of thermophysics*, 27(2):507–529, 2006.

Claudio Bombardelli, Hodei Urrutxua, Mario Merino, Jesús Peláez, and Eduardo Ahedo. The ion beam shepherd: A new concept for asteroid deflection. *Acta Astronautica*, 90(1):98–102, 2013.

WF Bottke, MICHAEL C Nolan, RICHARD Greenberg, and Robert A Kolvoord. Collisional lifetimes and impact statistics of near-earth asteroids. *Hazards due to comets and asteroids*, 337, 1994.

P. Bourdon. High power lasers for laser-matter interaction: An overview of available technologies, 2013.

Clark R Chapman. The hazard of near-earth asteroid impacts on earth. *Earth and Planetary Science Letters*, 222(1):1–15, 2004.

Clark R Chapman and David Morrison. Impacts on the earth by asteroids and comets: assessing the hazard. *Nature*, 367(6458):33, 1994.

Christopher F Chyba, Paul J Thomas, and Kevin J Zahnle. The 1908 tunguska explosion: atmospheric disruption of a stony asteroid. *Nature*, 361(6407):40–44, 1993.

Bruce Conway. Near-optimal deflection of Earth-approaching asteroids. *Journal of Guidance, Control and Dynamics*, 24(5):1035–1037, 2001.

Bruce A Conway. Optimal low-thrust interception of earth-crossing asteroids. *Journal of Guidance, Control, and Dynamics*, 20:995–1002, 1997.

Paul Cramp, Jun Wang, Suhit Das, Mike Grimshaw, Jason Farmer, Mark DeVito, Weimin Dong, Trevor Crum, Damian Wise, and Yan Feng. ¿ 360w and¿ 70% efficient gaas-based diode lasers. Technical report, DTIC Document, 2005.

Paul Crump, Weimin Dong, Mike Grimshaw, Jun Wang, Steve Patterson, Damian Wise, Mark DeFranza, Sandrio Elim, Shiguo Zhang, Mike Bougher, et al. 100-w+ diode laser bars show¿ 71% power conversion from 790-nm to 1000-nm and have clear route to¿ 85%. In *Lasers and Applications in Science and Engineering*, pages 64560M–64560M. International Society for Optics and Photonics, 2007.

CVI Laser Optics and Melles Griot. Introduction to Laser Technology, 2013. URL `https://www.cvimellesgriot.com/products/Documents/TechnicalGuide/Basic_Laser_Principles.pdf`.

Eric W Davis and Franklin B Mead Jr. Review of laser lightcraft propulsion system. In *AIP Conference Proceedings*, volume 997, pages 283–294. AIP, 2008.

Marilena Di Carlo, Massimiliano Vasile, and Edmondo Minisci. Multi-population inflationary differential evolution algorithm with adaptive local restart. In *2015 IEEE Congress on Evolutionary Computation (CEC)*, pages 632–639. IEEE, 2015.

Marilena Di Carlo, Massimiliano Vasile, and Edmondo Minisci. Adaptive multi-population inflationary differential evolution. *Soft Computing*, pages 1–31, 2019.

Derrek Drachenberg, Ivan Divliansky, Vadim Smirnov, George Venus, and Leonid Glebov. High-power spectral beam combining of fiber lasers with ultra high-spectral density by thermal tuning of volume bragg gratings. In *SPIE LASE*, pages 79141F–79141F. International Society for Optics and Photonics, 2011.

Christian Freitag, Rudolf Weber, and Thomas Graf. Polarization dependence of laser interaction with carbon fibers and cfrp. *Optics express*, 22(2):1474–1479, 2014.

Alison Gibbings, Massimiliano Vasile, Ian Watson, John-Mark Hopkins, and David Burns. Experimental analysis of laser ablated plumes for asteroid deflection and exploitation. *Acta Astronautica*, 90(1):85 – 97, 2013. ISSN 0094-5765. NEO Planetary Defense: From Threat to Action.

Alison Lorraine Gibbings. *Laser ablation for the deflection, exploration and exploitation of near Earth asteroids*. PhD thesis, University of Glasgow, 2014.

S Glasstone and P J Dolan. *The Effects of Nuclear Weapons*. Princeton University, US Government Printing Office, 3rd edition, 2007.

P Hammerling and J L Remo. NEO interaction with nuclear radiation. *Acta Astronautica*, 36(6):337–346, 1995. doi: 101016/0094-5765(95)00111-5.

Donald Hampton, James Baer, Martin Huisjen, Chris Varner, Alan Delamere, Dennis Wellnitz, Michael A'Hearn, and Kenneth Klaasen. An overview of the instrument suite for the deep impact mission. *Space Science Reviews*, 117(1–2):43–93, 2005.

Alan W Harris and Germano DAbramo. The population of near-earth asteroids. *Icarus*, 257:302–312, 2015.

Eric Honea, Robert S Afzal, Matthias Savage-Leuchs, Neil Gitkind, Richard Humphreys, Jason Henrie, Khush Brar, and Don Jander. Spectrally beam combined fiber lasers for high power, efficiency, and brightness. In *SPIE LASE*, pages 860115–860115. International Society for Optics and Photonics, 2013.

K R Housen and K A Holsapple. Experimental measurement of momentum transfer in hypervelocity collisions. In *46th Lunar and Planetary Science Conference*, number 2894, Texas, USA, March 2015.

W Hu and D J Scheeres. Spacecraft motion about slowly rotating asteroids. *Journal of Guidance, Control and Dynamics*, 25(4):765–775, July–August 2002.

Y el Jeong, JK Sahu, DN Payne, and J Nilsson. Ytterbium-doped large-core fiber laser with 1.36 kw continuous-wave output power. *Optics Express*, 12(25):6088–6092, 2004.

R Kahle, E Kührt, G Hahn, and J Knollenberg. Physical limits of solar collectors in deflecting Earth-threatening asteroids. *Aerospace Science and Technology*, 10:253–263, 2006. doi: 101016/jast200512004.

Charles J Knight. Theoretical modeling of rapid surface vaporization with back pressure. *AIAA journal*, 17(5):519–523, 1979.

Lee Kwok-san and Tong Shiu-sing. What is laser?, 2000. URL `http://www.hk-phy.org/articles/laser/laser_e.html#note`.

J-C Liou and Nicholas L Johnson. Risks in space from orbiting debris, 2006.

Lonnie Lucas and Jim Zhang. Femtosecond laser micromachining: A back-to-basics primer, 2012. URL `http://www.industrial-lasers.com/articles/2012/06/femtosecond-laser-micromachining-a-back-to-basics-primer.html`.

Christie Maddock, Joan Pau Sanchez Cuartielles, M Vasile, and G Radice. Comparison of single and multi-spacecraft configurations for NEA deflection by solar sublimation. In E Belbruno, editor, *New Trends in Astrodynamics and Applications III*, volume 886, pages 303–316. American Institute of Physics, 2007.

Jason G Matheny. Reducing the risk of human extinction. *Risk analysis*, 27(5):1335–1344, 2007.

C McInnes. Near earth object orbit modication using gravitational coupling. *Journal of Guidance, Control and Dynamics*, 30(3):870–873, 2007.

NASA. Near earth object survey and deflection analysis of alternatives. In *Report to Congress. March. NASA, Office of Program Analysis and Evaluation, Washington, DC*, 2007.

NEOSHIELD. D7.5.1: Trade offs of viable alternative mitigation concepts. Technical report.

DM Novak and Massimiliano Vasile. Improved shaping approach to the preliminary design of low-thrust trajectories. *Journal of guidance, control, and dynamics*, 34(1): 128–147, 2011.

Sanchez Cuartielles J P, Colombo C, Vasile M, and Radice G. Multi-criteria comparison among several mitigation strategies for dangerous near earth objects. *Journal of Guidance, Control and Dynamics*, 32:121–142, 2009.

Sang-Young Park and Daniel D Mazanek. Deflection of Earth-crossing asteroids/comets using rendezvous spacecraft and laser ablation. *Journal of Astronautical Sciences*, 53(1):21–37, Jan-Mar 2005.

Rüdiger Paschotta. Encyclopedia of Laser Physics and Technology. URL `http://www.rp-photonics.com/lasers.html`.

Claude Phipps. An alternate treatment of the vapor-plasma transition. *International Journal of Aerospace Innovations*, 3(1):45–50, 2011.

Claude Phipps, Mitat Birkan, Willy Bohn, Hans-Albert Eckel, Hideyuki Horisawa, Thomas Lippert, Max Michaelis, Yuri Rezunkov, Akihiro Sasoh, Wolfgang Schall, et al. Review: laser-ablation propulsion. *Journal of Propulsion and Power*, 26(4): 609–637, 2010.

Claude R Phipps. L adroit–a spaceborne ultraviolet laser system for space debris clearing. *Acta Astronautica*, 104(1):243–255, 2014.

CR Phipps, TP Turner, RF Harrison, GW York, WZ Osborne, GK Anderson, XF Corlis, LC Haynes, HS Steele, KC Spicochi, et al. Impulse coupling to targets in vacuum by krf, hf, and co2 single-pulse lasers. *Journal of Applied Physics*, 64 (3):1083–1096, 1988.

CR Phipps, G Albrecht, H Friedman, D Gavel, EV George, J Murray, C Ho, W Priedhorsky, MM Michaelis, and JP Reilly. Orion: Clearing near-earth space debris using a 20-kw, 530-nm, earth-based, repetitively pulsed laser. *Laser and Particle Beams*, 14(01):1–44, 1996.

A Poueyo-Verwaerde, R Fabbro, G Deshors, AM De Frutos, and JM Orza. Experimental study of laser-induced plasma in welding conditions with continuous co2 laser. *Journal of applied physics*, 74(9):5773–5780, 1993.

RW Powell, Cho Yen Ho, and Peter Edward Liley. Thermal conductivity of selected materials. Technical report, DTIC Document, 1966.

L. A. Ricciardi and M.o Vasile. Improved archiving and search strategies for multi agent collaborative search. In *EUROGEN*, 2015.

Alan R Robertson. Computation of correlated color temperature and distribution temperature. *JOSA*, 58(11):1528–1535, 1968.

DI Rosen, DE Hastings, and GM Weyl. Coupling of pulsed 0.35-μm laser radiation to titanium alloys. *Journal of applied Physics*, 53(8):5882–5890, 1982a.

DI Rosen, J Mitteldorf, G Kothandaraman, AN Pirri, and ER Pugh. Coupling of pulsed 0.35-μm laser radiation to aluminum alloys. *Journal of applied Physics*, 53 (4):3190–3200, 1982b.

A Rossi, F Marzari, and P Farinella. Orbital evolution around irregular bodies. *Earth, Planets, Space*, 51:1173–1180, 1999.

Pau Sanchez, Camilla Colombo, Massimiliano Vasile, and Gianmarco Radice. Multicriteria comparison among several mitigation strategies for dangerous near-earth objects. *Journal of Guidance, Control, and Dynamics*, 32(1):121–142, 2009.

Hanspeter Schaub and John L Junkins. *Analytical mechanics of space systems*. AIAA Education Series. AIAA, Virginia, USA, first edition, 2003.

SpaceX. *Falcon 9 Launch Vehicle Payload User's Guide*, 2009.

W J Tedeschi, J L Remo, J F Schulze, and R P Young. Experimental hypervelocity impact effects on simulated planetesimal materials. *International Journal of Impact Engineering*, 17:837–848, 1995.

Nicolas Thiry and Massimiliano Vasile. Statistical multicriteria evaluation of asteroid deflection methods. 2016.

Nicolas Thiry and Massimiliano Vasile. Statistical multi-criteria evaluation of non-nuclear asteroid deflection methods. *Acta Astronautica*, 140:293–307, 2017a.

Nicolas Thiry and Massimiliano Vasile. Theoretical peak performance and optical constraints for the deflection of an s-type asteroid with a continuous wave laser. *Advances in Space Research*, 59(5):1353–1367, 2017b.

David A Vallado and Wayne D McClain. *Fundamentals of astrodynamics and applications*, volume 12. Springer Science & Business Media, 2001.

M Vasile, A Gibbings, V Massimo, J-P Sanchez, D.G Yarnoz, S Eckersley, A Wayman, J Branco, D Burns, J-M Hopkins, C Colombo, and C McInnes. Light touch2: Effective solutions to asteroid manipulation. sysnova challenge analysis final report. Technical report, University of Strathclyde, 2013.

Massimiliano Vasile and Camilla Colombo. Optimal impact strategies for asteroid deflection. *Journal of Guidance, Control, and Dynamics*, 31(4), July 2008.

Massimiliano Vasile and Christie Maddock. On the deflection of asteroids with mirrors. *Celestial Mechanics and Dynamical Astronomy*, 107(1):265–284, May 2010.

Massimiliano Vasile and Christie Alisa Maddock. Design of a formation of solar pumped lasers for asteroid deflection. *Advances in Space Research*, 50(7):891–905, 2012.

Massimiliano Vasile and Nicolas Thiry. Nuclear cycler: An incremental approach to the deflection of asteroids. *Advances in Space Research*, 57(8):1805–1819, 2016.

Massimiliano Vasile, Alison Gibbings, Ian Watson, and John-Mark Hopkins. Improved laser ablation model for asteroid deflection. *Acta Astronautica*, 103:382–394, 2014.

Massimo Vetrisano, Nicolas Thiry, and Massimiliano Vasile. Detumbling large space debris via laser ablation. In *2015 IEEE Aerospace Conference*, pages 1–10. IEEE, 2015.

Massimo Vetrisano, Camilla Colombo, and Massimiliano Vasile. Asteroid rotation and orbit control via laser ablation. *Advances in Space Research*, 57(8):1762–1782, 2016.

MA Wise, JM Lafleur, and JH Saleh. Regression analysis of launch vehicle payload capability for interplanetary missions. In *61st International Astronomical Congress*, 2010.

Kouhei Yamaguchi and Hiroshi Yamakawa. Orbital deflection of potentially hazardous asteroids using a coulomb force attractor.

Sung-Moon Yoo, Young-Joo Songa, Sang-Young Park, and Kyu-Hong Choi. Spacecraft formation flying for Earth-crossing object deflections using a power limited laser ablating. *Advances in Space Research*, 43(12):1873–1889, 2009.

Federico Zuiani, Massimiliano Vasile, and Alison Gibbings. Evidence-based robust design of deflection actions for near earth objects celestial mechanics and dynamical astronomy. *Celestial Mechanics and Dynamical Astronomy*, 114(1-2):107–136, 2012.

List of Figures

List of Tables

List of Acronyms

ADR Active Debris Removal

AOCS Attitude and Orbit Control Subsystem

AU Carbon Fiber Reinforced Polymer

CBC Coherent Beam Combining

CBE Current Best Estimate

CCT Correlated Color Temperature

CNES Centre National d'Etudes Spatiales

CW Continuous Wave

DMM Design Maturity Margins

DPSSL Diode pumped solid-state lasers

EPS Electrical Propulsion Subsystem

ESA European Space Agency

FCU Flow Control Unit

FP7 7th Framework Programme

GEO Geostationary Orbit

GT Gravity Tractor

IADC Inter-Agency Space Debris Coordination Committee

IBS Ion Beam Shepherd

ITN Initial Training Network

JAXA Japan Aerospace Exploration Agency

KI Kinetic Impactor

LA Laser Ablation

LEO Low Earth Orbit

MOID Minimum Orbit Intersection Distance

NASA National Aeronautics and Space Administration

NEA Near-Earth Asteroid

NIR Near-Infrared

PCDU Power Conditioning and Distribution Unit

PHA Potentially Hazardous Asteroid

PMD Post-Mission Disposal

PPU Power Processing Unit

SBC Spectral Beam Combining

SDM Space Debris Mitigation

SSA Space Situational Awareness

SSO Sun-Synchronous Orbit

TSU Thruster Switch Unit

XFS Xenon Feed System

Appendix A

Correlated Color Temperature

Laser experiments conducted prior to this thesis attempted to verify if the temperature observed under the laser spot matches with the numerical predictions. According to the theoretical model developed earlier, it appears indeed that this temperature is the main driver of the different energy losses and also the key factor in establishing the vaporization rate. This appendix introduces an inexpensive strategy that could be used in complement of the spectral temperature measurements. Spectral measurements imply to record the full spectrum with a spectrometer and use Wien's displacement law to match the recorded peak with the one predicted for a black body. This approach however suffers from two disadvantages. First, most spectrometers have a better sensitivity in the visible range and need therefore a careful calibration procedure to avoid biased temperature measurements. Secondly, using Wien's displacement law means we are discarding the rest of the recorded curve in our temperature assessment.

A.1 Equipment

The laboratory equipment was assembled by Gibbings (2014) and is currently located in the James Watt building at the University of Glasgow. The equipment is visible on figure A.1 in which the vacuum chamber and the laser equipment can be seen. A pressure of the order of a milli-pascal can be reached using a vacuum pump that comprises two stages: a rotatory pump used to remove the majority of the air molecule

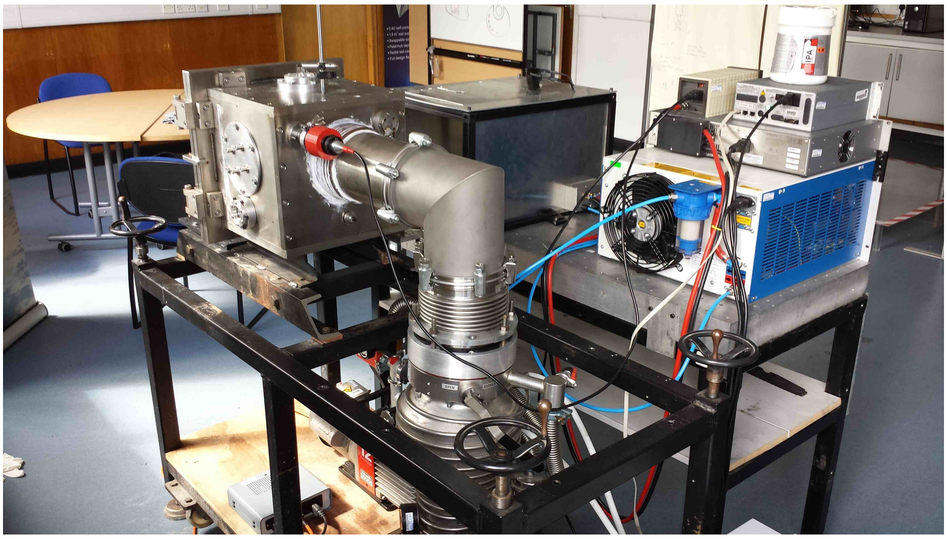

Figure A.1: Laboratory Equipment

in the test chamber and a diffusion pump using heated oil to capture the remaining air molecules. A continuous-wave fiber-coupled diode laser is available with a maximum optical power of 90W and operating in the near-infrared range (808nm).

A.2 Methodology

A non-intrusive approach must be considered due to the high temperature levels predicted. Assuming the asteroid sample approaches the ideal behaviour of a black body, an indirect temperature measurement can be performed by looking the spectrum of the light emitted during the ablation process. Curves on figure A.2 can be computed using the Plank law relating the spectral radiance to the wavelength:

$$S(\lambda) = \frac{2\pi c^2 h}{\lambda^5} \frac{1}{e^{\frac{hc}{\lambda k T}} - 1} \tag{A.1}$$

The peak wavelength can easily be computed in function of the temperature from equation A.1.

$$\lambda_{peak} = \frac{2.898}{1000T} \tag{A.2}$$

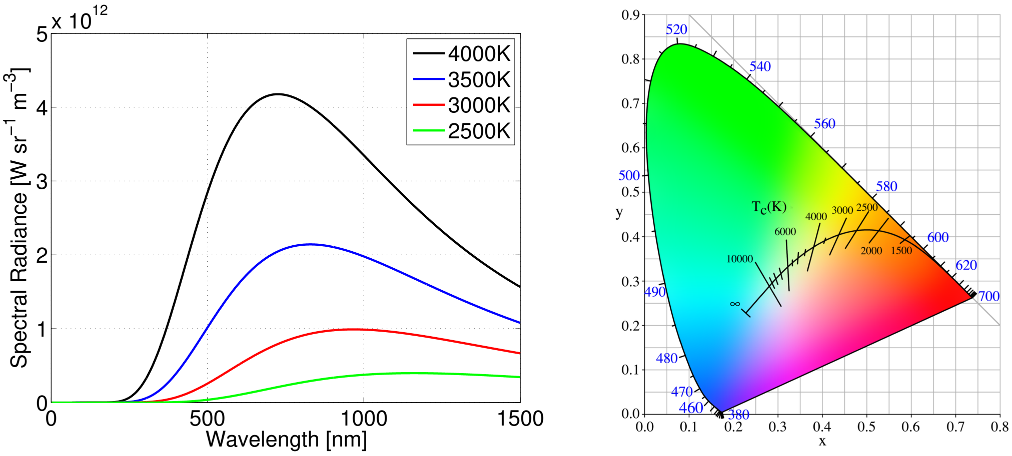

Figure A.2: Spectral radiance of a black body (left) and the CIE 1931 color space and the planckian locus(right)

Therefore, it appears that the higher the temperature is the more its spectrum will be shifted towards the higher frequency range. A logical approach consists thus in using a spectrometer to record the emission spectrum and try to match the peak observed with the appropriate temperature using the Wien displacement law in equation A.2. This technique was used in previous experiments but it leads to results that can be difficult to analyse in the case the sensitivity of the instrument in function of the wavelength is not a flat curve. We show here an alternative technique that can be used in complement of the spectrometer analysis and relies on the color temperatureRobertson (1968). The idea is just to consider a picture taken with a normal camera under the illumination provided by the natural emission of the ablation spot. Indeed each pixel of such a picture carries a temperature information encoded in its RGB combination. From equation A.1, we see that a warmer source will appear as containing more blue colors while a colder source will appear to contain more red colors. Somehow, the RGB information also needs to be processed in order to remove the brightness information which is irrelevant in the temperature determination. Knowing the RGB value, a simple matrix transformation allows to compute the XYZ tristimulus values.

$$\begin{pmatrix} X \\ Y \\ Z \end{pmatrix} = \begin{pmatrix} 2.768892 & 1.751748 & 1.1302 \\ 1 & 4.5907 & 0.0601 \\ 0 & 0.056508 & 5.594292 \end{pmatrix} \begin{pmatrix} R \\ G \\ B \end{pmatrix} \tag{A.3}$$

The proportion of each monochromatic component can then be computed by normalizing each tristimulus value by the luminance:

$$\begin{aligned} x &= \frac{X}{X+Y+Z} \\ y &= \frac{Y}{X+Y+Z} \end{aligned} \tag{A.4}$$

Last but not least, a correlated color temperature can be computed knowing the chromaticity value.

$$\begin{aligned} n &= \frac{x - 0.3320}{y - 0.1858} \\ CCT &= -449n^3 + 3525n^2 - 6823.3n + 5520.33 \end{aligned} \tag{A.5}$$

As an example, figure A.3 shows the application of the color technique to an image recorded during the ablation of a meteoroid sample. The temperature of pixels follows a Gaussian distribution whose average value is consistent with the temperature expected by the model derived in Chapter 3 of this thesis for asteroid materials.

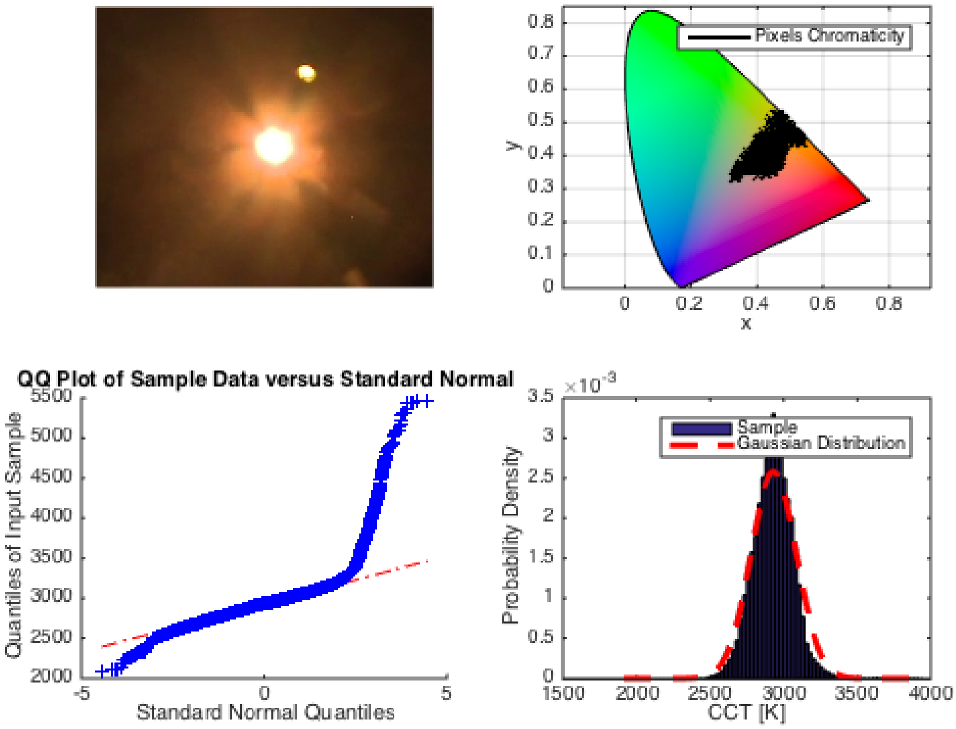

Figure A.3: Application of the colour technique on a picture taken during an ablation test on a meteoroid sample

Appendix B

The nuclear cycler mission concept and design

B.1 General Idea

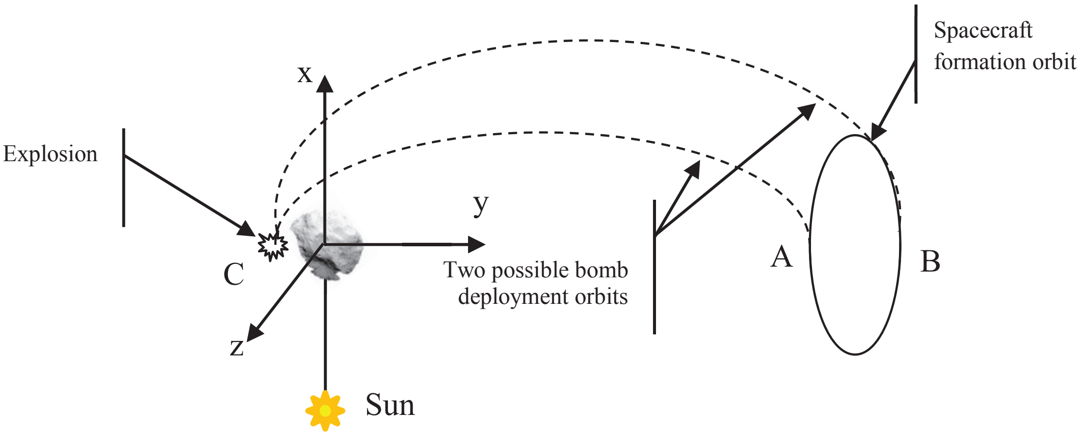

Figure B.1: Sketch (not to scale) of the nuclear cycler concept

The key idea underneath the nuclear cycler concept is to incrementally change the velocity of the asteroid by releasing and detonating a series of relatively small nuclear bombs from a vantage point at a safety distance from the asteroid. Fig. B.1 shows a possible configuration with a carrier-spacecraft flying in formation with the asteroid on a periodic orbit at a distance from the asteroid and releasing two bombs at two different times. The detonation occurs on the far side of the asteroid, with respect to the spacecraft so that the asteroid is shielding the spacecraft from radiations and debris. In this particular configuration, the orbit of the carrier and the one of the bomb are timed in such a way that by the time the bomb goes from point A to point C, the carrier has moved from point A to point B and by the time the bomb goes from B to C, the carrier has moved from B back to A, closing the cycle. A new cycle can now begin. In addition, the data from the previous explosions can be collected and analysed to control the altitude and timing of the subsequent explosions or to control the direction of the resulting $\delta\mathbf{v}$. In the remainder of this paper we will analyse only the special configuration in which point A corresponds to the perihelion of the orbit of the asteroid and point B the aphelion. In this case two bombs are released every revolution of the asteroid around the Sun.

B.2 Trajectory dynamics

The trajectory of the bomb, including the effect of the gravity of the asteroid, can be calculated with a shooting method by back-propagating the trajectory of the bomb from the desired detonation point to the carrier's orbit. The motion of the bombs and of the carrier spacecraft are governed by the following system of proximal motion dynamic equations:

$$\begin{aligned}
\ddot{x} &= -\ddot{r} + 2\dot{\theta}\dot{y} + \dot{\theta}^2 + \ddot{\theta}y - \frac{\mu_{sun}(r+x)}{r_{sc}^3} - \frac{\mu_{\mathrm{PHA}}}{\delta r^3}x + \frac{\partial U_{20+22}}{\partial x} \\
\ddot{y} &= -2\dot{\theta}(\dot{r} + \dot{x}) - \ddot{\theta}(r+x) + \dot{\theta}^2 y - \frac{\mu_{sun}}{r_{sc}^3}y - \frac{\mu_{\mathrm{PHA}}}{\delta r^3}y + \frac{\partial U_{20+22}}{\partial y} \\
\ddot{z} &= -\frac{\mu_{sun}}{r_{sc}^3}z - \frac{\mu_{\mathrm{PHA}}}{\delta r^3}z + \frac{\partial U_{20+22}}{\partial z}
\end{aligned} \tag{B.1}$$

with

$$\begin{aligned}
\ddot{\theta} &= -\frac{2\dot{r}r\dot{\theta}}{r^2} \\
\ddot{r} &= \dot{\theta}^2 r - \frac{\mu_{sun}}{r^2}
\end{aligned} \tag{B.2}$$

where μ_{sun} and μ_{PHA} are the gravity constants of the Sun and the asteroid, respectively. As a first approximation, the asteroid shape can be assumed to be an ellipsoid with $a_{\text{I}} \geq b_{\text{I}} = c_{\text{I}}$ the three semi-axes along the three body-fixed orthogonal axes. The value of the semi-axes is given in Table B.1. Note that the total expelled mass is assumed to be negligible compared to the mass of the asteroid, thus we used the conservative assumption that the mass of the asteroid remains unchanged. Furthermore, in the reduced model presented in this chapter, the spinning rate and axis are assumed to remain constant.

Table B.1: Orbital and physical properties of test asteroid.

Element		Measured Value
Semi-major axis	a_0	0.9224 AU
Eccentricity	e_0	0.1912
Period	T_0	323.5969 days
Mean motion	n_0	1.2876 $\times 10^{-5}$ deg/s
Mass	m_A	2.7×10^{10} kg
Gravitational constant	μ_{PHA}	$1.801599\times10^{-9} km^3/s^2$
Physical dimensions	a_I, b_I, c_I	196 m, 112 m, 112 m
Rotational velocity	w_{PHA}	3.3×10^{-3} deg/s
Total vaporisation Enthalpy	E_v	15 MJ/kg
Density	ρ_{PHA}	2650 kgs/m^3

The axis c_{I} is assumed to be aligned with the vector of angular momentum, which corresponds to the z-axis of the asteroid Hill frame $\mathcal{A}$ (see Fig. 4.1b). The gravity field of the asteroid is expressed as the sum of a spherical field $\frac{\mu_{\text{PHA}}}{\delta r^2}$ plus a second-degree and second-order field (Hu and Scheeres, 2002; Rossi et al., 1999):

$$U_{20+22} = \frac{\mu_{\text{PHA}}}{\delta r^3} \left[C_{20} \, (1 - \frac{3}{2} \cos^2 \varphi) + 3C_{22} \, \cos^2 \varphi \cos 2\alpha \right] \tag{B.3}$$

where φ is the elevation over the x-y plane and the harmonic coefficients C_{20} and C_{22} are a function of the semi-axes,

$$\begin{aligned} C_{20} &= -\frac{1}{10}(2c_{\text{I}}^2 - a_{\text{I}}^2 - b_{\text{I}}^2) \\ C_{22} &= \frac{1}{20}(a_{\text{I}}^2 - b_{\text{I}}^2) \end{aligned} \tag{B.4}$$

and α is defined as,

$$\alpha = \arctan\left(\frac{y}{x}\right) + w_{\text{PHA}} t$$

The initial conditions for the backward integration, in the case the bomb is released from point B, are:

$$\begin{aligned} x(\theta = 0) &= 0 \\ y(\theta = 0) &= y_C \\ z(\theta = 0) &= 0 \\ \dot{x}(\theta = 0) &= \delta v_C \cos\gamma \\ \dot{y}(\theta = 0) &= \delta v_C \sin\gamma \\ \dot{z}(\theta = 0) &= 0 \end{aligned} \tag{B.5}$$

The modulus of the velocity δv_C was varied from $v_{ex} + \epsilon_{ex1}$ to $v_{ex} + \epsilon_{ex2}$, with $v_{ex} = \sqrt{\frac{2\mu_{\text{PHA}}}{y_c}}$ at distance y_C from the centre of the asteroid, while the γ angle was constrained to be in the interval $[0.6 \quad \pi/2]$. The trajectory was then propagated backward for a true anomaly $\Delta\theta = \pi$ using an adaptive Runge-Kutta, Dormand-Prince scheme implemented in the $Matlab^{©}$ function $ode45$, with absolute and relative tolerance equal to $1e$-6 and $1e$-7 respectively. If the bomb is released from point B, the arrival conditions need to satisfy the constraints:

$$x(\theta = \pi)^2 + (y(\theta = \pi) - y_{\text{B}})^2 + z(\theta = \pi)^2 = 0 \tag{B.6}$$

This analysis, however, assumes that for each value of δv_{C} a particular spacecraft formation orbit is targeted, rather than targeting always the same orbit.Therefore, the $Matlab^{©}$ function $fmincon$ was used to find the optimal value of γ that satisfies the relaxed soft constraint $x(\theta = \pi)^2 + z(\theta = \pi)^2 = 0$ for different values of δv_{C}. As it is shown in Figs. B.2 this yields a continuous and compact set of trajectories. The minimum distance from the asteroid however is limited by the need to have the the bomb completing the transfer in half a revolution of the asteroid around the Sun. For low values of δv_{C} the gravity of the asteroid accelerates the turning of the velocity of the bomb leading to a crossing of the y-axes in less than half a period. The value of δv_C in this analysis, therefore, was set to quickly clear the Hill's sphere of influence of the asteroid. Figs. B.2 show a set of optimised trajectories superimposed to the theoretical ones obtained using the linear proximity equations. Fig. B.2a shows the case in which $y_C = -0.1287$ km, $\epsilon_{ex1} = -1.44917e - 5$ km/s and $\epsilon_{ex2} = -1.42417e - 5$ km/s while Fig. B.2b shows the case in which $y_{\rm C} = -0.210$ km, $\epsilon_{ex1} = 8.1178e - 6$ km/s and $\epsilon_{ex2} = 8.3678e - 6$ km/s. These two cases correspond to an optimal explosion along the semiminor and semimajor axes of the asteroid, respectively. Note that, according to Fig. 4.4, a variation of 81.3 m in the detonation altitude significantly decreases the effectiveness of the explosion. On the other hand, it is possible to find trajectories from point A or point B to any point C in the interval $[-0.1287, \;\; -0.210]$ hence it is possible to target the optimal detonation distance for each explosion. Fig. B.3 shows a close up of Fig. B.2a around point C. One can see that the bomb would approach the asteroid almost head on, although $\delta v_{\rm C}$ is so small that was neglected in the calculation of the deflection δv. In this, analysis the assumption is that the bomb has a guidance, navigation and control system that can compensate for any additional effect, like light pressure.

The propellant cost to deploy each bomb can be evaluated by computing the velocity difference at points A and B of the trajectory of the bomb and the trajectory of the spacecraft. The magnitude of the deployment Δv manoeuvre, at the beginning of the deflection cycle, is reported in Fig. B.4 for point A and B and for the two detonation altitudes. This translates into a mass fraction of maximum 5.546e-5 per bomb assuming a cold gas engine with an $I_{sp} = 68s$. Finally, the formation orbit of the carrier designed with the linear proximity equations (4.3) were reoptimised to keep into account the full dynamics. A small $\mathbf{\Delta v}$ correction manoeuvre was inserted at A and B to match the A-to-B trajectory with the B-to-A trajectory such that the A and B point remain the initial conditions of the bomb deployment trajectories and the periodicity of the formation orbit is maintained. The optimised correction manoeuvres, however, are of negligible size, even lower than the deployment manoeuvres, and are not reported here.

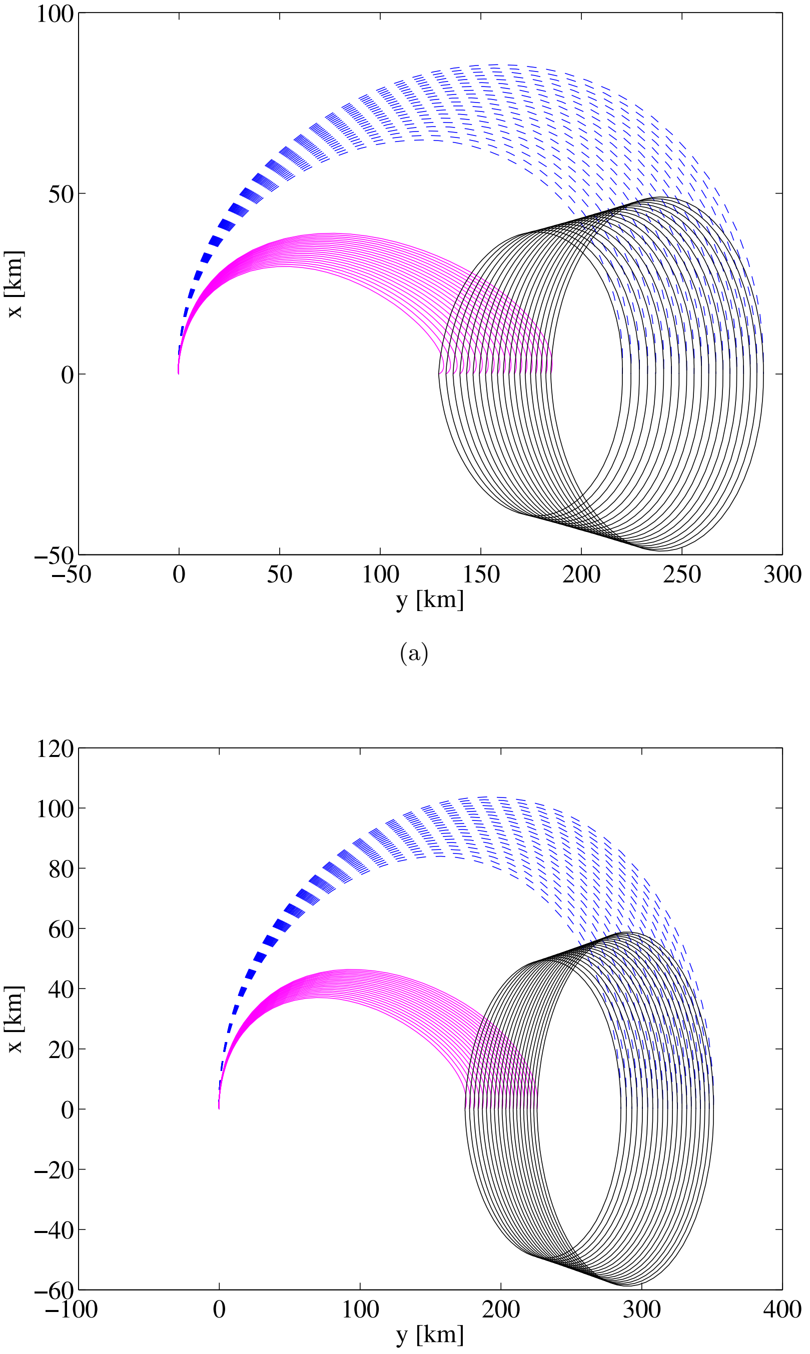

(a)

(b)

Figure B.2: Families of formation and deployment trajectories for spacecraft and bombs: a) detonation point at 210m, b) detonation point at 128m.

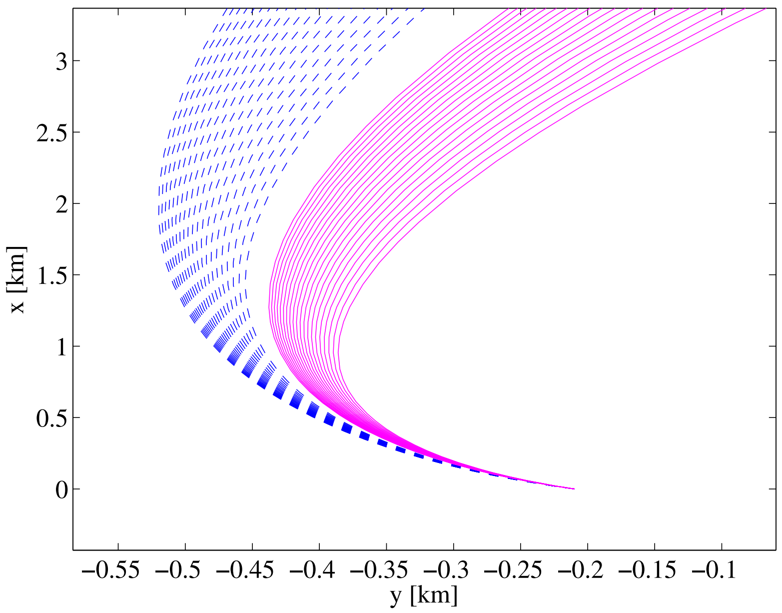

Figure B.3: Close up of the families of deployment trajectories for a detonation point at 210m.

At every explosion the velocity of the asteroid is modified and so are its orbital elements. As a consequence, the carrier needs to manoeuvre to maintain its relative orbital motion with respect to the asteroid. For the strategy presented in this paper, there is no out of plane component of the deflection, therefore, the spacecraft needs only an in-plane $\Delta \mathbf{v}_c$ correction. The component of this correction along the tangential direction has to compensate for the variation of the semimajor axis of the asteroid and, therefore, is of the same magnitude of δv_t in Eq.$\tilde{(}$4.1). Given that the explosion occurs at the apsidal points then $\delta v_t = \delta v$. Therefore, it is here assumed that the spacecraft compensates only for a variation in a and e with a single manoeuvre equal to δv at each explosion. This does not restore completely the exact initial proximal motion but guarantees anyway to maintain the formation with the asteroid. Furthermore, the result in Figs. B.2 demonstrates that one can generate a continuous set of formation orbits, at different distances from the asteroid, reaching the detonation point with different values of δv_{C}, hence at every explosion a new bomb deployment trajectory can be defined provided that the spacecraft maintains formation.

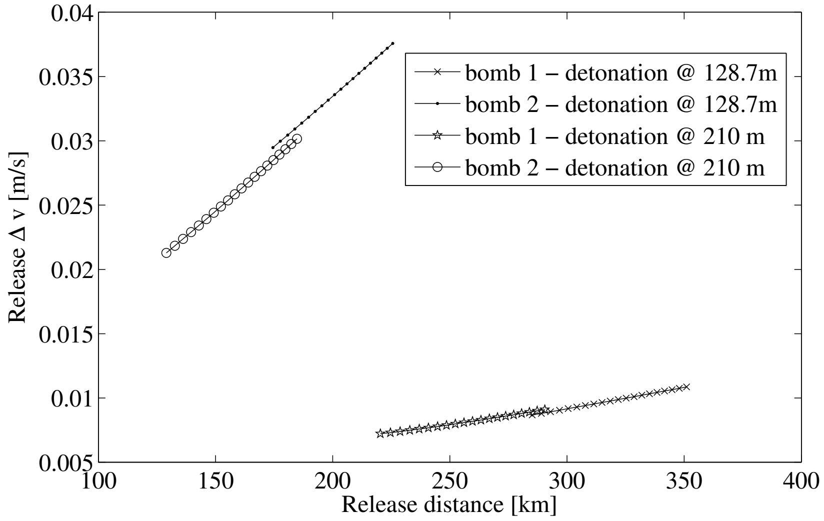

Figure B.4: Total Δv at the point of release of the bomb from the spacecraft

B.3 Comparison Between a Single Detonator and the Nuclear Cycler

The nuclear cycler method has been applied to the case of an Apophis-like asteroid considering two different warning times of 6 years and 3 years respectively. The warning time is here defined as the time from the first explosion to the expected impact of the un-deviated asteroid with the Earth. Relevant properties of this asteroid can be found in Table B.1. The initial inclination, right ascension, argument of the pericentre and mean anomaly were set so that the asteroid impacts the Earth on 13140 MJD.

An interesting first result is obtained by computing the total δv produced by either a single or a fractionated detonation for the same total mass of the bombs. The results of our model, in Fig. B.5, indicate that a fractionated explosion may be better than a single explosion for the same total mass. The explanation of this result is in the dependency of the δv on the view angle λ in Eq. (4.37) and the penetration depth z_{max}. Figure B.6 shows the optimal detonation altitude as a function of the spacecraft mass for a single interceptor. One can see that the optimal altitude is indeed lower for a smaller bomb, therefore, the fraction of the total released energy actually reaching the asteroid is bigger in this case.

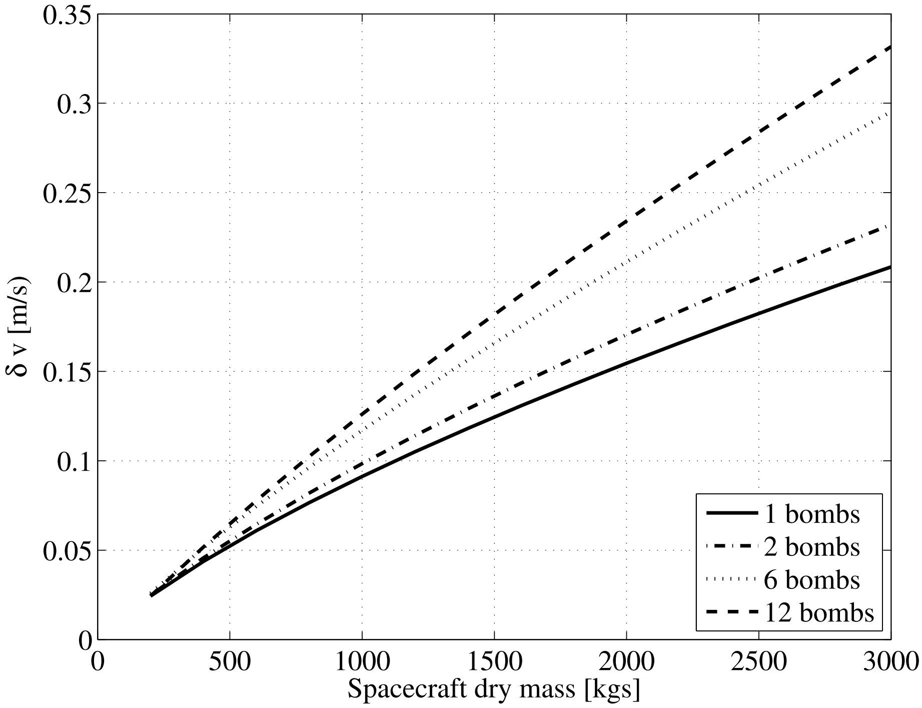

Figure B.5: Total δv as a function of the dry mass of the spacecraft for different numbers of explosions

However, once the deflection parameter b is used as performance indicator, one can see, in Figs. B.7, that the single interceptor method outperforms the cycler one, thanks to the fact that the whole velocity variation is delivered at the very beginning of the first cycle and thus its effect propagates for a longer period. The comparison is done by considering identical dry masses of the spacecraft with the cumulative mass of the nuclear bombs representing 30 % of the total dry mass of the spacecraft in both cases. For the single interceptor method, the whole mass of the spacecraft contributes to the ejecta, whereas only the mass of the bombs contributes to ejecta for the cycler method. Last but not least, in both cases, the detonation occurs at the optimal altitude. As one would expect, Figs. B.7 show that a longer warning time is beneficial in term of deflection distance. Also, a warning time of only 3 years constrains the maximum number of explosion to 6 for the nuclear cycler method if explosions occur only at the apsidal points. Another interesting result is obtained by normalising the value of the b parameter obtained for the case of a fractionated detonation with the result of the

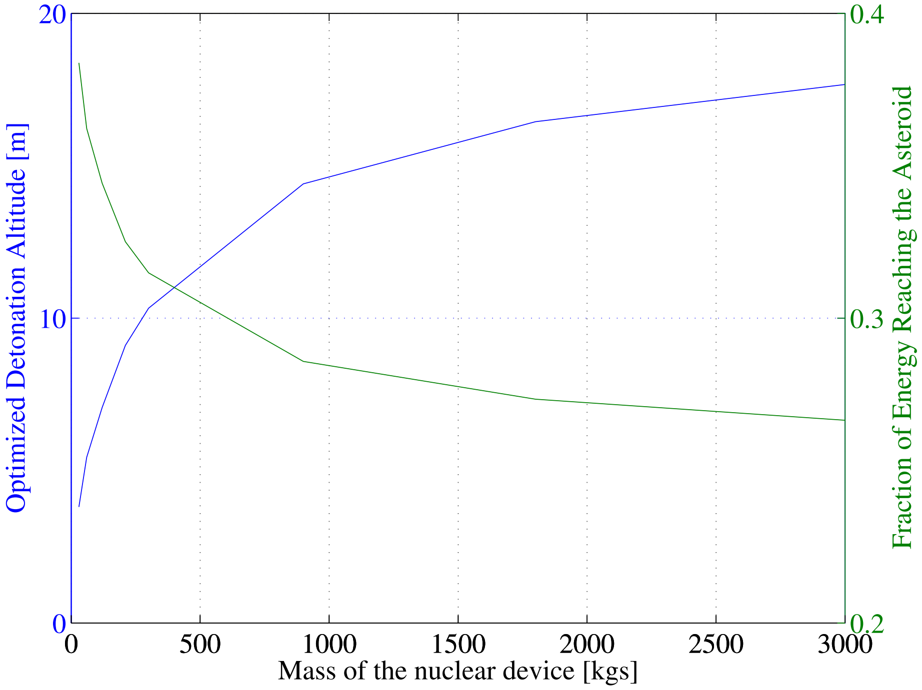

Figure B.6: Optimal altitude of detonation and fraction of the total energy reaching the asteroid for different sizes of the nuclear device

single interceptor method. The results in Figs. B.8 indicate that the mass efficiency (the ratio between b parameter and mass of the spacecraft) can be as low as 40% for small spacecraft and reduces to 75% for larger spacecraft. Note the interesting overtaking between the curves for 2 and 6 explosions for the 6 years lead time case when a mass larger than 1 ton is considered.

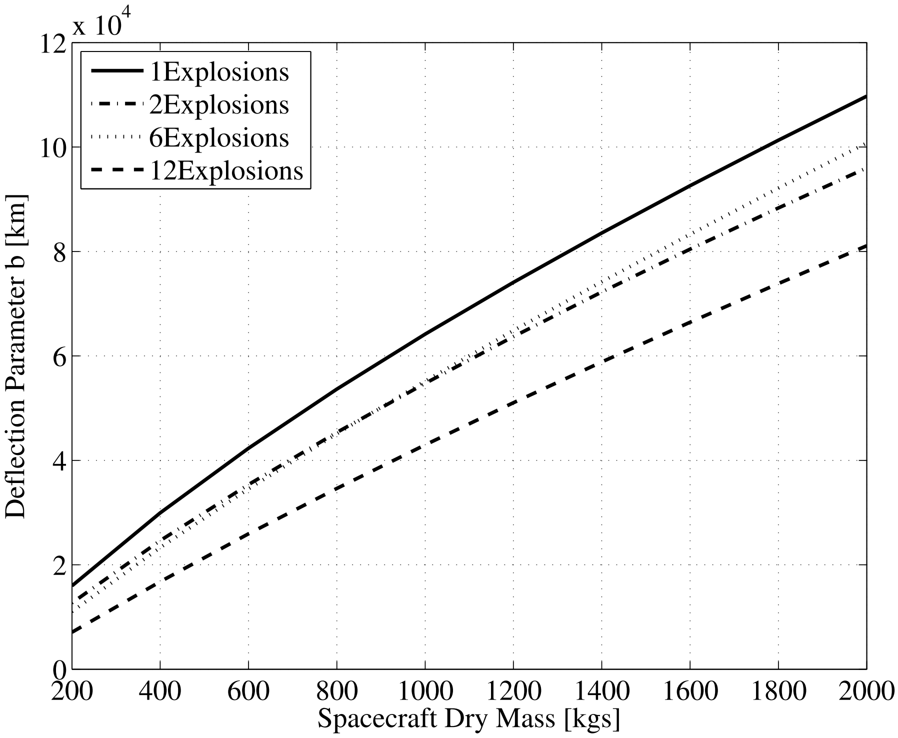

(a)

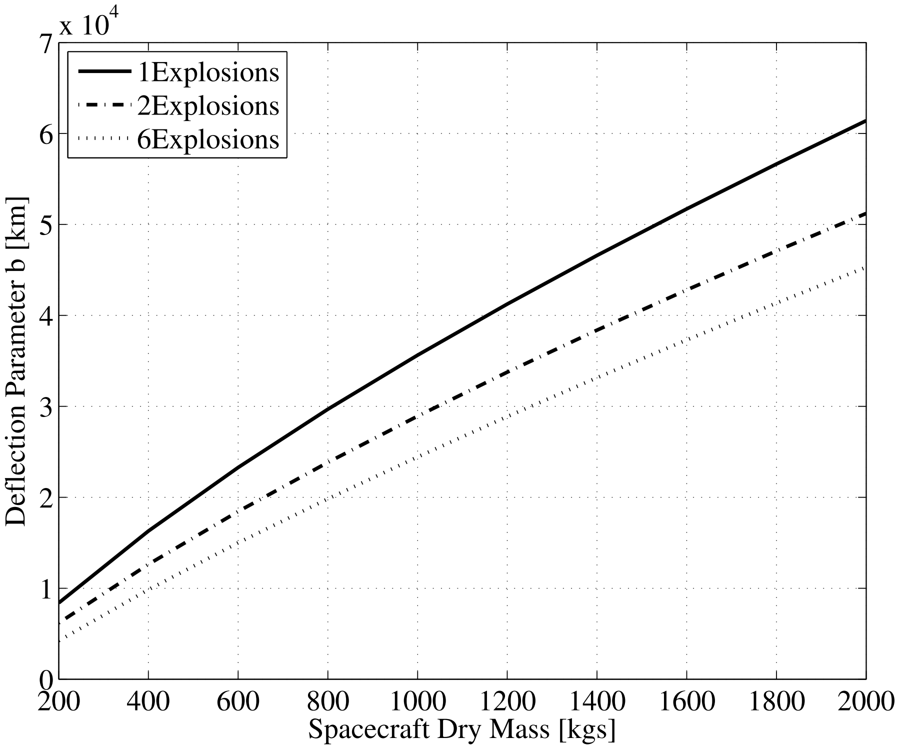

(b)

Figure B.7: Impact parameter for a varying number of explosions: a) 6 years lead time, b) 3 years lead time.

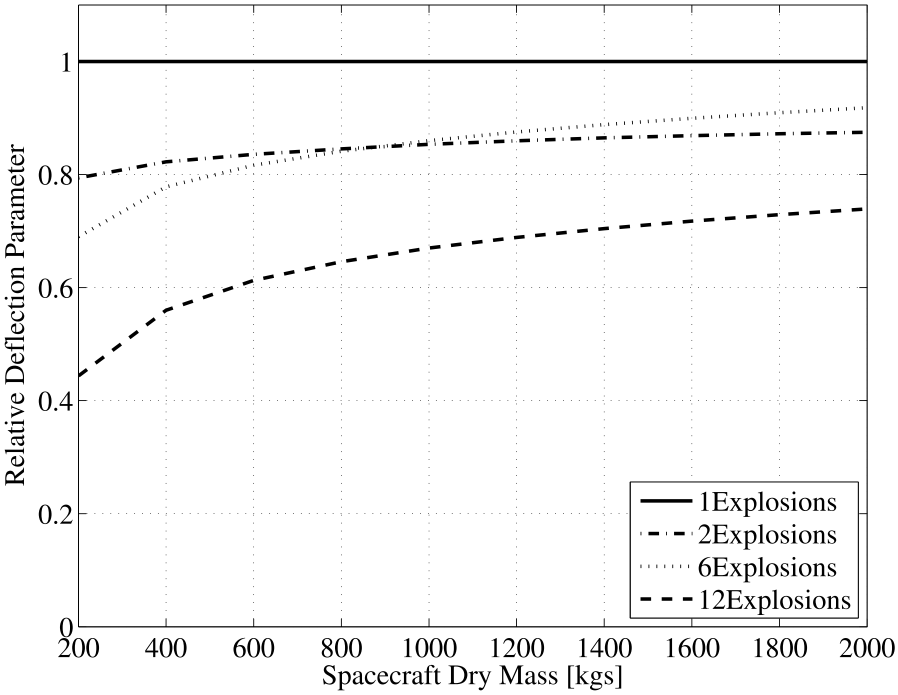

(a)

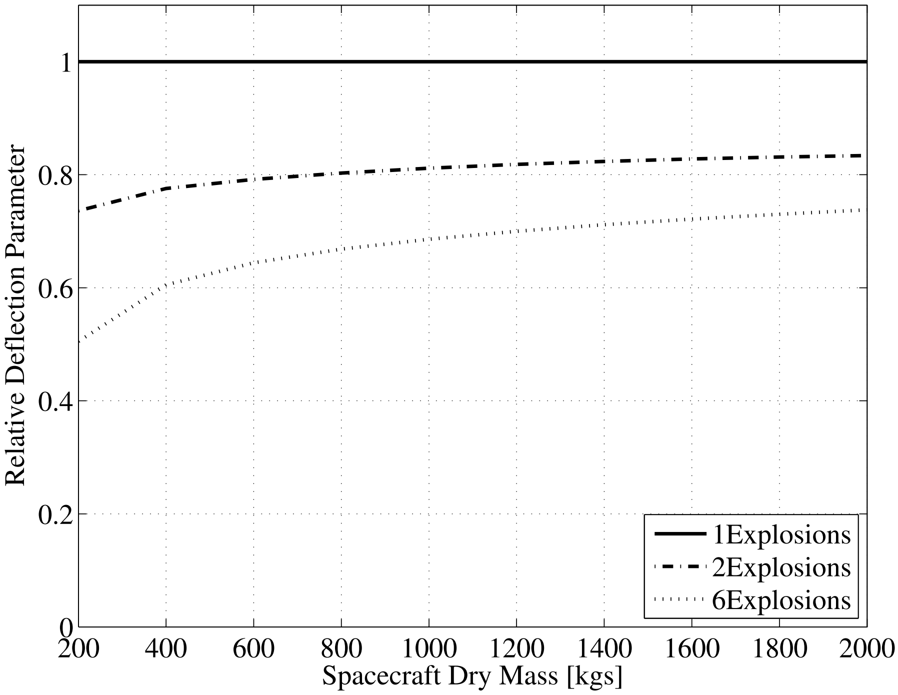

(b)

Figure B.8: Efficiency of the nuclear cycler method compared to the single interceptor method: a) 6 years lead time, b) 3 years lead time.

Appendix C

Spacecraft bus architecture for a laser deflection mission to an asteroid

The spacecraft is built around a cylinder containing the Xenon tank and the hydrazine tank. The Xenon tank will occupy an approximate volume of 260L which, assuming a spherical shape, would require sphere of diameter 0.8m. A parallelepiped shape with the dimensions 2m×1.6m×1.6m could easily fit in a medium launcher fairing while accomodating the tank, payload and all the other subsystems. A general configuration for the different panels of this box can be described as following:

- -X and +X Panels: Each panel supports one PPS-5000 thruster of 300mm diameter and the -X panel also features the marman ring (about 900mm diameter for Soyouz) through which the spacecraft is attached on the adaptor within the launcher fairing. The +X panel will also support the 2 star tracker cameras and a 140mm diameter opening through which the laser beam is exiting.
- -Y and +Y Panels: The -Y panel which is facing the sun during the nominal operations will carry the high gain antenna while the +Y panel will support the laser system and its optics which will be directly mounted on a 2m×1.6m radiator
- -Z and +Z Panels: Each face supports a 10.3m^2 solar array wing as well as a pair

of 1.2m^2 radiators which are mounted on the chassis on each side of the wing.

The architecture of the different spacecraft subsystems is detailed in the next paragraphs.

C.1 Electric Propulsion Subsystem

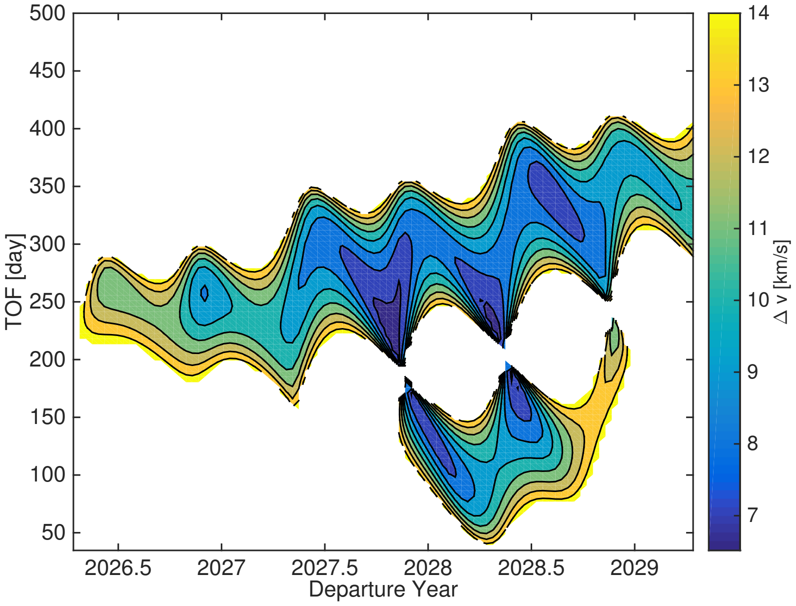

Figure C.1: Impulsive transfer cost as a function of the departure date and ToF

The transfer phase to the target needs to be considered. On figure C.1, one can see that an optimal transfer would require 6.5km/s using impulsive manoeuvres. The Tsiolkovski equation can be used to estimate the propellant mass required to achieve the transfer:

$$m_{prop} = m_{dry}\left(\exp\left(\frac{\Delta v}{I_{sp}g_0}\right) - 1\right) \tag{C.1}$$

Considering a LOX/LH2 combination with an I$_{sp}$ of 442s and a dry mass of 875kgs one can check with equation C.1 that the propellant required would amount to about 3 tons in order to achieve the minimum impulse required. Thus, a low-thrust transfer strategy should be favoured. Despite requiring a slightly higher Δv(which we assume

here around 8km/s, lacking better information at this stage), the higher Isp of an Ion engine allows significant mass savings due to the lower propellant mass.
A typical EPS architecture comprises the following elements:

- The thruster assembly which includes in this case the thrusters and the gimbals on which they can be mounted to change control the thrust orientation.
- The Power Processing Unit (PPU) which supplies the high voltage current required for the ion engines to work efficiently. The PPU usually also includes the Thruster Selection Unit (TSU) which allows to select which thruster is controlled by the PPU.
- The Xenon Feed System (XFS) or Flow Control Unit (FCU) which usually includes a high pressure tank, a Xenon Control Assembly (XCA) which regulates the pressure and Xenon flow rate to the thrusters and the plenum tanks. The mass of the XFS is typically around 12kgs, excluding the Xenon tank which is assumed to scale linearly with the propellant mass. The Dawn Xenon tank had a volume of 269L, could store up to 425kgs of Xenon and had a mass of 21.6kgs, giving a tankage fraction of 5.1%.

Three options were considered for the mission:

- option 1: A configuration with 2 Snecma PPS-5000 and 2 PPUs (with only one engine working at a time), offering the highest level of thrust but also the lowest Isp and therefore requiring more propellant.
- option 2: A configuration with 3 NSTAR engines (with 2 of the 3 engines working in the same time) which is essentially the same as the one use in the Dawn mission.
- option 3: A configuration with 2 QinetiQ T6 engines and 2 PPUs (with only one engine working at a time) which can be seen as a downscaled version of Bepicolombo's transfer module. This option offers the lowest thrust level but also the highest Isp and thus requires less propellant and less mass.

Table C.3 shows a comparative review of each option. Note that the dry masses for each option vary slightly due to the parametric models involved to estimate the mass of the Xenon tank, spacecraft structure and harness respectively. The thrust duration represents the time required to achieve a Δv of 6km/s in each scenario. Despite the higher mass, one can see that the first option allows for a faster thrust time. Also, a configuration with 2 engines would allow to place each of them on the opposite panels which could be advantageous during the later station-keeping operations in the vicinity of the asteroid. Moreover, Hall effect plasma thrusters are less sensitive to contamination issues. The configuration with the 2 Snecma PPS-5000 and 2 PPU/TSU units[1] is thus considered in the following. Note that the configuration selected could also be employed by an Ion Beam Shepherd mission so that with minor modification, the current design could serve for a dual demonstration mission comparing the capability of both IBS and Laser Ablation deflection technologies.

Table C.1: EPS Choice

Type	PPS-5000	2×NSTAR	QinetiQ T6
Power	5000W	2× 2300W	5000W
Thrust	240mN	2×91mN	145mN
Isp	2300s	3120s	4190s
Configuration			
PPU	2×14.5kgs	2×14.5kgs	2×14.5kgs
Thrusters	2×8.4kgs	3×8.4kgs	2×8.4kgs
XFS (excluding tank)	15kgs	15kgs	15kgs
Tank	21kgs	13.6kgs	9.4kgs
Performance			
EPS Dry Mass	81.7	74.4	70.1kgs
S/C Dry Mass	995.2kgs	921.1kgs	877.8kgs
Propellant	411kgs	267.4kgs	183.4kgs
Thrust duration	10722h/447d	15663h/653d	14427h/601d

C.2 Power Sub-System

The power subsystem must provide the required power for both the laser system and the electric engine. The electric engine is switched off while the laser is operating and

---

[1] `http://articles.adsabs.harvard.edu/cgi-bin/nph-iarticle_query?bibcode=2004ESASP.555E..65B&db_key=AST&page_ind=2&plate_select=NO&data_type=GIF&type=SCREEN_GIF&classic=YES`

vice-versa. Taking into account the 95% of high voltage conversion by the PPU to the plasma thruster and 96% of efficiency of the PCDU unit delivering the power from the solar panels to the different subsystems, the total power required was estimated around 6.43kW in order to fulfil the mission objectives. This number also account for a margin of 10% and an additional 560W for the avionics parts and AOCS subsystems. Over its lifetime, the solar panels will be subjected to different sources of radiations such as the solar proton flux or the galactic cosmic rays. The equivalent fluence of 1MeV particles was assumed not to exceed 1E+15 with a coverglass thickness of 100μm. This corresponds to an end of life efficiency of 26.6% if one considers using of the triple junction GaAs solar cells from azurspace [2]. Considering a relatively standard packing efficiency of 85%, one can compute from this that 2 solar array wings of 10.3m^2 each will be sufficient to fulfil the different power requirements.

Table C.2: Power subsystems mass budget

Component	number	CBE(kgs)	DMM(kgs)	CBE + DMM(kgs)
SA wing (10.3m^2)	2	26.5	5.4	31.9
PCDU	1	25	5	30
Total	-	78.1	15.7	93.8

C.3 Thermal Subsystem

The thermal subsystems will make use of a combination of honeycomb panels and heat pipes in order to maintain an acceptable temperature for the subsystems. The area of the radiators can be estimated from their working temperature is assumed to be 298K:

$$S_{radiators} = \frac{P_{dissipated}}{\epsilon \sigma T^4_{radiator}} = 7.6m^2 \tag{C.2}$$

Strapping the radiators to existing structural panels should enable an areal density as low as 5kgs/m^2, which accounting for a 10% margin gives a radiator mass of 41 kgs.

---

[2] `http://www.azurspace.com/images/pdfs/HNR_0003429-01-00.pdf`

C.4 AOCS Subsystem

The AOCS consists of 4 RSI 45-745/60 reaction wheels placed in a redundant tetrahedral configuration. To these a combination of 1N-hydrazine thrusters are added to facilitate orbit insertion and proximity manoeuvres required to compensate for the perturbations coming mainly from the solar radiation pressure on the solar wings. The other perturbations, coming mainly from the gravity of the asteroid and the laser recoil force can be compensated by the electric propulsion system (as they will act along the same axis) and should require only a negligible amount of Xenon propellant.

Table C.3: Perturbations

Quantity	SRP	Gravity	Laser Recoil
Formula	$\frac{P_{sun}}{c_{light}}$	$G\frac{m_{ast}m_{dry}}{d^2}$	$\frac{P_{laser}}{c_{light}}$
Force	$94\ \mu N$	$56.7\ \mu N$	$8.3\ \mu N$

Assuming complete absorption of light by the solar arrays, the amount of hydrazine propellant to compensate the SRP during 7 years can be computed as:

$$m_{hydrazine} \approx \frac{S_{arrays} \cdot 1371}{I_{sp}c_{light}g_0} \cdot 86400 \cdot 7 \cdot 365.242 \approx 25kgs \tag{C.3}$$

Considering a 20% margin, this amounts to 30kgs of hydrazine propellant. The AOCS will also include 2 star tracker cameras with a mass of 2kgs each.

C.5 Avionics

The avionics part comprises the non-scalable parts such as antennas and on-board computers. Those are assumed to represent 50kgs in the present study.

C.6 Structure & Harness

Parametric models are used for the structure and harness which are assumed to represent 20% and 5% of the launch mass respectively.